Progress in Materials Science 152 (2025) 101433

Contents lists available at ScienceDirect

Progress in Materials Science

journal homepage: www.elsevier.com/locate/pmatsci

MXenes and its composite structures: synthesis, properties, applications, 3D/4D printing, and artificial intelligence; machine learning integration

Vimukthi Dananjaya [a], Nethmi Hansika [b], Sathish Marimuthu [c], Venkata Chevali [d], Yogendra Kumar Mishra [e], Andrews Nirmala Grace [c], Nisa Salim [a], Chamil Abeykoon [f,*]

[a] School of Engineering, Swinburne University of Technology, Hawthorn, VIC 3122, Australia
[b] Department of Computer Engineering, Faculty of Engineering, Open University, Nawala, Sri Lanka
[c] Centre for Nanotechnology Research (CNR), Vellore Institute of Technology, Vellore 632014, Tamil Nadu, India
[d] Centre for Future Materials, University of Southern Queensland, Springfield Central, QLD 4300, Australia
[e] Mads Clausen Institute, NanoSYD, University of Southern Denmark, Alison 2, Sønderborg 6400, Denmark
[f] Northwest Composites Centre, Aerospace Research Institute, and Department of Materials, Faculty of Science and Engineering, The University of Manchester, Oxford Road, M13 9PL Manchester, UK

ARTICLE INFO

Keywords:
2D materials
Additive manufacturing
Transition metal carbides
Predictive modelling
Functional nanostructures

ABSTRACT

MXenes, a revolutionary class of two-dimensional transition metal carbides and nitrides, have emerged as exceptional materials for advanced composite applications due to their remarkable properties. MXene-based composites exhibit electrical conductivities exceeding 15,000 S/cm, thermal conductivities up to 60 W/m·K, and mechanical strengths surpassing 500 MPa, making them ideal for applications in energy storage, aerospace, and biomedical engineering. This review explores the synthesis of MXene-filled composites via chemical etching, intercalation (enhancing layer spacing by 20–50%), and functionalization (improving compatibility by 70%), and highlights how these processes shape the material's properties. Applications are discussed, including lithium-ion batteries with capacities exceeding 300 mAh/g and supercapacitors achieving energy densities over 60 Wh/kg. Furthermore, the integration of MXene composites into 3D printing technology enables resolutions as fine as 100 microns, offering unprecedented customization and

Abbreviations: ML, machine learning; d-MAX, derivatives of MAX components; DFT, density functional theory; 2D, two dimensional; 3D, three dimensional; STEM, scanning transmission electron microscope; SAED, selected area electron diffraction; SEM, scanning electron microscope; XRD, x-ray diffraction; TBAOH, tetrabutylammonium hydroxide solution; QD, quantum dots; TEM, transmission electron micrograph; MQD, MXene quantum dots; PL, photoluminescence; UV, ultra violet; UV-Vis, ultra violet-visible; DADS, decay-associated difference spectra; XPS, X-ray photoelectron spectroscopy; FTIR, fourier transform infrared spectroscopy; DMSO, dimethylsulfoxide; DMF, dimethylformamide; EDX, energy-dispersive X-ray spectrum; NMR, nuclear magnetic resonance; ZIB, zinc ion batteries; MOF, Metal-organic frameworks; LUMO, lowest unoccupied molecular orbitals; HOMO, highest unoccupied molecular orbitals; PVA, polyvinyl alcohol; PTP, Push-to-Pull; SPS, spark plasma sintering; DC, chemical dicatechol-6; MX, MXene nanosheets; VP, violet phosphorus; SBR, styrene-butadiene rubber; PBO, poly(p-phenylene-2,6-benzobisoxazole) iron oxide (Fe_3O_4) nanoparticles; PU, polyurethane; PA, polyamide; GO, graphene oxide; APTES, 3-aminopropyl triethoxysilane; EAA, poly (ethylene-co-acrylic acid); PBAT, poly (butylene adipate-co-terephthalate); OTR, oxygen transmission rate; WVPR, water vapor transmission rate; PDAEMA, poly(2-(dimethylamino)ethyl methacrylate); PEI, polyethyleneimine; SRNF, solvent-resistant nanofiltration; OTES, n-octyltriethoxysilane; OTAB, octadecyl trimethylammonium bromide; DDAB, didodecyldimethylammonium bromide.

* Corresponding author.
E-mail address: chamil.abeykoon@manchester.ac.uk (C. Abeykoon).

https://doi.org/10.1016/j.pmatsci.2025.101433
Received 9 September 2024; Received in revised form 2 January 2025; Accepted 12 January 2025
Available online 20 January 2025

precision in manufacturing. Machine learning plays a pivotal role in optimizing synthesis protocols, accelerating material discovery by 30–50%, and achieving predictive modeling accuracies above 90%, thereby revolutionizing the design and performance of MXene-based materials. This review will also presents a data-driven perspective on the synthesis, properties, and applications of MXene-filled composites, bridging advanced research and practical innovation to inspire transformative advancements across multiple industries.

1. Introduction

The field of material science and engineering has witnessed unparalleled advancements in recent times due to the convergence of sophisticated materials [1-3], additive manufacturing technology [4,5], and artificial intelligence [6,7]. The remarkable mechanical, thermal, and electrical capabilities of the MXene family of two-dimensional transition metal carbides/nitrides set them apart from the plethora of materials at the vanguard of this technological convergence [8,9]. In recent years, there has been a surge in interest in MXenes due to their extraordinary properties and wide variety of applications. The 2D transition metal carbides, nitrides, and carbonitrides in the MXenes family are distinguished by their high surface area, exceptional electrical conductivity, and mechanical robustness. The 'A' layer from MAX phases is usually selectively removed during their synthesis, and then different treatments are used to customize their characteristics for specific uses [8]. MXenes are excellent prospects for a wide range of applications due to their unique features, which include superior chemical stability [10], a highly electronic structure [11], and a high surface-to-volume ratio [12].

MXene improves materials' overall performance when added to composite constructions, and it also creates new opportunities for use in the energy [13], aerospace [14], healthcare [15], and environmental industries [16]. MXenes are incredibly effective in storing energy when used as electrode materials in supercapacitors [17], batteries [18], and electrochemical capacitors [19]. They have improved charge storage and quicker electrochemical kinetics because of their high conductivity, broad surface area, and superior ion transport characteristics. Furthermore, because of their surface chemistry, durability in adverse environments, and catalytic activity, MXenes have become effective catalysts for various electrochemical processes [20]. MXenes also have outstanding sensing properties and are used in gas sensing, biological diagnostics, and environmental monitoring [21]. Because of its vast surface area, chemical sensitivity, and electrical properties, analytes may be detected with high sensitivity and selectivity. Furthermore, MXenes show promise in medicinal applications such as drug delivery [22], tissue engineering [23], and bioimaging [24] due to their biocompatibility, adaptable surface chemistry, and ability to interact with biological molecules [25,26]. Overall, MXenes' remarkable qualities, distinct synthesis pathways, and range of valuable uses highlight their promise as revolutionary materials in several scientific and technological domains.

3D printing, a sub-sector of additive manufacturing, has emerged as a state-of-the-art method that gives precise control over composition and geometry for building complex objects [27]. The production of MXene-based materials and their composites has increased over the last several decades through 3D printing processes [28]. 3D printing's versatility allows for the creation of intricate MXene structures with unique properties, which speeds up the manufacturing of helpful parts and gadgets. Researchers may use MXenes' unique qualities, such as high electrical conductivity, mechanical strength, and chemical stability, to give printed products

PHRR, peak heat release rate; HPSi, hyperbranched polysiloxane; PTFE, polytetrafluoroethylene; LLDPE, Linear low-density polyethylene; PEG6-COOH, polyethylene glycol carboxylic acid; TENG, triboelectric nanogenerators; EMI, electromagnetic interference; PEO, polyethylene oxide; CNF, cellulose nano fibres; PS, polystyrene; DTAB, dodecyltrimethylammonium bromide; DDAB, dodecyldimethylammonium bromide; PEDOT:PSS, Poly (3,4-ethylenedioxythiophene) polystyrene sulfonate; PVF, Polyvinylidene fluoride; RuNP, Ru nanoparticles; RuSA, Ru single-atom; CV, cyclic voltammetry; EIS, electrochemical impedance analysis, and LSV, linear sweep voltage; HER, hydrogen evolution reaction; TOF, turn over frequency; GNP, graphene nanoplatelets; CNT, carbon nanotubes; COF, coefficient of friction; FLM, few layered mxene; LDH, layered doubled hydroxide; EMA, electromagnetic wave absorption; CMC, ceramic matrix composites; β-HBD, β-hydroxybutyrate dehydrogenase; DPV, differential pulse voltammetry; DIW, direct ink writing; IJP, inkjet printing; MWCNT, multiwalled carbon nanotubes; PAM, polyacrylamide; ANF, aramid nanofibres; IR, infrared; MSC, MXene micro supercapacitor; TEMPO, (2,2,6,6-tetramethylpiperidine-1-oxylradical)-mediated oxidized; VOC, volatile organic compounds; CVD, chemical vapour deposition; CT, computed tomography; PTT, photothermal therapy; POM, polyoxometalates; PDT, Photodynamic therapy; PSs, Photosensitizers; ROS, reactive oxygen species; HU, hounsfield units; MNOH, MXene nanocomposite organohydrogel; TDN, Tetrahedral DNA nanostructures; GCE, glass carbon electrode; ERGO, electrochemically reduced graphene oxide; CBZ, carbendazim; MIECS, molecular imprinting techniques (MIT)-based electrochemical sensors; XAS, X-ray absorption spectroscopy; NLiB, non-lithium-ion batteries; NMM, NiS_2-MoS_2@MXene; TMC, transition metal carbides; SAC, single-atom catalysts; WGS, water–gas shift; HDO, hydrodeoxygenation; DDH, direct dehydrogenation; CCS, carbon capture and storage; CO_2RR, carbon dioxide reduction reaction; OER, oxygen evolution reaction; N_2RR, nitrogen reduction reaction; AB, anionic dye; CoNW, cobalt nanowires; Pes, polyelectrolytes; NIR, near-infrared; MB^+, methylthioninium$^+$; TM, thermo-mechanical; PCM, phase change materials; rGO, reduced graphene oxide; PDA, polydopamine; MF, Melamine foam; NPCME, non-PCM emulsions; PEG, polyethylene glycol; PPF, pomelo peel foam; PW82, paraffin wax; SAL, stearyl alcohol; VASP, Vienna ab initio simulation package; PBE, Perdew-Burke-Ernzerhof; GGA, generalized gradient approximation; SVM, support vector machines; SVM, support vector machines, MSE, mean-square error; ANN, artificial neural network; PSO, particle swarm optimization; PINN, physics-informed neural networks; HTC, high-throughput screening; COD, crystallography open database; ISCD, inorganic crystal structure database; OQMD, open quantum materials database; LASSO, least absolute shrinkage and selection operator; MMO, monolayer metal oxides; KRR, kernel ridge; GPR, Gaussian process; C2DB, computational 2D materials database; LDPE, low-density polyethene.

these qualities by adding MXenes to 3D printing filaments or inks [29,30]. Furthermore, there is potential to maximize the performance of the produced composites for particular applications due to the ability to accurately manage the orientation and distribution of MXene particles inside the printed matrix [31]. 3D-printed MXene composites have the potential to handle a variety of technological difficulties and advance the area of additive manufacturing, from energy storage devices to structural components [32]. It is anticipated that more studies in this field will open up new avenues for creating sophisticated materials and gadgets with specialized characteristics and improved functioning. Compared to the 3D printing technique, 4D printing offers time or environmentally stimulated programmable shape transformation capability of materials [32]. This is especially applicable to MXene-based materials. The intelligent responsiveness of the MXene-filled composites can be further achieved by incorporating the 4D printing technique, which extends their applications in the fields of flexible electronics, wearable devices, and biomedicine. Furthermore, 4D technology allows for the more precise control of material behavior under different conditions, offering further optimization of adaptive properties and structural changes in MXene composites, hence driving innovative applications in state-of-the-art domains.

Machine learning (ML) techniques have emerged as important tools in materials science and engineering, providing new opportunities for accelerating the development and optimization of advanced materials such as MXenes and their integration into 3D printers [33]. Machine learning offers enormous promise for comprehending complex structure-property relationships [34], anticipating material behaviour [35], and guiding the design of MXene-based composites with tailored characteristics [36]. One of the key areas where machine learning excels is in the prediction of MXene synthesis parameters and material properties [37]. By leveraging large datasets encompassing various synthesis routes, precursor materials, and processing conditions, ML algorithms can identify trends and correlations, enabling the optimization of synthesis protocols for desired MXene properties [38]. For example, ML algorithms can predict the optimal conditions for chemical exfoliation or etching of precursor materials to yield MXenes with specific morphologies, layer thicknesses, surface chemistries, and electronic properties.

Furthermore, machine learning facilitates the rapid screening of MXene-based composite formulations and processing parameters for additive manufacturing via 3D printing [27]. With the growing interest in incorporating MXenes into 3D-printed structures for diverse applications, ML algorithms can streamline the material design process by modelling the relationships between composition [34], processing parameters [39], and final material properties. This predictive capability enables researchers to iteratively optimize MXene-loaded filament formulations, printing parameters (e.g., temperature, speed, layer height), and post-processing steps to achieve desired mechanical, electrical, or thermal performance metrics [40]. Moreover, machine learning-driven optimization extends beyond material synthesis and processing to the design of functional MXene-based devices and structures [41]. ML algorithms can assist in the virtual prototyping and design optimization of 3D-printed components, considering geometric constraints, loading conditions, and performance requirements. For instance, ML algorithms can generate design recommendations for MXene-infused scaffolds for tissue engineering applications, balancing porosity, mechanical strength, and biocompatibility [42,43]. Additionally, machine learning enables integrating data-driven quality control and defect detection strategies into the 3D printing process [33,44]. By analyzing sensor data, image data, and real-time feedback during printing, ML algorithms may detect flaws, deviations from required geometries,

Table 1
The critical gap in previous studies on MXene-based materials.

Study	Summary	How This Work is Different	How This Work is Helpful	Reference
MXene chemistry, electrochemistry and energy storage applications	Focuses on MXene composites for energy storage applications, emphasizing material properties and electrochemical performance.	Broadens the scope by integrating insights on energy storage, aerospace, and biomedical applications, including advanced thermal and electrical properties.	Provides a multi-disciplinary perspective on MXene composites, aiding researchers in exploring new applications beyond energy storage.	[52]
MXene-integrated composites: regenerative medicine, infection therapy, cancer treatment, and biosensing.	Highlights MXene's role in drug delivery, imaging, and tissue engineering, with a focus on biocompatibility and functionality.	Expands beyond biomedical uses to include aerospace and environmental applications, with added emphasis on mechanical and thermal properties.	Offers a unified view of MXene potential across biomedical, aerospace, and industrial sectors, promoting cross-sectoral innovations.	[53]
3D printing of freestanding MXene architectures for current-collector-free supercapacitors	Explores the use of MXenes in additive manufacturing, specifically 3D printing, emphasizing challenges and innovations in printing processes.	Goes beyond 3D printing challenges to discuss synergies between 3D printing, material customization, and machine learning.	Bridges additive manufacturing and advanced materials, showcasing strategies for custom-designed MXene composites.	[54]
Recent advance on machine learning of MXenes for energy storage and conversion.	Discusses machine learning's role in predicting MXene properties and synthesis optimization but lacks integration with 3D printing or broader applications.	Integrates machine learning with 3D printing and diverse application areas, presenting a holistic framework for MXene composite advancements.	Presents a forward-looking approach by combining AI-driven materials design with real-world manufacturing techniques.	[55]
MXene-Filled Composite Structures: Synthesis, Properties, Applications, 3D/4D Printing, and AI Integration	Comprehensive review of MXene composites, emphasizing synthesis, properties, and multi-domain applications. Highlights integration with 3D/4D printing and machine learning for material optimization.	Combines synthesis, advanced properties, and diverse applications with a focus on additive manufacturing and AI-driven innovations, presenting a holistic approach.	Provides an integrative perspective across material design, manufacturing, and optimization using emerging technologies, guiding researchers in developing next-generation MXene-based solutions.	This work

and process instabilities, allowing for real-time corrections. This proactive method improves production productivity, lowers material waste, and assures the repeatability and dependability of 3D-printed MXene composites.

Moreover, integrating MXenes into robots is another area in which machine learning is critical [45]. MXene-based materials have distinct features, including flexibility, conductivity, and environmental stability, making them ideal candidates for creating sophisticated robotic systems [45-47]. Machine learning methods can help design and control of MXene-based robotic structures, improving mechanical performance, sensing capabilities, and autonomous behavior [48]. Using ML-driven methodologies, researchers may investigate innovative topologies, material combinations, and control strategies for MXene-enhanced robots, opening up new possibilities in sectors such as soft robotics [49], wearable devices [50], and human-machine interaction [51]. This collaboration of MXene materials, 3D printing technology, and machine learning algorithms lays the path for the next generation of intelligent and adaptable robotic systems with unrivalled capabilities and adaptability.

This review paper aims to comprehensively explore the synthesis, properties, and applications of MXene-filled composite structures, with a specific focus on the transformative influence of 3D printing and machine learning. As we delve into the synthesis methods and properties of MXene-filled composites, we will unravel the intricacies of incorporating this remarkable material into various matrices. From there, the discussion will extend to the diverse applications of these composites, showcasing their versatility in addressing challenges across different industries. Integrating 3D printing technologies marks a pivotal point in the evolution of MXene-filled composites, offering unparalleled precision and design flexibility. We will delve into the advancements and challenges in utilizing 3D printing for fabricating MXene-filled composite structures, emphasizing the impact on material customization and manufacturing efficiency. Furthermore, this review will explore the symbiotic relationship between machine learning and the optimization of MXene-filled composites. From predictive modelling to materials discovery, machine learning algorithms are revolutionizing the way we approach material science. Case studies illustrating the successful amalgamation of machine learning techniques with MXene research will underscore the potential for accelerated development and breakthroughs in this field. In examining the convergence of 3D printing and machine learning in the realm of MXene-filled composite structures, we aim to provide insights into synergies that can push the boundaries of material science.

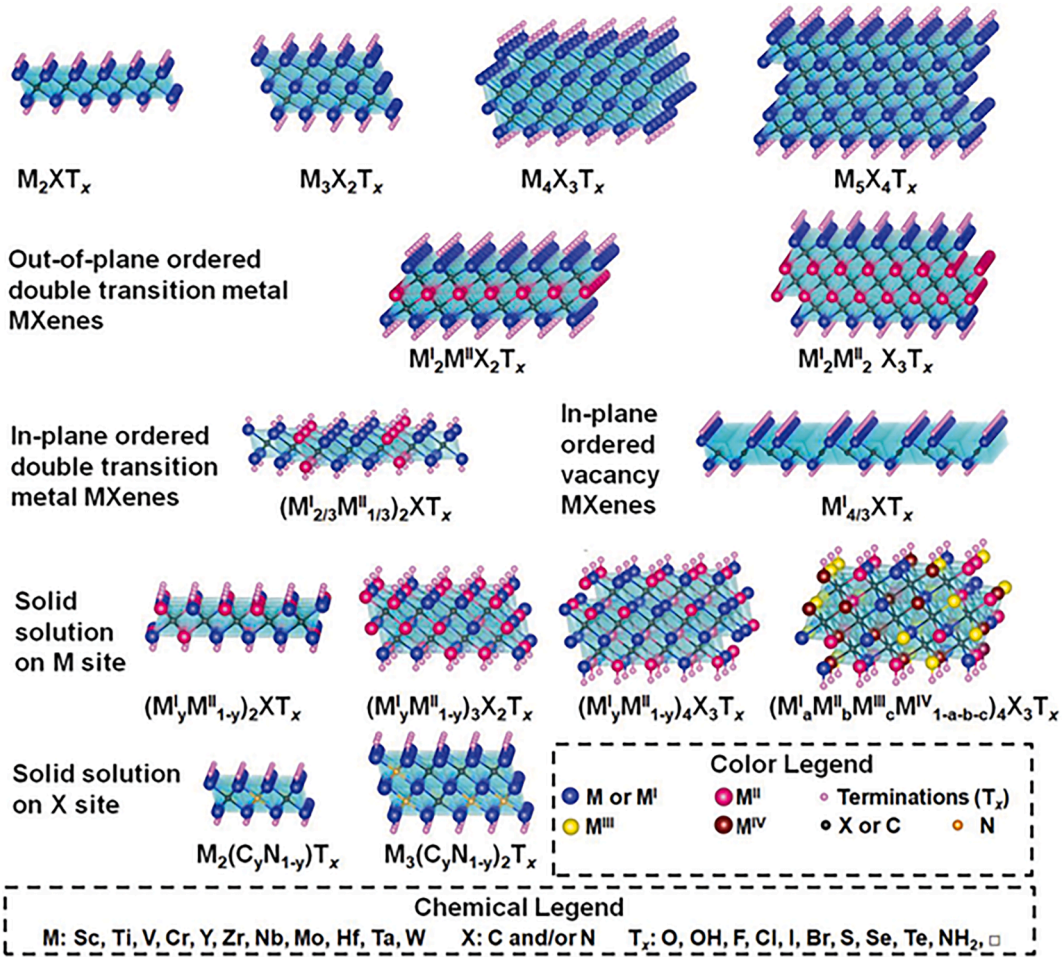

Fig. 1. MXene types and compositions. Reprinted from the Ref. [77].

Recent reviews published in the past two to three years have largely focused on specific areas of MXene research, such as energy applications, biomedical uses, printing technologies, or machine learning applications as shown in Table 1. While these works have provided valuable insights, they often address these topics in isolation. The primary novelty of this review lies in its comprehensive approach, bringing together all these key application areas under one cohesive framework. By integrating discussions on energy applications, biomedical advancements, 3D/4D printing technologies, and machine learning-driven innovations, this review offers readers a unified perspective on the multifaceted potential of MXene-filled composites.Additionally, the inclusion of tables summarizing critical data and advancements further enhances the accessibility of this information, enabling readers to easily compare and understand the synthesis techniques, properties, and applications of MXene-based materials across diverse fields.

The possibilities presented by this technology offer improvements not only in material properties but also pave the way for groundbreaking applications with implications for sustainability, efficiency, and performance. This study will expand the comprehension of these technologies' revolutionary potential as we traverse the complexities of MXene-filled composites and their interaction with 3D printing and machine learning. Moroever, we aim to stimulate more research and development at the intersection of materials science, additive manufacturing, and artificial intelligence by synthesizing current knowledge and adopting a forward-looking viewpoint.

2. Types of MXene and their structure

The structural appearance of MXene may be explained as (MX), M pattern with n+1 layers of element X (carbon/nitrogen) and n layers of transition elements of metal M. The structural pattern of MXene is presented in Fig. 1. MXenes, which include M_2X, M_3X_2, and M_4X_3, have been given several formulas [1]. Image scanning verifies MXenes' multilayer pattern. A significant amount of research is done using computational simulations to investigate novel stable compounds and analyze the structures of MXenes [56-58]. These investigations have yielded six distinct kinds of MXene structures, including ordered out-of-plane double-M elements such as Mo_2TiC_2 and $Mo_2Ti_2C_3$ and mono-M elements such as Ti_2C and Nb_4C_3. as well as ordered in-plane double-M elements such as ($Mo_{2/3}$), in which separate M elements are positioned in the basal plane [59]. There are two possible ways that vacancies might be distributed: randomly, as in $Nb_{1.33}CT_x$ [60], or systematically, as in $Mo_{1.33}CT_x$ [61] and $W_{1.33}CT_x$ [62,63]. These computational investigations make investigating new and stable MXene compounds easier, offering insightful information about the structural characteristics of MXenes [64]. Table 2 shows different MXene types, and their synthesis method, properties and applications. It is possible that MXenes containing a doublet of transition metals have been discovered and exist in two forms: ordered form (transition elements are arranged in a suitable sequence) [65] and solid solution form (two transition elements can fill the M sites at random) [66]. For example, (Cr_2V) C_2 forms the ordered solution, while $(TiV)_3C_2$ is accessible as a solid solution [67]. Important factors governing MXene's applicability in environmental engineering include its physical condition and ordered structure. Many methods for creating flaky nanomaterials with exceptional properties have been developed recently.

A chemical etching technique was used in 2011 to create MXenes. This involved exfoliating the laminar proportionate "A" from the matrix component (MAX) in ammonium bi-fluoride (NH_4HF_2), fluoric acid (HF), or fluoric acid combined with lithium fluoride (LiF). This was followed by an additional sonication process at room temperature [68]. The word "MAX" refers to the chemical makeup of the parental components that belong to $M_{n+1}AX_n$, where n can be any of the following: 1, 2, or 3. 'A' can be any of the elements in IIIA/IV A: Ga, Al, Si, In, Ge, Pb, Sn, P, S, Cd, or As.

These days, MXenes may also be derived from laminated phase components, such as zirconium and holmium, which are categorized as derivatives of MAX components (d-MAX) [69]. Carbide MXenes can be produced by selectively etching Al-C sublayers generated from $Zr_3Al_3C_5$ and $Hf_3[Al(Si)_4C_6]$ and Si fused Al-C, respectively [70]. Silicon can improve ternary carbide layer etching during the etching process by creating a weak adhesive link between the Hf-C/Al(Si)-C sublayers [71]. The physical and chemical properties of materials based on MXene are heavily influenced by surface functional groups, affecting the materials' suitability for various environmental applications [72]. Different oxygen (-O), fluorine (-F), and hydroxyl (-OH) functional groups often form their formation onto MXene surfaces. Because of this, MXenes are written as $M_{n+1}X_nT_x$, where T stands for the functional groups that have been exfoliated off the surface. Ti_3C_2 MXene, for example, can have at least three distinct notations: $Ti_3C_2O_2$, $Ti_3C_3(OH)_2$, and $Ti_3C_2F_2$ [73]. Generally speaking, MXene consists of a mixture of these functional groups, meaning that different synthetic techniques have a relative impact on the involved quantities. In general, a hydrophilic surface facilitates the adsorption of polar and ionic species. It has been noted that F group components are typically not chosen when MXenes are used for adsorptive purposes. Because hydroxyl and oxygen groups are intended to be far more stable, F group terminations might be made up for by employing OH groups following rinsing or storage in water [74]. Therefore, –O and –OH functional groups are involved in a number of terminations related to MXenes that may be achieved by modifying chemical etching techniques. This demonstrates that, despite their greater atomic weight, MXenes can show improved adsorptive efficacies compared to other nanomaterials based on carbon, such as graphene [7]. Lately, chemical vapour deposition technology has been intentionally used to synthesize bare MXene (MO_2C) without adding functional groups [75]. Their exceptional physical characteristics have been effectively investigated using density functional theory (DFT) [76]. It is known that the metallic constituents that do not terminate are highly active and have a higher level of chemical reactivity than other constituents. Therefore, further research in this area must focus on the adsorptive properties of MXenes without the connection to functional groups.

3. Synthesis of MXene

The evolution of MXene synthesis methods influenced their electrical properties [134], physicochemical properties [135], and an

Table 2
An overview of all MXene classifications

Reference	Year of discovery	MXene Category	Precursor	Etching Technique	Properties	Applications
[78-83]	2011	$Ti_3C_2T_x$	Ti_3AlC_2	Ti_3AlC_2 in 50% HF (Hydrogen fluoride)	Outstanding volumetric capacitance, heat resistance, simple machinability, and exceptional thermal and electrical conductivity	Sensors, supercapacitors, antibacterial components, batteries
[84-86]	2012	Ti_2CT_x	Ti_2AlC	Ti_2AlC in 10% HF	P-type semiconductor properties, photoexcitation, gas sensitivity, nonlinear optical properties, good electrical conductivity, and superior mechanical properties	Pulse modulators, electrode coatings, supercapacitors, membranes, field effect transistors, transmissive saturable absorbers
[87]	2012	$Ti_3(CN)T_x$	Ti_3AlCN	Ti_3AlCN in 30% HF	High electrical and thermal conductivity, good thermal stability, tough and fatigue-resistant	Solar cells, Sensors, Supercapacitors, Electromagnetic Shields, Ultrafast Photonics,
[88-91]	2012	$Ta_4C_3T_x$	Ta_4AlC_3	Ta_4AlC_3 in 50% HF	Metallic conductivity, small band gaps, a plastic layer structure, and the hydrophilic nature, aqueous stability, subcellular-level interactions, biocompatibility, partial electron transformation, optical properties, absorption, colloidal stability, pH dependent surface charge	Supercapacitors, sodium-ion batteries, lithium-ion batteries, and lithium-sulfur batteries, biomedical and immune engineering applications
[92-97]	2013	V_2CT_x	V_2AlC	V_2AlC in 50% HF	Good electrical conductivity, chemoresistitivity,mechanical strength, and electrochemical pseudo-capacity, larger active area per mass	Gas sensors, metal ion batteries,
[18,98-102]	2013	Nb_2CT_x	Nb_2AlC	Nb_2AlC in 50% HF	Outstanding conductivity, near zero bandgap, electrocatalytic, photocatalytic, electromagnetic properties	Secondary batteries, Li-ion battery, Na ion battery, K ion battery, Li-S battery, supercapacitors, sensors, photodetector, perovskite solar cells,
[103-108]	2014	$Nb_4C_3T_x$	Nb_4AlC_3	Nb_4AlC_3 in 50% HF	High electrical conductivity, photodetection, higher catalytic activity, high volumetric capacitance	Large-area conductive films, binders and current collectors of energy storage devices, battery and supercapacitor electrodes, antennas, and electromagnetic interference shields, structural composites, fibres, protective coatings, nano-resonators, textiles, and membranes
[109-112]	2015	Mo_2CT_x	Mo_2Ga_2C	Mo_2Ga_2C in 50%HF	Excellent catalytic activity, electrochemical stability, hydrophilicity, electrical conductivity, lower overpotential, efficient and cheap energy conversion, excellent hydrogen adsorption capacity	Hydrogen evaluation reactors, energy storage devices, humidity detectors, gas sensors
[113]	2015	$(Cr_2Ti)C_2T_x$	Cr_2TiAlC_2	Cr_2TiAlC_2 in 48-51% HF	Higher thermal conductivity and electrical conductivity	Thermoelectricity, protective coatings, low friction surfaces, and high-temperature electrical contacts
[114]	2015	$(Mo_2Ti)C_2T_x$	Mo_2TiAlC_2	Mo_2TiAlC_2 in 48-51% HF	Larger electronic properties, excellent thermal and magnetic properties	Metal ion batteries and water purification
[115]	2016	$Zr_3C_2T_x$	$Zr_3Al_3C_5$	$Zr_3Al_3C_5$ in 50% HF	Energy stability	High-temperature applications
[13,116]	2016	$(Mo_2Sc)C_2T_x$	Mo_2ScAlC_2	Mo_2ScAlC_2 in 48% HF	-	-

(*continued on next page*)

Table 2 (*continued*)

Reference	Year of discovery	MXene Category	Precursor	Etching Technique	Properties	Applications
[117]	2016	$Ti_4N_3T_x$	Ti_4AlN_3	Ti_4AlN_3 in 50% HF	Visible light absorption at energies greater than ~2.0 eV, high conductivity and stability in aqueous media, semiconducting ability, low-temperature semiconductor-to-metal transition under a magnetic field, enhanced efficiency and reliability for grid storage solutions	Electrocatalysis and (opto) electronic applications, semiconductors
[118-121]	2016	$(Mo_2Ti_2)C_3T_x$	Mo_2TiAlC_2	Mo_2TiAlC_2 in 50% HF + TBAOH (Tetrabutylammonium hydroxide)	Excellent capping performance, low density, outstanding metal conductivity, large specific surface area, higher capacitance	Vacuum-assisted filtration, laminate films, capacitors
[122]	2017	$Mo_{1.3}CT_x$	$(Mo_{2/3}Sc_{1/3})_2AlC$	$(Mo_{2/3}Sc_{1/3})_2AlC$ in 48% HF	High capacitance, electronic transport properties, crack healing properties.	Capacitors, conventional batteries
[123,124]	2017	V_2NT_x	V_2AlN	Ammoniation of V_2C	Improved opto-electronic and magnetic properties	Biosensors, water purification
[123,125,126]	2017	Mo_2NT_x	Mo_2C	Ammoniation of Mo_2C	Photoreduction performance	Optoelectronic devices
[71,127]	2017	$Hf_3C_2T_x$	$Hf_3[Al(Si)]_4C_6$	$Hf_3[Al(Si)]_4C_6$ in 35% HF	Intermediate strength within the range between strong physisorption and weak chemisorption	Cathode additives, electrolytes, reusable biosensors
[63]	2018	$W_{1.3}CT_x$	$(W_{2/3}Sc_{1/3})_2AlC$ or $(W_{2/3}Y_{1/3})_2AlC$	$(W_{2/3}Sc_{1/3})_2AlC$ or $(W_{2/3}Y_{1/3})_2AlC$ in 48% HF	High specific surface area and electrical conductivity	Energy devices
[105,128,129]	2018	$Nb_{1.33}CT_x$	$(Nb_{2/3}Sc_{1/3})_2AlC$	$(Nb_{2/3}Sc_{1/3})_2AlC$ in 48% HF	Higher electrical conductivity and capacitance	Supercapacitors
[130-133]	2018	$V_4C_3T_x$	V_4AlC_3	V_4AlC_3 in 40% HF	Electrocatalysis, structural stability, adsorption, electrochemical activity	Li-S batteries, electrocatalytic devices

extensive variety of applications. MXene synthesis processes are classified into three types: etching, top-down, and bottom-up [136]. The MXenes layered structures are created by etching the "A" components from the MAX phases of the parent three-dimensional (3D) layer. The top-down procedure was previously regarded as the most common approach for synthesizing MXenes, as shown in Fig. 2. In contrast to the top-down fabrication method, which often necessitates a large number of precursor materials, the bottom-up synthesis manufacturing method necessitates few organic or inorganic molecules/atoms when carefully creating the structure.

Through the selective chemical etching of a few atomic layers formed from carbide, nitride, and carbo-nitride pre-treatment agents, at least 20 MXenes have been obtained thus far [137]. Etchants can be broadly categorized into two groups, for example, aqueous salts containing fluorine ions [138]. In the early phases, MXenes are distinguished from MAX components by completely immersing MAX

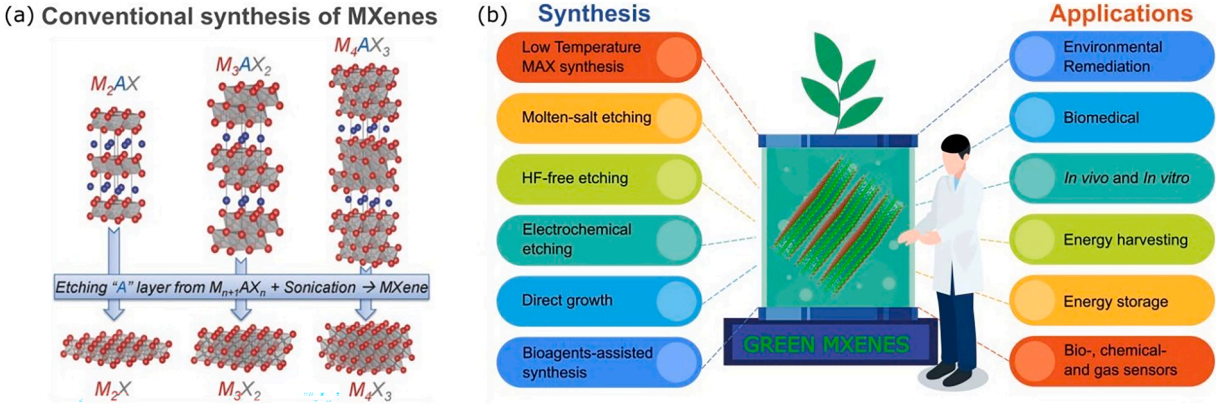

Fig. 2. (a) Crystal structure transition of the MAX phase and typical exfoliation into MXenes. Adopted from the reference [141]. (b) The green method to MXene synthesis and its possible uses. Adopted from the reference [142].

systems in certain acids and breaking down M-A bonds. The two decisive criteria in such a technique are the length of the corrosion and the total agitation. The methods for the production and use of MXene are listed in Table 2. Top-down and bottom-up mechanisms are the two primary methods used to synthesise 2D MXenes. While the bottom-up strategy [139] focuses on forming MXenes from atoms/molecules, the top-down method [140] correlates to the exfoliation of massive crystal amounts into single-layered MXene sheets.

3.1. MAX phases for MXenes

The MAX phases are nano-laminated layered solids with unique properties, including stiffness, lightweight, oxidation and creep resistance, metallic conductivity, and exceptional thermal shock resistance [143-145]. Hans Nowotny and his colleagues made significant contributions to the field of crystal chemistry throughout the 1960s [146]. The M_2BX, also known as the MAX phases, was among the numerous families found [147]. This family had around 50 members. Helga Rohde and Hans Kudielka initially described the MAX phases, Ti_2SC and Zr_2SC, in 1960 [148]. Here, M is an early transition metal, A is a group A element, and X might be C or N. One of them changed the name to align with Nowotny's American periodic table, which labels B elements as A and vice versa. In 1988, the International Union of Pure and Applied Chemistry (IUPAC) resolved the uncertainty by numbering the columns of the periodic table. After the discovery of Ti_3SiC_2 and Ti_3GeC_2, the family grew to $M_{n+1}AX_n$, where n might be 1 or 2 [149]. Schuster, a student of Nowotny, identified the Ti_3AlC_2 phase in 1994 [150]. In 1999, the discovery of the Ti_4AlN_3 phase led to an increase in the number of MAX phases to three [118]. Transmission electron micrographs of thin films have shown areas with $n > 3$. Ternary phases crystallize in the space group P63/mmc, and the Mn+1AXn notation is used to describe their stoichiometry in Table 3. Short notations for M, A, and X include 211 ($n = 1$) for M_2AX, 312 ($n = 2$) for M_3AX_2, and 413 ($n = 3$) for M_4AX_3, among others. The short format will be used throughout. The MAX phases were primarily overlooked until 1996 when Barsoum and El-Raghy discovered their exceptional characteristics in dense, single-phase Ti_3SiC_2 samples [151]. Barsoum and colleagues pioneered the creation and characterization of multiple MAX phases. In 2011, Ti_3AlC_2 was selectively etched with HF to create the first 2D MXene, $Ti_3C_2T_Z$, with surface terminations (O, OH, F) replacing the Al [78]. The MXene era began a year later with the discovery that selective etching of Al layers could be used for additional Al-containing MAX phases [152]. The unique features of 2D materials, such as hydrophilic and metal-like conductors, have sparked much investigation. Since its discovery in 2011, the number of citations and articles on MXenes has almost quadrupled annually. MXene research has become a global enterprise. The MAX phases are necessary for MXenes to exist. The ability to create unique MXenes from various MAX stages sparked renewed interest in discovering new ones. In 2019, Sokol et al. documented 155 MAX phases [153]. Over the past few years, the number of MAX stages has more than doubled. This work aims to catalogue all known MAX phases, with a focus on newer ones. It also highlights advances in the overall number of MAX phases (i.e., 342) and their symmetrical variants.

While certain classic MAX phases are machinable, it is still being determined if this is true for all documented MAX phases to date. The MAB stages are comparable to the MAX phases. The latter are layered borides comprising a transition metal (M), an A-group element (A), and boron. MAB phases differ significantly from MAX phases in terms of structure. MAX phases have a hexagonal P63/mmc structure, whereas MAB phases have more structural and compositional variations, including orthorhombic (M_2AB_2, M_3AB_4, M_4AB_6, M_4AB_4, $M_2A_2B_2$) [154-157], tetragonal (M_5AB_2) [158], and hexagonal (M_2AB_2, M_3AB_4) symmetries [159]. The hexagonal MAB phases have flat B-layers that create a honeycomb lattice. In contrast, the B-layer in the B-based MAX phase produces a hexagonal lattice.

The "classic" MAX phases belong to space group P63/mmc, where M is an early transition metal, A is an A-group element (groups 12-16), and X can be C, N, B, or P. The term "classic" refers to Nowotny's findings, where n might range from 1 to 6 but does not always imply age. Recently, B-containing MAX phases have been identified [160]. According to the traditional definition, it falls under the first group of MAX phases. Bottom-up synthesis of MAX phases allows for direct synthesis, including powder metallurgy and thin film deposition. This category includes ternary MAX phases and alloys, as well as multi-element solids with disorder on M-sites in high-entropy MAX phases [161], as long as they follow the hexagonal P63/mmc space group symmetry and can be synthesized in a single step. Bottom-up MAX phases include both out-of-plane ordered o-MAX phases and in-plane ordered i-MAX phases [162], which are produced mainly by powder synthesis. The i-MAX phase crystallizes in either orthorhombic or monoclinic C2/c and C2/m symmetry [151], with minor changes in stacking patterns.

The top-down synthesis of MAX phases is identical to the first, but it includes A-site features beyond groups 12-16. The modification of the A-group layers is what distinguishes a top-down synthesized MAX phase rather than the chemistry. These phases are commonly generated from a bottom-up MAX phase precursor, with the A-layer being partially or completely changed in post-synthesis operations. We refer to two approaches: (i) the molten salt method [163] for substituting group 12 to 16 elements with a more diversified group containing transition metals, including Mn, Fe, Co, Ni, Cu, and Zn. (ii) Thermally driven exchange processes can replace Al, Si, and Ga layers with Au or Ir in MAX phase thin films [164]. Top-down synthesized phases exhibit in-plane order within the A-layers [165]. Finally, there are a few outliers known as MAX phases, whose chemistry differs from the typical pattern. Phases consist of $M_{n+1}X_n$ building blocks interleaved by a double layer of A. Examples include Mo_2Ga_2C, Ti_2Au_2C, Nb_2Bi_2C, $Ti_3Au_2C_2$, and $Ti_3Cd_2C_2$.

3.2. MXene Synthesis Methods

MAX phases exfoliate into MXenes; this is an inevitable process in the synthesis of MXene-filled composites and directly influences their structural and functional performance. Table 4 shows the various etching processes of MXene from MAX phase. Of the various methods developed, chemical etching has emerged as the most developed route for the selective removal of the A-layer in MAX phases, especially with the use of HF or HF-derived solutions, such as LiF + HCl. These MXenes display layered structures with surface

Table 3
Max categories of MXene

Max category	MAX Phase	Ref.
AlC	Ti_2AlC, V_2AlC, Cr_2AlC, Ta_2AlC, Nb_2AlC, Hf_2AlC, Hf_3AlC_2	[166]
	Zr_2AlC	[167]
	Ti_2AlN	[168]
	Ti_3AlC_2	[169]
	Zr_3AlC_2	[170]
	Ta_3AlC_2, Ta_6AlC_5	[171]
	V_4AlC_3	[172]
	Nb_4AlC_3	[173]
	Ta_4AlC_3	[174]
	Ti_4AlN_3	[175]
	$Ti_5Al_2C_3$	[176]
SiC	Ti_4SiC_3, $Ti_5Si_2C_3$, $Ti_7Si_2C_5$	[177]
	Ti_3SiC_2	[178]
PC	V_2PC	[179]
	Nb_2PC	[180]
SC	Ti_2SC	[181]
	Zr_2SC	[182]
	Nb_2SC	[183]
	Hf_2SC	[184]
SB	Zr_2SB, Hf_2SB	[185]
	Nb_2SB	[186]
FeC	Ta_2FeC, Nb_2FeC, Ti_2FeN	[187]
CoC	Nb_2CoC, Ta_2CoC	[188]
NiC	Nb_2NiC, Ta_2NiC	[189]
CuC	Nb_2CuC	[190]
ZnC	Ti_2ZnC, V_2ZnC, Ti_3ZnC_2	[191]
	Nb_2ZnC	[192]
ZnN	Ti_2ZnN	[193]
GaC	Ti_2GaC, Nb_2GaC, Ta_2GaC, Cr_2GaC, Ti_3GaC_2, Ti_4GaC_3	[194]
	V_2GaC, Mo_2GaC	[195]
	Mn_2GaC	[196]
	Mo_2Ga_2C	[197]
GaN	Ti_2GaN, V_2GaN, Cr_2GaN	[198]
GeC	V_2GeC, Cr_2GeC	[199]
	Nb_2GeC	[200]
	Zr_2GeC	[201]
	Ti_4GeC_3, $Ti_5Ge_2C_3$, $Ti_7Ge_2C_5$, Ti_3GeC_2	[202,203]
AsC	V_2AsC, Nb_2AsC	[204]
SeC	Zr_2SeC	[205]
	Hf_2SeC	[206]
SeB	Zr_2SeB, Hf_2SeB	[207]
CdC	Ti_2CdC, Ti_2CdN	[208]
	$Ti_3Cd_2C_2$	[209]
InC	Ti2InC, Zr2InC, Hf2InC	[210]
	Nb_2InC	[211]
	Zr_3InC_2, Hf_3InC_2	[212]
	Ti_3InC_2	[213]
InN	Ti_2InN, Zr_2InN	[214]
SnC	Ti_2SnC, Zr_2SnC, Hf_2SnC	[215]
	Sc_2SnC	[216]
	V_2SnC	[217]
	Nb_2SnC	[218]
	Lu_2SnC	[217]
	Zr_3SnC_2, Hf_3SnC_2	[219]
	Ti_7SnC_6, Ti_3SnC_2, Ti_7SnC_6	[220]
SnN	Hf_2SnN	[221]
SnB	Nb_2SnB	[222]
SbP	Ti_2SbP, Zr_2SbP, Hf_2SbP	[223]
SbC	Nb_2SbC, Ti_3SbC_2	[189]
TeB	Hf_2TeB	[224]
IrC	Ti_3IrC_2	[225]
PtC	Nb_2PtC	[189]
AuC	Ti_3AuC_2, $Ti_3Au_2C_2$	[225]
	Ti_2Au_2C	[226]
	Mo_2AuC	[227]
	Nb_2AuC	[189]
	Cr_2AuC	[228]
AuN	Ti_2AuN	[229]

(*continued on next page*)

Table 3 (*continued*)

Max category	MAX Phase	Ref.
TlC	Zr_2TlC, Hf_2TlC, Ti_2TlC	[230]
PbC	Zr_2PbC, Hf_2PbC	[231]
	Sc_2PbC	[232]
	Ti_2PbC	[233]
	Zr_3PbC_2, Hf_3PbC_2	[234]
BiC	Nb_2Bi_2C	[189]

Table 4
A description of the various etching processes used to make MXenes.

Etching Method	Advantages	Disadvantages	Etchant	MXene type	Ref.
HF wet chemical etching	High efficiency, appropriate for most MXene preparations	HF is highly corrosive and presents operational concerns.	HF, HF + HCl	Ti_2CT_x	[238]
				Nb_2CT_x	[239]
				Mo_2CT_x	[240]
				Ti_2NT_x	[241]
				$V_{(2-x)}CT_x$	[242]
				Ti_3CNT_x	[243]
				$Mo_{1.33}CT_x$	[244]
				$Nb_{1.33}CT_x$	[245]
				$W_{1.33}CT_x$	[62]
				$Ta_4C_3T_x$	[246]
				$Mo_2TiC_2T_x$	[247]
				$Mo_2Ti_2C_3T_x$	[248]
				$V_4C_3T_x$	[131]
				$Nb_4C_3T_x$	[249]
				$Zr_3C_2T_x$	[115]
				V_2CT_x	[250]
				$Ti_3C_2T_x$	[251]
Fluoride salt/acid wet chemical etching	The capacity to remove surface material on a part-wide basis doesn't make extensive use of chemicals.	Corrosive chemicals and nature	LiF, NaF, CsF, CaF_2, KF, NH_4F with HCl, H_2SO_4	Mo_2CT_x	[252]
				Ti_2CT_x	[253]
				Ti_3CNT_x	[254]
				$Ti_3C_2T_x$	[255]
				V_2CT_x	[250]
				Nb_2CT_x	[256]
				$W_{1.33}CT_x$	[62]
Fluoride salt wet chemical etching	Precise etching method, easy disposal of by-products	Costly processing	NH_4HF_2, NH_4F	$Ti_3C_2T_x$	[257]
Alkali treatment wet chemical etching	Low cost, simple to access raw resources, and minimal operational risk	Needs a long reaction time and a high reaction temperature.	NaOH	$Ti_3C_2T_x$	[258]
UV-induced wet chemical etching	Enhanced precision and control over the etching process	Large energy requirement and costly method	UV light + H_3PO_4	Mo_2CT_x	[259]
Molten fluoride salt etching	Less caustic and hazardous raw materials are used.	High temperatures and a protected environment are required.	KF + LiF + NaF	$Ti_4N_3T_x$	[118]
Molten Lewis acid salt etching	Significantly increased safety, high adaptability to etch non-Al MAX precursors and the capacity to give MXenes surface functionality that can be controlled	Leads to MXene clays that cannot be dissolved in water, hence impeding further processing.	$ZnCl_2$, $CuCl_2$, $NiCl_2$, $FeCl_2$, AgCl, $CoCl_2$, $CdCl_2$, $CdCl_2$, $CdBr_2$	$Ti_3C_2T_x$	[260-263]
				Ta_2CT_x	[188]
				Ti_2CT_x	[264]
				Ti_3CNT_x	[264]
Electrochemical etching	Low cost, simple to access raw resources, and minimal operational risk	It is necessary to add more power supplies.	HCl, NH_4Cl + TMAOH	Ti_2CT_x	[265]
				$Ti_3C_2T_x$	[266]
				Ti_3CNT_x	[267]

terminations like -OH, -F, and -O, which dramatically impact their chemical activity and compatibility with matrices in composites [235]. The HF-based etching technique, while effective, poses environmental and safety hazards that further open the door to utilizing milder alternatives, such as the alkaline etching process. These indeed realize more stable MXenes that could compromise conductivity and exfoliation efficiency, and their optimization therefore needs to be carefully considered for each composite application.

Intercalation-assisted exfoliation and mechanical methods represent different ways of obtaining high-quality MXenes for composites. Intercalation, assisted with typical agents like dimethyl sulfoxide or urea, expands the layers of MXene by weakening the interlayer van der Waals forces and thus allows for easy delamination without significant structural damage [236]. This allows enhanced solvent dispersibility and controlled functionalization in line with composite requirements. Among these are ball milling and ultrasonication, which are all mechanical exfoliation methods and generally depend on physical separation of the MXene layers, mostly without heavy chemical modification. Though very effective, these mechanical methods might introduce structural defects into the material that will affect the mechanical or electrical properties of the ensuing MXene-based composites.

Advanced exfoliation techniques, including plasma-assisted and electrochemical etching, have been developed to create promising

pathways toward synthesizing MXenes with precise control over layer thickness and functionalization. Plasma and laser irradiations are able to exfoliate while simultaneously functionalizing the MXenes, yielding defect-free nanosheets suitable for high-performance applications. Electrochemical etching represents another 'green' approach, since it relies on anodic oxidation [237]. Scalability is still poor. In particular, all these methods are of interest for composite systems, whereby defect density and layer uniformity are of essence for achieving optimal thermal, mechanical, or electrical performances. By tuning exfoliation in accordance with a particular composite design, researchers are in a position to exploit special properties of MXenes that would be hardly applicable for various applications.

3.2.1. Etching

There are several methods for preparing MXenes. Different terminal functions can be added to the M atoms to complete their coordination spheres and decrease their surface Gibbs free energy, thanks to variations in their etching techniques. Therefore, their manufacture is greatly influenced by the MXene's surface characteristics. Various kinds of preparation techniques are covered in this article.

3.2.1.1. Hydrofluoric Acid (HF) Etching. Owing to the extensive study conducted on MXenes, etching techniques have been applied extensively, particularly the HF acid etching approach, which remains the most popular technique. In 2011, Naguib et al.[78] suggested using HF acid etching to create the Ti_3AlC_2 MAX phase. The HF acid produces H_2 while removing Al layers from the Ti_3AlC_2 MAX phase by a straightforward displacement process. $Ti_3C_2T_x$ (where T stands for the -O, -F, and -OH) and H_2 are also produced when deionized water reacts with the HF acid solution. Ti_2AlC, $(Ti_{0.5}Nb_{0.5})_2AlC$, Ti_3AlCN, Ta_4AlC_3, $(V_{0.5}Cr_{0.5})_3AlC_2$, Nb_2AlC, and many MAX complexes of $Zr_3Al_3C_5$, Ti_3SiC_2, and Mo_2Ga_2C were effectively stripped into MXenes by HF acid etching [68]. Since 2011, HF acid etching has been the most effective production method for MXenes materials. The final product's characteristics, such as the kinds and concentration of defects, the thickness and lateral size of the MXene phases, and the species and contents of the surface terminal groups, are greatly influenced by processing variables like the temperature, length of the etching reaction, and concentration of the HF aqueous solution [268,269]. Effective use of these selective methods has allowed for the successful creation of MXene phases with various compositions and layers. High-quality MXenes layers are partly designed by the temperature, time interval, and density of F ions during the HF acid etching process [270]. $Ti_3C_2T_X$ creates a superb layered structure with high concentrations of HF, which is challenging to do with other acid solutions, as validated by Alhabeb et al. [271]. MXenes produced using the HF acid etching method maintained their distinct surface features and their –O, –OH, and –F functions. Using ion-beam and electron microscopy, Shuck et al. [169] and Jawaid et al. [272] recently investigated the etching behaviour of MAX-phase Ti_3AlC_2 in various etching chemicals at the atomic scale. They looked at how the etching agents and etching time affected the structure of the Ti_3AlC_2 phase and found that, despite their contact with the HF etchant, the edge Al atoms at the mid layers of the MAX-phase Ti_3AlC_2 are not erased. Additionally, the HF etchant caused the grain boundary to be etched. Ti_3AlC_2 was etched for three hours using the bulk etching approach, as seen in the scanning transmission electron microscope (STEM) micrograph, which showed several etched areas. Additionally, the extension of the MAX-phase Ti_3AlC_2's d-spacing (i.e., 0.97 nm) to 1.02 nm is demonstrated by the selected area electron diffraction (SAED) pattern, indicating the successful conversion to $Ti_3C_2T_X$ MXene at the etching boundary. Also, $Ti_3C_2T_x$ MXene was synthesized by Cho et al. [273] through a combination of ball milling and chemical etching from Ti_3AlC_2 powder. The study examined the effects of ball milling and etching durations on the physiochemical properties and the electrochemical performance of the resulting Ti_3C_2 MXene. Notably,

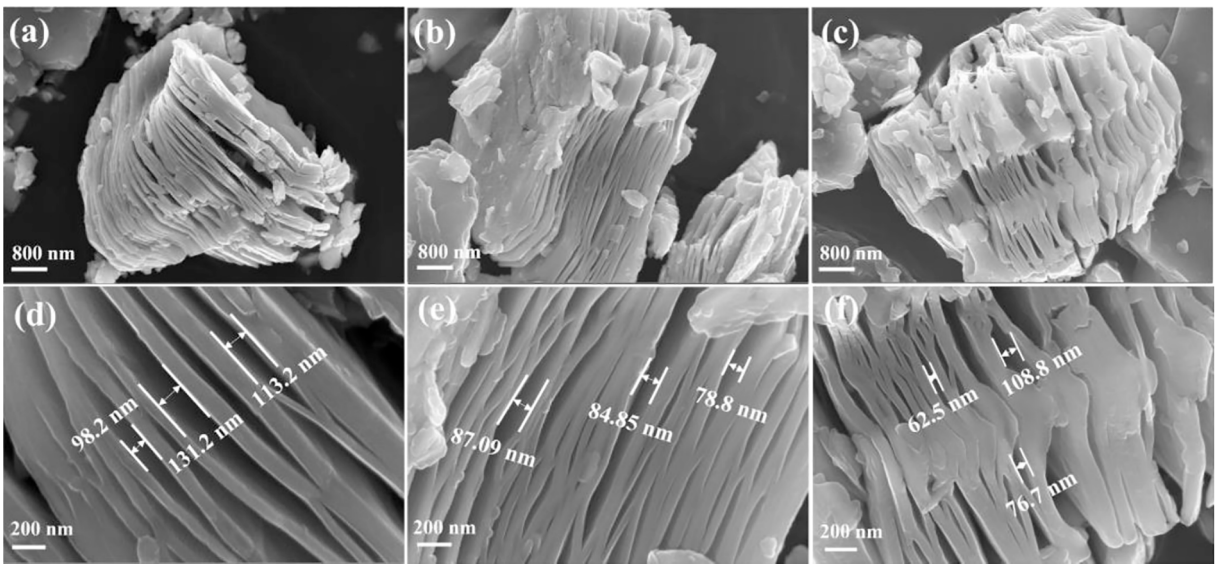

Fig. 3. FESEM images of MXene prepared with varying HF etching durations: (a, d) BM-12H, (b, e) M-24H, and (c, f) M-48H. Reprinted with the permission of the Ref. [273]

the MXene treated via 6 h of mechanochemical processing followed by 12 h of chemical etching (BM-12H) demonstrated electric double-layer capacitance behavior, achieving an enhanced specific capacitance of 146.3 F g^{-1}, surpassing the performance of samples treated for 24 and 48 h. The SEM images of the prepared MXene using various etchants are displayed in Fig. 3.

3.2.1.2. The Modified Acid Etching Method. Researchers are developing methods to stop HF acid from being used directly to remove the Al layers from MAX phases since acid fluoride solutions are toxic and destructive. Original-location HF acid etching is the most used method; instead of HF acid, fluoride salts (LiF, NH_4HF_2, FeF_3, KF, and NaF) and HCl are used in its place [261,274,275]. $AlF_3{\cdot}3H_2O$ is often produced as an unwanted byproduct in the production of MXenes by etching Al or Ga layers of the MAX phase with HF acid. We must shed light on the elements that lead to the production of this impurity to synthesize MXenes that are devoid of it. As a result, customized etching techniques are frequently used. For example, Cockreham et al. [276] determined the circumstances in which the byproduct $AlF_3{\cdot}3H_2O$ formed during the cobalt fluoride etching process (i.e., CoF_2/CoF_3). The CoF_3/MAX sample's scanning electron microscope (SEM) micrograph displayed no $AlF_3{\cdot}3H_2O$ impurities. The cation's intercalation, which reduces the inner force between layers and may delaminate the material layers during ultrasonication, improves the MXenes interlayer distance created using the modified acid-etching technique. A study by Zhang et al. [264] presented an improved etching approach for Ti_3C_2 MXene production. There were two processes in the process: etching Ti_3AlC_2 with different concentrations of $FeCl_3$ and washing it with a low concentration of HF. At ambient temperature, $FeCl_3$ eroded the Al layers of Ti_3AlC_2 by a metal displacement process, producing Ti_3C_2 nanosheets with an accordion-like shape. When the resulting Ti_3C_2 MXene was evaluated as a working electrode for supercapacitors, it outperformed an unmodified Ti_3C_2 electrode, obtaining a maximum specific capacitance of about 213.2F/g at 0.5 A/g in a 6 M KOH electrolyte solution. The technique is easy to apply, effective, and uses less HF. This study demonstrates the potential to use metallic cations with increased redox potentials to synthesize different MXene-based frameworks. Consequently, this method simplifies the previously mentioned laborious multi-step synthesis procedure, allowing few-layer MXene to be synthesized in a single step.

3.2.1.3. Reformulated Acid Etching Based on Fluoride. To avoid the considerable toxicity that HF etching generates, researchers have been working hard to develop more effective methods for removing the atom layers from MAX. Strong acids combined with a mixture of fluoride salts (KF, NaF, LiF, and NH_4F) can also be used to etch MAX precursors in addition to HF [277]. It has been shown that strong acids and fluoride salts may selectively etch atoms, causing the cations (K^+, Na^+, Li^+, and NH_4^+) to intercalate in situ. Water decreases MXene layer contact while increasing interlayer space between MXene layers. It is important to remember that the concentration of strong acid and fluoride salt might affect the final MXene fragments' size and quality. For instance, a second sonication step is necessary for the multilayered Ti_3C_2 produced by the clay technique (5M LiF/6M HCl) to delaminate into single flakes. This often leads to the production of microscopic faulty MXene flakes [278].

3.2.1.4. Etching of Melted Salts. MXene may also be made by heating the MAX phases, such as Ti_4AlN_3, at 550 °C under argon shielding in a molten mixture of fluoride salts (LiF, NaF, and KF; a weight ratio of 29:12:59) [118]. In thirty minutes, the etching process may be finished. Ti_nN_{n-1}, which is less stable than Ti_nC_{n-1}, can be dissolved in HF or other acids containing fluoride when employed as an etching agent. Consequently, one advantage of the molten-salt etching approach is its very short processing time. It is necessary to perform further cleaning (with DI H_2O and H_2SO_4) and delamination (in a TBAOH solution). The x-ray diffraction (XRD) patterns of the resulting delaminated Ti_4N_3 show that its crystallinity is lower than those of the MXene produced by HF etching. The resultant product also exhibits the TiO_2 phase. One advantage of the molten salt etching procedure over the HF and fluoride-based acid etching is the production of MXenes with poor stability in the HF or fluoride-based acid solution. On the other side, this method has the following drawbacks: (a) A large quantity of heat and energy is used in the etching process; (b) the resulting MXenes show low purity and crystallinity; and (c) there are a lot of surface flaws and vacancies in the resulting MXenes [261]. Liu et al. [279] recently reported synthesizing MS-$Ti_3C_2T_x$ by intercalating tetrabutylammonium hydroxide (TBAOH) and then sonicating the layers to separate them. Cl-terminated MS-$Ti_3C_2T_x$, as obtained, was used as an anode in a Li-ion battery, resulting in a high specific capacity and remarkable rate capability. Clear, distinct-edged $Ti_3C_2T_x$ nanosheets with a lateral dimension of approximately 600 nm.

3.2.1.5. Fluoride-free etching. While many etching conditions have been established for the synthesis of MXenes, most synthesis methods need chemicals based on fluoride or HF, which may lead to the formation of -O and -F terminations on the MXene interface. Specifically, MXenes-based supercapacitors' electrochemical performance is reduced by -F terminations [280-282]. Therefore, fluoride-free manufacturing processes are needed to achieve satisfactory electrochemical performances. Using a NaOH solution as the etching agent, Li et al. [283] created an alkali-assisted hydrothermal etching method to create Ti_3C_2 MXene. Alkali and Al have a high interaction, which makes alkali a potential etchant for the Ti_3AlC_2 MAX phase. Acquiring multi-layered MXenes with excellent purity remains a significant difficulty. Since the Ti_3C_2 MXene skeleton needed not to be harmed, a high alkali concentration (27.5 M) and high temperature (270 °C) were employed in the Bayer process to etch Al layers. Chen et al. [284] reported the creation of a $Ti_3C_2T_x$ MXene that contains chloride and is devoid of fluoride by electrochemical etching. $Ti_3C_2T_x$ was delaminated by sonication during synthesis without using any hazardous organic intercalant. The resulting $Ti_3C_2T_x$ nanoflakes had a thickness of around 3.9 nm, and their dispersion in an aqueous media was highly stable. Because the Ti-atoms are arranged hexagonally at the MXene$Ti_3C_2T_x$ 002 surface of (SAED Mxpattern of the $Ti_3C_2T_x$ exhibits hexagonal symmetry. The HR-TEM image clearly showed that the lattice fringe, with a d-spacing of 0.27 nm, may be attributed to 100 planes of the $Ti_3C_2T_x$ MXene. The low performance of MXenes in Li-ion batteries and supercapacitors is caused by the surface-attached −F, which significantly hinders the transportation of electrolyte ions and sacrifices the electrochemically active sites, as per theoretical predictions and experimental results. Moreover, Khan et al. [285] studied a

hydrothermal green synthesis of fluorine-free MXene. They described a hydrothermal alkali etching method that uses sodium hydroxide (NaOH) and MAX solution to create $Ti_3C_2T_x$@Al-NaOH (T_x= -OH, -O) MXene without fluorine. The sample $Ti_3C_2T_x$@Al-NaOH that was etched in NaOH solution for 15 h shows ideal electrochemical characteristics. Furthermore, in a 1 M sulfuric acid electrolyte solution, the $Ti_3C_2T_x$Al-NaOH samples with NaOH concentraAtions of 22.5, 25, 30, 35, and 40 M, respectively, exhibit higher rates of charge-discharge and pseudocapacitive effect, with corresponding specific capacity values of 378, 445, 565, 365, and 176 Cg^{-1}. After a constant cycling of almost 8000 times, their retention rates remain at 94%, 199%, 150%, 113%, and 29%. As the capacitance value of the $Ti_3C_2T_X$-Al-NaOH (30 M) for 15 h surpasses (by about 465%) that of the multilayer $Ti_3C_2T_x$ MXene generated using standard hydrofluoric acid etching, it is shown to have tremendous promise as a candidate electrode building supercapacitors along with other energy storage devices. a very beneficial method for achievinghelpful surface chemical fine-tuning. Therefore, it would be ideal to fabricate MXenes utilizing F-free techniques.

3.2.2. *Bottom-up Synthesis Approaches*

While bulk precursors offer scalability, many researchers favor the creation of materials from their elemental components owing to the precise control this method allows in material chemistry, hence enabling custom-tailored designs. Among the prominent bottom-up synthesis methods that have been applied to the synthesis of MXenes, CVD, PE-PLD, and solid-state direct synthesis stand out.

3.2.2.1. Chemical Vapor Deposition (CVD). CVD was a process that was involved in depositing MXene film on the surface of metals through the flow of precursor gases over heated substrates. In 2017, Wang et al. [286] reported ultrathin crystal layers of tantalum carbide, nitride, and boride on copper-tantalum surfaces by using precursors such as C_2H_2, NH_3, and B powder. The CVD process had, however, poor scalability and limited active transition metals. A recent work overcame these difficulties and synthesized Ti-based MXenes via CVD, where $TiCl_4$ reacted with methane or N_2 gas on a titanium surface to form the MXene Ti_2CCl_2 or Ti_2NCl_2, respectively [287]. This synthesis allows for scalable production of MXenes, opening new avenues to the study of novel MXene phases and morphologies that had not been possible so far, such as the first chloride-terminated nitride MXene, Ti_2NCl_2 [288].

3.2.2.2. Plasma-Enhanced Pulsed Layer Deposition (PE-PLD). The advantages of PE-CVD are combined with pulsed-layer deposition in PE-PLD to enable continuous single crystal film growth at lower temperatures [289]. Using this technique, films of Mo_2C as thick as 25 nm have been fabricated by focusing a 248 nm laser beam on a Mo target [290]. Although still in the proof-of-concept stage, possible applications for these Mo_2C films include catalysis and optoelectronics.

3.2.2.3. Solid-State Direct Synthesis. In 2019, the solid-state direct synthesis of 3D ordered Y_2CF_2 crystals from YF_3 and graphite powder through high-temperature reactions was reported for the first time by Druffel et al. [291]. This approach has also been expanded by Wang et al. [287] to prepare Ti-based and Zr-based MXenes by heating a mixture of titanium metal, graphite, and $TiCl_4$ in a sealed quartz ampoule at 950 °C for two hours. Through this approach, it would be much easier to precisely control the termination groups according to the precursors.

3.2.3. *Up-Botom Synthesis*

The synthesis of up-bottom synthesis provides a hybrid methodology combining techniques of bottom-up with top-down. The major methods in this category include the template method and structural editing protocols.

3.2.3.1. Template Method. Salt-templated synthesis was first demonstrated by Xiao et al.[292] in 2017 when MoN was synthesized using salt in the following four steps: 1) preparation of 2D MoO_3 templates, 2) coating salt on the template, 3) synthesizing MoN by ammoniation, and 4) washing to remove the templates. A variant of this approach has been applied to create 3D structures of 2D MXenes to improve their surface area for applications in batteries and supercapacitors. An aqueous solution of MXene was coated with

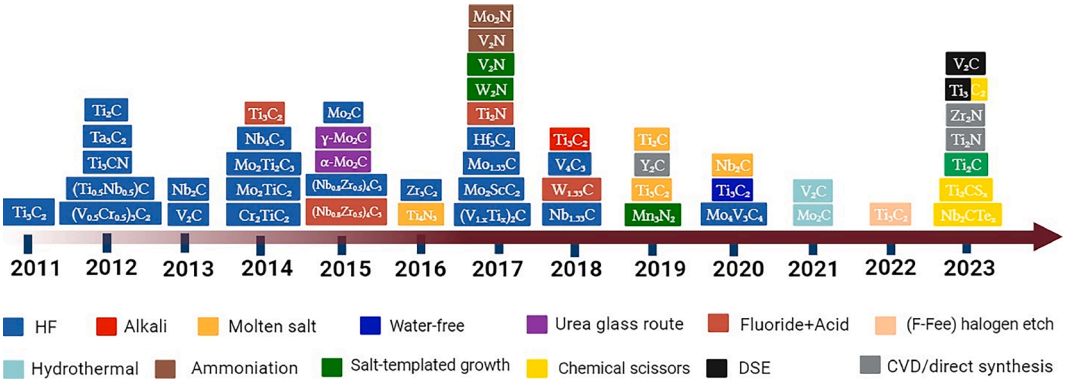

Fig. 4. A summary of various MXene types, their corresponding synthesis methods, and the timelines of their development. Reprinted with the permission of Ref. [294]

a polymer that was later removed by heating.

3.2.3.2. Structural Editing Protocol. A new strategy for the manipulation of MXenes, known as structural editing, relies on "chemical scissors" to precisely control the synthesis of MXene according to Ding et al. [293]. This approach includes four paths: 1) opening the non-van der Waals gap in MAX phases, 2) atomic replacement via metal ion intercalants, 3) removal of terminations, and 4) stitching 2D nanosheets into unique MXene or MAX phases. These steps can be stopped at any point to produce different MXene properties, such as improved tensile strength in termination-free MXenes or novel MAX phases with diverse terminations.

Several MXenes have been experimentally fabricated up to date, and their synthesis methods and corresponding years of reporting are presented in Fig. 4.

3.3. Mxene quantum dots synthesis

3.3.1. Top-Down Approach

The top-down approach has been around for a while, particularly when it comes to the creation and synthesis of nanomaterials. These techniques frequently entail bulky 2D or 3D precursor material into necessary tiny quantum particles [295]. The top-down method has been successfully applied to convert various three- and two-dimensional bulk precursors, such as graphite, carbon nanotubes, graphene, MoS_2 crystals, WS_2 powder, black phosphorus, and g-C_3N_4, into quantum dots. These include the following processes: ball-milling [296], liquid exfoliation [297], chemical etching, electrochemical intercalation, hydrothermal/solvothermal treatment, ultra-sonication, microwave irradiation, and others. Most top-down methods define the catalysts' initial O-containing functions on their surface, which makes it easier for defects to form in the catalysts [298]. The bulk molecules can break into small quantum particles thanks to the surface imperfections, which act as reactive sites [299]. Because this method may be used at low temperatures, it is pretty important. Large-scale production is also possible with this approach, which may employ abundant raw resources. However, there are downsides, such as the limited yield and the requirement for specific treatments. The most often used top-down methods of producing MXene include acid reflux, hydrothermal, solvothermal, ball-milling, intercalation, and ultra-sonication. The specifics of top-down methods for MXene synthesis are covered in this section.

3.3.1.1. Hydrothermal approach. Using a high-pressure autoclave filled with precursor materials, aqueous solutions are heated above the boiling point of water in this heterogeneous reaction technique. The quantum dots (QD) size, shape, morphology, and characteristics may be changed by utilizing the combined effects of the high temperature, high pressure, and the pH of the solution [300]. In addition, the pH of the solution, the temperature of the reaction, and the duration of the reaction all matter greatly in the synthesis of MXene. Because of the pH and temperature on the length of the reaction/response, normal reaction temperatures for the synthesis of MXene are 6 to 9 and 100 to 180 °C [301]. In addition, the size, characteristics, and thickness of the material may be changed by modifying the hydrothermal reaction's parameters. Xue et al. [302] used a hydrothermal method to produce water-soluble Ti_3C_2 MXene and found that the characteristics, thickness, and size of MXene could be adjusted by raising the hydrothermal reaction temperature to 79 °C. Particles having average diameters of 2.9, 3.7, and 6.2 nm and average thicknesses of 0.99, 0.91, and 0.89 nm were produced from the MXenes at 100, 120, and 150 °C. These results indicate that the majority of the particles are composed of monolayers. Ti_3C_2 QDs display -NH surface functions during the reaction, and at a lower temperature (100 °C), a novel MXene structure is generated in which the d-spacing value can be verified. Conversely, the MXene that was created at 120 °C had a fusion structure with TiO_2 on the surface and CTi in the core. Nevertheless, an amorphous MXene structure developed due to most Ti atoms being etched away at a high temperature (150 °C). Xiao and colleagues [303] state that the MXene structure cannot be formed below 100 °C. They varied the reaction temperature from 60 to 80 and 100 °C to create MXene ($Ti_3C_2T_x$). At 60 °C, a large number of nanoribbons, including a few $Ti_3C_2T_x$ nanoflakes, formed in place of MXene. As the temperature rose to 80 °C, the size of the particles shrank, and different-sized nanodots were produced. A consistent distribution of ultrafine nanodots is produced on nanolayers at 100 °C. Using various hydrothermal settings, more MXenes have been made [304,305]. Using the resultant precursors of the elements, MXene with doped heteroatoms has also been synthesized by applying different hydrothermal conditions. By using L-cysteine as a source of nitrogen and sulfur and Nb_2C nanosheets as a precursor material, Xu and colleagues synthesized heteroatom-co-doped Nb_2C MXene (S, NMXene) at 160 °C using the hydrothermal technique. MXene's particle size ranged from 2.6 to 4.7 nm. With a lateral size of 3.56 nm, the synthesized S, N-MXene, is noticeably smaller than that of the MXene (i.e., 2.4 nm) and N-MXene (i.e., 2.66 nm). With an average thickness of 1.74 nm, the S, N-MXene demonstrated the development of a monolayer [306]. Lately, Peng et al. [307] have used low-toxicity etchants ($NaBF_4$, HCl) to create 2D MXene (h-Ti_3C_2) using the hydrothermal process. The resulting h-Ti_3C_2 MXene showed a layered structural shape. The h-Ti_3C_2 nanoflakes' chosen region HR-TEM micrograph showed d-spacing of around 0.264 nm and ~0.155 nm, which corresponded to the (0−110) and (0−210) planes of the Ti_3C_2, respectively. It is important to remember that the hydrothermal etching process is an effective way to prepare Ti_3C_2 and does not require HF acid.

MXene blocks can be reduced in size to the 10 nm level, at which point they form MXene quantum dots (MQDs), which have a number of unique physical and chemical characteristics in addition to some of the clear benefits of the MXene block's two-dimensional parent atoms [308,309]. MQDs have a more specific surface area, excellent biocompatibility, more tunable characteristics, improved capacity to hybridize with other nanomaterials, and simpler doping or functionalization compared to MXenes blocks [310,311]. For instance, MQDs have distinct electrical and optical characteristics superior to those of MXene nanosheets because of their quantum restrictions and edge effects [8]. They also have a high dielectric constant and absorption coefficient, making it simple to split them into electrons and holes [309]. In addition, MQDs have far less cytotoxicity than MXenes, making them a better option for identifying

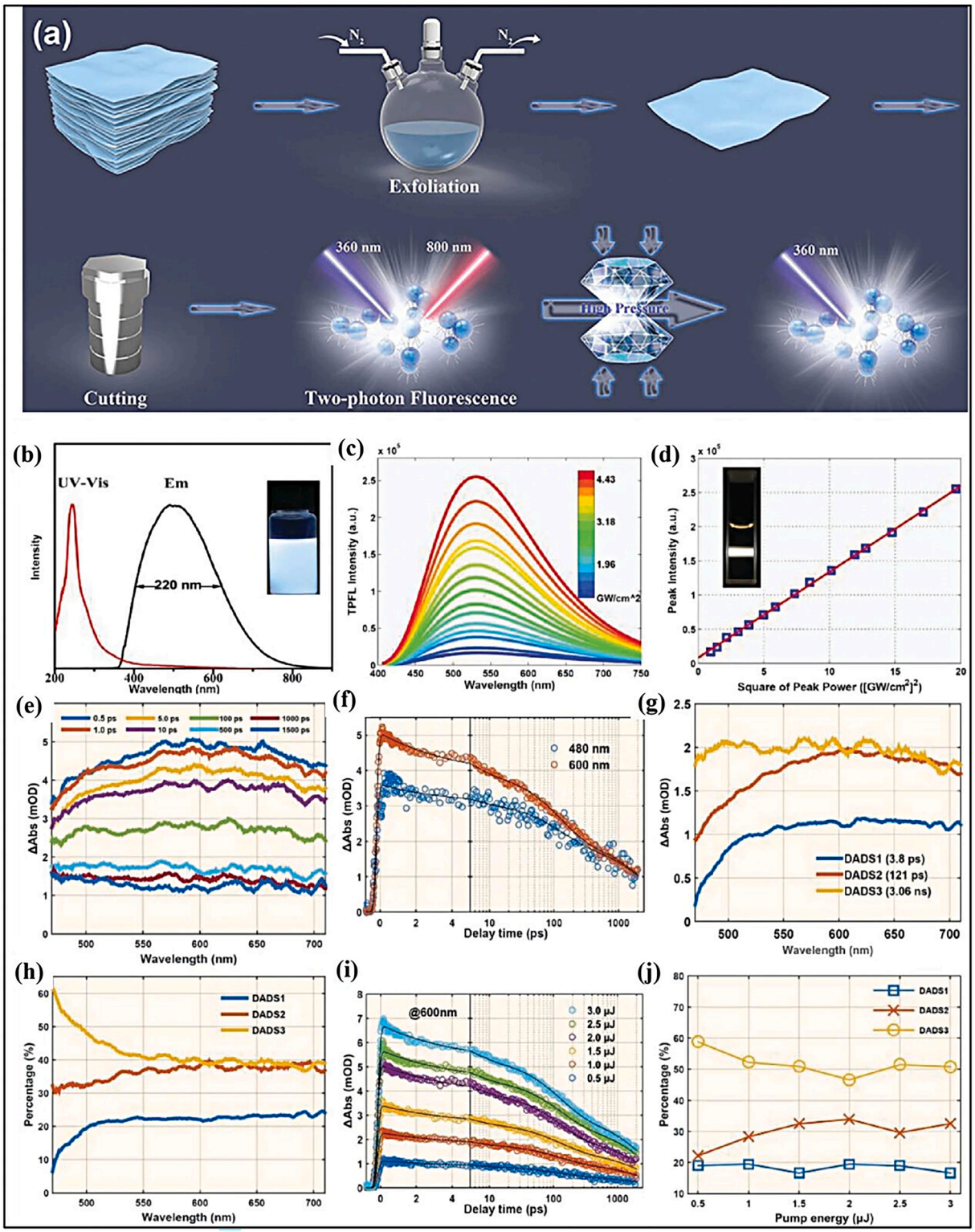

(caption on next page)

Fig. 5. a) Schematic of Ti_3C_2 preparation and application. b) UV-vis absorption, fluorescence excitation, and emission spectra (the inset image is taken in UV light). b) Two-photon spectra with varying laser ultrasonication. c). UV-Vis spectra of Ti_3C_2 MQD d).The relationship between two-photon emission intensity and laser excitation intensity squared has a linear slope of one. e) Ti_3C_2 MQD TA spectra at the given delay durations of 0.5 ps to 1.5 ns. f) Kinetic decay traces between 480 and 600 nm. Black solid lines represent fitted curves. g) Global fitting with five exponential decay functions yielded five decay-associated difference spectra (DADS). h) The percentage contributions of the three decaying processes to the overall dynamic at different wavelengths based on fitted DADS. i) The percentage of the contributions of the three decay mechanisms to the overall dynamic of surface state at various excitation energies. j) The percentage contributions of the three decay mechanisms to the overall dynamics of the core state at various excitation energies. Reproduced with permission Ref. [316].

chemicals in living things [312]. As presented in Fig. 5, size dependency, long-term stability, and tunable photoluminescence (PL) are further features of MQDs [313]. Compared to MXenes, MQDs have broader excitation strengths from an 800 nm femtosecond pulse laser (the inset displays a picture of a Ti_3C_2 MQD solution with the 800 nm laser flowing through).

Potential in the sensing arena because of these benefits [314,315]. The adjustable PL characteristics [316], excellent hydrophilicity [317], strong biocompatibility [310], ease of functionalization [318], and low cost [319] of MQDs have led to a great deal of effort in the development of practical sensors up to this point, with MQDs serving as essential components. High performance may be obtained by sensors based on MQDs because of their unique features [320-322].

3.3.1.2. Exfoliation. Exfoliation methods have become a crucial stage in the synthesis process for the faster breakdown of large materials into more miniature sheets or particles [323]. Some kinds include chemical oxidation, thermal oxidation, and ultrasonic exfoliation. These are often used when increasing the surface area or pore volume is the desired outcome [301,324]. The sonication method has emerged as a low-energy substitute for traditional solvothermal and hydrothermal methods. Zhang et al.[325] used one-step ultrasonic exfoliation procedures to develop MXene-based fluorescent QDs. With the resulting QDs, an outstanding fluorescence quantum yield of 7.7% was noted. High selectivity and sensitivity for Fe^{3+} detection in blood and saltwater were two major benefits of the QDs' excitation-dependent and pH-independent emission properties. Similarly, a publication used ultrasonication methods in an N_2 atmosphere to create MQDs, which were then collected by centrifugation. Acetonitrile and a non-aqueous ionic liquid were combined to provide the electrolyte for this system. Before creating MQDs, the authors used synchronous fluorination and electrochemical etching to create MXene layers, which served as precursors for the final MQDs. The authors compare the MQDs produced in this manner and those acquired using HF etching. According to some of the reported results, the MQDs produced from electrochemically etched and fluoridated MXene demonstrated improved colloidal stability [326]. To generate MXenes and its derivatives, standard etching procedures require the use of hazardous etchants like zinc chloride and HF in addition to other organic solvents [260].

It's interesting to note that the saturable absorption intensity of the resulting QDs was similar to that of graphene, which is helpful for a lower mode-locking threshold in laser radiation. Yang et al. [326] describe creating Nb_2C QDs by layer cutting and interlayer delamination simultaneously, with the aid of a 10-h strong sonication treatment, to create a uniform, ultrasmall nano-fluorophore for cell imaging and selective metal ion detection. The intense excitation-dependent fluorescence was created by a well-defined structure with several functional groups, as demonstrated by the characterization data. The quantum confinement effect of the ultrasmall lateral dimension and the surface imperfections brought on by the oxygen-containing species were identified as the causes of the QDs' strong PL emission. Based on the pH investigations, it is known that at pH values higher than 5, the Nb_2C QDs significantly deprotonate, leading to the development of a high negative surface charge. Thus, the QDs' stability and fluorescence intensity in this pH range were caused by electrostatic repulsion.

3.3.1.3. Electrochemical Etching. When using the HF acid etching approach, terminal groups may appear randomly on the MXene surfaces [305,327,328]. These are hazardous to the environment; thus, in order to make the etching process ecologically benign, the delamination and intercalation stages must be improved. The quest has now reached the laboratories for a fluorine-free synthesis of MXene that offers adequate up-scale manufacturing with good yield.[76,87] Nowadays, electrochemical exfoliation pathways are favored over chemical and ultrasonic exfoliation methods [271]. Their non-hazardous and environmentally friendly nature is a benefit. Furthermore, this technique is a viable substitute for preventing the irreversible flaws caused by prolonged exposure to ultrasonic radiation and significant oxidations. The earlier exfoliation methods also take a lot of time and may call for specialized equipment [329].

As a backup plan, the researchers suggest synthesizing co-doped MQDs with nitrogen and chlorine using the electrochemical etching technique [330]. The electrolyte environment was created by adding tetramethylammonium hydroxide and NH_4Cl, which subsequently interacted with the Ti and C layers over a sizable region. While the Cl and Ti ions interacted to form Ti–Cl termination, the applied electrical potential within the workstation led the carbon layers at the defect edges to fracture through their interaction with electrolyte ions. To create Cl, N Ti_3AlC_2 MXene QDs, the stripping of bulk Ti_3AlC_2 MAX phase (working electrode) was improved. Moreover, N was intercalated concurrently by the formation of new bonds. Because of the bulk Ti_3AlC_2's high conductivity, the process only needed a little energy and allowed for co-doping by selectively adding the proper electrolytes. The X-ray photoelectron spectroscopy (XPS) examination for C, N, O, and Cl could confirm the synthesis of the Cl, N-Ti_3AlC_2 MQDs. Later, the authors provided a model of the Cl, N-Ti_3AlC_2 scavenging process. It was suggested that $Ti_3C_2T_X$ MQDs be produced by electrochemical exfoliation, and to achieve stability, they were heavily fluorinated. The final product's structure and shape were examined using TEM images, and the XPS data's lack of aluminium species demonstrated that the Al layer had thoroughly exfoliated from the precursor. The intensity observed

was determined to be 10^{-3} GW cm^{-2}, leading to the suggestion that the resulting-prepared QDs be employed as saturable absorbers. Moreover, extremely mode-locked pulses were produced by adding fluorinated MQDs to the ytterbium-doped fibre laser.

3.3.1.4. Hydrothermal Technique. One of the most widely used methods for creating MQDs is hydrothermal synthesis, which involves delamination of the MXene precursor [331-333]. The nucleation of the crystal and subsequent growth are the two main stages in the process [334]. The 2D MXene sheets break and assemble when exposed to high pressure and temperatures. They react with metal hydroxides after the medium's pH may be adjusted to be either basic or acidic, which, at a faster rate, ultimately generates the necessary MQDs. Occasionally, the arrangement permits argon gas to pass through to stop the sample from oxidizing [335]. In this case, heterogeneous processes that take place in the aqueous phase at high temperatures and pressures can produce pure crystals. Compared to other approaches, the method's main benefits include size control, high yield, and minimal energy needs.

The synthesis of QDs using hydrothermal methods depends on various parameters interrelated to each other for controlling size, morphology, and properties. Among others, the important ones involve the type and thickness of the precursor materials, such as MXenes [334]. The exfoliation efficiency is directly related to such properties; thinner precursors may allow a more homogeneous breakdown and, hence, result in smaller QDs. When thicker or less reactive precursors are used, non-homogeneous exfoliation may result in QDs of larger size variation or irregular morphologies.

Reaction temperature and duration are equally important in determining the characteristics of QDs. Higher temperatures hasten the decomposition of the precursor material, with higher kinetic energy supporting fragmentation to form smaller QDs. However, extended use of such high temperatures could cause agglomeration, resulting in larger clusters rather than discrete QDs [336]. Precision in reaction time will contribute to balancing the size reduction and prevent the onset of aggregation, since this process can compromise the QDs' photonic properties. The added concentration of acid or base in the reaction medium has been crucial in order to modulate the speed of etching. Acidic conditions favored a rapid decomposition of the precursor, and it favored small QDs. However, excess acidity can lead to over-etching and even damage to the surface integrity of QDs. In contrast, basic environments suppress etching and yield larger-sized QDs with well-preserved surface terminations. Since pH tuning allows for precise control over the reaction rate and final morphology of QDs.

The dispersion behavior and surface chemistry of synthesized QDs are greatly affected by the choice of solvent. Most often, aqueous solvents are used because of their simplicity and owing to the ability of hydrophilic surface terminations to enhance dispersibility in polar media. Organic solvents can provide enhanced stability or functionalization of QDs through designed surface interactions suitable for particular optoelectronic or catalytic applications. Solvent environment impacts uniformity of particle growth, thus contributing to controlled size distribution [116]. Other factors are the modification of the surface terminal groups, atmosphere of reaction, and addition of additives. These further refine the functional properties of QDs. Surface functionalization by terminal groups influences the electronic and photonic behavior, thus allowing further fine-tuning for applications in light emission or charge transport. The reaction atmosphere, inert or oxidative, determines the oxidation state and stability of QDs. Remaining additives include stabilizing agents or surfactants, which prevent agglomeration and enhance dispersibility so that QDs maintain their unique nanoscale properties during and after synthesis [285].

The system's ambient conditions impact the water's density and dielectric constant, further altering the shape and response rate. As a result, the process enables controllability to produce the intended result [337]. It has been reported that the hydrothermal approach may be used to cut bulk-layered MXene and produce water-soluble Ti_3C_2 MQDs [302]. Here, MQDs were created at various temperatures by the researchers, who then acquired colloidal MQDs with various morphologies. With a 10% quantum yield, the synthesized MQDs exhibited a robust quantum confinement effect. FTIR, XPS, and XRD were used to examine the surface composition and functional groups of the prepared MQDs. The MQDs' excellent surface passivation is demonstrated by the PL intensities, which were mostly constant for varying pH levels. The hydrothermal temperature was one of the variables that determined the size and makeup of the MQDs produced using this process [338].

A research by Xue et al. [302] showed that a product's crystallinity frequently decreased as temperature increased. This will change the composition of the surface, which will change the behavior of the fluorescence. Subsequent investigation revealed that the MQDs produced at a high temperature (150 °C) were more cytotoxic than the MQDs-100 and MQDs-120; nonetheless, based on the luminescence records, the MQDs-150 were advised for use in Zn^{2+} detection. Zn^{2+} ions cause a considerable drop in PL intensity, while no quenching or increase in fluorescence was seen when using other metals.

3.3.1.5. Solvothermal Method. These days, organic solvents, including ethanol, dimethylsulfoxide (DMSO), and dimethylformamide (DMF), are used in place of aqueous solvents in the solvent-thermal approach, improving the process [324]. Compared to the hydrothermal method, the solvothermal technique is more straightforward to regulate regarding MQD shape, size, and dispersion [339,340]. The study emphasizes the solvothermal method for manufacturing $Ti_3C_2T_x$ MQDs with electroluminescence and photoluminescence characteristics. Three distinct varieties of MQDs were created, each with a unique amine dose ratio. To produce N-MQDs, the synthesized QDs were subjected to several centrifugation cycles and then dried thoroughly. The characterization data indicate that the resulting MQDs showed varying diameters in response to various solvothermal periods, which also affected the luminescence intensity of the particles. The space lattice information findings showed a high crystalline characteristic and validate the N-MQDs' tailoring [341].

Similar to this, an article describes how MXene nanosheets were sliced into MQDs using a straightforward solvothermal technique, which resulted in good photobleaching resistance [342]. The synthesized N-doped MQDs were used as a fluorescent nanoprobe to detect, ascorbic acid and Cr (VI) simultaneously. The MQD's outstanding water solubility can be attributed to the abundance of

hydrophilic groups on its surface, as demonstrated by the FTIR characterization data. Siya Lu et al.'s intriguing work shows how to create Ti_3C_2 MQDs with a brilliant two-photon white fluorescence. The researchers also saw huge shifts in the released light in high-pressure experiments. In this case, the Al MAX phase was etched to produce the Ti_3C_2 MXene sheets. The sheets were then sliced, and functionalized MQDs were obtained via a two-step solvothermal method [316]. Transient absorption studies were carried out to learn more about the luminescence process of the produced QDs. The photophysical properties of the produced MQDs. The findings suggested that the observed white fluorescence was caused by the synergistic interaction between the surface state and core of Ti_3C_2 MQDs. The finished product showed no evidence of significant harm to the host layers or strong emissions, and every characterization verified the safety of the preparation technique [316].

This technique enables strategic control over the crystal's growth, phase, or even growth direction. The method is well-known for being straightforward and for its ability to prevent MXenes from oxidizing. Furthermore, the produced shock waves and sonic cavitation facilitate the evacuation of gas. It has been shown that MQDs made without fluorinated agents exhibit increased biocompatibility. Nevertheless, a few disadvantages that have restricted the application of solvothermal/hydrothermal procedures include their extended duration, the use of organic solvents that are carcinogenic, and their lower rate of repeatability [343].

3.4. Post-synthesis storage and processing

The narrative does not finish when MXenes are created and delaminated. Further modifications of MXene characteristics will occur according to how they are handled and stored. These factors often get even less attention than synthesis procedures and protocols. These factors are almost always selected and discussed anecdotally but are hardly ever recorded in the literature. The time it takes to fabricate a device from synthesis is typically not stated in publications. However, it is reasonable to anticipate that $Ti_3C_2T_x$ utilized away immediately after delamination will differ from that used months later [344]. Naturally, the duration of this period varies depending on the method used to create MXene. Although MXenes vary quantitatively and measurably over time depending on all the circumstances and factors mentioned above, objective explanations of the timeframes employed from post-synthesis to device manufacture are rare [40]. For instance, the way MXene delaminates, edge oxidation, and the proportion of single to few-layer flakes will vary depending on whether it is kept as a wet or dry multilayer. After delaminating, how is the material stored before being used? is it kept in an open or covered vessel? What kind of temperature? Has it degassed or not? In the light or the dark? What pH, ionic concentration, and MXene concentration is it kept at in storage? Ever had it frozen? Once again, there are a lot of unseen factors that are crucial to performance but are neither taken into account nor disclosed while fabricating devices. MXenes are 2D sheets by nature;

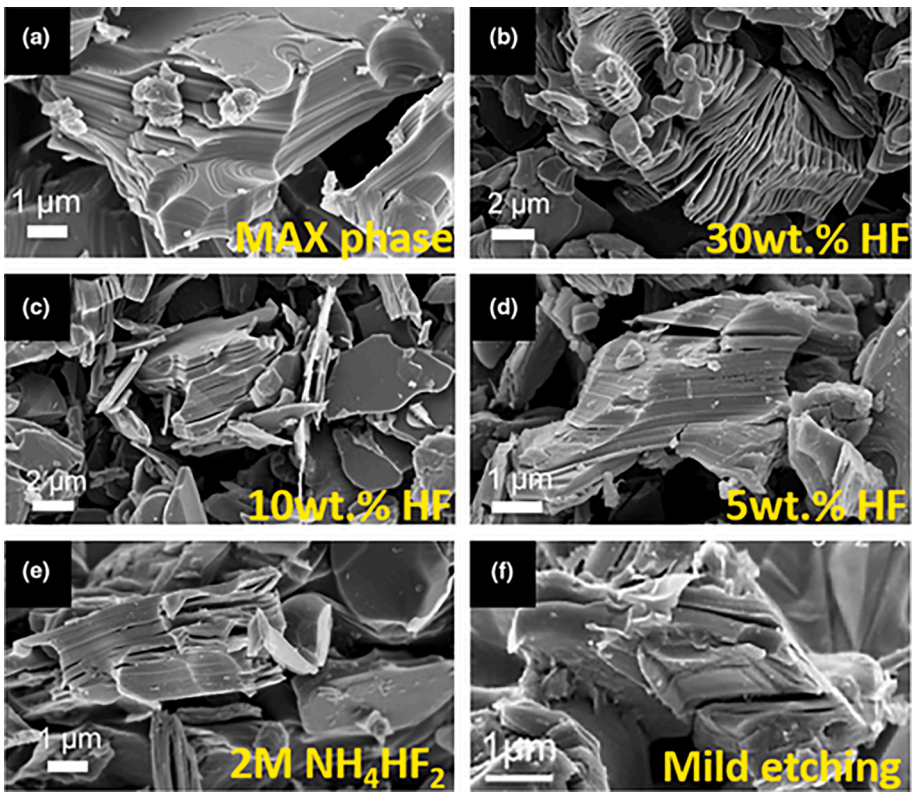

Fig. 6. SEM images of a) MAX phase; multilayered $Ti_3C_2T_x$ powder synthesized with: b) 30 wt.% HF; c) 10 wt.% HF; d) 5 wt.% HF; e) ammonium hydrogen fluoride; and f) 10 M LiF in 9 M HCL (mild etching). Reprinted with permission from Ref. [354].

therefore, variations in packing density, flake contact, alignment, and other characteristics impact how well the device works. Using conductivity as an example, it is evident that interflake contact and packing density have a significant impact on electron transport; yet, quantification of these macroscopic properties has received little attention. The qualities that are obtained vary depending on the method used to make the films, such as spray coating, vacuum filtering, blade coating, etc [345]. In addition, several parameters, including vacuum strength, MXene concentration, film surface, and pore size were chosen specifically for vacuum filtering in the process of creating these films. The film formation may also be influenced by the particular vacuum filtering configuration. These processing factors again compound when the produced structures, such as heterostructures, grow more complicated.

It's critical for the MXene community to realize that several number of variables influences device performance and effective MXene attributes and apparently random decisions [346]. These factors actually matter, even if many of them are almost undetectable in writing. These seemingly little decisions can greatly impact the measured performance in some situations or not at all. In any event, the impacts cannot be measured or even the scale of these effects cannot be understood if they are not disclosed.

4. Properties of MXene

MXenes are a class of transition metal carbides, nitrides, and carbonitrides that are two-dimensional and have a variety of characteristics that make them, attractive materials for various uses [347]. Excellent electrical conductivity is one of MXenes' noteworthy characteristics. This characteristic results from their particular unique structure, in which functional groups divide the layers of transition metals to provide conductive pathways [348]. MXenes are appealing for electronic devices, sensors, and energy storage applications because of their excellent electrical conductivity [349]. Apart from their conductivity, MXenes have exceptional mechanical characteristics [350]. Because of their strength and flexibility, they are well-suited for applications that call for strong, long-lasting materials. MXenes' electrical and mechanical qualities make them a viable option for composites and innovative structural materials. The hydrophilicity of MXenes is another noteworthy characteristic. MXene layers' hydrophilic surfaces enable effective interaction with water molecules. This feature is useful for water purification applications as MXenes may be used to absorb impurities and pollutants [351]. MXenes' hydrophilic character also enhances their biocompatibility, indicating that they are suitable for biomedical applications, including biosensing and medication administration [352]. Moreover, MXenes have optical characteristics that could be adjusted. MXenes' optical properties may be controlled by researchers through structural and compositional modifications, which makes them a viable option for use in photodetectors, optoelectronics, and other optical devices [353]. The flexibility of MXenes in a wide variety of technological applications is improved by its versatile optical characteristics.

4.1. Morphologies and Surface Chemistries

The resulting MXene morphologies are significantly influenced by the etching technique and etchant concentration. Using the HF etching technique with varying HF concentrations, starting from the MAX phase (Fig. 6a), forms accordion-like m-MXene, where greater HF concentration corresponds to more evident openings of MXene lamellas (Figs. 6b–d). Fig. 6e,f illustrates how LiF-HCl and other fluoride-based etching methods produce m-MXenes with minuscule MXene lamella holes. These mild-etching methods (light LiF-HCl and fluoride-based approaches) have actually eliminated the "A" element by a low concentration of in-situ generated HF (i.e., 3–5 wt%), even if they have a comparable shape with the MAX phase. Consequently, XRD and energy-dispersive X-ray spectrum (EDX) studies should be carried out to determine the effectiveness of Al's removal from the MAX, rather than relying just on the accordion-like shape [271]. Recent methods used to study the flake stacking and surface terminations of different MXenes include nuclear magnetic resonance (NMR) spectroscopy [354], neutron scattering [355], and electron energy-loss spectroscopy[356] and TEM [357]. These investigations verified that MXene surface terminations are distributed randomly rather than exhibiting a certain kind of functionality in a particular area. The DFT simulations showed that water molecules are hydrogen linked to the -OH groups, whereas -OH and -F are directly attached to the surface of MXene flakes [358]. Furthermore, there aren't any nearby -OH terminations. The realistic map of surface terminations on Ti_3C_2 sheets provided by these investigations can be utilized to anticipate the characteristics of the sheets. It is noted that interlayer interactions can be explained by hydrogen bonding between the O and/or F atoms on one side of the nanosheet and the -OH surface groups of the opposite side, as well as van der Waals bonding between the sheets, based on the neutron scattering measurements of $Ti_3C_2T_x$ [359]. The quantity of -OH compared to the -O and -F moieties positioned on the opposite surface, as well as the orientation of the -OH groups concerning the layers, determine the strength of interlayer hydrogen bonding [360,361]. On the sheet surfaces, hydrogen bonds are developed when there are water molecules between the layers. Additionally, the $Ti_3C_2T_x$ sheets may slide easily past one another due to the intercalation of cations, which may alter the sheets' rheological characteristics and also give them a clay-like behavior [362].

4.2. Theoretical Capacity

$Ti_3C_2T_x$ MXene, in particular, has a high specific capacitance because it has a large number of pseudocapacitive sites [363,364]. The valence state of Ti that links to the oxygen surface groups constantly changes as a result of the protonation of oxygen functional groups. This results in the amazing pseudocapacitive charge storage characteristics of MXenes in the acidic electrolyte [365] and the electrochemical process may be described as [366]. Using Faraday's law, the maximum theoretical capacity of $Ti_3C_2T_x$ in the potential range of −0.6–0 V may be calculated to be around 615 C g^{-1}. Nonetheless, at a voltage window of 0.55 V, the empirically obtained values are around 135 C g^{-1}, which is much less than the predicted capacity. The minimal use of active sites or incomplete redox reactions caused by the small potential range are two possible causes. Platinum or gold are usually used as current collectors for the

electrochemical analysis of MXenes. Nevertheless, this might divide water into a possible range of interest and reduce Coulombic efficiency due to the recurrent charge-discharge process. Nevertheless, this might divide water in the possible range of interest and reduce the Coulombic efficiency due to the recurrent charge-discharge process. Lukatskaya et al.[366] employed glassy carbon as current collectors for the MXene electrode to prevent this and were able to obtain a sizeable potential window of 1 V. This is so that the inherent capacity of various materials in the relevant potential range may be probed without causing water to split, thanks to glassy carbon's remarkable overpotential for hydrogen evolution reactions [367,368]. Consequently, the 90-nm-thick electrodes demonstrated an outstanding rate performance and a specific capacitance of up to 450 F g^{-1}, translating into an extremely high volumetric capacitance of around 1500 F cm^{-3}[366]. Through surface chemistry modification and/or heteroatom doping, MXene's theoretical capacitance can be pushed further. For instance, Yang et al.[369] used solvothermal treatment to effectively create flexible and freestanding N-doped $Ti_3C_2T_x$ films. In the 3 M H_2SO_4 electrolyte, the resulting nitrogen-doped $Ti_3C_2T_x$ films demonstrated an ultrahigh capacitance of 2836 F cm^{-3} (927 F g^{-1}) at 5 mV s^{-1}, setting a record for all known MXene-based materials.

Moreover, Wen et al.[370] presented a novel design for a lithium-MXene composite (Li-MXene) anode that significantly lowers the interfacial Li ion transport resistance between the garnet solid-state electrolyte and Li metal anode. When considered as electrodes, Li-MXene symmetric cells had very little interfacial resistance (5 Ω cm^2). The pure Li-based equivalent exhibited inadequate garnet contact, leading to a significantly higher interfacial resistance of 1291 Ω cm^2. Concurrently, LiF was in-situ produced at the Li-MXene/garnet interface due to the presence of fluorinated functionalized surfaces on MXene. This successfully separated electron transport and inhibited the production of dendritic Li. It was possible to achieve a high critical current density of up to 1.5 mA cm^{-2}. These findings stimulate further study using MXene as an addition towards novel composites and imply that varying additives with different functional groups may tune the characteristics of Li metal anode. Fang et al.[371] studied on a layered CaV_4O_9-MXene ($Ti_3C_2T_x$) composite that was assembled using CaV_4O_9 nanosheets on $Ti_3C_2T_x$, and he examined its electrochemical performance as a potential new cathode for zinc ion batteries (ZIB)s. The layered 2D structure created by CaV_4O_9 nanosheets attached to MXene's surface through interlamination effectively improved CaV_4O_9's electrical conductivity while preventing MXene nanosheet stacking. The structure also made fast ion and electron movement possible. The effects of adding different quantities of MXene on the electrochemical characteristics and morphology were further discussed. At 0.1 A g^{-1}, the composite exhibited an enhanced reversible capacity of 274.3 mA h g^{-1}, superior rate capabilities at 7 A g^{-1}, and after 2000 cycles, at a current density of 1 A g^{-1}, a high specific capacity of 107.6 mA h g^{-1} couldd be provided. The electrochemical performance has improved because of its distinct layered structure, high electrical conductivity, and pseudo capacitancepseudo-capacitance behavior.

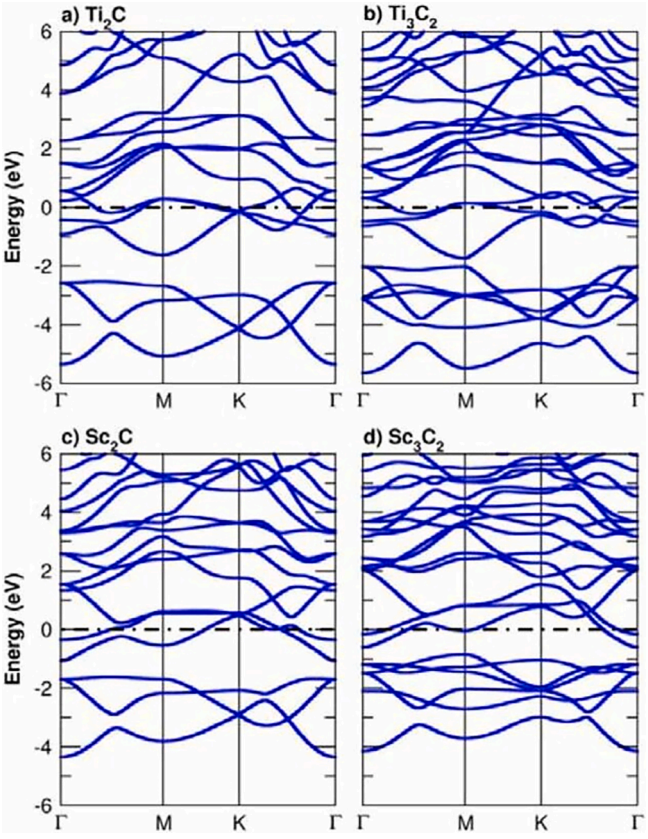

Fig. 7. Electrical band structures of monolayer level Ti_2C, Ti_3C_2, Sc_2C, and Sc_3C_2 systems. Reprinted from Ref. [375].

4.3. Electronic Band Structure

The metallic behaviourbehaviour of MXene, which is similar to MAX phases and has a well-fixed electron density close to the Fermi level, is one of its most significant characteristics.68 The insertion of new Ti-X bonds can modify the metallic behaviour. MXenes exhibits a narrow band-gap semiconductor characteristic through modification of the functional terminal groups. Most MXenes have indirect band gaps, except for $Sc_2C(OH)_2$, which has a straight band gap [354,372]. Their electronic characteristics are determined mainly by the electronic structure of the MXene surface, which is controlled by surface functionalization [373,374]. Because their oxidation states are almost equal and permit the admission of a single electron, -F and -OH groups have comparable impacts on the electrical structures of MXene, as shown in Fig. 7. -O- groups, on the other hand, act differently sincethey accept two electrons in the equilibrium state, in the equilibrium state [134]. The band structure topology of MXene can be either simple or non-trivial, depending on their spin-orbit interaction.

Moreover, MXene may be divided into metallic, semi-metallic, and semiconducting forms based on their electrical conductivity. $Ti_3C_2T_x$ filtrated film has strong intrinsic electronic/ionic conductivities and is rich in chemical elements compared to graphene [376-379]. The $Ti_3C_2T_x$ film exhibits superior metallic conductivity in experiments compared to other 2D metal sulfides/hydroxides [380]. For example, Yang et al.[381] realized the demand pulse laser generating based on MXenes and the nonlinear optical response at the visible region for the fisrt time. To realize passive Q-switched visible bulk laser encompassing the spectrum range of orange (607 nm), red (639 nm), and deep red (721 nm), the few-layer MXene $Ti_3C_2T_x$ was constructed and used as a saturable absorber (SA). For each of the three wavelengths, the shortest pulse widths and, the most extraordinary average output powers were (111 mW, 426 ns) at 607 nm, (150 mW, 264 ns) at 639 nm, and (115 mW, 328 ns) at 721 nm, respectively. Based on their experimental findings, the MXene $Ti_3C_2T_x$ SA appeared to be a promising and effective optical modulator in the visible range.

Nevertheless, the electrical conductivity of $Ti_3C_2T_x$ was primarily determined by its morphological and surface features, as a large flake size and good contact between individual flakes are typically associated with high conductivity [382]. For instance, Lipatov et al. [383] reported an extremely high breakdown current density in the newly developed two-dimensional material $Ti_3C_2T_x$ MXene. Individual high-quality monolayer $Ti_3C_2T_x$ flakes were prepared by an improved synthesis method, and Lipatov found that they exhibited the best values reported for $Ti_3C_2T_x$ flakes to date, with electrical conductivities of up to 11,000 S cm^{-1} and field-effect electron mobilities of up to 6 cm^2 V^{-1} s^{-1}. The breakdown current densities of around 1.2 × 10^8 A cm^{-2} were observed in all the

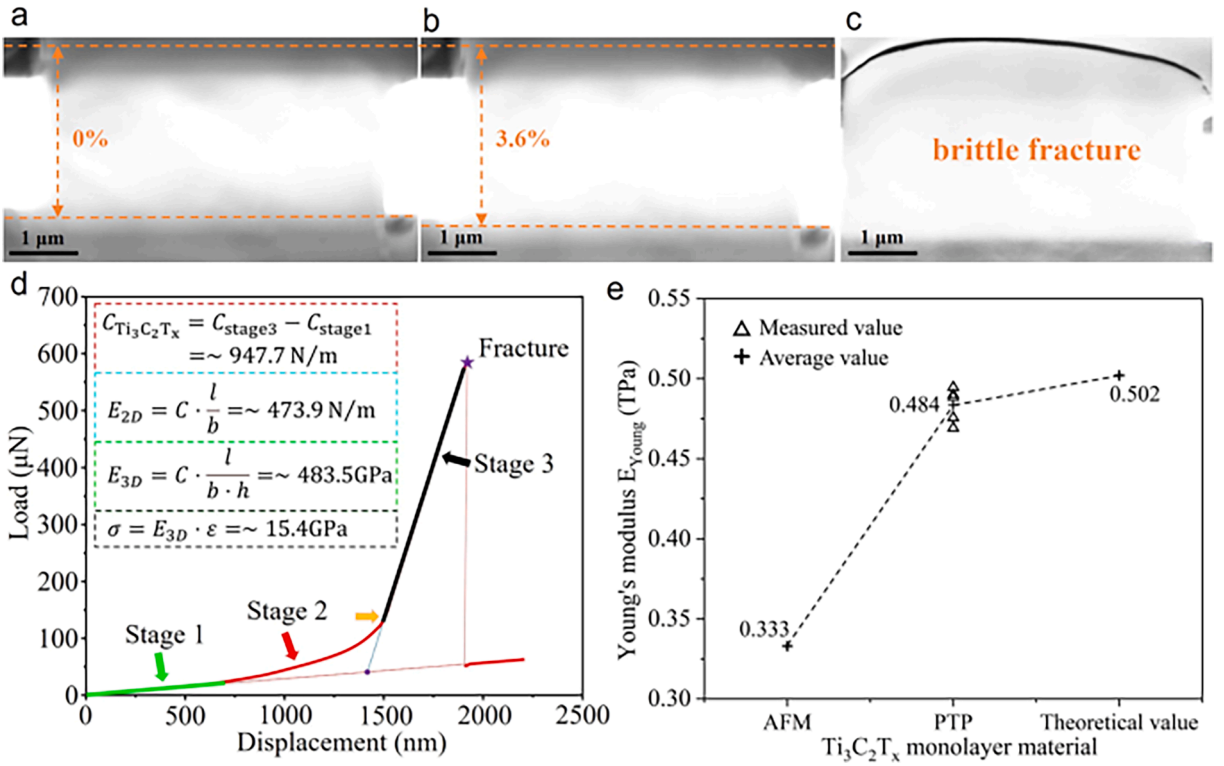

Fig. 8. (a). The SEM scan reveals that the $Ti_3C_2T_x$ specimen was fully tightened with 0% strain. (b) The SEM picture of the sample prior to tensile fracture reveals a peak strain of 3.6%. The orange dotted lines indicate the two boundaries of the examined sample. (c). The brittle fracture morphology of the sample following failure and the accompanying data. (d). The measured load-displacement curve. The insertion formula illustrates the mechanical property calculation method. Tensile strength (σ), 2D and 3D Young's modulus may be determined using C, l, b, h, and ε, representing the sample's tensile stiffness, stretched length, breadth, thickness, and strain. (e). Young's modulus of $Ti_3C_2T_x$ monolayer compared to AFM indentation test, "Push-to-Pull" (PTP) in situ tensile, and theoretical values. Reprinted from the Ref. [396].

flakes, and these values are on par with the best two-dimensional materials, such as graphene. $Ti_3C_2T_x$ is a potential material for nanometer-thin interconnects due to its extraordinary combination of high electrical conductivity and high current-carrying capacity. It also justified further research into the breakdown of current densities of other materials from the extensive MXene family. Additionally, several investigations have revealed that some MXenes have band gaps ranging from 0.05 to 2.87 eV, indicating semiconducting qualities [384-386]. MXenes are, therefore, effective cocatalysts and can increase reactivity by combining with semiconductors [387-390].

4.4. Mechanical Properties

MXenes exhibit remarkable mechanical properties, which are directly linked to their unique 2D structure, surface terminations, and strong covalent bonding within the layers. These properties can be further tuned for diverse engineering applications through careful manipulation of their composition and integration into composites as shown in Fig. 8. For example, the mechanical flexibility of delaminated MXene nanosheets, especially monolayer $Ti_3C_2T_x$, has been a subject of intense investigation [391]. Lipatov et al. [392] utilized atomic force microscopy (AFM) and nanoindentation to measure the elastic properties of monolayer and bilayer $Ti_3C_2T_x$ nanosheets. Their experiments determined an effective Young's modulus of 0.33 TPa, derived from force-displacement curves during nanoindentation, which closely matches the theoretical in-plane modulus of 502 GPa [393]. This agreement validates the intrinsic stiffness of the Ti-C lattice, governed by the strong covalent Ti-C bonds. Furthermore, under tensile testing, monolayer MXenes withstood biaxial strains up to 9.5% and uniaxial strains of 18% and 17% along the x and y crystallographic directions, respectively. This exceptional tolerance is attributed to the reversible stretching and compression of Ti-C bonds, a property that becomes even more pronounced with oxygen surface functionalization. Oxygen atoms, through their strong interaction with titanium, enhance the bonding strength, raising the strain at break to 20–28%.

The incorporation of MXenes into polymer matrices has been demonstrated as an effective strategy to improve their mechanical performance while preserving or even enhancing their other functional properties. For example, chitosan was integrated into $Ti_3C_2T_x$ films to enhance their tensile strength from 8.2 MPa to 43.5 MPa, a nearly 5.3-fold increase [394]. This improvement was attributed to the formation of hydrogen bonds between chitosan molecules and the surface terminations of the MXene sheets, which improves nanosheet alignment and load transfer. Similarly, Ling et al. [395] showed that the addition of polyvinyl alcohol (PVA) to $Ti_3C_2T_x$ matrices resulted in composites with significantly enhanced mechanical properties. The PVA matrix provided effective load distribution and maintained sheet dispersibility, enabling the composites to support five times their own weight without failure. These polymer-MXene composites exhibit a balance of strength, flexibility, and electrical conductivity, making them ideal for applications in flexible electronics, electromagnetic interference shielding, and structural reinforcements.

Further investigations into the mechanical properties of MXenes at the nanoscale have revealed their anisotropic behavior, which depends heavily on their structural orientation and thickness. Firestein et al. [397] used advanced techniques, including quantitative nanomechanical mapping and in situ tensile testing within a transmission electron microscope (TEM), to study Ti_3C_2 nanosheets. Their results highlighted a Young's modulus ranging from 80 to 100 GPa perpendicular to the basal plane, significantly lower than the in-plane modulus due to weaker interlayer interactions [398]. The tensile strength of 40 nm thick Ti_3C_2 nanosheets reached up to 670 MPa, indicating a strong dependence of mechanical strength on nanosheet thickness. This thickness effect arises from increased defect density and reduced interlayer interactions in thinner sheets, emphasizing the need for precise thickness control in applications requiring high tensile strength.

MXenes have also been explored for reinforcement in ceramics and metallic composites to enhance mechanical performance under extreme conditions. Cygan et al. [398] synthesized Ti_3C_2-Al_2O_3 composites via spark plasma sintering (SPS) with Ti and Mo surface modifications to counteract MXene's susceptibility to oxidation during high-temperature processing. These modifications strengthened interfacial bonding, resulting in a 10% and 15% increase in hardness and fracture toughness, respectively. This study demonstrates how surface engineering can mitigate MXene degradation and improve compatibility with ceramic matrices. Similarly, Chen et al. [399] fabricated $Ti_3C_2T_x$/Al composites with a nacre-inspired laminated architecture using self-assembled aluminum flakes coated with $Ti_3C_2T_x$. The design improved interfacial bonding, reduced strain gradients, and enabled a 53.4% increase in tensile strength and a 68.46% increase in elongation, highlighting the effectiveness of layered structures in balancing strength and ductility.

Advanced hybrid designs have further enhanced MXene mechanical properties through innovative molecular architectures. Kim et al. [400] developed Dicatechol Crosslinked MXene (MX@DC) films using the mussel-inspired dicatechol-6 (DC) as a crosslinking agent. This brick-and-mortar arrangement significantly improved toughness (by 513%) and Young's modulus (by 849%) compared to bare MXene films. These improvements arose from strong covalent interactions between the DC molecules and MXene surfaces, which enhance interfacial adhesion and dissipate mechanical stress more effectively. Collectively, these studies underline the transformative potential of MXenes in creating high-performance materials for structural, electronic, and multifunctional applications. The ability to tailor their mechanical properties through structural, compositional, and hybridization strategies opens new avenues for the development of robust, flexible, and lightweight materials in advanced engineering domains.

4.5. Optoelectronic Properties

Solution processing of MXene nanosheet dispersions makes it simple to manufacture MXene-based thin films with superior mechanical flexibility and electrical conductivity [401]. Furthermore, the solution-processed films may be dried naturally with good optoelectronic characteristics, negating the need for a postdeposition annealing step [402]. Comparing MXenes to other 2D materials like graphene, these advantages point to their significant potential in transparent conductive coatings, transparent energy storage

devices, and photothermal conversion [403]. For instance, highly conductive MXene-based transparent films with an outstanding optical transmittance of around 93% at a thickness of 4 nm were produced by spin-coating MXene aqueous solution [404]. The optical transmittance was inversely lowered by increasing the film thickness; when the transmittance fell to 86%, the sheet resistance also dropped to 330 Ω sq^{-1} [405]. In fact, a single layer of nanosheets (about 1.2 nm thick) resulted in a ~3% transmittance loss, which is comparable to the ~2.3% loss per layer, or 0.34 nm, of graphene nanosheets [406]. It is important to note that thin film production methods matter; to the optoelectronic performance of spin-coated $Ti_3C_2T_x$ MXene is often superior to that of spray-coated or sputtered transparent MXene films [407]. For example, in the spin-coated $Ti_3C_2T_x$ film aligned with big flakes, the figure of merit, FoM_e (defined as the ratio of DC conductivity to optical conductivity), reached 15, but for the spray-coated films, it was between 0.5 and 0.7 [408]. Furthermore, spin-coated films showed incredibly low optical absorption, which is essential for developing photovoltaic cells and high-performance displays [409]. Compared to other MXene kinds, $Ti_3C_2T_x$ has the finest optoelectronic characteristics to date [410]. As an illustration, V_2CT_x has a FoM_e of 6.5 [411], but $Ti_3C_2T_x$ has a FoM_e of 5 [412].

Furthermore, Ma et al. [417] demonstrated an optoelectronic synapse based on MXene/violet phosphorus (VP) van der Waals heterojunctions, enabling cross-modal experience of vision and smell. Thanks to conductive MXene's effective separation and transportation of photogenerated carriers, VP's photoelectric responsivity was significantly increased by up to 7 orders of magnitude, with a maximum value of 7.7 A W. Excited by UV light, a variety of low-power consumption synaptic activities were exhibited, including excitable postsynaptic currents, paired-pulse facilitation, short- and long-term plasticity, and "learning-experience" behaviour. Moreover, the suggested optoelectronic synapse displayed unique synaptic behaviours across multiple gas environments, which

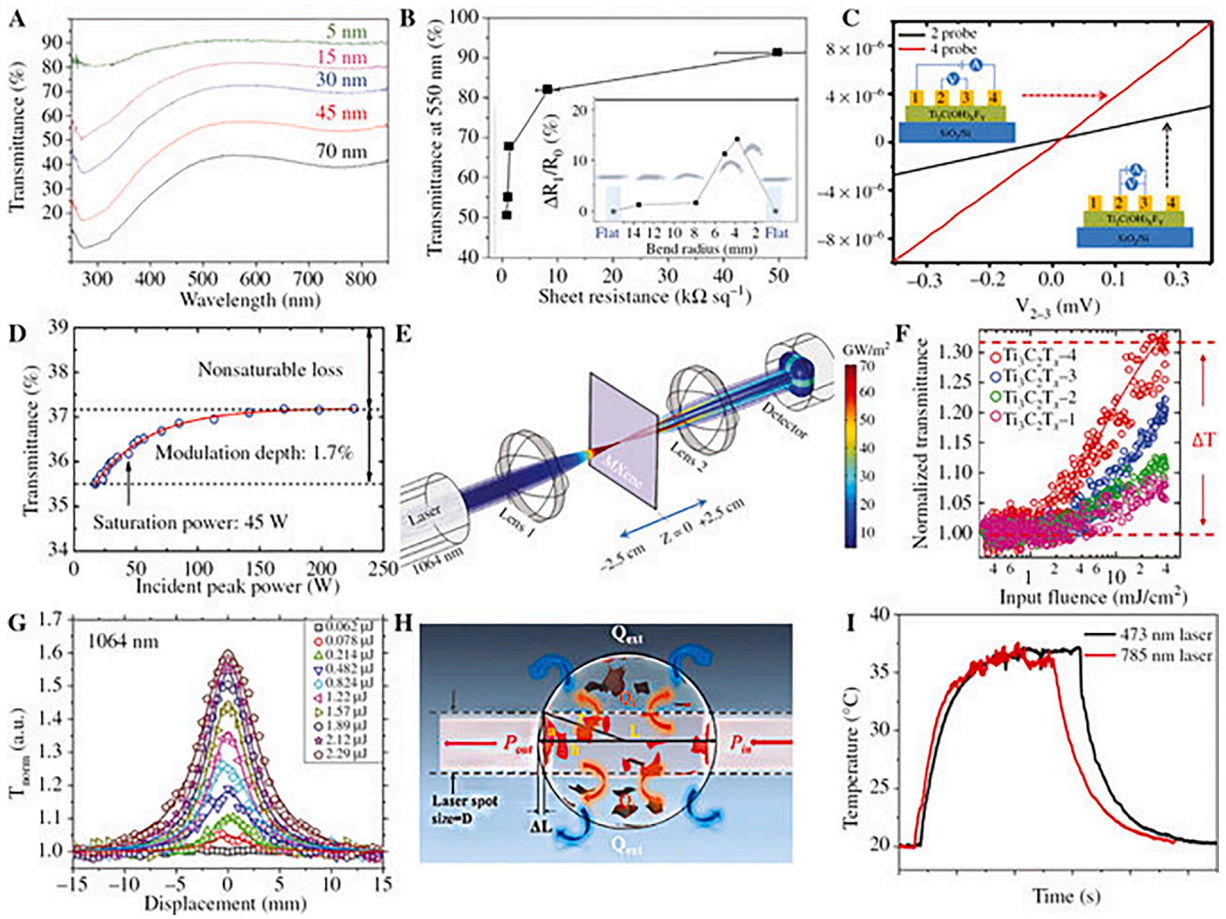

Fig. 9. The optical characteristics of MXenes. (a) UV-vis spectra of spray-coated $Ti_3C_2T_x$ films of varying thickness. (b) Transmittance at 550 nm of sprayed $Ti_3C_2T_x$ films plotted against sheet resistance. The inset displays the bending properties of spray-coated $Ti_3C_2T_x$ films. Reprinted with permission from Ref. [413] (c) Four-probe measurement to determine the conductance of a single Ti_2CT_x nanosheet and the contact resistance between Ti_2CT_x and a metal electrode. Insets show schematics of four probe measurements. Reprinted with permission from Ref. [414] (d) The nonlinear energy-dependent transmission curve of a side-polished fibre with a Ti_3CNT_x monolayer coating. Reprinted with permission from the Ref. [415](e) Implementation of the open aperture Z-scan approach. Laser density is determined by the z position. (f) Nonlinear transmittance of $Ti_3C_2T_x$ film vs input fluence. Reprinted with permission from Ref. [416] (g) Position-dependent nonlinear transmittance of $Ti_3C_2T_x$ was characterized using open aperture Z-scan. Reprinted with permission from Ref. [392](h) Schematic of a droplet of $Ti_3C_2T_x$ solution illuminated by a laser. (i) Time-resolved temperature profile of a $Ti_3C_2T_x$ droplet exposed to two different lasers. Reprinted with permission from the Ref. (A-B) Reproduced by permission of Ref.[330].

allowed it to model how visual and olfactory information combine to provide cross-modal perception, as shown in Fig. 9. This innovation offers a promising foundation for applications like neurorobotics and virtual realityhighlights that highlights the immense potential of VP in optoelectronics.

Percolation issues with very transparent conductive films are another matter that needs to be taken into account. Films typically experience a sharply elevated sheet resistance as their thickness approaches a certain point, known as the percolation threshold [418-420]. The percolation issue is unavoidable and undesired in real life. However, the spin-coated MXene films have a sheet resistance that scales nearly inversely with film thickness [404]. Usually seen in bulk-like films, this behaviour suggests that there are no obvious percolation issues. The MXene-based transparent films may be made suitably thin without significantly sacrificing their electrical conductivity, thanks to their exceptional optoelectronic qualities. MXene can function as transparent supercapacitors without the need for extra current collectors as a result.

4.6. Thermal Properties

Comprehending the thermal stability of MXene is crucial for applications as well as solution/thin film storage. It was discovered that the environment and the chemical makeup of MXenes significantly impacted their thermal stability by the combination of thermogravimetric and mass spectrometry investigation [393,421]. According to recent research, as shown in Fig. 10, $Ti_3C_2T_x$ (where T_x = F or OH) was stable at 500°C and maintained its hexagonal crystal structure in the Ar environment up to 800°C [422]. Thermogravimetric study indicated that $Ti_3C_2T_x$ converted to TiC and experienced a significant weight loss at 800 °C in an argon (Ar) environment [423]. Conversely, $Ti_3C_2T_x$ MXene undergoes partial oxidation at 200 °C to anatase TiO_2 nanocrystal and complete conversion to rutile TiO_2 at 1000 °C upon annealing in an oxygen environment [424]. $Ti_3C_2T_x$ MXene could be converted into TiO_2 with diverse crystal structures and morphologies by adjusting the heating rate, annealing temperature, and oxidation duration, resulting in various MXene-based hybrids and derivatives [425,426].

On the other hand, MXenes that have exposed metal atoms on their surface frequently exhibit high surface energy and are thermodynamically metastable, leading to spontaneous oxidation in air [427,428]. Effective O_2 dissociation occurs in the Ti_2C MXene due to significant interaction between the approaching O_2 molecules and the unsaturated Ti 3d orbitals on the virgin Ti_2C surface [429,430]. As such, the thermodynamic stability of the Ti_2C is compromised by the adsorbed O on it [431,432]. Additionally, MXene's exceptional heat conductivity is advantageous for electrical equipment. For example, Kang et al. [433] looked into MXene-coated cellulose hybrid fibres, namely their electrical characteristics, heating performance, and thermal stability. The manufacturing technique included continuously dipping cellulose fibres into an aqueous MXene solution, resulting in MXene-coated cellulose hybrid fibres. He validated the uniform coating of MXene sheets on cellulose fibre surfaces, with increasing content during the dip coating cycle, as shown by XRD and SEM examination. MXene's strong thermal conductivity served as a heat source, influencing the thermal stability of cellulose fibres at lower temperatures. Furthermore, increased temperatures affected the electrical characteristics of MXene/cellulose hybrid fibre composites. Interestingly, the longitudinal electrical conductivity of MXene-coated cellulose fibre composites increases by 0.06 S cm^{-1} following the last coating cycle, revealing the effective and conductive nature of the layer-by-layer MXene network established on the cellulose fibres. Moreover, Nguyen et al.[434] developed Pt-infiltrated MXenes, which have dramatically higher electrical and thermal conductivity. Both in-plane and cross-plane electrical/thermal conductivity improved dramatically (about 2.4/1.8 times and 6.6/5.0 times, respectively). Electrothermal heaters built with Pt-infiltrated MXene have exceptional efficiency, a rapid heating rate, and superior stability. Moreover, a single-layered Ti_3C_2 hybrid SiO_2 filler (Ti_3C_2-h- SiO_2).

Work by Ma et al.[444], developing a high-performance styrene-butadiene rubber (SBR) elastomer composite was discovered that incorporating SiO_2 not only improved the uniform dispersion of Ti_3C_2-h- SiO_2 in the SBR matrix but it also endowed the surface of $Ti3C_2$-h- SiO_2 with nano protuberances for immobilizing more rubber chains, resulting in better interfacial interaction between Ti_3C_2-h- $SiO_2$and the SBR matrix. Thus, the tensile strength of the SBR/ Ti_3C_2-h-SiO_2 elastomer composite was increased by 174% when compared to the unfilled SBR. Furthermore, the wet skid resistance and rolling resistance of the SBR/ Ti_3C_2-h- SiO_2 elastomer composite were significantly enhanced. Remarkably, the SBR/ Ti_3C_2-h- SiO_2 elastomer composite's incredible thermal conductivity (0.401 W m^{-1} K^{-1}) and electrical conductivity (4.87×10^{-4} S m^{-1}) were similar to that of the SBR/reduced graphene oxide (rGO) elastomer composite, suggesting that Ti_3C_2-h- SiO_2's conductivity may be competitive with that of rGO.

Also, for heat conductive and electrical insulating devices, Liu et al. [445] created a nacre-inspired outstanding poly(p-phenylene-2,6-benzobisoxazole) (PBO)/MXene hybrid film using a sol-gel-film conversion approach and a homogenous gelation procedure. The nanocomposite film was electrically insulating (2.5×10^9 Ω cm) and had outstanding mechanical properties (tensile strength of 416.7 MPa, Young's modulus of 9.1 GPa, and toughness of 97.3 MJ m^{-3} due to the optimized brick and mortar structure and strong bridging and encircling effects of the fine PBO nanofibre network on the MXene nanosheets. The synergistic alignment of PBO nanofibres and MXene nanosheets results in an in-plane thermal conductivity of 42.2 W m^{-1} K^{-1}. The film also had high thermal stability and flame retardancy. This innovation expands the possibilities for creating high-performance thermally conductive yet electrically insulating composites.

MXene's thermal conductivity varies with lateral size. For instance, in a 5-μm flake at ambient temperature, the thermal conductivity of Hf_2CO_2 was expected to be 86.25 W m^{-1} K^{-1}, and in a 100-μm flake, it rose to 131.2 W m^{-1} K^{-1}.[446] Hf_2CO_2 had a thermal expansion value of 6.094×10^{-6} K^{-1} at ambient temperature. The thermal conductivity of single-layer Mo_2C at ambient temperature is increased from 48.4 to 64.7 W m^{-1} K^{-1} by n-doping MXene in the armchair direction [439].

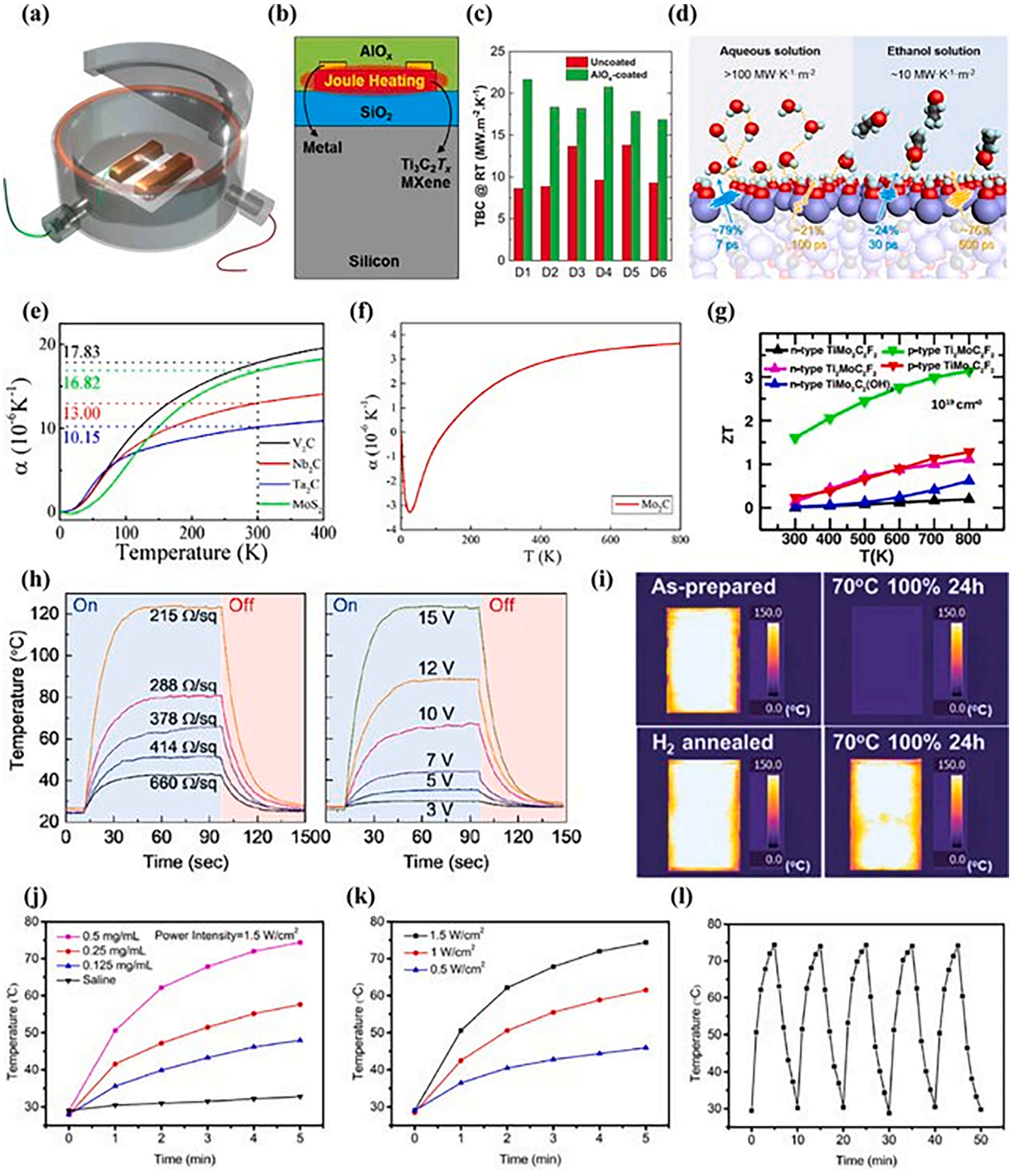

(caption on next page)

Fig. 10. (a) A schematic of the experimental setup for measuring the thermal diffusivity of a thin $Ti_3C_2T_x$ sheet using the TET approach.[83] Reproduced with permission from reference [435]. (b) Schematic of self-heating/sensing device for detecting thermal conduction at $Ti_3C_2T_x$-SiO_2 interface. (c) TBC was calculated using six separate devices with and without an encapsulating layer at room temperature (RT). Reprinted with permission from reference [436]. (d) Thermal conduction at the MXene–liquid interface. Reproduced with permission from reference [437]. (e) Coefficient of thermal expansion for V_2C, Nb_2C, and Ta_2C and (f) Mo_2C as a function of temperature. Reproduced by permission of the reference. [438 439]. (g) Thermoelectric figure of merit based on Ti and Mo for double transition metal MXenes. Reproduced by permission of Ref. [440] (h) Temperature as a function of time for $Ti_3C_2T_x$-based thin films, illustrating how external voltage magnitude (right panel) and sheet resistance (left panel) affect Joule heating efficiency. Reproduced from ref. [441]. (i) Evaluation of the Joule heating efficiency (for the as-prepared and hydrogen-annealed $Ti_3C_2T_x$ films) in a warm, humid atmosphere before and during the oxidation treatment. Reproduced by permission of the reference. [442] The effects of the photothermal impact of $Ti_3C_2T_x$ MXene microspheres on temperature change are determined by (j) the concentration of the active species and (k) the power density of the incident irradiation. (l) Stability test of MXenes' photothermal conversion capabilities. Reproduced from ref. [443].

4.7. Magnetic Properties

Applications for spintronic devices require materials with strong and tunable magnetic moments. Notwithstanding the diversity of MXenes, most of them have non-magnetic ground states, whether they are bare or not [447,448]. The strong covalent connection that exists between the transition metal and the X element is the reason for this. However, it has been hypothesized that some bare MXenes are innately magnetic, as shown in Fig. 10. These include the ferromagnetic Cr_2C [449] and Ti_2N [450], as well as the anti-ferromagnetic Cr_2N [451] and Mn_2C [452]. In the case of MXenes, the magnetism might be caused by surface terminations [453], defects in monolayers [450], and intrinsic features of the transition metal [454]. As previously mentioned, the most prevalent MXenes, such as Ti_3C_2, are non-magnetic, yet reports of various magnetic structures have been made in certain instances. For instance, Dong et al.[455] found that regardless of the kind of surface terminations, $Ti_2M_nC_2T_x$ MXenes are ferromagnetic in the ground states. $Ti_2MnC_2T_x$ is a member of a recently discovered class of ordered double-transition-metal MXenes [456], whereby one or two transition metal layers are positioned between the layers of another metal. The study of double-transition-metal MXenes with Ti atoms as the core layer by Sun et al.[457] demonstrated that distinct cation configurations and terminations result in a range of magnetic ordering and characteristics that differ from the single transition metal carbides that have been identified up to this point. A unique MAX phase with in-plane chemical order, which was dubbed i-MAX, is $(M_{2/3}, M_{1/3})_2AX$ are i-MXenes, which include $W_{4/3}C$ and $Nb_{4/3}C$, and they were formed by etching the A-element atoms from the i-MAX phases [458]. Earlier, Zhu et al.[459] had demonstrated that the energetically advantageous location for Li adsorption is on top of C and had discovered for Nb_2C a theoretical in-plane lattice constant value in accordance with the experimental one.

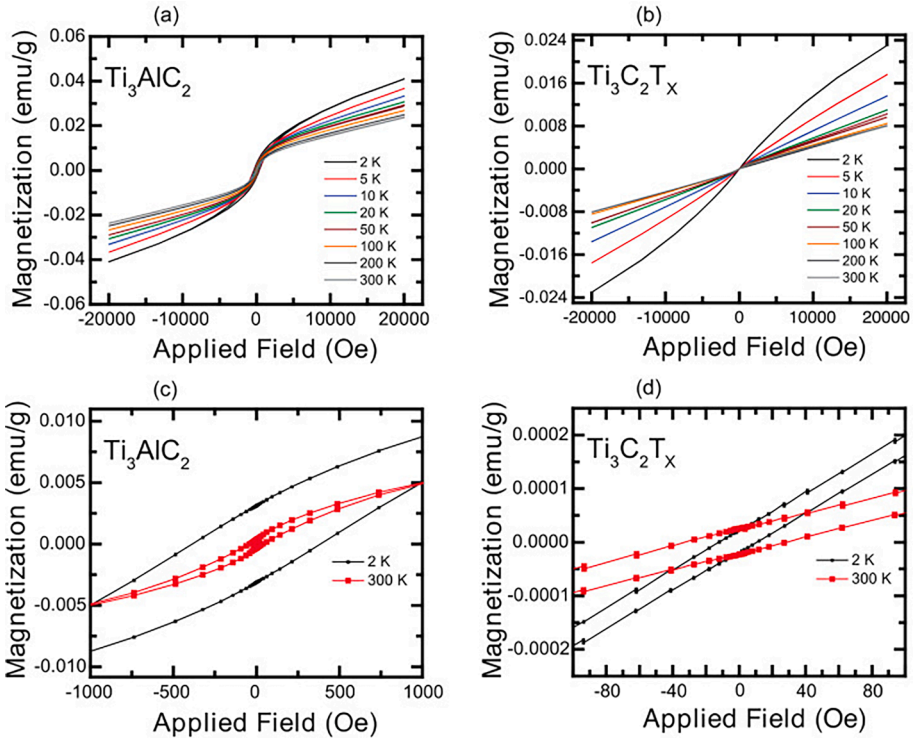

Fig. 11. Magnetization vs external magnetic field for samples of LiF-etched $Ti_3C_2T_X$ (b,d) and Ti_3AlC_2 (a,c). Reprinted from Ref. [464].

With a generic formula of $(M_{2/3}, M_{1/3})_2AX$, Gao and Zhang et al. [458] focused on the magnetic characteristics of i-MXenes in 2020. They specifically looked at the situations in which M, or the dopant element, is magnetic and one of the transition metals other than Tc using DFT computations. They discovered that 62 of the 319 i-MXenes were magnetic. Furthermore, the magnetic configuration of six can vary according to their geometries (hexagonal or rectangular), which need the application of strain. As a result, i-MXenes' magneto-crystalline anisotropy may be improved. Kumar et al. [460] conducted a thorough theoretical investigation of the magnetic characteristics of nitrogen-based MXenes, which contain one more electron per unit cell in comparison to carbon-based ones. The authors proposed a straightforward model to forecast the magnetic behaviour of M_2NT_2, supposing that the only electrons capable of generating magnetism are those occupying the non-bonding d-orbitals. They discovered five nitride MXenes (Mn_2NF_2, Mn_2NO_2, $Mn_2N(OH)_2$, Ti_2NO_2, and Cr_2NO_2) with strong ferromagnetic ground states by applying their model to M_2NT_2 MXenes containing transition metals from the third period of the periodic table. The magnetically ordered phases were stable because the curie temperatures for all terminations were likewise much higher than room temperature.

Bandyopadhyay et al. studied the point defect generation processes in MXenes [461]. Due to unpaired electrons in the spin split d-orbitals, they discovered that only a tiny percentage of the faulty MXenes develop a magnetic character. Consequently, they proposed that the application of inherent point defects may alter the magnetic characteristics of MXenes. Additionally, Scheibe et al. [462] studied the impact of various terminations on $Ti_3C_2T_x$'s magnetic characteristics. Researchers discovered that while the naked TiC samples behaved paramagnetically, the same as the samples with F or S-based terminations, the behaviour of the samples changed to ferromagnetic or paramagnetic. As a result, modulating the surface terminations can change the magnetic characteristics of $Ti_3C_2T_x$. Cr_2C is a ferromagnetic half-metal that becomes an antiferromagnetic semiconductor when it is terminated by F, H, OH, or Cl groups.

Most recently, Sobolev et al.[463] investigated the feasibility of immediately delaminating multilayer $Ti_3C_2T_x$ MXene sheets by cultivating iron oxide magnetic nanoparticles inside the interlayer gap. It was discovered that when the mass fraction of particles reached a level similar to or higher than that of MXenes, the development of these particles is followed by a significant improvement in the yield of single-layer MXene and correct magnetic characteristics in the resultant composite. The discovered method was applied to simplify synthesis methods to produce magnetic nanoadsorbents based on MXene that have adjustable characteristics. The neighbouring sheets spread as a result of the iron salt intercalation of the ML $Ti_3C_2T_x$ structure, creating empty nucleation sites for more MNP development. As a result, when the MXene concentration decreased, so did the size of the resultant MNPs. The magnetic properties of MXenes and MAX phases are presented in Fig. 11.

As a result, the mutual concentration of reagents was used to carefully adjust the magnetic properties, such as M_S, M_R/M_S, and μ_0H_C, of the resulting composites, from almost superparamagnetic to much more bulky. The sample had a good delamination rate and magnetic characteristics appropriate for the suggested use: the removal of MXene-based nano adsorbents from water using a magnetic field when the number of MNPs was more than the original MXenes. The MXene- iron oxide (Fe_3O_4) nanoparticles (MNP) nanocomposites showed a notable Cu^{2+} adsorption capability of 105.8 mg/g in the carried-out adsorption investigation. The described methodology may be effectively used to the fabrication of nanoadsorbents and offers a facile way to synthesize magnetic MXene-MNP composites. In another study[463], he also investigated the feasibility of directly delaminating multilayer $Ti_3C_2T_x$ MXene sheets through the growth of iron oxide magnetic nanoparticles inside their interlayer gap. They discovered that their development is followed by an effective augmentation of single-layer MXene yield and appropriate magnetic characteristics of the resultant composite, with a mass fraction of particles equal to or greater than that of MXenes. The method that was developed may also be utilized to streamline the synthesis procedures to produce magnetic nanoadsorbents based on MXene that have adjustable characteristics.

4.8. Gas Barrier Properties

MXenes' impermeable characteristic makes it possible to enhance polymers' barrier qualities, preventing gases and tiny molecules from penetrating. When compared to their neat polymer equivalents, NCs filled with graphene and layered silicates are known to have much better barrier qualities [465,466]. The tortuosity model, which explains how the diffusion of a tiny molecule will have to travel a longer, more convoluted path around impermeable filler particles, can be used to describe this phenomenon. That diffusion path can get significantly longer if these particles have larger aspect ratios than it would in an empty polymer. The permeability of nylon-6 was decreased by 94% and up to 90% with 1.74 vol % DHT-treated Ti_3C_2 in epoxy NCs, according to Carey et al.'s [467] study on the water vapour barrier characteristics of both nylon-6 and epoxy NCs [468]. While there have been few reports of MXene-filled separation membranes, there have been few investigations on the permeation and barrier characteristics of MXene NCs. The impact of Ti_2CT_z on membranes for solvent dehydration of isopropanol and water mixtures was investigated by Liu et al. [86,469]. Through $Ti_3C_2T_z$/Pebax/ polyurethane (PU) (where Pebax is a commercial copolymer of polyamide (PA) and polyether) membranes, Shamsabadi et al. [470] measured the gas permeability of H_2, CO_2, N_2, and CH_4. They found improved CO_2/N_2 selectivity, which was attributed to the gas solubility contribution of the functional groups on the $Ti_3C_2T_z$ nanosheets, particularly the high CO_2 adsorption capacity of the hydroxyl groups.

Moreover, Seo et al.[471] utilized MXene and graphene oxide (GO) together for the first time to cover a nylon 6 substrate (often used in storage tanks) with an H_2 gas barrier. A simple two-step procedure was developed using the carbodiimide process to covalently link MXene and GO via 3-aminopropyl triethoxysilane (APTES). In comparison to the pristine MXene and GO, the MXene-GO hybrid nanofiller (f-MXene-GO) showed a more significant gallery gap between the nanosheets. Furthermore, GO was also somewhat decreased by APTES's amine functional groups. The efficiency of APTES grafting to improve the interaction with poly (ethylene-co-acrylic acid) (EAA) was shown by a rise in the gallery gap between both MXene layers in the f-MXene-GO/EAA nanocomposite when compared to MXene/EAA. In contrast to GO/EAA, MXene/EAA had a greater H_2 gas barrier and better mechanical qualities, but it adhered to the nylon 6 substrate less firmly. f-MXene-GO/EAA demonstrated a prudent amalgamation of barrier and adhesion

characteristics. In comparison to nylon 6, the 10 wt% f-MXene-GO/EAA coated layer demonstrated a very poor H_2 permeability coefficient (0.03 cc.mm.m^{-2} d^{-1} atm^{-1}) and a notable 89% decrease in the H_2 gas transmission rate. Also, Shi et al. [472], applied MXene coatings on pipe steel using a straightforward spin-coating technique and a colloidal solution. By creating a barrier against diffusion, MXene coatings provided exceptional corrosion protection and hydrogen resistance. In the experiment, the diffusion coefficient dropped and the MXene coating's hydrogen permeability was one-third that of the substrate. The mechanistic analysis showed that the concentration of the d-MXene colloidal solution controls the thickness of a single coating, while the number of spin-coated layers influenced the MXene coatings' hydrogen resistance. The enhancement in hydrogen resistance might be restricted, nevertheless, by the harm that the H^+ and F^- containing colloidal solution causes to the sample surface. Furthermore, by using melt mixing, Wang et al. [473] created the biodegradable poly (butylene adipate-co-terephthalate)/MXene (PBAT/ $Ti_3C_2T_x$) composite casting films. The observation made using a SEM revealed that the $Ti_3C_2T_x$ nanosheets were well-suited to the PBAT matrix. When the concentration was less than 2 wt%, $Ti_3C_2T_x$ served as a nucleating agent to increase the crystallinity. The mechanical tests demonstrated that, in comparison to those of pure PBAT, the addition of 1.0 wt% $Ti_3C_2T_x$ concurrently increased the tensile stress, elongation at break, and Young's modulus of the PBAT/ $Ti_3C_2T_x$ nanocomposite. The mechanical dynamical experiments demonstrated that the PBAT nanocomposite's storage modulus in a glassy state was greatly enhanced by the inclusion of $Ti_3C_2T_x$. The oxygen transmission rate (OTR) of PBAT-1.0 with 1.0 wt% $Ti_3C_2T_x$ was the lowest at 782 cc/m^2·day and 10.2 g/m^2·day when compared to pure PBAT. The increased effective diffusion route length for gases caused by the presence of $Ti_3C_2T_x$ nanosheets is responsible for the improvement in gas barrier characteristics. The OTR and water vapor transmission rate (WVPR) of PBAT-1.0 were further decreased to 732 cc/m^2·day and 6.5 g/m^2·day, respectively, with the biaxial stretching. The improved water vapor and water barrier properties of the PBAT composite sheets suggests a possible use in green packaging. Also, MXene can implement as a protective coating for the salty environments as shown in Fig. 12.

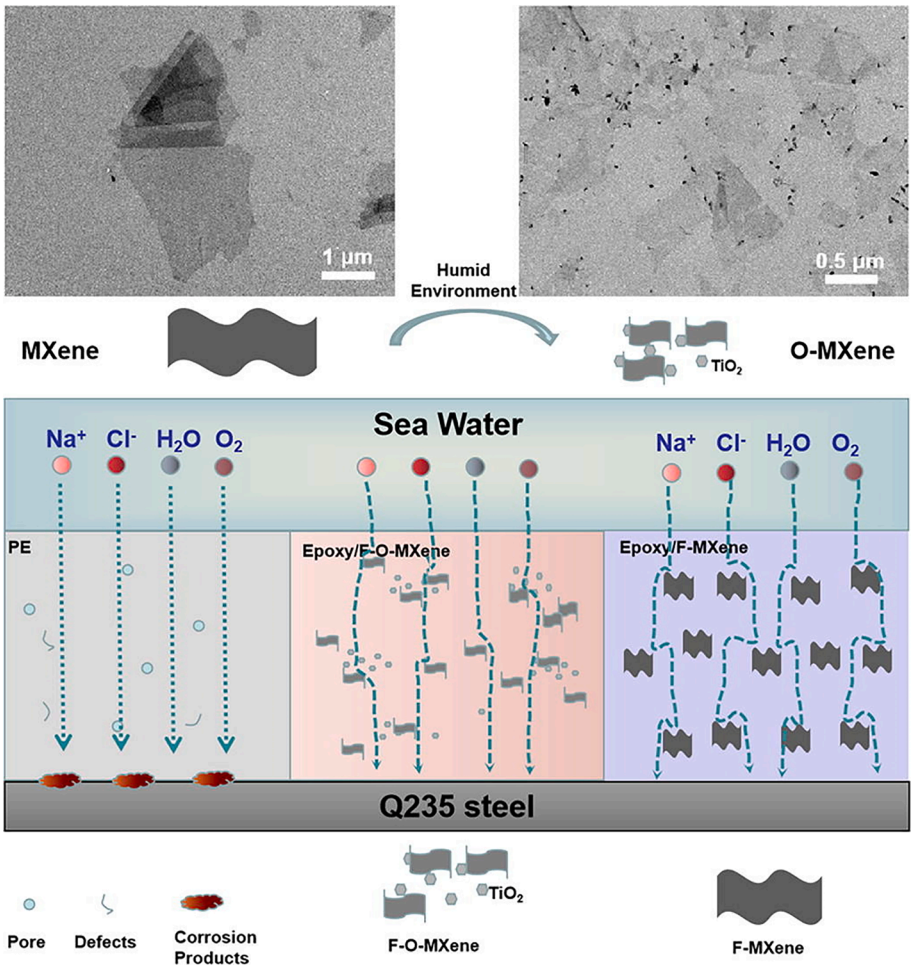

Fig. 12. Barrier properties of MXene for steel under marine environment. Reprinted with the permission from the Ref. [474].

4.9. Stability of MXene

Stability of MXenes, important representatives of two-dimensional materials, is closely related to their structural composition, surface chemistry, and environmental interactions. Basically, the structure of MXenes consists of early transition metals such as Ti, Nb, Mo arranged in a layered manner, interleaved with carbon or nitrogen atoms. The elimination of "A" layers during synthesis introduces the following surface terminations, for example: –F, –O, –OH, which strongly influence their stability. For example, the electron density redistribution caused by these terminations may strengthen or reduce the resistance to oxidation [236]. The MXene, especially of the titanium type, such as Ti_3C_2, presents high electronegativity differences and strong affinity between Ti and oxygen, thereby making it highly susceptible to oxidation. In most instances, the resultant compound is often TiO_2, which irreversibly changes the properties of MXenes [150].

Environmental factors, such as temperature and oxygen and humidity levels, have been considered among the very important parameters governing the stability of MXenes. With increased temperatures, this process can be accelerated because heat provides energy to cross the different activation barriers of the oxidation processes. At room temperature, atmospheric oxygen becomes active with the MXene surfaces, starting a gradual conversion into oxides. Under humid conditions, water molecules further facilitate hydrolytic degradation through interactions with surface terminations that facilitate further oxidation [475]. It has been illustrated that not only does a higher relative humidity accelerate degradation, but it also escalates the rate of delamination in MXene dispersions, which undermines their structural integrity. Storage media are another variable to take into consideration; MXenes stored in aqueous dispersions are a delicate balance between colloidal stability and chemical degradation, where it is a matter of pH and ionic strength.

Other factors include zeta potential, particle size distribution, and interlayer spacing, which are colloidal properties that determine the stability of MXene. As would be expected, a highly negative zeta potential stabilizes MXene dispersions through enhanced electrostatic repulsion between sheets that promotes non-agglomeration. The addition of multivalent cations, for example, Ca^{2+} or Mg^{2+}, neutralizes surface charges and leads to the aggregation and eventual destabilization of particles [476]. Moreover, smaller MXene flakes with larger surface area-to-volume ratios have a higher tendency toward oxidation due to the fact that more activity can take place on their surfaces. The interlayer spacing can be modulated based on the hydration level or intercalated ions and, therefore, either stabilizes or destabilizes MXenes depending on whether it restricts or facilitates diffusion of reactive species like O_2 or H_2O [383].

Chemical functionalization and structural modifications have become the critical means toward enhancing MXene stability. Covalent grafting or noncovalent interactions of polymers, including polyaniline and polyethylene glycol, have been shown to shield MXenes from oxidation via the creation of protective barriers. Encapsulation in inert matrices, like silica or polymer resins, limits exposure to oxidative agents. Reducing agents such as ascorbic acid or sodium sulfite may be added during storage that, upon reaction with oxidative species, greatly extend the MXene lifespans [65]. The surface chemistry can also be tailored by selective termination-for example, by minimizing –OH groups in favor of –F or –O terminations-which enhances the oxidative resistance due to modification of environmental agent interactions with the material [477].

Optimized synthesis and storage conditions are necessary to ensure functionality in MXene. The nature of the synthesis route itself, using either HF etching or milder LiF/HCl etching, determines both the extent and nature of surface termination and thus directly influences stability [478]. After synthesis, MXenes benefit from inert atmosphere storage, such as in argon or nitrogen, or at lower temperatures to diminish the kinetics of degradation. Further mitigation against degradation is achieved by the use of passivating agents during storage or when in dispersion. Recent research also involves the investigation of solvent engineering, including dispersing MXenes in aprotic solvents such as dimethyl sulfoxide or ionic liquids, which reduce hydrolytic and oxidative stresses

Table 5
Surface-modified MXenes and their methods of preparation

Surface functionalized 2D MXenes	Sample	Synthesis method	Solvent or atmosphere reaction	Temperature (°C)	Ref.
Functionalized MXenes by small molecules	$NaAlH_4$-modified Ti_3C_2	Ball milling	Ar	—	[483]
	FePc-modified Ti_3C_2	Self-assembly	Dimethylformamide (DMF)	—	[484]
	$C_{12}E_6$-modified Ti_3C_2	Sonication	Water	40	[485]
	Et-modified Nb_2C	Hydrothermal approach	Ethanol	100	[486]
Functionalized MXenes by macromolecules	Sodium alginate-modified Ti_3C_2	Vacuum-assisted filtration	Deionized water	Room temperature	[487]
	PPy modified Ti_3C_2	In situ polymerization	Deionized water	Room temperature	[488]
	PS modified Ti_3C_2	Electrostatic assembly	Deionized water	50	[489]
	PVA modified Ti_3C_2	Vacuum-assisted filtration	Deionized water	Room temperature	[490]
	PDDA modified Ti_3C_2	Vacuum-assisted filtration	Deionized water	Room temperature	[490]
Functionalized MXenes by single heteroatoms	V-Doped Ti_3C_2	Hydrothermal approach	Water	120	[491]
	S-Doped Ti_3C_2	Solution blending	Deionized water	155	[492]
	S-Doped Ti_3C_2	Heat and milling treatment	Ar	1650	[493]
	N-Doped V_4C_3	Heat treatment	Ammonia	350–550	[494]
	N-Doped Nb_2C	Hydrothermal approach	Deionized water	150	[495]
	P-Doped V_2C	Heat treatment	Ar	300–500	[496]

[437,479]. In-depth understanding of these parameters will allow for the stabilization of MXenes in long-term energy applications, catalysis, and electronics.

4.10. Property and Surface Modification

The narrative doesn't finish when MXenes are created and delaminated. Further modifications of MXene characteristics will occur according to how they are handled and stored. These factors often get even less attention than synthesis procedures and protocols.The length of time it takes to fabricate a device from synthesis is typically not stated in publications. However, it is reasonable to anticipate that $Ti_3C_2T_x$ utilized right away after delamination will differ from that used months later. Naturally, the duration of this period varies on the method used to create MXene. For instance, the way MXene delaminates, edge oxidation, and the proportion of single to few-layer flakes will vary depending on whether it is kept as a wet or dry multilayer. After delamination, the material is stored in either an open or a covered vessel, under specific temperature conditions. It may or may not undergo degassing and is kept either in light or in darkness, depending on the requirements. The storage conditions also include maintaining specific pH levels, ionic concentration, and MXene concentration. Additionally, it is noted whether the material has ever been frozen during storage. Table 5 presents the surface-modified MXene types along with their preparation methods.

Modifying the surface via surfactants, covalent functionalization, or surface functional group tuning is one of the best approaches to achieve homogeneous dispersion of a nanofiller into a polymer matrix. Using this method to create NCs has been the subject of many papers since Chen et al.'s report on poly(2-(dimethylamino)ethyl methacrylate) PDAEMA-grafted V_2CT_z [480]. The grafting of four functional groups—-NH_2, -COOR, -C_6H_6, and -$C_{12}H_{26}$—on the surface of $Ti_3C_2T_z$ was investigated by Hao et al. [481]. The method used to accomplish this functionalization was to mix ethanol, water, and ammonium with the dried powder of colloidal $Ti_3C_2T_z$, stir for 24 h, and then add either 3-aminopropyl)triethoxysilane, (γ-methacryloxypropyl)trimethoxysilane, (methyl aniline)triethoxysilane, or (dodecyl)triethoxysilane for —-NH_2, -COOR, -C_6H_6, and -$C_{12}H_{26}$-grafted Ti_3C_2, respectively. Another twenty-four hours were spent stirring, centrifuging, and drying after this. After that, the grafted MXene was used to create membranes based on polyethyleneimine (PEI) or PDMS for investigations on solvent transport. The highest flux improvement ratio for isopropanol, ethyl acetate, toluene, and n-heptane, respectively, was obtained by incorporating —-NH_2, -COOR, -C_6H_6, and -$C_{12}H_{26}$. This result was shown to be independent of the membrane matrix (PEI or PDMS). Additionally, solvent-resistant nanofiltration (SRNF) membranes' capacity to reject impurities was improved by extending the solute molecules' transport pathways. By modifying the functional groups on the surfaces of $Ti_3C_2T_z$, the permeation and rejection trade-off in SRNF may be customized [481]. This change in the surface group functionality emphasizes how important the surface chemistry of MXene is; the 4-h sonication period is a disadvantage of this method, however. Additional efforts towards these silane modifications of ML MXene are recommended.

Wang and Shi et al. [482] introduced chitosan membranes packed with imidazolium brush-functionalized Ti_3C_2 (QMXene-NH_2) via a solution-based technique. When 7.5 wt% QMXene-NH_2 was added, these membranes' ion-exchange capacity was found to be dramatically enhanced [37]. Additionally, their water absorption and swelling ratios decreased, falling to 85.4% and 18.4%, respectively. In this work, colloidal MXene was created by ultrasonically sonicating HF-etched $Ti_3C_2T_z$ in an ethanol, ammonia, and water solution for four hours.

According to Chen et al.'s [497] investigation, the guided bone regeneration characteristics of poly(lactic acid) membranes were affected by n-octyltriethoxysilane (OTES)-modified colloidal $Ti_3C_2T_z$. The incorporation of OTES-MXene resulted in these membranes exhibiting excellent biocompatibility, including improvements in cell adhesion, proliferation, osteogenic differentiation, in addition to improved ultimate tensile strengths. Si et al. [498] prepared PS NCs using colloidal $Ti_3C_2T_z$ modified by cationic surfactants, namely, octadecyl trimethylammonium bromide (OTAB), didodecyldimethylammonium bromide (DDAB), and DTAB. This modified $Ti_3C_2T_z$ was subsequently dispersed in N, N-dimethylformamide (DMF) via ultrasonication for 1 h, after which PS was added and dissolved. The resulting composite material was isolated by flocculation, dried, and compression mouldedmoulded at 195 °C for 10 min. Samples were generated using DTAB-Ti_3C_2, OTAB-Ti_3C_2, and DDAB-Ti_3C_2, all at a functionalized MXene content of 2 wt%. Improvements in thermal resistance, flame retardancy, and the production of volatile combustion products were noted, with a 26.4% reduction in the peak heat release rate (PHRR) of PS/DDAB-T. The length of the cationic surfactant was found to increase the basal spacing of $Ti_3C_2T_z$; however, XRD patterns of the generated NC were not reported, and the discussion regarding dispersion was limited to EDS mapping of Ti, which clearly showed agglomeration of $Ti_3C_2T_z$ particles [498]. Hyperbranched polysiloxane (HPSi), which possesses terminal amino groups following hydrolysis and condensation and permits the intercalation between the MXene sheets, was used by Wei et al. [499] to modify colloidal $Ti_3C_2T_z$ for PDMS/MXene NCs. Theoretically, this should enhance MXene's compatibility and dispersion inside the PDMS matrix. Given the slight change in d-spacing post-treatment, it is improbable that the big HPSi molecule was effectively intercalated, even if the authors claim to have done so according to the following approach. This process involved gradually adding colloidal $Ti_3C_2T_z$ to an ethanol-based HPSi solution while continuously sonicating the mixture for one hour. The product was filtered and vacuum-dried for a further 12 h after mixing for 12 h. This HPSi-d-Ti_3C_2 was first trapped by short-chain PDMS, and then it was added to the pre-reacted long-chain PDMS matrix to create a bimodal composite. After being put into a polytetrafluoroethylene (PTFE) mould, the finished product was exposed to UV light and radiation for eight seconds to cure it. The XRD spectra demonstrated that HPSi had intercalated, and the authors report that HPSi-d-Ti_3C_2/PDMS had a dielectric constant of 23.7 at 100 Hz, which was significantly higher than that of unfilled PDMS (2.8 at 100 Hz), with a dielectric loss of 0.11 at 103 Hz and a percolation threshold of 1.43 vol%. Merely comparing HPSi-d-Ti_3C_2 and d-Ti_3C_2 filled PDMS was the sole presentation of the mechanical characteristics that were examined [499]. Surprisingly, given the massive size of HPSi, HPSi-$Ti_3C_2T_z$ did not exhibit a significant increase in basal spacing at 0.8 Å. Although the authors assert differently, there are additional diffraction peaks in the pattern of HPSi-d- $Ti_3C_2T_z$, and the amorphous peak they assign to the structure of HPSi is relatively faint.

Carey et al. [479] synthesized modified $Ti_3C_2T_z$ via DHT and investigated the stability of these modified MXene MLs in non-polar solvents, including p-xylene, n-hexane, cyclohexane, chloroform, and toluene. Linear low-density polyethylene (LLDPE) NCs were made by solvent mixing, melt extrusion, and injection molding, using the stability of DHT- $Ti_3C_2T_z$ in p-xylene. These 1.12% vol% DHT-Ti_3C_2 NCs showed increases in their elastic moduli and tensile strengths of 11% and 32%, respectively. The moduli dropped by around 2% and the tensile strength rose by about 9.2% in the absence of the DHT treatment. Furthermore, Lee et al. [500] described a chemically significant method of surface modification: using esterification chemistry, "solvent-like" polymers such as polyethylene glycol carboxylic acid (PEG6-COOH) were covalently bonded to MXenes. Without oxidizing the two-dimensional $Ti_3C_2T_x$ flakes or altering the structural ordering, surface modification of $Ti_3C_2T_x$ with PEG6-COOH at substantial ligand loading (up to 14% by mass) significantly increased dispersibility in a variety of nonpolar organic solvents (e.g., 2.88 mg/mL in chloroform). Moreover, the nanoscale assembly of homogeneous microstructures of piled MXene-PEG6 flakes into organized thin films with good electrical conductivity (~16,200 $S{\cdot}cm^{-1}$) was enhanced by cooperative contacts between polymer chains. Most significantly, the degree of functionalization (incorporation of valency) of MXene were adjusted thanks to our covalent surface modification technique using ω-functionalized PEG6 ligands (ω-PEG6-COOH, where ω: $-NH_2$, $-N_3$, $-CH{=}CH_2$).

Once again, there are a lot of unseen factors that are crucial to performance but are neither taken into account nor disclosed while fabricating devices. MXenes are 2D sheets by nature, therefore variations in packing density, flake contact, alignment, and other characteristics impact how well the device works. Using conductivity as an example, it is evident that interflake contact and packing density have a major impact on electron transport; yet, quantification of these macroscopic properties has received little attention. The qualities that are obtained vary depending on the method used to make the films, such as spray coating, vacuum filtering, blade coating, etc. In addition, several parameters including vacuum strength, MXene concentration, film surface, and pore size were selected specifically for vacuum filtering in the process of creating these films. The film formation may also be influenced by the particular vacuum filtering configuration. These processing factors again compound when the produced structures grow more complicated, such as heterostructures.

It's critical for the MXene community to realize that device performance and effective MXene attributes are influenced by a number of variables and apparently random decisions. These factors actually matter, even if many of them are almost undetectable in writing. These seemingly little decisions can have a big impact on the measured performance in some situations or not at all. In any event, the impacts cannot be measured or even the scale of these effects cannot be understood if they are not disclosed.

5. Composite Structures of MXene

MXene is an excellent filler material for creating various composite materials because of morphological characteristics, layered structures, and great flexibility. This allows for the complementing assimilation of multiple MXene materials' remarkable capabilities. Because of this, MXenes and composites linked to MXenes have received a lot of interest from the scientific community recently for a variety of uses. In the field of physical sciences, including physics, chemistry, material sciences, and a wide range of applications, polymers and hybrid materials are just as important as metal oxides. The oxide materials take on a broad range of structural geometries and electronic structures, giving rise to their insulator, metallic, and semiconductor specifications [387,501,502]. The large density and small particle size of oxide particles have led to the manifestation of unique physical and chemical properties [503,504]. Among these oxide compounds are Fe_2O_3 [505], CeO_2 [506], V_2O_5 [507], TiO_2 [508], Al_2O_3 [509], and many more. Moreover, due of their similar chemical amalgamation of particles, polymers and hybrid materials are the synthesis and assembly of two or more substances and compounds (both organic and inorganic) with massive macromolecules and repeating of huge molecular chains. The majority of these hybrid materials fall within the 1 μm scale range, which makes them useful for creating a variety of composites within this range [510,511]. These materials are made up of several polymers that are connected to pre-condensate and cold mixture. Additionally, hybrid materials have a host of superior qualities, including resistance to corrosion, surface adhesion, acid toughness, chemical resistance, and quick changes in ambient temperature [512]. Polysulfides, polyesters, polyurethanes, alkyds, cellulose, polyvinyl alcohol, and other polymers and hybrid materials are among them.

5.1. Polymer Composites

MXene-filled polymer composites exhibit enhanced mechanical, thermal, and electrical properties due to the high aspect ratio, conductivity, and functional surface chemistry of MXenes. These composites have potential applications in energy storage, electromagnetic interference shielding, and flexible electronic devices, driven by the synergy between the polymer matrix and MXene fillers. Table 6 presents several recent studies that used MXene as a filler in polymer composites. In 2014, the most extensively researched MXene to date, $Ti_3C_2T_z$, was combined to the hydrophilic polymers PVA and PDDA, in the first report of an MXene polymer NC [395]. Ti_3AlC_2 was etched in 50% HF at room temperature (RT) for eighteen hours while being continuously stirred to create $Ti_3C_2T_z$. Following etching, water was used to wash the MXene multilayers (MLs) until a pH of 6 was achieved. After drying for 24 h at room temperature, the powder was submerged in dimethyl sulfoxide (DMSO) for 18 h at room temperature. It was then separated by adding water and centrifuging the mixture. This isolated DMSO-intercalated ML MXene powder was mixed with water in a 300:1 ratio, and the mixture was sonicated under flowing argon (Ar) for five hours. Centrifugation was employed to extract and use the colloidal supernatant exactly as it was. These colloidal suspensions were mixed with solutions of PVA or PDDA in different ratios, and the resulting NC films with MXene concentrations of 0, 40, 60, 80, 90, and 100% were created by vacuum-assisted filtering. This is a fairly standard process for making MXene colloidal suspensions; however, since then, the acid concentration has decreased to 10–20%, and the use of DMSO has become less common. Instead, lithium or other cations are added during etching to aid in delamination upon sonication.

Table 6
A summary of recent studies on MXene filled polymer composites

Ref.	Polymer	MXene	Processing	Fabrication Method	Properties
[513]	Polyacrylamide	d-Ti_3C_2	Solvent	In situ polymerisation	With only 6 wt% (1.7 volume percent) MXene loading, the conductivity of the as-prepared composite samples was dramatically enhanced to 3.3×10^{-2} S m^{-1}. The samples are also bendable.
[514]	PDMS	d-Ti_3C_2	In situ curing	Unidirectional freeze-drying method	Excellent electrical conductivity of 5.5 S/cm was demonstrated by the resulting 3D-MXene/PDMS nanocomposites, which was about 14 orders of magnitude greater than that of the plain PDMS. In contrast, the nanocomposites exhibit a 220% increase in heat conductivity at a modest MXene level of 2.5 vol% as compared to neat PDMS.
[499]	PDMS	d-Ti_3C_2 HPSi-d-Ti_3C_2[b]	In situ curing	Vacuum-assisted impregnation	Percolation thresholds (fc) for d-$Ti_3C_2T_x$/PDMS and HPSi-d-$Ti_3C_2T_x$/PDMS composites, which were made with varying filler loadings, were 1.32 and 1.43 vol%, respectively. At 102 Hz, 1.40 vol% HPSi-d-$Ti_3C_2T_x$/PDMS has a dielectric constant of 23.7, which is 1.5 times more than 1.28 vol% d-$Ti_3C_2T_x$/PDMS and 8.5 times greater than pure PDMS. Meanwhile, HPSi-d-$Ti_3C_2T_x$/PDMS composite still has a comparatively low dielectric loss (0.11 at 103 Hz).
[515]	Acrylic resin	$Ti_3C_2T_x$	Solvent	Solution casting	The $Ti_3C_2T_x$ and AE ($Ti_3C_2T_x$/AE) and CNT-COOH@$Ti_3C_2T_x$/AE composite films had percolation thresholds (fc) of 1.38 vol% and 1.51 vol%, respectively. The dielectric constant of 1.42 vol % CNT-COOH@ $Ti_3C_2T_x$/AE is 120 at 102 Hz, 30 times more than AE and 1.29 times greater than 1.26 vol% $Ti_3C_2T_x$/AE. Simultaneously, 1.42 vol% CNT-COOH@ $Ti_3C_2T_x$/AE dielectric loss stays at a comparatively low level (0.15 at 102 Hz).
[516]	PVA	$Ti_3C_2T_x$	Solvent	Multilayered casting method	The electrical conductivity of the 27-μm-thick PVA/MXene multilayered film (containing 19.5 wt% MXene in total) was 716 S/m, the maximum EMI SE was 44.4 dB, and the specific EMI SE (SSEt) was 9343 dB cm^2 g^{-1}4.57 W/mK, which was about 23-fold higher than that of plain PVA. Furthermore, the multilayered construction provided the film with exceptional anti-dripping performance.
[517]	PVA	Ti_3C_2	Solvent	Multilayered casting method	These thin films can be tuned by varying their thickness to have tensile strengths ranging from 138 MPa to 225 MPa, EMI-specific shielding effectiveness normalised to thickness and density up to 24 550 dB cm^2 g^{-1}, and sheet resistance ranging from 855 sq^{-1}-3.27 k sq^{-1} (corresponding to a range of conductivity ranging from 53 S m^{-1} to 125 S m^{-1}). Because of the nacre-like brick-and-mortar structure, this composite is the strongest MXene-based LbL film developed to date.
[518]	PVA	$Ti_3C_2T_x$	Solvent	Solution blending and dip-coating	MXene provided the polymer matrices with superior anti-dripping and thermal stability.
[519]	PVA	$Ti_3C_2T_x$	Solvent	Solution casting and vacuum-assisted filtration	The dielectric characteristics of the flexible thin films were excellent (solution casting at 10.0 wt% MXene: $\varepsilon' = 370.5$ and tan = 0.11 and VAF at 10.0 wt% MXene: $\varepsilon' = 3166$ and tan δ = 0.09**).**
[520]	PVA	f-Ti_2CT_x	Solvent	Freeze-drying	As exceptional electromagnetic interference EMI shielding materials, its predicted specific shielding effectiveness may approach 5136 dB cm^2 g^{-1} with an ultralow filler content of only 0.15 vol% and a reflection effectiveness of less than 2 dB, indicating superb absorption-dominated shielding performance.
[521]	PVA-PPy	Ti_3C_2	Solvent	Solution casting	1D nanofibres and 2D nanosheets were discovered to significantly improve the mechanical characteristics of the hydrogel hosts, with a noteworthy tensile strength of 10.3 MPa and a considerable elongation of more than 380%. Furthermore, the as-fabricated hierarchical structure efficiently encourages electrolyte diffusion while exhibiting exceptional capacitive properties such as an outstanding gravimetric specific capacitance of 614 F g^{-1} (at 1 A g^{-1}) and unprecedented stability during cycling (100% capacitance retention over 10 000 cycles).
[522]	PVA	$Ti_3C_2T_x$	Solvent	Vacuum-assisted impregnation	The resulting hybrid aerogels have an ordered cellular architecture, with graphene sheets acting as the inner skeleton and compactly bonded $Ti_3C_2T_x$ sheets acting as cell wall shells. The porous and highly conductive architecture (up to 1085 S m^{-1}) is highly efficient in endowing an epoxy nanocomposite with an excellent electrical conductivity of 695.9 S m^{-1} and a remarkable EMI-shielding performance of more than 50 dB in the X-band at a relatively low $Ti_3C_2T_x$ content of 0.74 vol%, which are the best results so far for polymer nanocomposites with similar MXene loadings.

(*continued on next page*)

Table 6 (*continued*)

Ref.	Polymer	MXene	Processing	Fabrication Method	Properties
[523]	PVA	$Ti_3C_2T_x$	Solvent	Solution coating	Compared to MXene/PVA composite films, MXene@SiO_2/PVA composite films demonstrated reduced dielectric losses at low frequencies (from 20 Hz to 10 kHz). At 100 Hz and room temperature (RT), MXene@SiO_2/PVA hybrid films with 2.5 wt % MXene loading and 5 wt% (with regard to MXene content) SiO_2 coating had a dielectric constant of 27.2 (a 292.5% increase compared to neat PVA film) and a dielectric loss of merely 0.057 (a 259.6% reduction compared to MXene/PVA composite film). Furthermore, across the temperature range of RT to 60°C, this SiO_2-coated composite film showed steady dielectric characteristics (dielectric constant and loss change from 27.2 to 29.3 and 0.057 to 0.104, respectively).
[524]	PAA	$Ti_3C_2T_x$	Solvent	Solvent casting	Loaded samples showed a 30.96% boost in the modulus of elasticity and a 10.9% rise in ultimate tensile strength. The unique form of the stress-strain plot revealed a water barrier phenomenon in the case of these MXene-containing composites. The results of differential scanning calorimetry show a 15 ℃ rise in crystallisation temperature (T_c), with a crystallisation enthalpy 18% lower than plain nylon-6 and a degree of crystallinity of 60-70%, indicating that MXene operates as a site for heterogeneous nucleation.
[525]	Poly(vinyl alcohol) and poly(ethylene oxide)	$Ti_3C_2T_x$	Solvent	Electrospinning	$Ti_3C_2T_x$/ polyethylene oxide (PEO solution showed a high change in viscosity and conductivity, with increases of 11% and 73.6% above the basal polymer, respectively). X-ray diffractograms revealed that Ti_3C_2/PEO had a high degree of crystallisation while Ti_3C_2/PVA had a slight drop in crystallinity.
[526]	cellulose nanofibre	$Ti_3C_2T_x$	Solvent	Multilayered fabrication	The mechanical strength (112.5 MPa) and toughness (2.7 MJ m^{-3}) of alternating multilayered film carbon nanofibres (CNF) @MXene were higher than those of freestanding MXene film and homogeneous CNF/MXene film. Meanwhile, the electrical conductivity of the directly connected MXene layers rose from 2 (homogeneous CNF/MXene film) to 621-82 S m^{-1} (CNF@MXene films). CNF@MXene films demonstrated exceptional EMI shielding effectiveness of 40 dB in the X-band and K-band along with excellent specific shielding effectiveness up to 7029 dB cm^2 g^{-1} at a thickness of only 0.035 mm when combined with the extra "reflection-absorption-zigzag reflection" mechanism among the alternating multilayers. Furthermore, the superior mechanical flexibility ensured steady EMI shielding and electrical qualities, which can endure the folding test 1000 times without noticeable loss.
[527]	PP	$Ti_3C_2T_x$	Solvent	Oxygen-free fast-drying assisted solution casting and melt blending	Ultrathin two-dimensional (2D) polypropylene/titanium carbide ($Ti_3C_2T_x$) nanocomposites with considerably higher tensile strength (35.3%), ductility (674.6% increase), storage modulus (102.2%), and early degradation temperature (79.1 °C change).
[498]	PS	Ti_3C_2	Solvent	A co-coagulation plus compression molding technique	The cationic-modified Ti_3C_2/polystyrene (PS) nanocomposites exhibited significant improvements in their thermal stability, as evidenced by temperature increases of 20 °C for dodecyltrimethylammonium bromide (DTAB) - Ti_3C_2/PS, 25°C for OTAB- Ti_3C_2/PS, and 23 °C for DDAB- Ti_3C_2/PS at 5% weight loss, respectively. The increased flame-retardant qualities of PS were likewise achieved by the modified MXene nanosheets. PHRR for PS/OTAB-Ti_3C_2, PS/DDAB- Ti_3C_2, and PS/DTAB-Ti_3C_2 was around 26.4%, 21.5%, and 20.8% lower than that of clean PS.
[528]	PA	$Ti_3C_2T_x$	Solvent	Film casting	The MXene filler's percolation threshold inside the coPA matrix was discovered to be 0.05 vol.%, and the composite filled with 5 wt.% (1.8 vol.%) of MXene had the highest electrical conductivity, measuring 1.4×10^{-2} S·cm^{-1}. The electrical conductivity of the MAX phase, which served as the precursor for the synthesis of MXene, was 172 S·cm^{-1}, whereas the electrical conductivity of the MXene as synthesized was 9.1 S·cm^{-1}. UV spectroscopy verified that the produced composite films were more transparent than 75%, even for samples that contained 5% weight of MXene.

(*continued on next page*)

Table 6 (*continued*)

Ref.	Polymer	MXene	Processing	Fabrication Method	Properties
[529]	PI	$Ti_3C_2T_x$	Solvent	Film casting	The MCF-5/epoxy EMI shielding nanocomposites demonstrated optimal electrical conductivity of 184 S/m and maximum EMI SE of 46 dB, 3.1×10^4, and 4.8 times greater than that of MCF-0/epoxy nanocomposites (without $Ti_3C_2T_x$ MXene), respectively, when the mass fraction of MCF was 4.25 wt% (MCF-5). Additionally, there was an 11% and a 13% rise in the equivalent hardness of 0.31 GPa and Young's modulus of 3.96 GPa, respectively.
[530]	PAM	Ti_3C_2	Solvent	Film casting	With only 6 wt% (1.7 volume per cent) MXene loading, the conductivity of the as-prepared composite samples was dramatically enhanced to 3.3×10^{-2} S m^{-1}. The samples are also bendable.
[531]	PU	$Ti_3C_2T_x$	Solvent	Wet-spinning	It is shown that the conductivity is present at a shallow percolation threshold of ≈1 wt%, which is less than the values previously reported for polymer composites based on MXene. When employed as a strain sensor, the MXene/PU composite fibres exhibit a tremendous detecting strain of ≈152% and a high gauge factor of ≈12900 (≈238 at 50% strain).
[532]	PANI	$Ti_3C_2T_x$	Solvent	Dry filteration	The MXene/PANI composites in a paraffin matrix showed a maximum reflection loss of -56.30 dB at 13.80 GHz with a thickness of 1.8 mm when they had an appropriate PANI concentration. Furthermore, the adjustable thickness varied from 1.5 to 2.6 mm, and the effective absorption bandwidth (>90%) covered the X-band (8–12.4 GHz) to Ku-band (12.4–18 GHz).
[533]	PAP and PPy	$Ti_3C_2T_x$	Solvent	Layer deposition	The f-MC/Ppy bases sensor was the most sensitive sensor, which had a sensitivity of 0.00232 kPa^{-1} in the range of 126 to 168 kPa. The sensitivity of the f-MC/CNPs-based sensor was 0.00017 kPa^{-1} in an extensive range of 68–168 kPa.
[534]	PEDOT and PSS	$Ti_3C_2T_x$	Solvent	Solvent mixing	When evaluated at room temperature, it showed an improved response over pure Poly(3,4-ethylenedioxythiophene) polystyrene sulfonate (PEDOT: PSS) and pure $Ti_3C_2T_x$. It also had a high response ratio of the, most significant response and the second highest response (5.54).
[535]	PVDF	$Ti_3C_2T_x$	Solvent	Triplex solution casting	Compared to PVDF and mono-layered composites, the sandwich composite exhibits better overall electrical performance. Its breakdown strength is around 350 MV m^{-1}, its permittivity is approximately 26 at 100 Hz, and its energy density (efficiency) is approximately 12.5 J cm^{-3} (~64%) at breakdown strength.

This is accomplished by introducing lithium or other cations into interlayer spaces in place of directly employing HF by combining HCl and fluoride salts.

Due to its vast research base, ease of synthesis, and relative stability when it comes to oxidation in comparison to other MXenes, $Ti_3C_2T_z$ has been the subject of the majority of research to date. Curiously, though, Chen et al. [480] grafted poly(2-(dimethylamino) ethyl metchacrylate) (PDMAEMA) brushes on ML vanadium carbide (V_2CT_z) via self-initiated photografting and photopolymerization of 2-dimethylaminoethyl methacrylate in just the second publication on polymer MXene NC. The scientists discovered that the transmittance of aqueous suspensions of V_2C@PDMAEMA could be regulated by varying the temperature thanks to the thermoresponsive phase separation behavior of PDMAEMA, which has a lower critical solution temperature of around 40 °C. The advantages of MXenes and polymers are combined in MXene-polymer composites, which lead to an increased mechanical toughness, increased interlayer spacing between MXene layers, and increased structural stability. Consequently, MXene-polymer composites can demonstrate outstanding performance in a range of applications, particularly in photothermal conversion, energy storage, EMI shielding, sensing, and triboelectric nanogenerators (TENGs).

Layered components must be fully and homogeneously dispersed throughout the polymer matrix to optimise the NC characteristics. It is crucial to remember that monolayers may not always be the best option for mechanical reinforcement. This was shown in the instance of graphene polymer NCs by Gong et al. [536], where trilayer graphene with a layer thickness of 1 nm produced the highest composite modulus. Because MXene's exfoliation may be decreased to an optimal degree, ML MXene may be favourable for usage in polymeric NCs in addition to its scalability benefits. Thus, to get both dispersion and exfoliation simultaneously, the process by which the NCs are made has a crucial effect on their structure and, by extension, their characteristics. Melt blending, in situ polymerization, and solvent blending/casting/filtration are the primary methods used in NC processing. Despite this observation, using a variety of approaches is not unusual.

5.2. Metal Composites

These composites offer a unique combination of properties derived from both components, such as high electrical conductivity, mechanical strength, and thermal stability. MXene metal composites have attracted significant attention for their potential

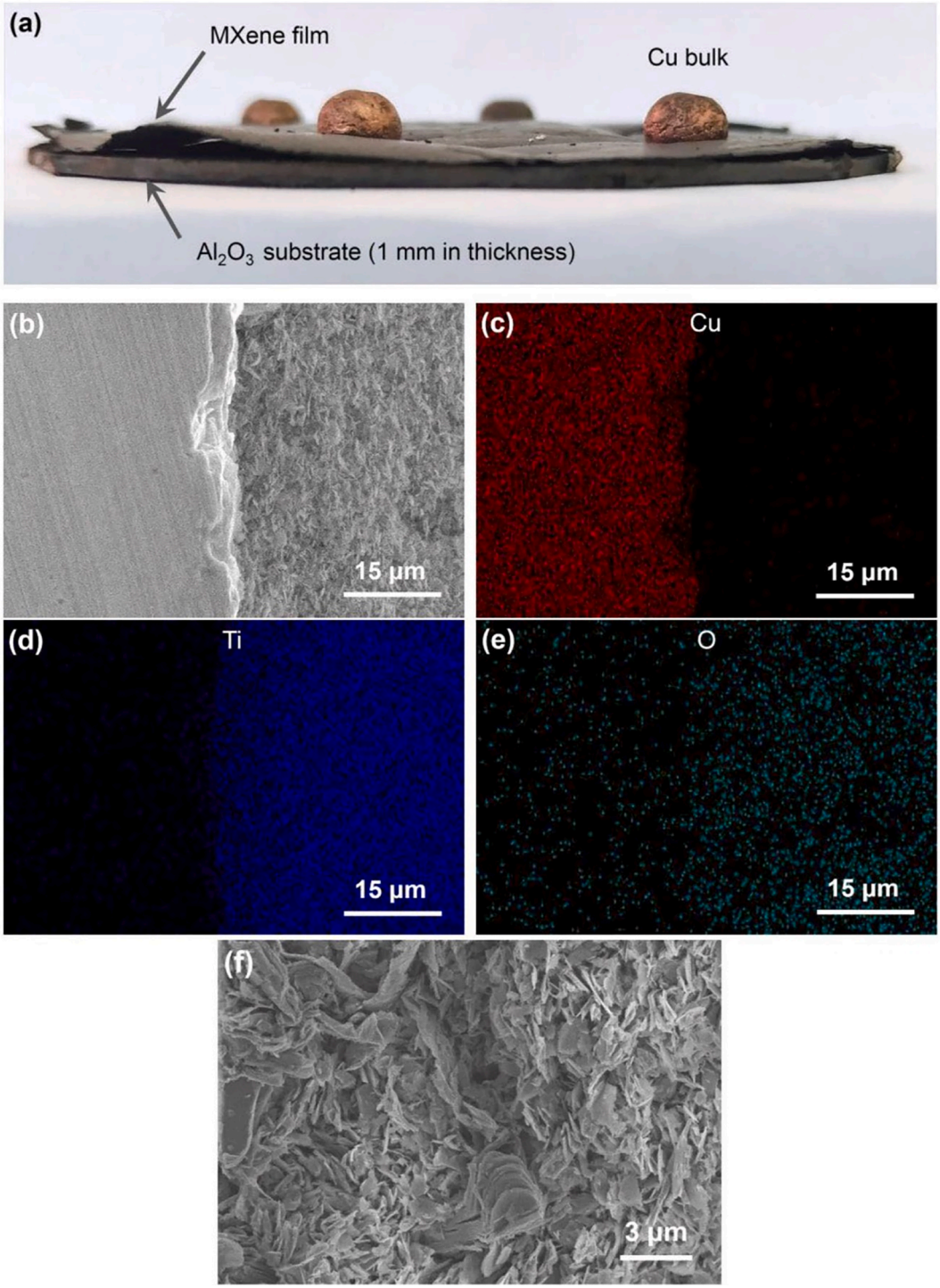

Fig. 13. The wettability test optical snapshot (a) shows the interface between Cu bulks and MXene film. The secondary electron SEM image (b–e) shows the elemental mapping that corresponds to the interface between Cu bulk and MXene film. (b) The SEM picture; (c) Cu, (d) Ti, (e) O; and (f) Enlarged SEM iamages of the MXene film region. Reprinted with the permission of Ref. [541].

applications in various fields, including energy storage, electromagnetic interference shielding, catalysis, and sensing.

Al/MXene: Deionized water was added to the beaker containing Al powder, and it was mechanically agitated and ultrasonicated in an ice bath. Subsequently, MXene was gradually added to the Al suspension while stirring. The required MXene/Al powder combination was subsequently obtained by filtering and drying the suspension in a vacuum furnace. Finally, the MXene/Al powder combination was consolidated using the Spark plasma sintering (SPS) method [537]. $Ti_3C_2T_x$/Al composites were made via pressureless sintering, and hot extrusion was the next step in the procedure. Pressureless sintering was conducted under process conditions of 650 °C and 1 h in Ar, while the hot extrusion process was conducted at a temperature of approx. 450 °C. Composite properties were assessed based on the addition of $Ti_3C_2T_x$ aggregate at 0.5 wt% to 3 wt%. In contrast to pure Al, the composites' tensile strength (148 MPa) and Vickers hardness (0.52 GPa) were markedly improved by 92% and 50% as the $Ti_3C_2T_x$ content reached 3 wt% [538]. $Ti_3C_2T_x$ MXene has been the subject of recent investigations using powder metallurgy techniques as an Al-reinforcing material [537]. In the initial mechanical investigation of MXene/Al composites, non-delaminated multilayer $Ti_3C_2T_x$ powder and Al powder were combined using ball milling, pressureless sintering at 650 °C in an Ar atmosphere, and hot rolling [539]. Delaminated few-layer flakes of $Ti_3C_2T_x$ in Al powder combined in water under sonication were utilized in another investigation [537]. These were then subjected to SPS at 580 °C for 20 min under 50 MPa and hot extrusion. Tensile strength was improved by 50% when non-delaminated $Ti_3C_2T_x$ powder up to 3 wt % was combined with Al [538]. However, few-layer delaminated $Ti_3C_2T_x$ improved tensile strength by 66% when $Ti_3C_2T_x$ was included in Al at just 0.2 wt% [537]. Furthermore, investigations on the mechanical strength of non-delaminated MXene in Cu matrices have been conducted, as shown in Fig. 13. In one work, non-delaminated multilayer $Ti_3C_2T_x$ powder was mixed using an ethanol solution and a Cu precursor, which was produced by reductive heat treatment at 60 °C. Cu was then obtained by SPS at 800 °C under 35 MPa for five minutes, with a temperature ramp rate of 50 °C/min [540].

RhNi/MXene: The one-step wet chemical approach was used to create the RhNi/MXene nanocatalyst. In a two-neck round-bottom flask, 100 mg of MXene is dissolved in 2 mL of water (30 mL) and sonicated for 30 minutes to produce a homogenous dispersion. Next, add 100 L of a 0.8 mmol/mL rhodium chloride combination and 100 L of a 0.2 $mmol{\cdot}L^{-1}$ nickel chloride solution to the previously described MXene solution and stir gently for 20 minutes at a speed of 220 rpm using electromagnetic stirring. Subsequently, 0.5 mL of 2.0 M NaOH solution containing 24 mg of sodium borohydride ($NaBH_4$) (1.3 $mol{\cdot}L^{-1}$) is added to the combination indicated above and agitated rapidly for three hours at 0 °C. An ice-bath is used to maintain a low enough temperature to inhibit the production of RhNi nanoparticles. Centrifugation and deionized water washing are the steps involved in creating the RhNi/MXene nanocatalysts [542]. The production of nitrogen-doped MXene-based composite catalysts for improved HER performance was investigated by Wu et al. [543]. They were able to successfully insert nitrogen-doped carbon (N-C) with extensively scattered ruthenium (Ru) onto the MXene surface by thermally decomposing $RuCl_3$ combined with melamine and formaldehyde resin. Ru nanoparticles (Ru NPs) and Ru single-atom (Ru SA) percentage were both influenced by the calcination temperature, which was necessary to enable the synergistic improvement of HER efficiency by Ru NPs and Ru SA. $Ti_3C_2T_x$-N/C-Ru-600 (TNCR-600), the resultant catalyst produced at a calcination temperature of 600 °C, had remarkable HER activity ($\eta 10 = 17$ mV) and stability (160 h) in an alkaline environment. This work offered fresh insights into the design and control of high-performance Ru-based catalysts for hydrogen generation, while also presenting a straightforward and efficient method for creating composite catalysts. For Ni/MXene composites, following two rounds of magnetic stirring to dissolve the ingredients, the mixture was heated in a Teflon-lined stainless-steel autoclave. The goods were repeatedly rinsed with deionized water and 100% ethanol. The black granules had eventually been dried out over night [544]. Gothandapani et al.[545] used the calcination of Ni-MOF at 650 °C to create Ni composite with MXene (Ni-Ti_3C_2), which was then characterized by XRD, FE-SEM, FTIR, and BET analysis. In comparison to Ti_3C_2, the resulting Ni composited Ti_3C_2 had a higher porosity and surface area following calcination. The resultant material was further examined by cyclic voltammetry (CV), electrochemical impedance analysis (EIS), and linear sweep voltage (LSV) in an alkaline media. It was also employed as an electrode for the Hydrogen Evolution Reaction (HER). Because of the surface area and easily accessible catalytic active sites, the derived Ni-Ti_3C_2 in basic medium exhibits a modest Tafel value of 56.15 mV/dec with an acquired voltage of 181.15 mV, providing outstanding mass transfer qualities for the derived Ni-Ti_3C_2 composite in basic medium. In basic media as opposed to acidic medium, the HER reaction kinetics in Ni-Ti_3C_2 MXene composite were shown to be more favorable. The charge transfer resistances for Ti_3C_2 and Ni- Ti_3C_2 in acidic medium were determined to be 3.98 Ω and 2.34 Ω, respectively, based on the EIS plot, whereas in basic medium they were found to be 3.12 Ω and 1.98 Ω. The lower resistance of Ni-Ti_3C_2 in basic media indicates that it has a stronger electrocatalytic activity than Ti_3C_2. In basic medium, the cyclic stability of Ni-Ti_3C_2 was greater than that of Ti_3C_2. Consequently, the produced composite is a possible catalyst for HER applications, according to the overall results.

$PdCl_2$/MXene: To produce dsDNA, the dsDNA was spread out in distilled water, heated to 95 °C for 20 minutes, then quickly cooled in an ice water bath. Subsequently, 1 mL solution of DNA was mixed with 1 mL of 1 mg/mL Ti_3C_2 distribution, sonicated for 30 minutes in a cold-water tub, and centrifuged for 10 minutes at 10,000 rpm and it was again dispersed in 7.5 mL of deionized water. To create PdNP-modified MXene nanosheets, 1 mL of 0.01 M $PdCl_2$ was added to Ti_3C_2/DNA process and vigorously stirred for 20 minutes. After 30 minutes of sonication, 100 μliters of 0.1 M $NaBH_4$ was gradually added to an ice water bath. Subsequently, 400 mL of 0.1 M $NaBH_4$ was carefully placed into an ice water bath and stirred for 30 minutes. 1.2 mL of 0.01 M $H_2PtCl_6.6H_2O$ was then stirred for 20 minutes. The Ti_3C_2/DNA/Pd/Pt nanocomposite was ultimately made after three centrifugations [546]. In the study by Karatas et al.[547], methylamine-borane hydrolysis was used to examine the catalytic activity of a palladium-doped cryo-MXene catalyst that was synthesized utilizing a wet impregnation technique. Different analytical approaches were used to characterize the palladium nanoparticles that were doped on the surface of the MXene substrate by chemical reduction of Pd^{+2}. Liquid nitrogen was used to cryogenically treat the produced palladium-doped MXene phases at a temperature of -160 °C. With a turnover frequency (TOF) of 45.8 for 298 K, the palladium-doped cryo-MXene catalysts demonstrated exceptional catalytic activity in the hydrolysis of methylamine-borane. Furthermore, even after the five cycles, the palladium-doped cryo-MXene showed good stability.

Ti_3C_2 MXene@Au composite was prepared using the self-reduction technique. Stirring was used to create a solution of Ti_3C_2 MXene (100 mg) and ultrapure water (100 mL). Next, to initiate the self-reduction, $HAuCl_4$ (3 mL/0.1 mol·L^{-1}) was gradually added to the solution while being constantly stirred. After thirty minutes of work, the suspension was centrifuged and thoroughly cleaned with ultrapure water. Ultimately, the Ti_3C_2 MXene@Au composite was produced by 48 h of lyophilization at −60 °C [548]. The Au/ $Ti_3C_2T_x$ nanocomposite was created by a process of chemical reduction. In this procedure, a reducing agent was added to the metal-containing solution, and stirring helped the reduction process even more. $Ti_3C_2T_x$ MXene was then added to the previously described combination. Following the end of the reaction, the solution was washed three times with deionized water and drained using cellulose filter paper with 0.1 μm pore size. After filtering, the material was dried in vacuum oven at 80 °C for two hours [549].

In a different investigation, the non-delaminated $Ti_3C_2T_x$ powder in Cu matrices was mixed with Cu and $Ti_3C_2T_x$ powders by high-energy ball milling at 350 rpm in Ar. The samples were then sinterted by vacuum heated pressing at 1040 °C and 25 MPa for 30 minutes, with a temperature ramp rate of 1.5 °C/min [501]. According to these tests, non-delaminated $Ti_3C_2T_x$ powder mechanically strengthened the Cu matrix, outperforming the pure Cu matrix by up to 50% [540]. The use of delaminated few-layer $Ti_3C_2T_x$ MXene is anticipated to be much more successful in enhancing the mechanical characteristics compared with multilayer $Ti_3C_2T_x$ powder, even though the processing conditions used in these investigations on Al and Cu matrices were not similar. Because single-flake MXene has a larger surface area for stress transmission from the metal matrix to the delaminated MXene 2D flakes, it is generally stronger than its multilayer powder cousin. Prior research on 2D nanomaterial filled metal matrix composites has demonstrated that the rise in surface area is a critical component [550]. Furthermore, secondary bonding such as van der Waals between flakes of MXene occurs in multilayer MXene particles, and it is weaker than primary in-plane M-X bonding. Larger gains in mechanical qualities may result from the usage of single-flake MXenes, which will guarantee that the MXene materials solely include primary bonding as the reinforcing material. Compared to graphene nanoplatelets (GNPs), carbon nanofibres (CNFs), carbon nanotubes (CNTs), ceramic and refractory particles, single-flake $Ti_3C_2T_x$ sheets significantly increased the strengthening effectiveness of Al composites [538]. Table 7 illustrates how MXene may enhance metal composites' mechanical qualities in comparison to competing reinforcing materials.

Additionally, delaminated single-flake $Ti_3C_2T_x$ MXene has been studied as a potential addition for Mg-Li composites. $Ti_3C_2T_x$ Mg-Li MMCs were created via a molten-gelation mixing procedure in which the metal was sonicated at temperatures higher than 500 °C to integrate $Ti_3C_2T_x$ [476]. Tensile yield strength has improved by 128 percent compared to the matrix metal because of this procedure. A

Table 7
Properties, applications and synthesis method of MXene-metal composites

Ref	Metal Composite	Method	Properties	Applications
[549]	Au/$Ti_3C_2T_x$	Chemical reduction	Microstructure	Electrochemical and catalytic performance
[548]	Ti_3C_2/Au/CdS	Self-reduction	Microstructure	Photocatalytic hydrogen production activity
[554]	MXene/AuNPs	Self-reduction		Catalytic performance
[538]	$Ti_3C_2T_x$/Al	Pressureless sintering followed by hot extrusion	Microstructure and mechanical properties	Solid lubricant
[537]	Few layered MXene (FLM)/Al composite	Self-assembly protocol and powder metallurgy	Microstructure, mechanical properties	Automotive, aerospace, packaging industries
[555]	MXene/MgAl- layered doubled hydroxide (LDH)	In situ synthesis		Anticorrosion
[556]	Ti_2C/Au-Ag	Machine learning		Electrochemical and SERS intelligent analysis
[557]	MOF-derived MnO_2/Mn_3O_4 and Ti_3C_2 MXene/Au	Enzymatic inhibition		Electrochemical pesticides detection
[558]	MXene/Ag	Direct reduction method		Lithium-ion batteries
[559]	Ag-$Ti_3C_2T_x$ and Ag-Nb_2CT_x Composites	Simultaneous self-reduction and oxidation	EMI shielding	Wireless technologies and radar systems
[560]	Ag-$Ti_3C_2T_x$ and Ag-Nb_2CT_x	Self-chemical reduction	Electromagnetic Interference	EM wave shielding
[561]	MXene-$Ag_{0.9}Ti_{0.1}$	Self-reduction		Electrocatalytic activity
[476]	$Ti_3C_2T_x$ /Mg-Li	Liquid metal gelation	Mechanical properties	Alloys, batteries and supercapacitor
[544]	$Ti_3C_2T_x$ /Ni	In-situ hydrothermal	Electromagnetic wave absorption (EMA)	Electromagnetic wave absorption
[562]	FeNi/$Ti_3C_2T_x$	Facile in situ hydrothermal	Microstructure, magnetic and microwave absorption	Radar detection technology
[541]	Ni-MXene/Cu composites	High energy ball milling	Microstructure, mechanical and wettability	Automotive and aerospace industries
[546]	Ti_3C_2/DNA/Pd/Pt	In-situ process		Sensor and catalytic performance
[563]	Pd/MXene	One-step soft solution processing	Microstructure, surface-enhanced Raman spectroscopy	Sensors, catalysis, biomedical
[564]	$Ti_3C_2T_x$MXene/Zn	Facile in situ electroplating	Flexibility, wettability, electronic conductivity	Energy storage system
[565]	MXene/Cu	High energy ball milling	Microstructure, mechanical	Automotive and aerospace industries
[566]	MXene/Sb	One-step electrodeposition approach	Flexible	Catalyst, batteries, sensors

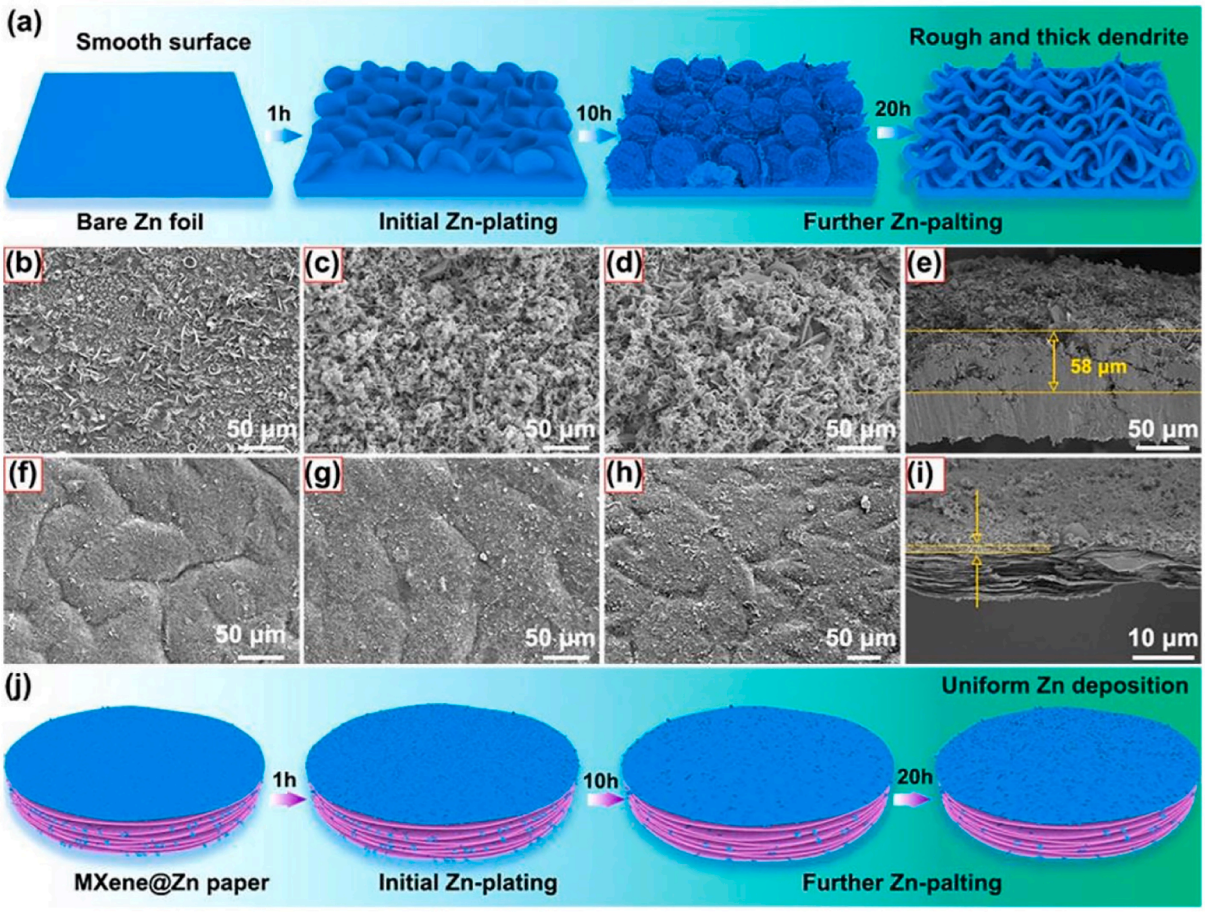

Fig. 14. Evolution of morphology and schematic representation of zinc deposition. Diagrammatic deposition on the $Ti_3C_2T_x$ MXene@Zn paper (j) and Zn foil (a). Typical top-view SEM pictures of Zn deposition in 2 M $ZnSO_4$ electrolyte following plating capacities of 1 mA·cm^{-2}, 10 mAh·cm^{-2}, and 20 mAh·cm^{-2} on Zn foil and 1 mA·cm^{-2}, 10 mAh·cm^{-2}, and 20 mAh·cm^{-2} on $Ti_3C_2T_x$ MXene@Zn paper, respectively. Cross-sectional SEM pictures of the materials that correspond to panels d and h, respectively: (e) commercial Zn foil and (i) $Ti_3C_2T_x$ MXene@Zn paper. Reprinted with authorization from Ref. [567].

three-fold increase in flake thickness and the discovery of mixed hexagonal and cubic phases in the recovered flakes indicated a partial phase change of $Ti_3C_2T_x$ [476]. As it has shown in high-temperature annealing of $Ti_3C_2T_x$, these modifications may represent partial phase transitions of $Ti_3C_2T_x$ to mixed Ti_2C and TiCy phases [551]. Future investigations of embedded MXene flakes in MMCs will be able to clarify the whole attribution of this phase shift in molten phase infiltration [476].

The mechanical strength and intrinsic characteristics of MXene surface terminations also influence the tribological characteristics of MXene metal matrix composites. Increased hardness and reduced plastic deformation of the $Ti_3C_2T_x$ reinforced Al composites were responsible for a ~2.5 times reduction in the coefficient of friction (COF) of a 3 wt% non-delaminated multiple-layer $Ti_3C_2T_x$ reinforced Al composite over 300 cycles in metal matrix composites within a ball-on-plate setup with a 5 N load [538]. Also, MXene-Zn metal composites have reported a significant property development in the composite structures as shown in Fig. 14. A 26-wt% delaminated single-flake $Ti_3C_2T_x$ in Cu composite (Fig. 15), fabricated by electrodeposition processes via multilayer $Ti_3C_2T_x$ and a Cu-containing precursor, showed a 19-fold reduction in wear rate and a 2-fold decrease in COF compared to its pure Cu counterpart in a similar configuration under a 1 N load. The $Ti_3C_2T_x$-tribolayer that developed at the contact site was thought to have improved wear behavior because it decreased the shear force needed to move the interface [552]. The decreased interlayer sliding friction between terminated MXene sheets in this tribolayer is responsible for the lower shear force needed for contact motion [553].

5.3. Ceramic Composites

High electrical conductivity, high-temperature phase stability, and young's modulus of MXenes make them promising for use in ceramic matrix composites (CMCs). Furthermore, MXenes' strong negative zeta potentials (–32 to –45 mV) and solution processability [568] make them excellent choices for CMCs' wet or slurry-based solution processing of green bodies without particle agglomeration, which is observed in more traditional nano fillers [569]. Furthermore, the usage of traditional surfactant components is rendered

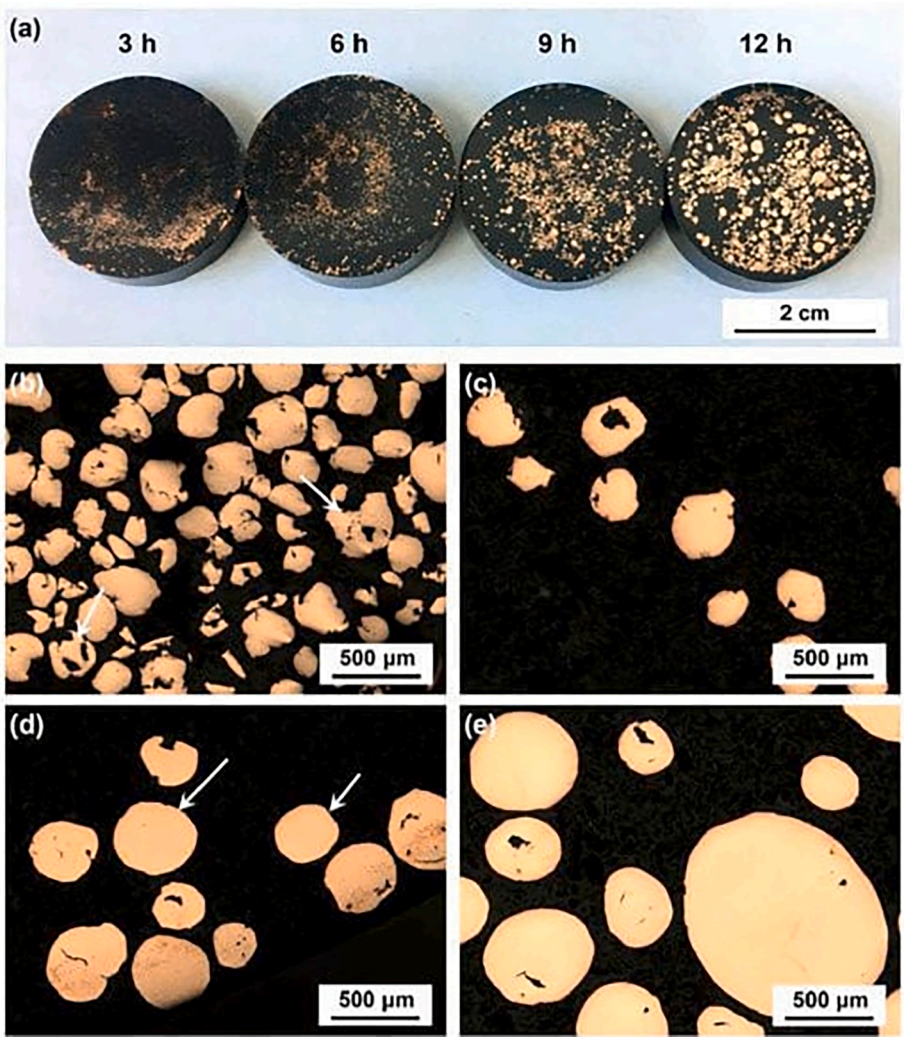

Fig. 15. (a) An optical photo of the 3MXene-Cu composite powders implanted in bakelite using 3, 6, 9, and 12 high-energy ball milling; (b–e) An optical microscope photo of the composite powder in (a) that is, correspondingly, (b) 3 h, (c) 6 h, (d) 9 h, and (e) 12 h. Reprinted with the permission of Ref. [940].

unnecessary by the negative zeta potential of as-synthesized MXenes. It is intended that the solution-processing of MXene CMCs be scalable and maybe incorporated into current green body mixing techniques. Surface groups like -F, -Cl, -O, and -(OH) are responsible for MXenes' negative zeta potential [570-572]. Because of the electrostatic interaction between MXene and the ceramic grains, these surface charges cause MXene to adsorb to the oppositely charged ceramic particles. Further research into high-energy mixing techniques may be done on MXenes' prolonged colloidal stability in non-aqueous solvents such as alcohols and processability in dry powder forms. In addition to solution-processing, other methods such as milling, reactive bonding, and chemical infiltration are investigated [573]. When creating green bodies of mixed MXene CMC powders via sol-gel processes, the dynamic surface chemistries of MXene can also have an impact. The kind of ceramic matrix—which may be divided into oxides and non-oxides—determines the preparation of MXene CMC green bodies and the sintering pathways for MXene-CMCs. Zinc oxide and alumina oxide systems have been studied thus far in terms of oxides. Research employing alumina as a matrix has only included multilayer MXene particles. For instance, alumina and multilayer $Ti_3C_2T_x$ particles were combined via ball milling in ethanol for 20 h. The green body that resulted was sintered for one hour at 1500 °C in air (Fig. 16 a,b) [574]. The composite showed around 300 percent improvement in fracture toughness, 150 percent increase in bending strength, and 300 percent increase in hardness. However, the MXene phase decomposed into titanium oxide because of the prolonged sintering periods in an oxygen-rich environment, which may have an impact on the mechanical characteristics of these composites.

In ceramic oxide matrices, there are ways to lessen MXene oxidation. Recently, the possibility of incorporating sputtered multilayer MXene particles containing Mo and Ti into alumina matrices has been explored [398]. A protective barrier was created by sputtering transition metals onto MXene particles, preventing MXene from oxidizing inside the oxide matrix. Using wet attrition milling in isopropanol, the sputtered MXene particles were combined with alumina (particle size 140 nm). The combination was sintered using

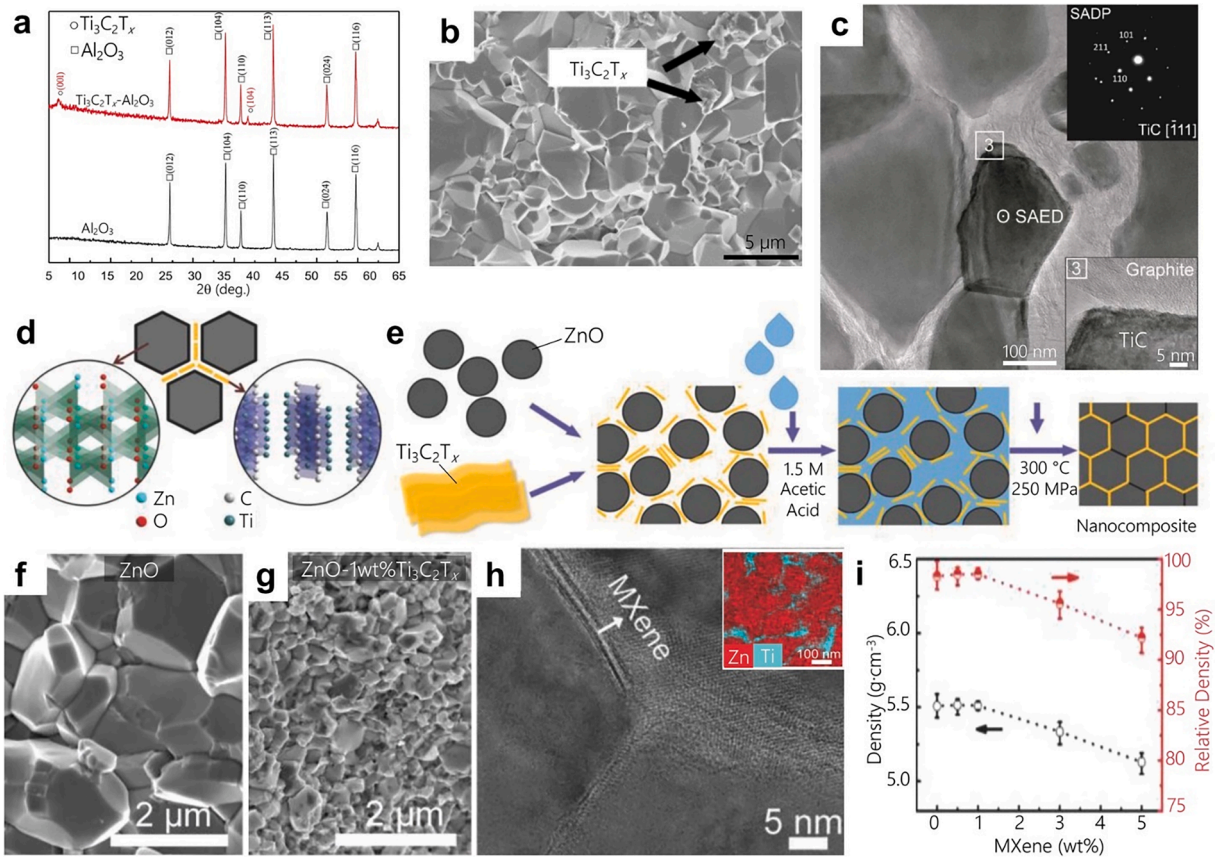

Fig.16. (a) Prior to sintering, MXenes ceramic matrix composites with matrices like Al_2O_3 and ZnO were subjected to XRD patterns of their Al_2O_3 and Al_2O_3 2 wt% $Ti_3C_2T_x$ powder mixes. (b) Al_2O_3 2 wt% $Ti_3C_2T_x$ composite SEM micrographs made by sintering at 1500 °C. Reprinted from the permission of Ref. [574]. (c) High-resolution TEM picture of Al_2O_3 2wt% $Ti_3C_2T_x$ showing the production of TiC, as shown by selected area electron diffraction (SAED) of the sintered MXene. The bottom inset of the resultant TiC and alumina matrix [398] demonstrates the presence of graphitic carbon at the grain boundaries. Diagrammatic representation of (d) ZnO-$Ti_3C_2T_x$ nanocomposites' grain boundary and (e) the cold sintering method of manufacture. cols sintered pure ZnO and ZnO 1wt% $Ti_3C_2T_x$ composite SEM images. MXene 2D flakes are seen at the ZnO grain boundaries in this h TEM picture of a cold sintered ZnO 1wt% $Ti_3C_2T_x$ sample. Zn is displayed in red and Ti is exhibited in blue in this energy dispersive x-ray spectroscopy of ZnO 1wt% $Ti_3C_2T_x$, exhibiting MXenes at the grain boundaries. ZnO-$Ti_3C_2T_x$ nanocomposites' densities and relative densities after one hour of cold sintering at 300 °C. Reprinted from the permission of Ref. [575].

SPS at 1400 °C for three minutes while under a 35 MPa uniaxial pressure. Compared to monolithic alumina, the resultant CMCs containing 0.5 wt% $Ti_3C_2T_x$ showed enhanced hardness (10%) and fracture toughness (15%) [398]. TiC particles were produced via high-temperature (1400 °C) composite sintering of $Ti_3C_2T_x$, as predicted by the high-temperature phase change behavior of MXenes (Fig. 16 c). At the grain boundaries of this resultant TiC and alumina matrix, graphitic carbon was found (Fig. 16 c bottom inset). When $Ti_3C_2T_x$ particles are etched with 48% hydrofluoric acid for 24 h, the outer surfaces of the particles etched, which may explain the presence of carbon at the grain boundaries [576]. On the other hand, Mo_2C is visible at the grain boundaries of sintered composites containing Mo-sputtered MXene particles, indicating an interaction between Mo and graphitic carbon during the sintering process.

Low-temperature sintering techniques are another way to stop MXenes from oxidizing when combined with oxide matrices. The use of cold-sintering for single-flake $Ti_3C_2T_x$ MXene mixtures including submicron ZnO particles has been investigated. ZnO particles were combined with 0.5 to 5 wt% of $Ti_3C_2T_x$ single-flake solution to create the composite mixes. The mixtures were then sonicated for 15 minutes and freeze-dried for 72 h. Following a mixture of the resultant ZnO-$Ti_3C_2T_x$ powders with about 20 wt% of 1.5 M acetic acid (1 gramme of powder with 0.2 gramme of acetic acid), the wet powders were sintered for one hour at 250 MPa at 300 °C [575]. Fig. 16 d, e depicts the schematic of the ZnO-$Ti_3C_2T_x$ composites' cold sintering process. ZnO grain development was inhibited by the addition of MXene flakes at the grain boundaries (see Figs. 16 f and g). With the addition of 5 wt% $Ti_3C_2T_x$, MXenes significantly increased the electrical conductivity of ZnO by five orders of magnitude. The presence of MXene flakes at the ZnO grain boundaries is seen in Fig. 3h. This phenomenon improved the electrical conductivity of ZnO-$Ti_3C_2T_x$ CMC by providing an effective channel for electron transport [575]. CMCs have also used MXenes' great mechanical stiffness, two-dimensional layered structure, and EMI shielding capabilities in non-oxide ceramics. $Ti_3C_2T_x$ multi-layer particles containing Si_3N_4 were ball-milled in isopropanol medium for ten hours [60]. Using SPS, the green bodies were sintered at 1750 °C for 30 minutes at an uniaxial pressure of 30 MPa. The characterization findings showed that high densification required the use of an oxide sintering additive, namely ZrO_2. On the other hand, the sintered composite did not

exhibit any MXene in the final CMCs when the oxide addition was applied. The 0.7 wt% $Ti_3C_2T_x$-ZrO_2-Si_3N_4 composite's fracture toughness at 5.2 MPa $m^{1/2}$ was found to be 15% more than that of a pure Si_3N_4 sintered under comparable circumstances. In a different investigation, $Ti_3C_2T_x$ MXene was combined with a polymer (hyperbranched polyborosilazanrcentage of 3–10 wt% [577]. Polymerization was then carried out for two hours at 400 °C, followed by pyrolyzation at 1000 °C and annealing to create TiC/SiBCN ceramics. The resultant MXene-derived TiC reinforced SiBCN composite demonstrated stable performance at greater temperatures (up to 600 °C) in both air and argon atmospheres, along with strong X-band absorption [578]. Overall, the increased thermal stability of the CMCs is probably due to the layered production of nanocrystalline non-stoichiometric TiC_y crystals at the grain boundaries.

SiC composites were created using Ti_2CT_x MXene as a filler [579]. After solution-processing 1 to 3 wt% Ti_2CT_x few-layer MXene flakes in isopropanol, they were combined with β-SiC (420 nm particle size) in a planetary ball mill for ten hours. The green bodies were then sintered using SPS under 50 MPa uniaxial pressure for 30 minutes at 1900 °C in vacuum, with a heating rate of 50 °C per minute. Compared to pure SiC (~98.5%), sintered CMCs showed better densification, with relative densities of 99.5% in composites with 1 wt% Ti_2CT_x addition. Composites containing 1 wt% MXene demonstrated a minimal 10% improvement in hardness and a 66% increase in fracture toughness when compared to pure SiC. MXene ceramic composites are still in their infancy, with few investigations having been conducted in this area. But because MXenes change into bulk carbides at high temperatures [39], comprehension and expectations of MXene CMCs can be enhanced by the abundance of information available on bulk 3D crystalline carbides used as reinforcements in CMCs. It has been demonstrated that adding additional fillers to CMCs often prevents excessive grain formation while enhancing densification, sinterability, and increased oxidation stability [580,581]. High-temperature materials like ZrB_2 and HfB_2 ceramics are often processed better with the addition of monocarbide 3D crystalline filler phases like SiC, WC, and VC [582-585]. It has been shown that the bending strength of composite materials may be enhanced by the presence of transition metal carbide phases at the ceramic matrix's grain boundaries [586]. This is achieved by enhanced intergranular bonding between the ceramic grains through diffusion. The intrinsic synergetic phase compatibility between carbide reinforcements and elevated temperatures ceramics is the cause of this intergranular bonding [354]. These carbide phases can provide CMCs a variety of beneficial material features in

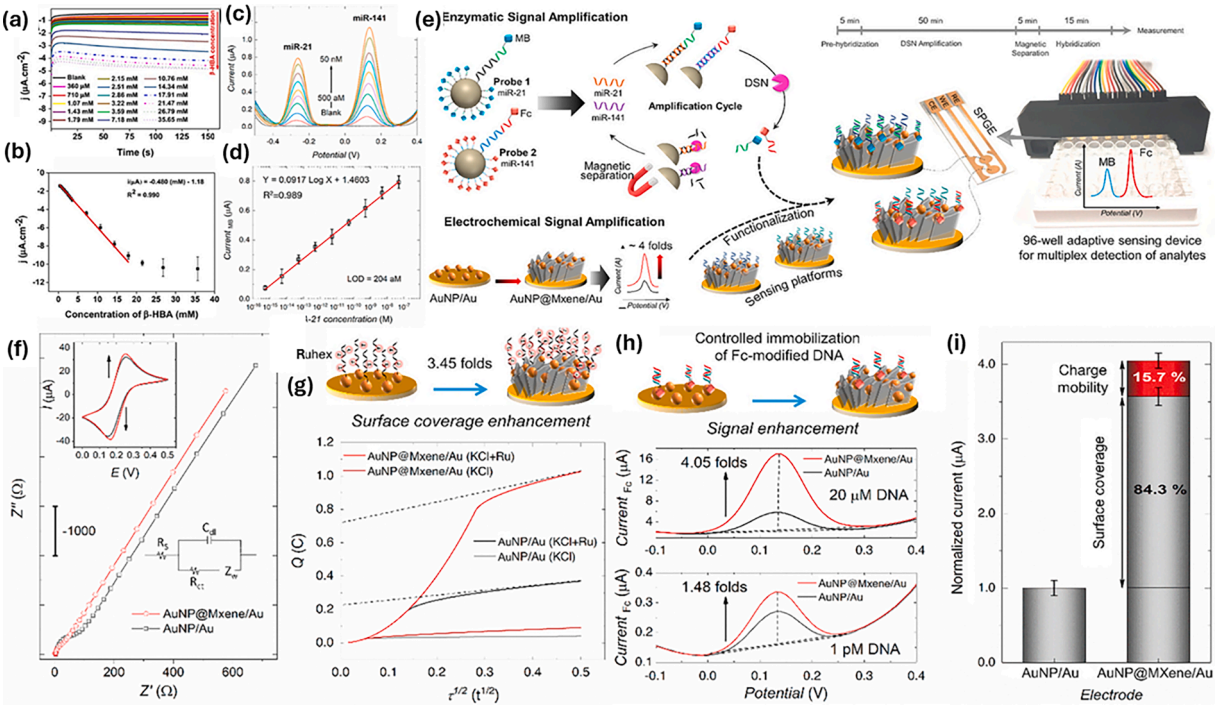

Fig. 17. (a) At an applied potential of −0.35 V vs. Ag/AgCl (3 M NaCl) in PBS pH 7.4, the amperometry i-t curve obtained at the Au-PCB/Ru/MXene-β-HBD-NAD-GA-BSA electrode (b) The matching linear calibration curve for β-HBA (n = 3)+ amperometric determination. Reproduced from Ref. [599], (c) The manufactured biosensor device's typical DPV response to the repeated detection of successive quantities of miR-21 and miR-141 in HEPES buffer (pH 7.4). (d) Corresponding regression figure showing the peak values of MB and Fc's oxidation current as a function of miR-21 concentrations. (e) Schematic diagram showing the whole multiplex and concurrent detection of miR-21 and miR-141 test process. The related cyclic voltammograms of AuNP/Au (black) and AuNP@MXene/Au (red) are displayed in the inset. (f) Nyquist plots (Z′ vs.—Z″) produced for AuNP/Au and AuNP@MXene/Au and the analogous Randles circuit model; The studies were conducted in PBS (pH 7.4) containing 0.1 M KCl and 5 mM of Fe $(CN)_6$ 4−/3−, with a CV scan rate of 50 mV/s. (g) The typical chronocoulometric behavior of RuHex on AuNP/Au and AuNP@MXene/Au in 20 mM KCL and hexaammineruthenium (iii) chloride (200 μM) + KCl (20 mM) is displayed. The dashed lines represent the intercept values and the outward stretching tangents that are projected to the Y-axis. (h) Differential pulse voltammetry (DPV) curves produced following hybridization with uncleaved Fc-labeled DNA sequences (DSN products of 20 μM and 1 pM miR-141 reaction) for Base141/AuNP/Au and Base141/AuNP@MXene/Au. (i) The normalised oxidation current peak value of Fc was statistically analyzed. Reproduced with permission from Ref. [600].

addition to intergranular strengthening because of their inherent mechanical and electrical characteristics, which also enhance their oxidation stabilities [587]. Since MXenes have surface groups that allow them to make primary bonds with ceramic matrices, they are a particularly promising class of carbide nano filler. They may be thought of as organized carbon vacancy carbides [551] with strong internal M-X ionic/covalent bonding.

5.4. Bio Composites

MXene-loaded biocomposites combine the remarkable characteristics of MXenes with the adaptation and environmentally friendly nature of biocomposites [588]. Also, they offer a novel and exciting direction in materials research. MXenes provide unique attributes to biocomposites, a type of material consisting of a matrix supplemented with natural fibres or polymers, and they have a potential to produce a hybrid that is both more effective and more biodegradable [589,590].

MXenes and biocomposites together provide a wide range of applications, especially in the fields of energy storage [591], biomedical implants [592], and flexible [593] and wearable electronics [594]. These composites are compatible with live tissues due to their biocompatibility [595]. It qualifies them for use in implanted medical devices [596]. MXene-loaded biocomposites can also be used in high-performance, lightweight electronics due to their superior mechanical strength and electrical conductivity [597]. MXene-loaded biocomposites are more appealing overall because of their sustainable and ecologically beneficial qualities [598]. Moreover, they meet the rising need for materials that are environmentally sensitive across a range of sectors. With an emphasis on sustainability and performance, this new subject has a lot of potential to advance materials engineering.

Enzymes, the first natural recognition components used in biosensors, may efficiently and precisely react with targeted analytes, resulting in an electrochemical response. By immobilising enzymes on MXenes to create biosensors, the enzymes can offer flexibility to the biosensors, meanwhile the MXenes operate as transducers, maximising their electrical conductivity, vast surface area, and biocompatibility. MXenes' huge surface area combined with their distinctive laminar architecture allows for enzyme immobilisation across a vast region. As shown in Fig. 17, Lee et al. [599] developed enzymatic beta-hydroxybutyrate biological sensors for amperometric detection employing β-hydroxybutyrate dehydrogenase tuned $Ti_3C_2T_x$-type MXene nanosheets. The biosensors were successfully utilised for the measurement of β-hydroxybutyrate in spiked blood specimens. $Ti_3C_2T_x$'s laminar disintegration allowed for the immobilisation and encapsulation of the enzyme, creating a favourable milieu over β-hydroxybutyrate dehydrogenase (β-HBD) for retaining its bioactivity and stability for extended periods of time.

6. 3D and 4D printing of MXene composites

6.1. 3D printing of Mxene composites

The basic idea of 3D printing involves a step-by-step method that involves creating a 3D model, pre-processing to prepare for printing, filling the material, starting the printing process, and finishing [601,602]. First, a 3D model of the target object is created using modelling software or 3D scanning. Then, the model is prepared for printing by slicing into layers and creating printer instructions in order to convert it into a format that can be read by a 3D printer [603]. The preferred material can be broad ranging, including ceramics and metals to food and plastics, is then fed into the 3D printer. The printer begins printing by depositing material layer-by-layer in accordance with the pre-generated instructions. Post-processing may be necessary after printing involving removing support structures or finishing operations such as surface enhancement through sanding, painting, or polishing [7].

3D printing technologies fall into three groups: (1) liquid-based methods (like stereolithography), (2) solid-based methods (like fused deposition modelling), and (3) powder-based methods (like selective laser sintering) [425]. When it comes to applications like energy storage systems, material selection is crucial in the 3D printing process. As shown in Fig. 18, metals, polymers, composites, ceramics, and new smart materials such as MXenes are widely used. MXenes are recognized for their unusual features, which include electric conductivity, increased surface area, and diversified surface chemistry. MXene adaptability extends to a wide range of applications, including transparent conductors, catalysts, fillers in composites, and nanoscale superconductivity as presented in Fig. 18. [27].

In the realm of energy storage, 3D printing has revolutionized electrode assembly in supercapacitors and batteries. The distinct advantages include the rapid and repetitive production of multiple components using a single 3D printing machine [605]. Moreover, the ability to modify printed ink and pre-programmed printing allows for adjustments in shape and microstructure, enhancing overall electrochemical performance. The precise manipulation of microstructure, energy and power density, and areal load is achievable through 3D printing technologies [606].

Notably, direct ink writing (DIW) and inkjet printing (IJP) are commonly employed 3D printing processes for energy storage, utilizing ink-like materials dispersed with electrode-active chemicals in a solvent. Specialized materials engineering and process fusion may be required for the adaptation of other 3D printing techniques in energy storage applications [604].

The adoption of commercial conductive poly(3,4-ethylenedioxythiophene)-poly(styrenesulfonate) (PEDOT:PSS) ink has led to various applications due to its tunable electrical properties, structural stability, redox activity, and biocompatibility. Notably, 3D printing has been employed to create electrodes and current collectors for micro-supercapacitors, particularly on flexible substrates [607]. Researchers often incorporate MXenes into PEDOT:PSS inks to enhance printability while regulating interconnectivity between printed layers, making MXenes the most frequently investigated material for supercapacitor fabrication via direct ink writing (DIW) [608]. In addition to efficient ion and electron transport, MXene nanosheets induce a hierarchical porous structure within PEDOT domains. An eco-friendly gel ink was developed by combining aqueous PEDOT:PSS, an appropriate amount of ethylene glycol, and

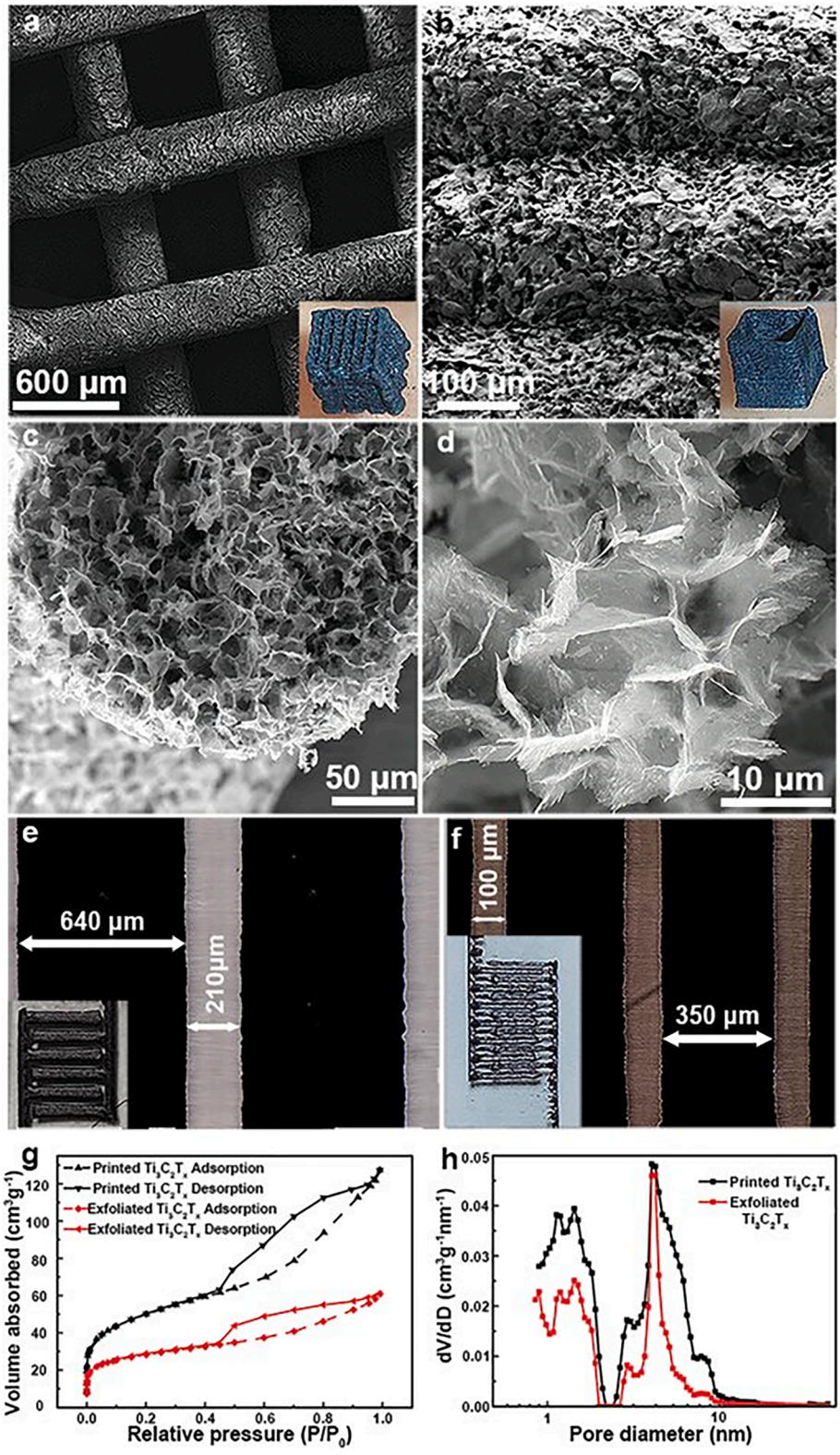

(caption on next page)

Fig. 18. Multiscale buildings created in 3D and frozen-dried. a,b) SEM and optical photos (inset) of the hollow rectangular prism and freestanding $Ti_3C_2T_x$ microlattice produced through 330 and 250 μm nozzles, respectively. c,d) The cross-sectional SEM pictures of one filament inside the microlattice in demonstrate how the freeze-drying process preserves shape and creates porous interior structures. e,f) Three-dimensional printed interdigitated patterns with finger thicknesses and gaps of 640 and 210 μm (e) and 350 and 100 μm (f) in $Ti_3C_2T_x$ are shown in optical microscope pictures and optical photos (inset). Reprinted with the permission of Ref. [604].

MXene nanosheet catalysts. During the printing process, freeze-drying was employed to verify the structural integrity. Leveraging DIW, the number of fabrication layers could be precisely controlled, allowing management of the as-fabricated electrode capacitance. This approach not only reduces manufacturing time and costs but also minimizes material waste. 3D printing of micro-supercapacitors yields substantial areal capacitances, rapid charge-discharge behavior, and stable cycling performance. Using aqueous-based inks, these capacitances remain consistent across varying thicknesses, even at low temperatures and under unusual conditions. Additionally, direct ink writing (DIW) additive manufacturing enhances fuel cell electrode design, creating intricate architectures with superior properties compared to batteries and supercapacitors. DIW offers several advantages: it excels at constructing complex structures that are challenging to make conventionally, making it ideal for customized medical implants and intricate lattices. Furthermore, DIW works with polymers, ceramics, metals, and composites, enabling multi-material integration. Its high resolution allows for micron-sized features, and it minimizes material waste by depositing material only where needed. Despite challenges like speed, post-processing, and costs, ongoing research in diverse fields leverages DIW's potential for efficiency and innovation. Advances in materials and processes can unlock transformative possibilities across industries [609].

Several reviews on MXene based composites for 3D printing applications are published recently. For example, Polychronopoulos et al. [610] focuses on DIW technique and explains 3D printed electrodes and ink design aspects. Huang et al. [611] elucidates the microeletrode design and integration of MXenes into MSCs utilizing both supported and free-standing architectures. Matias et al.[609] details $Ti_3C_2T_x$ MXenes into smart 3D printed structures for sensors, biosensors, electromagnetic shielding, and environmental remediation by employing contemporary advancements in AI and connectivity features. Salas et al.[27] concentrated around the development of polymeric/MXenes composites for printable electronics using photocurable resins with $Ti_3C_2T_z$ MXenes using Digital Light Processing technology to obtain complex 3D composite structures.

3D-printed MXene electrodes show significant potential for the creation of future-oriented electrochemical devices, since they provide better performance, customisation, and design freedom. To this purpose, it is critical to enhance the 3D printing capability of MXene ink and solve the restacking phenomena of MXene nanosheets. A hybrid ink composed of cellulose nanofibres (CNFs), MXene, along with multiwalled carbon nanotubes (MWCNTs) is created by Zhou et al.[612] and printed into high-fidelity, customised,

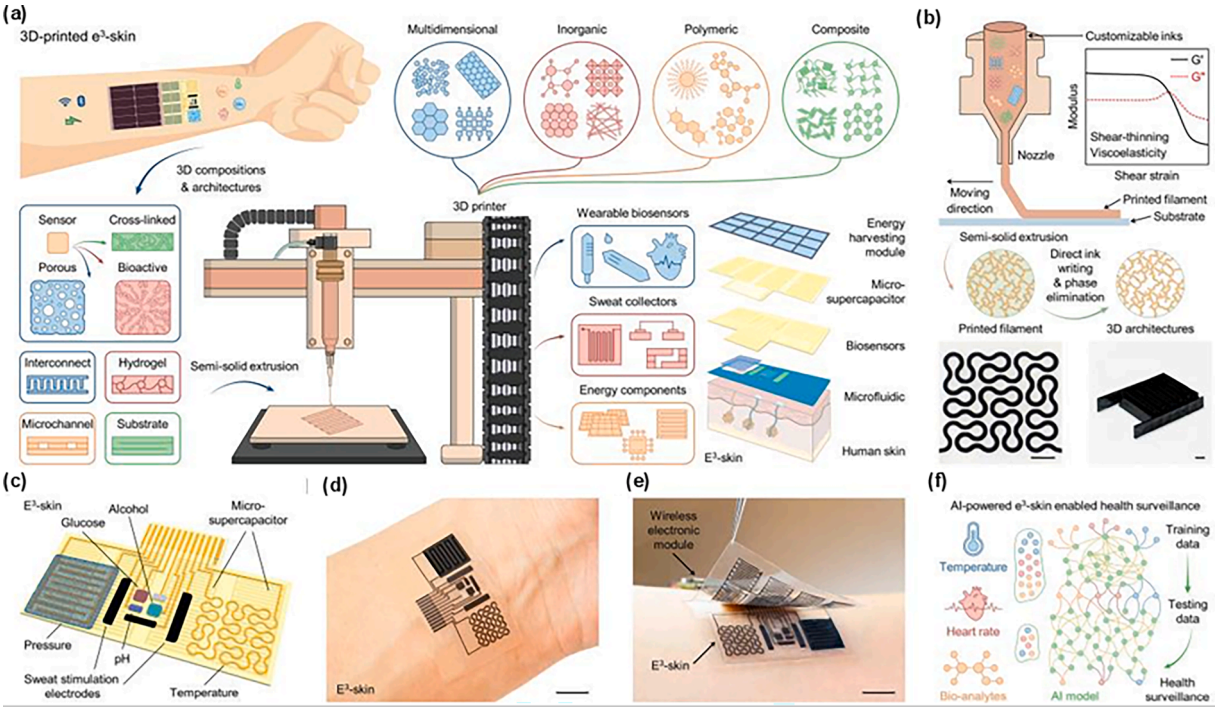

Fig. 19. (a) Schematic depiction of SSE-based three-dimensional printing of the wearable e3-skin, including multisensory sensing and power management. (b) Schematic example of SSE printing techniques for creating 2D and 3D structures. (c) A schematic representation of the 3D-printed e3-skin. (d) and a fully functional wireless e3-skin apparatus (e) worn by a human subject. Scale bars measure 1 cm. (f) Machine learning-powered multifunctional e3-skin for personalised health monitoring. Reprinted with the permission of Ref. [614].

freestanding electrodes utilising controlled direct-ink-writing technology. The addition of waterproof CNFs and extremely conductive MWCNTs additionally improved the rheology characteristics of MXene ink, but it also bridged the horizontally orientated MXene nanosheets, leading to a more integrated internal structure and improved inter layering separation of MXene. As a result, the 3D-printed elastic electrode had consistent conductivity, increased surface area accessibility, better wettability, and superior electrochemical performance. In situ radical polymerisation was also used to create a hydrogel electrolyte of cellulose nanofibre/polyacrylamide (CNF/PAM). A flexible interdigitated supercapacitor with an elevated energy density of 21.7 μW h cm^{-2} at 0.3 mW cm^{-2} was reported. This was achieved by overlaying the CNF/PAM hydrogel electrolyte upon two 3D printed electrodes. The findings of this study give important insights into developing MXene-based inks for 3D printing forthcoming super capacitors that are flexible.

Peng et al.[613] added high-viscosity aramid nanofibres (ANFs) to improve the rheology of MXene inks with low concentrations. MXene and ANF's abundant linked networking and hydrogen bonds enhanced viscosity and yield stress by up to 103 Pa·s and 200 Pa, correspondingly. This optimisation enabled the use of low-concentration MXene/ANF (MA) inks in direct ink writing as well as other high-viscosity processing methods. The printable MXene/ANF inks, which had a high conductivity of 883.5 S/cm, were utilised to print shields with customised structures, resulting in an adjustable electromagnetic radiation shielding effectiveness of 0.2-48.2 dB. Moreover, the MA inks have changeable infrared (IR) emissivity when the ANF ratio was changed in conjunction with the printing design, suggesting the potential for infrared anticounterfeiting. Particularly, created MXene/ANF objects had exceptional mechanical flexibility along with durability in the environment, which were due to the additional reinforcement and safeguarding properties of ANF. These discoveries have major practical consequences since adaptable MXene/ANF inks may be utilised to produce flexible printed electronics in a customisable, scalable, and cost-effective manner.

As shown in Fig. 19, Song et al.[614] found 3D-printed epifluidic digital skin for multimodal health surveillance using machine learning. Wearable technology combined with physiochemical sensors promise to develop strong interpretative and predicting platforms for immediate health monitoring. However, the development of such multimodal gadgets is challenging to completely implement using typical manufacturing procedures for at-home personalised applications. Song offered a universal semisolid extrusion-based three-dimensional printing method that fabricates an epifluidic elastic electrical skin (e3-skin) with excellent performance multifunctional physiochemical sensing abilities. He showed that the e3-skin may be used as a long-term surveillance platform to collect individuals' physiological states in real time while they are performing normal daily activities. It was further demonstrated that by combining information gathered through e3-skin using machine learning, an individual's level of behaviour impairments (i.e., response time and inhibition control) following alcohol use could be anticipated. The e3-skin sets the way for future autonomous production of customisable wearable devices, which will be widely used for frequent monitoring of health and medical purposes.

Hussain et al. [404] studied foldable 2D MXenes for multifunctional future-oriented energy storage. The advent of portable electronics has created several opportunities for academics to customise the growing demand for future electronics. MXenes, a class of two-dimensional in nature (2D) transition-metal carbides and nitrides, have exceptional flexibility and other desirable features, making them ideal for wearable electronics. This study focused on the synthesis of MXenes for flexible and wearable applications, using techniques like wet-spinning, electrospinning, 3D printing, bi-scrolling, and coating. Furthermore, the paper wentt over the considerable advances and accomplishments obtained in adaptive and wearing MXene-based supercapacitors. It also discussed the problems

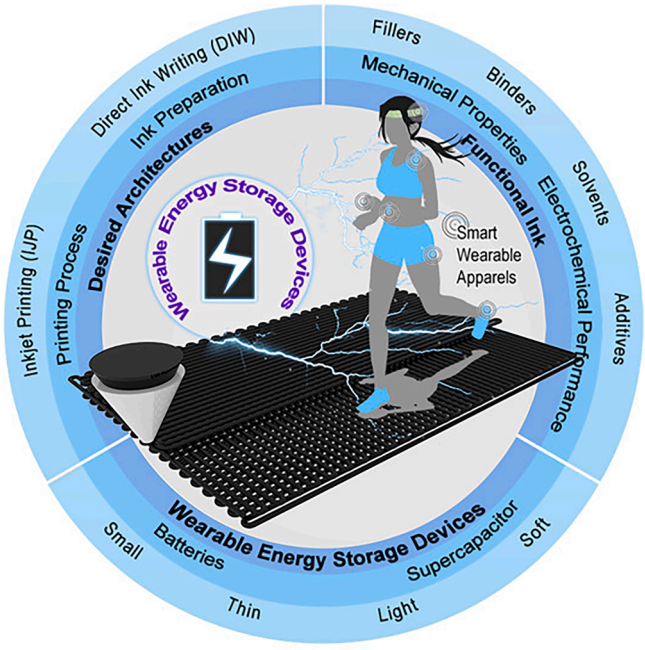

Fig. 20. Schematic representation of Mxene and 3D printing on wearable electronics.

Table 8
Different applications of 3D printed MXene composites

Application area	Materials	3D printing technology	Ref.	Research Findings
Sensors	Mxene, Poly vinylalchohol	Binder Jetting	Li et al. [615]	The sample exhibited conductive behaviour on the order of mS m^{-1}, indicating the possibility of strain monitoring and storing energy.
	Mxene, Polyurathane	Digital light processing	Li et al. [616]	The produced MXene-PAR compound, which had 0.1% w/w fillers, has tensile strength and elongation at break of 23.3 MPa and 404.3%, respectively, which was a 100.8% and 37.8% improvement over the control. The stretchy sensors demonstrated long-term operational stability.
	Nitrogen-doped porous MXene, melamine-formaldehyde,	Electrospinning	Tao et al. [617]	The linked mesh architecture enabled the electrolyte to permeate the porous network and thoroughly saturate the material surface, thus reducing the ion transport channels.Uniform nitrogen doping improved pseudocapacitive performance, providing good electrochemical performance and long-term durability. It achieved an energy density of 12.78 Wh kg^{-1} at a power density of 12.78 Wh kg^{-1} at a power density of 1080 W kg^{-1}, with cycling stability reaching 5000 cycles.
Energy Storage	Ti_3C_2, Zn^{2+}	Direct Ink Writing	Fan et al. [618]	By combining the electrical double-layer capacitive behaviour of Zn^{2+} with the pseudocapacitive behaviour of H^+, the resulting 3D-printed (3DP) MXene cathode created a dual-ion storage mechanism that can be systematically investigated using a broad range of in situ/ex situ electroanalytic characterisations. As a result, the 3DP MXene cathode outperformed the most advanced ZICs with a favourable areal capacitance with 1006.4 mF cm^{-2} at 0.38 mA cm^{-2} and good rate capability (184.4 F g^{-1} at 10 A g^{-1}). More astonishingly, ZIC complete cells with a 3DP Zn anode and a 3DP MXene cathode offered an ultralong lifespan (86.5% retention of capacity over 6000 cycles at 10 mA cm^{-2}) combined with a competitive energy/power ratio of 0.10 mWh cm^{-2}/ 5.90 mW cm^{-2}.
	Cellulose nano fibres, MXene, CNT, Polyacryloamide	Direct-ink-writing	Zhou et al. [612]	The 3D-printed flexible electrode displayed stable conductivity, better wettability, increased surface area accessibility, and superior electrochemical performance. At 0.3 mW cm^{-2}, it provided an elevated energy density of 21.7 μW h cm^{-2}.

and potential opportunities for MXenes as wearable devices that store energy. The integration and growth of MXenes-based energy storage devices into various wearable gadgets (Fig. 20) offer great potential for the future of the electronic industry.

As a result of their metallic-like conductivity, negative zeta potential, the presence of polar surface functional groups, and their tunable electronic properties, MXenes have attracted considerable attention. Table 8 presents the various applications of 3D printed MXene composites. The electrode materials used in the fabrication of wearable devices must be hydrophilic in nature to be efficient. Since MXene exhibits a high degree of hydrophilicity due to the presence of -OH and -O surface terminations, it is suitable for use as a supercapacitor electrode on fibrefibrefibre surfaces. Several strategies have been employed in the development of MXene-based SC electrode materials. Further, 3D printing is being used to fabricate MXene fabrics for use in wearable devices. Compared to existing active materials used in conventional printing, the fabricated MXene micro supercapacitors (MSCs) have significantly higher volumetric capacitance and energy density. It is evident from this that MXene ink offers excellent potential for various applications. There is a significant challenge in minimizing the size and maximizing ion transport in electrodes while maintaining a high level of efficiency. However, there is evidence that high-concentration MXene ink, capable of extrusion printing, may be useful in fabricating electrochemical devices with a wide range of electrode thicknesses and structures. By doing so, compact electronic devices can be developed with efficient ion transport within the electrodes. Using 3D printing technology, wearable smart devices can be assembled easily. In their study, Cao et al. [619] used TEMPO(2,2,6,6-tetramethylpiperidine-1-oxylradical)-mediated oxidized CNFs and MXene hybrid inks for 3D direct-to-write printing to assemble wearable textiles and fibres. Ethanol was effective in solidifying hybrid inks with good rheological properties. Smart fibres and textiles are in comparison to traditional fibres that have a single purpose and are highly responsive to a variety of witha single purpose and are highly responsive to various external stimuli, including photothermal, electrothermal, and electromechanical stimuli. The material [572] is a 2D $Ti_3C_2T_x$ (the most studied MXene material) with ideal viscoelastic properties and is suitable for extrusion-based 3D printing of freestanding, high-specific surface area architectures.

Another significant benefit of MXenes beyond other functional substances is their ability to produce aqueous or organic inks without additional additives. Consequently, researchers tried to print MXenes employing DIW [620]. Zhang et al. [621] used this characteristic to create 2D titanium carbide ($Ti_3C_2T_x$) MXene inks in both aqueous and organic solvents. They could directly draw conductive tracks, micro-supercapacitors, and ohmic resistors onto paper substrates. MXenes' strong electrical conductivity and also pseudocapacitive behaviour, along with DIW's spatial homogeneity and excellent printing precision, resulted in orders of magnitude improvements in volumetric capacitance along with energy density. Nevertheless, the conductive properties of 3D-printed MXene frameworks are greatly dependent on the orientation of the MXene flakes [620]. Orangi et al. [622] demonstrated that the alignment of MXene flakes in printed $Ti_3C_2T_x$ structures may be adjusted by varying the printing conditions and DIW ink properties. This might be another option for enhancing the electrical characteristics of DIW-fabricated MXene devices. Yang et al. [604] demonstrated that MXene platelets having a high aspect ratio enhanced viscosity at extremely low concentrations, making the ink more printable. They

developed viscoelastic inks using 2D $Ti_3C_2T_x$ with a large lateral size (about 8 μm). The 3D printing procedure, along with the post-printing freeze-drying approach, resulted in the assembling of 2D flakes to create a porous architecture inside the filaments, preventing the flakes from restacking normally. As an outcome, the overall area of printed structures increased dramatically as compared to traditional procedures (such as casting or vacuum filtering). Printable energy storage devices that had enormous specific areas exhibited remarkable efficiency, combining significant capacitance along with energy density. This study demonstrated that DIW using MXene inks may be used to the production of powerful functional and structural components in a variety of sectors. In another work, Yu et al. [623] created folded nitrogen-doped MXene nanosheets using the melamine-formaldehyde templating approach to solve the difficulty of restacking 2D sheets, which normally reduces the electrochemical properties of the devices. In this method, they not just stopped MXene nanosheets from stacking, they additionally doped nitrogen throughout MXene frameworks, resulting in excellent device performance.

MXenes, a family of two-dimensional transition metal carbides and nitrides, have garnered significant attention due to their remarkable properties. One critical advantage of MXenes is their ability to form aqueous and organic inks without requiring additional additives. Researchers have harnessed this property to explore direct ink writing techniques for MXene-based devices.

1. **Conductive Tracks and Micro-Supercapacitors:**
- Zhang et al. [621] formulated 2D titanium carbide ($Ti_3C_2T_x$) MXene inks using both aqueous and organic solvents. They achieved direct writing of conductive tracks, micro-supercapacitors, and ohmic resistors on paper substrates. The combination of MXenes' high electrical conductivity and pseudocapacitive behavior with the spatial uniformity and high printing resolution of DIW led to substantial improvements in volumetric capacitance and energy density.
2. **Controlling MXene Flakes Orientation:**
- The conductivity of 3D printed MXene structures significantly depends on the orientation of MXene flakes. Orangi et al. [622] demonstrated that adjusting printing parameters and ink characteristics in DIW can control the orientation of MXene flakes within printed $Ti_3C_2T_x$ structures. This approach offers a promising route to enhance the electrical properties of DIW-fabricated MXene devices.
3. **Viscoelastic Inks and Surface Area Enhancement:**
- Yang et al. [604] developed viscoelastic inks of 2D $Ti_3C_2T_x$ with large lateral sizes (approximately 8 μm). By employing a 3D printing process followed by freeze-drying, they prevented the restacking of MXene flakes. As a result, the surface area of printed structures significantly improved compared to conventional techniques like casting or vacuum filtration. These high-specific-area structures exhibited excellent performance in terms of capacitance and energy density.
4. **Nitrogen-Doped MXene Nanosheets:**

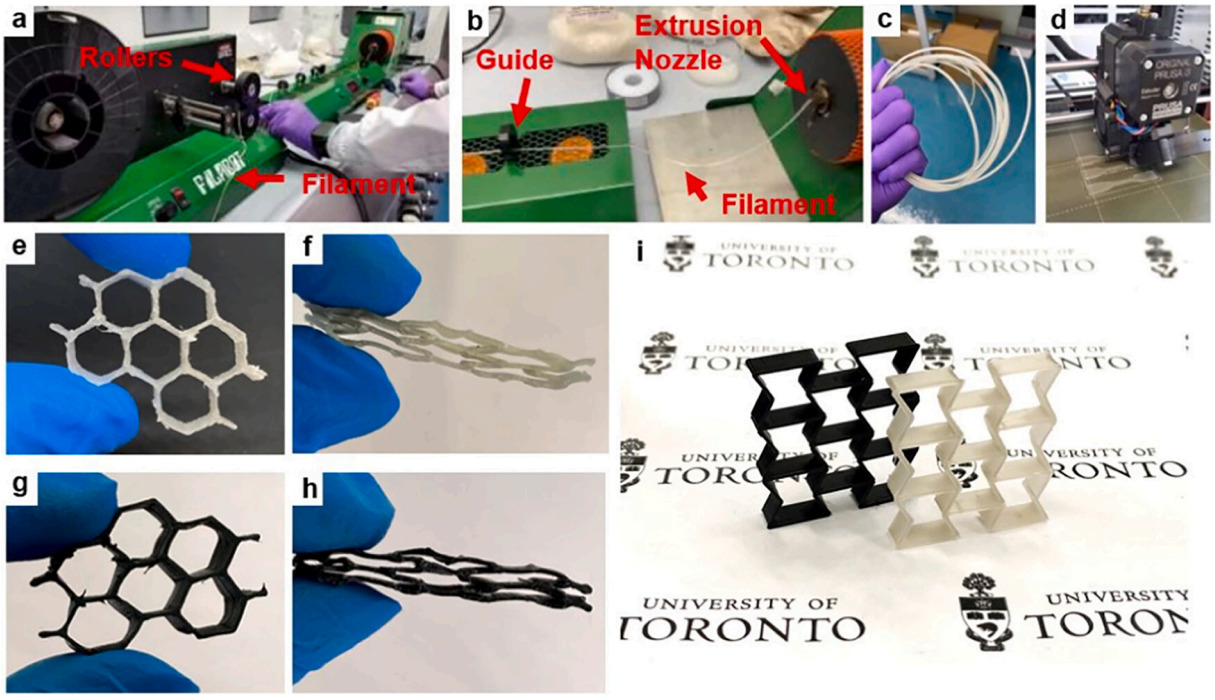

Fig. 21. The 4D printing process of MXene SMPC filament involved: (a, b) filament extrusion, (c) the extruded filament, (d) 4D printing of the SMPC filament, (e) a 0 wt% honeycomb printed structure, (f) the 0 wt% honeycomb printed structure programmed into a deformed flat state, (g) a 2 wt% honeycomb printed structure, (h) the 2 wt% honeycomb printed structure programmed into a deformed flat state, and (i) 0 and 2 wt% 4D printed auxetic structures. Reprinted with the permission of the Ref. [624]

- Yu et al. [623] addressed the challenge of restacking in 2D MXene sheets by developing crumpled nitrogen-doped MXene (MXene-N) nanosheets. Their melamine-formaldehyde templating method not only prevented restacking but also introduced nitrogen into the MXene frameworks. This novel approach led to commendable electrochemical device performance.

5. **Future Directions:**

- While $Ti_3C_2T_x$ inks have been successfully formulated for DIW, the broader MXene family comprises around 30 compounds. Researchers anticipate that formulating viscoelastic inks for other MXenes could unlock a myriad of untapped applications. These may include flexible electronics and supercapacitor-based energy storage devices.

In summary, DIW of MXene inks holds immense promise for advancing functional and structural materials across various industries. As research continues, we eagerly await further breakthroughs in MXene-based printing technologies and their real-world applications.

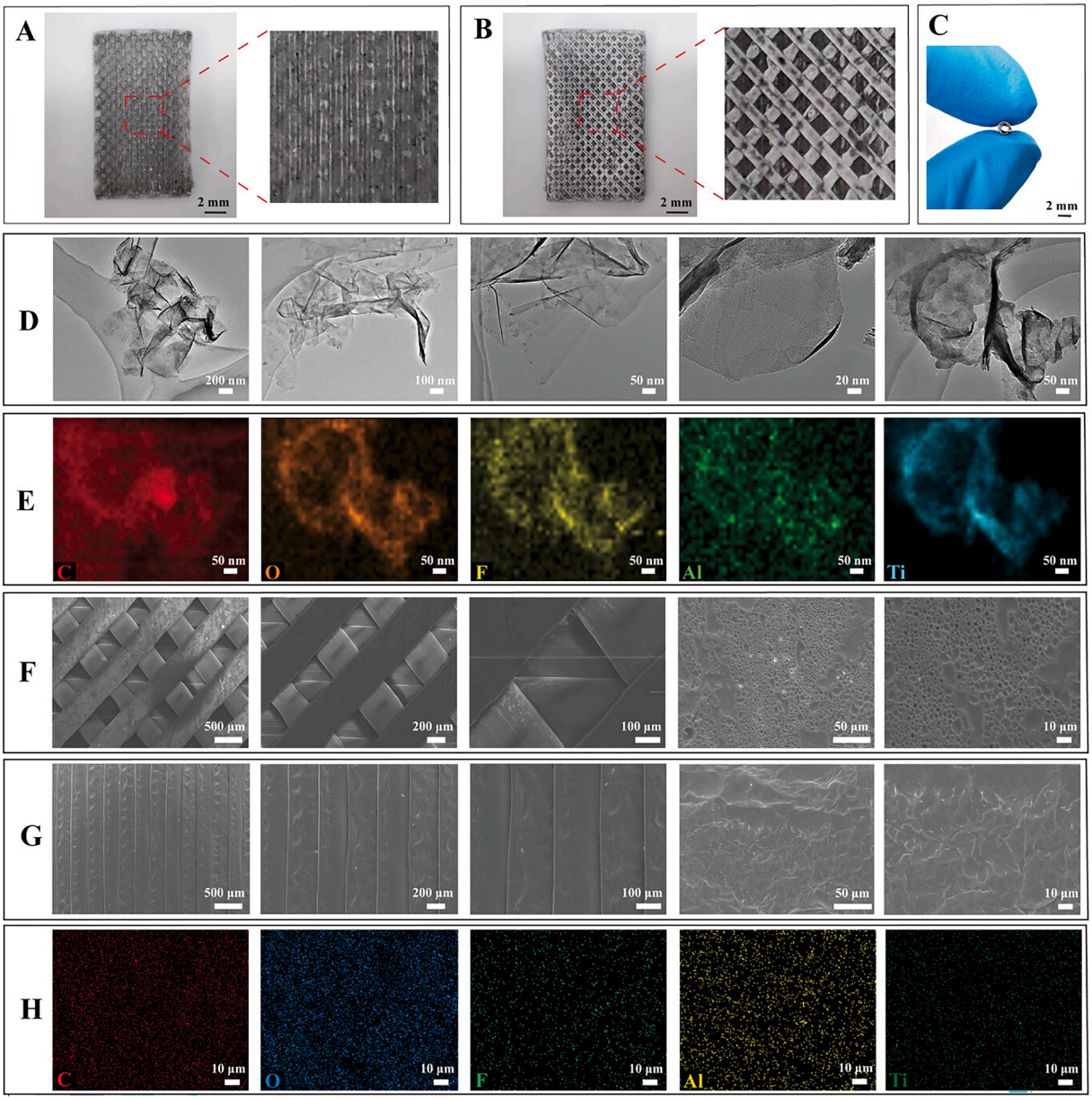

Fig. 22. Optical and morphological characterization of MXPLT conduits included analyses of: (A) the guide layer structure, (B) cross-layer structure, and (C) the cross-sectional morphology when curled into a tube. (D) TEM imaging revealed the detailed nanostructure of $Ti_3C_2T_x$ MXene, while (E) EDS analysis confirmed its elemental composition. SEM imaging showcased the (F) cross-layer and (G) guide layer structures of the MXPLT, and (H) EDS analysis of the MXPLT provided insights into its elemental distribution. Reprinted with the permission of the Ref. [625]

6.2. 4D printing of Mxene based composites

6.2.1. Shape-Memory and Programmable Actuation in MXene Composites

The incorporation of MXenes into 4D-printed matrices addresses challenges in conventional shape-memory materials, such as limited electrical or thermal response efficiency. MXenes, with their metallic conductivity (e.g., Ti_3C_2 has conductivity as high as ~8000 S/cm), serve as pathways for heat and electricity, thereby enhancing the actuation response of polymer matrices. Studies have demonstrated that MXene-polymer composites exhibit higher actuation forces and shorter response times than their polymer-only counterparts. This makes them ideal for deployable aerospace systems, programmable biomedical implants, and reconfigurable

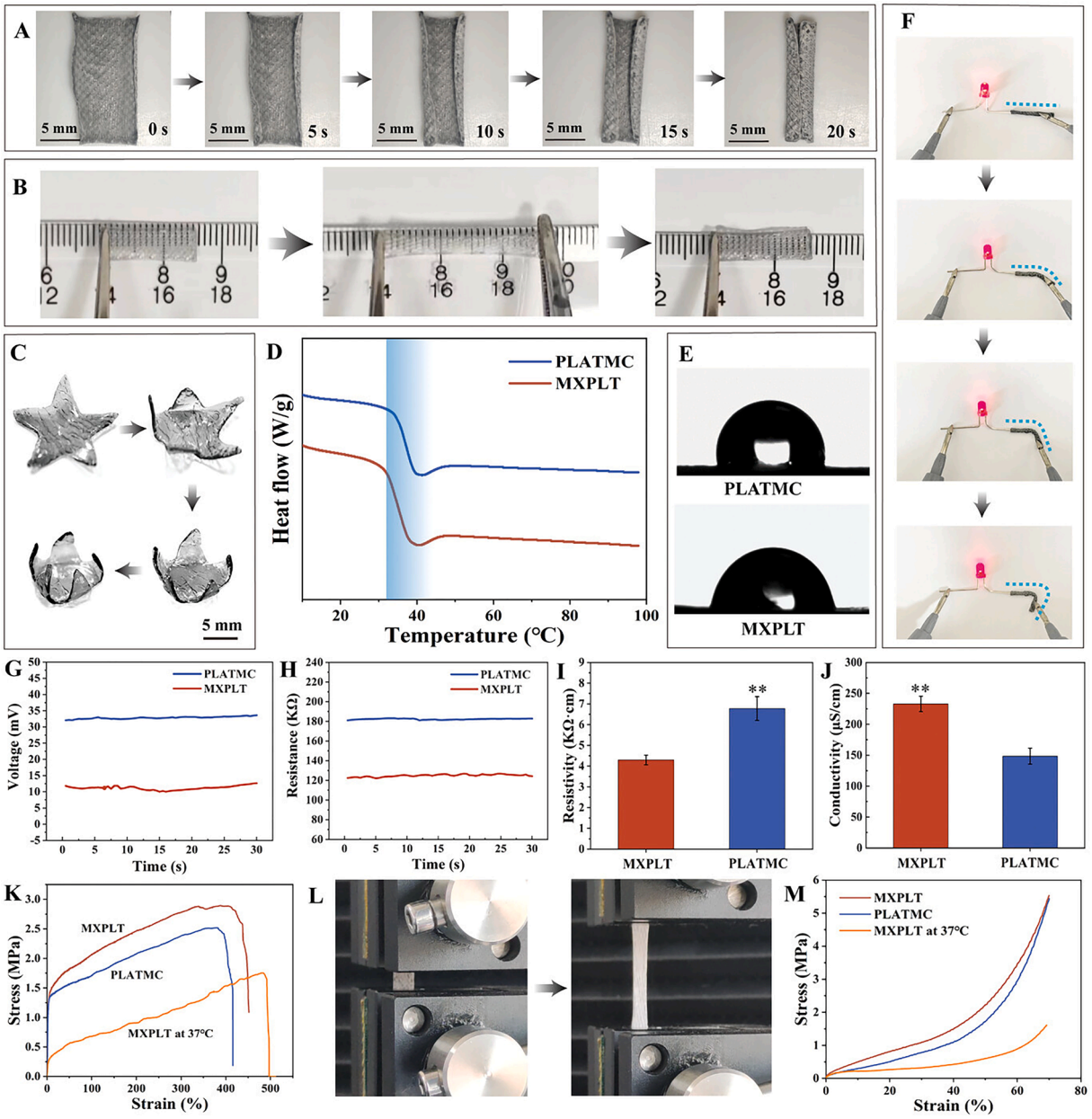

Fig. 23. Characterization of MXPLT NGCs involved analyses of: (A) dynamic shape recovery at 37 °C, (B) stretching behavior, and (C) morphological changes of a 4D-printed five-pointed star. (D) Differential scanning calorimetry (DSC) curves showed distinct thermal transitions for PLATMC fibrous mats. (E) Water contact angle tests demonstrated improved hydrophilicity for MXPLT. Electrical performance was assessed through (F) LED illumination under bending, (G) voltage tests, (H) resistance tests, (I) resistivity tests, and (J) electrical conductivity measurements, all showing significant enhancements for MXPLT compared to PLATMC. Mechanical evaluations included (K) tensile stress-strain curves, (L) images from tensile testing, and (M) compressive stress-strain analysis, confirming MXPLT's superior mechanical strength ($p < 0.01$). Reprinted with the permission of the Ref. [625]

electronics. For instance, McLellan et al. [624] was fabricated shape memory polymer composites (SMPC) composed of a TPU:PLA polymer blend with embedded MXene (Ti_3C_2) flakes as shown in Fig. 21. The addition of 0.5 wt% MXene significantly improved the mechanical, thermal, and morphological properties, while a 2 wt% MXene loading enhanced the shape memory effect, enabling a fast recovery of approximately 98% of the original shape in under 14 seconds. Rheological and thermal properties were assessed, and 3D printing with material extrusion demonstrated the composites' potential for rapid shape memory actuation in 3D/4D printed structures, showcasing their suitability for large deformations in deployable designs.

6.2.2. *Enhanced Functionalization Through Dynamic Property Tuning*

4D printing enables the spatial control of MXene distribution within polymer matrices, which is vital for anisotropic property tuning. For example, MXenes can be aligned during the printing process using magnetic or electric fields, resulting in composites with directional electrical conductivity or mechanical stiffness. This ability to create gradient structures allows the production of multifunctional devices such as sensors that simultaneously exhibit high sensitivity and structural integrity. Moreover, this tunability

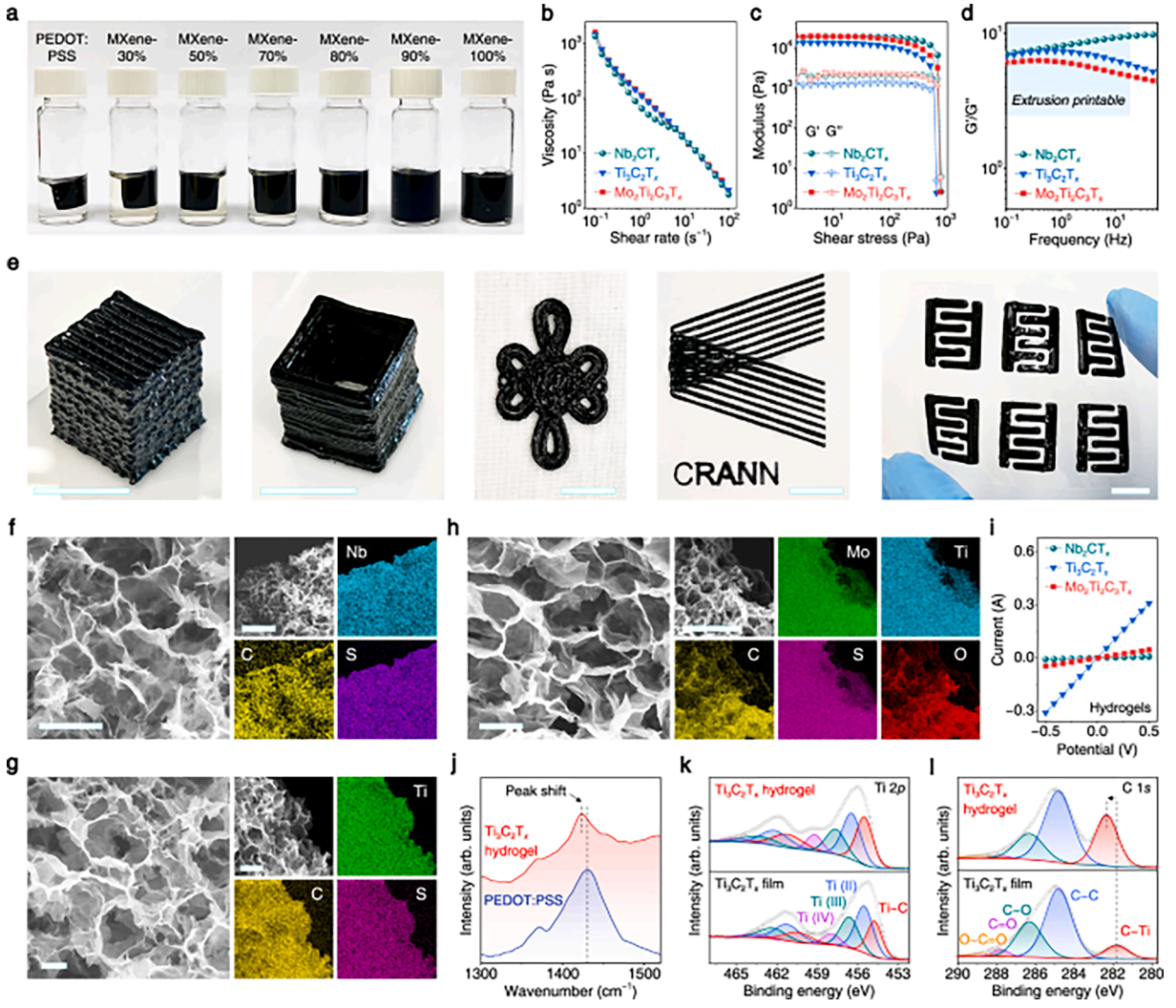

Fig. 24. (a) Images of $Ti_3C_2T_x$ hydrogels that were self-assembled and had varying MXene levels. (b) Viscosity for Nb_2CT_x, $Ti_3C_2T_x$, and $Mo_2Ti_2C_3T_x$ inks as a function of shear rate. (c) For Nb_2CT_x, $Ti_3C_2T_x$, and $Mo_2Ti_2C_3T_x$ inks, the storage modulus (G′) and loss modulus (G″) as a function of the shear stress are shown. (d) The G′ to G″ ratio's frequency dependency for Nb_2CT_x, $Ti_3C_2T_x$, and $Mo_2Ti_2C_3T_x$ inks. Images of 4D-printed MXene hydrogel architectures (from left to right): flexible $Mo_2Ti_2C_3T_x$ hydrogel MSC units on PET film, Nb_2CT_x hydrogel Chinese knot on cloth, $Ti_3C_2T_x$ hydrogel rectangular hollow prism on glass slide, and Nb_2CT_x hydrogel "CRANN" logo on PET film. In (e) each scale bar represents one centimetre. (f) Nb_2CT_x hydrogel SEM and energy-dispersive X-ray spectroscopy (EDX) mapping pictures. (g) SEM and $Ti_3C_2T_x$ hydrogel EDX mapping pictures. (h) SEM and EDX mapping pictures of the hydrogel $Mo_2Ti_2C_3T_x$. In f–h EDX mapping photos, all scale bars are 20 μm, and in (f–h) SEM images, all scale bars are 5 μm. (i) I-V curves of 10 × 2 × 2 mm hydrogels of Nb_2CT_x, $Ti_3C_2T_x$, and $Mo_2Ti_2C_3T_x$. (j) Raman spectra of 4D-printed $Ti_3C_2T_x$ hydrogel and pure PEDOT:PSS sheet. High resolution 4D-printed $Ti_3C_2T_x$ hydrogel and filtered $Ti_3C_2T_x$ film. (k) Ti 2p and l C 1s XPS spectra. All binding energies were calibrated at 284.8 eV, which is the peak of C 1s. Reprinted with the permission of Ref. [32].

supports applications in energy storage, where graded structures optimize ion transport pathways in supercapacitors or batteries.

6.2.3. Improved Fabrication of Complex Architectures

The layer-by-layer precision of 4D printing facilitates the fabrication of MXene-containing materials with intricate architectures, such as interdigitated electrodes or hierarchical porous structures. These geometries are particularly advantageous in applications like microfluidic systems or piezoresistive sensors. For instance, the combination of MXene's high intercalation capacity with 4D-printed hierarchical porosity improves the performance of stimuli-responsive flow control devices, achieving higher adaptability to dynamic operational environments.

6.2.4. Synergistic Advancements in Stimuli-Responsive Properties

MXenes are known for their ability to form hydrogen bonds or electrostatic interactions with polymers, which enhances the stability and responsiveness of the composite to external triggers. For example, MXene-polymer hydrogels used in 4D printing exhibit faster water desorption rates under thermal stimuli due to the high thermal diffusivity of MXenes. These properties enable the design of moisture-responsive actuators and smart textiles with superior performance compared to traditional materials. A novel strategy was integrated by Wang et al. [625] using 4D printing technology with poly(L-lactide-co-trimethylene carbonate) (PLATMC) and $Ti_3C_2T_x$ MXene nanosheets to impart shape-memory properties to nerve guidance conduits (NGCs) (Fig. 22). When activated at body temperature, the printed sheet-like structure rapidly self-rolled into a conduit-like form, allowing for optimal wrapping around nerve stumps. This design improved nerve fixation and streamlined surgical procedures. Additionally, microchannels precisely fabricated via 4D printing, combined with the conductive properties of MXene nanosheets, introduced electrical conductivity. The Mxene-PLATMC (MXPLT) scaffolds were fabricated using 4D printing technology, with MXPLT ink deposited into cuboid structures featuring a microchannel inner layer for nerve cell growth and a robust outer layer for mechanical stability (Fig. 23). Shape-memory properties of the PLATMC material allowed the scaffolds to be temporarily flattened and then self-curled at 37°C, forming nerve conduits with precise diameters to repair sciatic nerves. Recovery tests, including complex deformations like a five-pointed star, demonstrated the scaffolds' excellent 4D printing performance and self-curling capabilities, enabling effective surgical implantation and nerve regeneration. This feature guided and directed nerve cell migration, significantly accelerating peripheral nerve injury (PNI) healing. Leveraging these advancements, the developed NGCs showed exceptional potential in promoting nerve regeneration, achieving notable improvements in muscle morphology and restored sciatic nerve function, comparable to results observed with autologous nerve transplantation.

6.2.5. Applications in Intelligent Systems and Energy Storage

The combination of MXenes' high conductivity, environmental stability, and large intercalation capacity with the programmable nature of 4D printing makes it possible to engineer materials for next-generation devices. These include shape-recoverable electrodes in flexible electronics, reconfigurable EMI shielding structures, and self-regulating drug delivery systems. For example, 4D-printed MXene-based films with tunable optical or electrical properties have shown potential for smart windows or adaptive sensors. A universal 4D printing technology was developed by Li et al. [32] to fabricate MXene hydrogels with customizable geometries, applicable to various MXenes such as Nb_2CT_x, $Ti_3C_2T_x$, and $Mo_2Ti_2C_3T_x$ as shown in Fig. 24 A black dispersion of MXene (Nb_2CT_x, $Ti_3C_2T_x$, or $Mo_2Ti_2C_3T_x$), PEDOT:PSS, and additives was centrifuged to form solid-like inks with a concentration of ~50 mg/mL, which were then 3D-printed into various structures. After printing, the MXene sols were heated at 90°C to form hydrogels, which were treated with H_2SO_4 to enhance their mechanical strength, followed by washing to remove impurities, resulting in MXene hydrogels with 80 wt.% MXenes and ~4.2 wt.% solid content. The hydrogels exhibited 3D porous structures, high electrical conductivity, and strong mechanical properties, achieving ultrahigh capacitance and impressive energy/power densities, along with excellent low-temperature tolerance and rate capabilities that outperform most existing devices.

7. Applications

7.1. Sensors and Biomedical applications

Because of their unique qualities and adaptability, MXenes composites have become attractive options for sensing applications. These materials are appropriate for detecting a range of analytes due to their large surface area, variable surface chemistry, and superior electrical conductivity. MXenes composites have exceptional sensitivity and selectivity towards gases, including ammonia [626], nitrogen dioxide [627], and volatile organic compounds (VOCs) [628], which is one field of sensor research. For example, to create an Ohmic contact and Schottky heterojunction in a single gas sensing channel, a completely flexible paper-based gas sensor combined with the $Ti_3C_2T_x$-MXene nonmetallic electrode and the $Ti_3C_2T_x/WS_2$ gas sensing film was created by Quan et al. [627] for the first time. Outstanding $Ti_3C_2T_x$ and WS_2 nanoflakes physical and chemical characteristics include excellent conductivity, efficient charge transfer, and many active sites for gas sensing in $Ti_3C_2T_x/WS_2$ nanoflakes. With compared to the Au interdigital electrode combined with the $Ti_3C_2T_x/WS_2$ sensor (4.8%) and the MXene electrode integrated with the $Ti_3C_2T_x$ sensor (0.2%), respectively, the gas sensor's reaction to NO_2 (1 ppm) at room temperature is 15.2%, which is about 3.2 and 76.0 times higher. According to the results of first-principles density functional theory calculations, the suppression of metal-induced gap states, work function matching, and heterojunction control effect were primarily responsible for the increase in gas sensing performance. This study offered a novel method for building flexible gas sensors using gas sensing materials and conductive electrodes based on MXene on paper. MXene composites' high surface-to-volume ratio promotes effective gas adsorption and interaction, which improved sensor performance [629]. The type

of interaction between NH_3 molecules adsorbed on MXene layers has been studied by Banu et al.[630]. Density functional theory was used to evaluate the NH_3 adsorption energies on the surface of MXenes (M_2C, M = Cr and Fe) and related oxygen-functionalized forms (O-MXenes or M_2CO_2). The on-top sites were initiated for NH_3 adsorption on M_2C and M_2CO_2, according to DFT-D_4 simulations. The E_{ad} for the Cr_2CO_2 reaction was −0.29 eV less than that of Cr_2C. Fe_2C and its O-terminated MXene likewise exhibited this trend. This implied that the molecule would adsorb more forcefully on Cr2C than on its surface, which is O-terminated. According to Bader charge analysis, the electron density distribution between the negatively charged N of NH_3 and the positively charged Cr/Fe surface would be crucial to the adsorption process regarding the induced net charges on M_2C MXenes. Additionally, DOS simulations showed that MXenes' magnetic properties and electrical conducting behavior made them appropriate for gas sensor applications.

MXenes composites also show great promise in biosensors, where their exceptional biocompatibility and ability to be customized for detecting certain biomolecules are valuable features as shown in Fig. 21 [631]. MXene surfaces can be functionalized with biomolecules or nanoparticles to create biosensors for uses in food safety, environmental monitoring, and disease diagnosis [632]. MXenes composites, which offer quick reaction times, high sensitivity, and low detection limits for a range of biomarkers, have demonstrated tremendous promise in electrochemical biosensors [633].

Additionally, the use of MXenes composites in environmental sensing is being investigated; in particular, their potential for identifying pollutants [634], heavy metals [635], and other contaminants in soil [636] and water [637] is being investigated. Sensors with increased affinity for certain target analytes may be created by altering the surface chemistry of MXene composites, allowing for precise and dependable detection even at trace quantities. These sensors have a great deal of potential for monitoring the environment and helping with cleanup projects, which will support resource conservation and sustainability. Hilal et al. [638] aimed to improve the electrical characteristics, environmental stability, and gas-sensing capability of $Ti_3C_2T_X$ MXene flakes by precisely controlling their thickness and termination. A hybrid approach combining immiscible solutions, high-pressure processing, and stirring was used to produce MXene flake thicknesses inside the MXene layer on the Si-wafer that are less than 100 nm. Defunctionalizing MXene at 650 °C while under vacuum and H_2 gas in a chemical vapour deposition (CVD) furnace is the first step towards achieving functionalization control. Iodine and bromine vaporisation from a bubbler connected to the CVD is then used to refunctionalize the material. Significantly, the addition of iodine significantly changed MXene due to its bigger atomic size, decreased electronegativity, decreased shielding effect, and decreased hydrophilicity (contact angle: 99°). It enhances the film conductivity (749 S m^{-1}), surface area (36.2 cm^2 g^{-1}), and oxidation stability in aqueous/ambient conditions (21 days/80 days). Furthermore, it greatly improved the gas-sensing capability in terms of response times (90/100 s), sensitivity (0.1119 Ω ppm^{-1}), and responsiveness (0.2% and 23% to 50 ppb and 200 ppm NO_2). I-MXene's selectivity towards NO_2 was improved by the metallic properties of MXene and the reduced shielding effect of the –I-terminals. This strategy opens the door for the creation of stable, highly effective gas-sensing two-dimensional materials with bright future research opportunities. Moreover, Majhi et al.[639] suggested using V_2CT_x MXene-derived, urchin-like V_2O_5 hybrid compounds (V_2C/V_2O_5 MXene) to create a chemiresistive gas sensor for room temperature gas sensing applications. When used as the sensing material for acetone identification at room temperature, the as-prepared sensor demonstrated excellent performance. In addition, the V_2C/V_2O_5 MXene-based sensor responded to 15 ppm acetone more strongly (S% = 11.9%) than did the pristine multilayer V_2CT_x MXenes (S% = 4.6%). The composite sensor also showed outstanding long-term stability, short response-recovery time, good repeatability with little amplitude variation, great selectivity among various interfering gases, and a low detection level at ppb levels (250 ppb) at ambient temperature. The potential for H-bond formation in multilayer V_2C MXenes, the synergistic impact of the recently produced composite of urchin-like V_2C/V_2O_5 MXene sensor, and strong charge carrier transport at the interface of V_2O_5 and V_2C MXene are all responsible for these increased sensing capabilities. Therefore, the unique combination of electrical, mechanical, and chemical properties exhibited by MXenes composites makes them highly attractive for sensor applications across diverse fields. Continued research and development in this area are expected to lead to the commercialization of MXene-based sensors for real-world applications, addressing critical challenges in healthcare, environmental protection, and safety monitoring.

Biomedical MXenes and related composites have been used in a variety of biomedical applications, including biosensing [642], bioimaging [24], therapeutic diagnostics [643], implants [644], and antibacterial medicines [645], due to their intriguing physicochemical features. MXenes, as unique nanomaterials, have sparked significant interest in biosensor development due to their exceptional structural qualities, good biocompatibility, and superior electrical properties [646]. The major performance characteristics of high-performance receptors are high selectivity, a low limit of detection (LOD), high sensitivity, a fast reaction time, and a wide linear range [647]. Of course, they should have a cheap manufacturing cost for commercial scale-up production.

MXene-based materials have prospective uses in biosensors and serve an important diagnostic function [648]. Imaging technology is critical for early cancer diagnosis [649], accurate tumor location [650] and staging [651], cancer therapy guidance [652], and cancer recurrence detection [653]. MXene nanosheets have outstanding physicochemical qualities, making them ideal for diagnostic imaging. They may be used with a variety of imaging modalities, including X-ray computed tomography (CT) [595], magnetic resonance imaging (MRI) [654], photoacoustic imaging [655], and fluorescence imaging [656]. Imaging approaches based on innovative MXene-based reagents can help overcome some of the frequent issues and limitations associated with present reagents. For example, compared to traditional imaging agents, 2D MXene-based reagents exhibit effects of quantum size for photoluminescence (PL) cell imaging, which can improve intrinsic photothermal characteristics for PA imaging and elemental contrast for X-ray CT imaging.

Due to their superior physicochemical features and unique structural characteristics, MXenes have been used in a variety of biomedical applications. In addition to biosensor and diagnostic applications, different kinds of MXenes and their composites have been created for therapeutic applications [657], including drug delivery systems [22], conventional photothermal therapy (PTT) [658], photodynamic therapy (PDT) [659], immunotherapy [660], and synergistic combinations of multiple technologies for treatment.

Because of their unique structure, MXenes may be used to create gene/drug delivery systems that allow for more focused drug delivery, reduced drug toxicities [661], and improved drug pharmacokinetics [22]. MXene materials' nanoscale size allows for effective intravenous administration to the sick location and accumulation during therapy. Furthermore, the two-dimensional planar topology gives MXenes their typical enormous specific surface area, giving numerous places for medicinal compounds to attach on the surface of the laminar structure. Cancer is currently a serious illness that endangers human health and kills millions of people throughout the world each year. MXene-based materials can efficiently assault cancer cells by controlled drug release and enhanced cellular absorption of the payload [662].

Cancer, one of the deadliest illnesses to human health, is treated primarily with surgery, chemotherapy, and radiation therapy [663]. However, surgery alone seldom removes all malignant tissues, while radiation kills cancer cells while being more damaging to normal tissues and cells. In recent years, new photothermal therapy (PTT) has received a lot of attention for its outstanding efficacy in cancer treatment [658]. A photothermal nanomaterial (PAT) is given to the cancer spot without causing damage to the healthy tissue

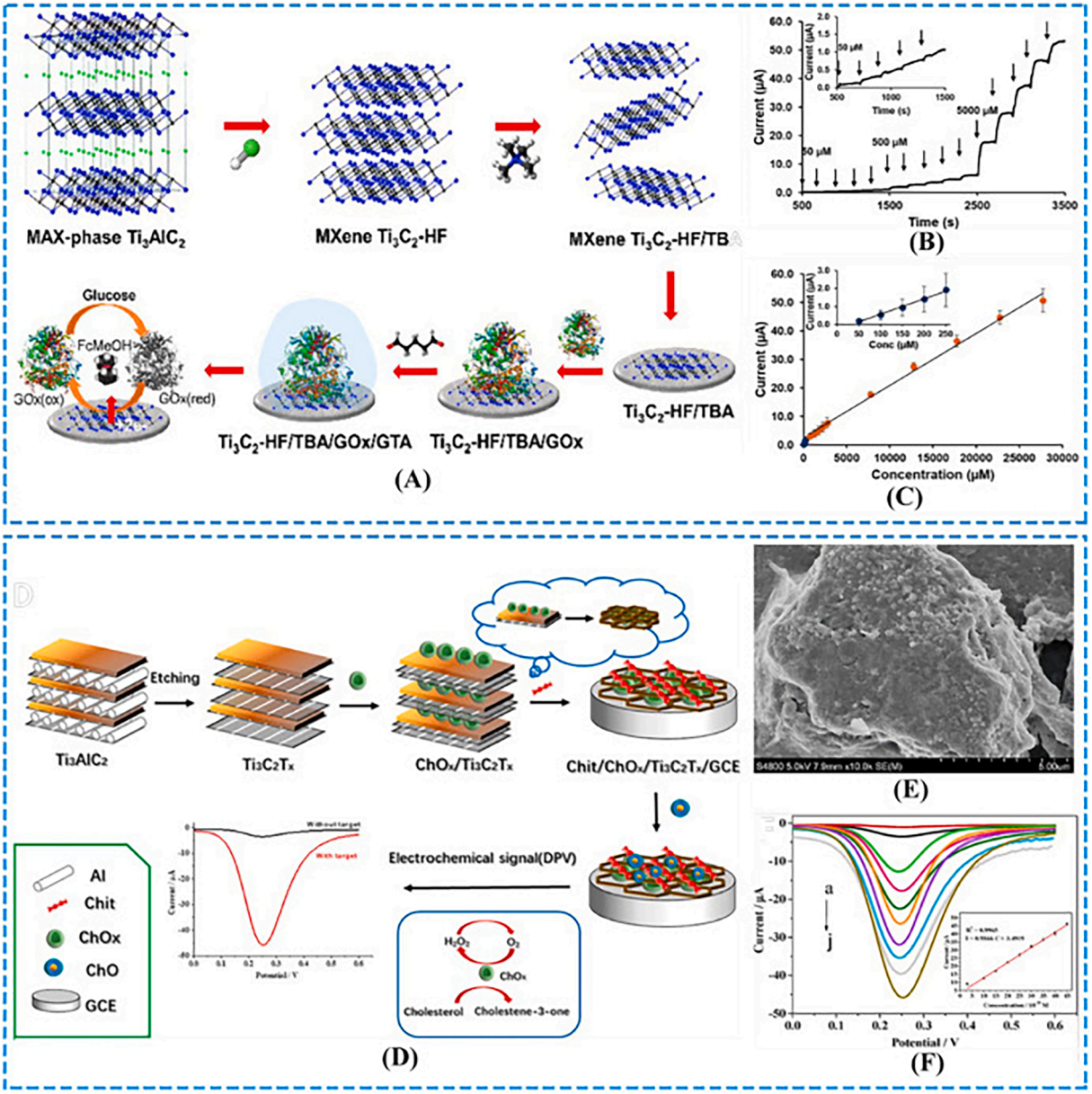

Fig. 25. (A) Flow diagram showing how MXene-based glucose sensors are made. Ti_3C_2-HF/TBA-based glucose sensor (B) chronoamperometry and (C) calibration plot. Reprinted from the permission of Ref. [640]. (D) The $Ti_3C_2T_x$/GCE/Chit/ChOx preparation procedure. (E) MXene and MXene/Chit/ChOx/film SEM images. (F) Comparative pulse voltammetry of the $Ti_3C_2T_x$/GCE/ChOx/Chit biosensor. Reprinted from the permission of Ref. [641].

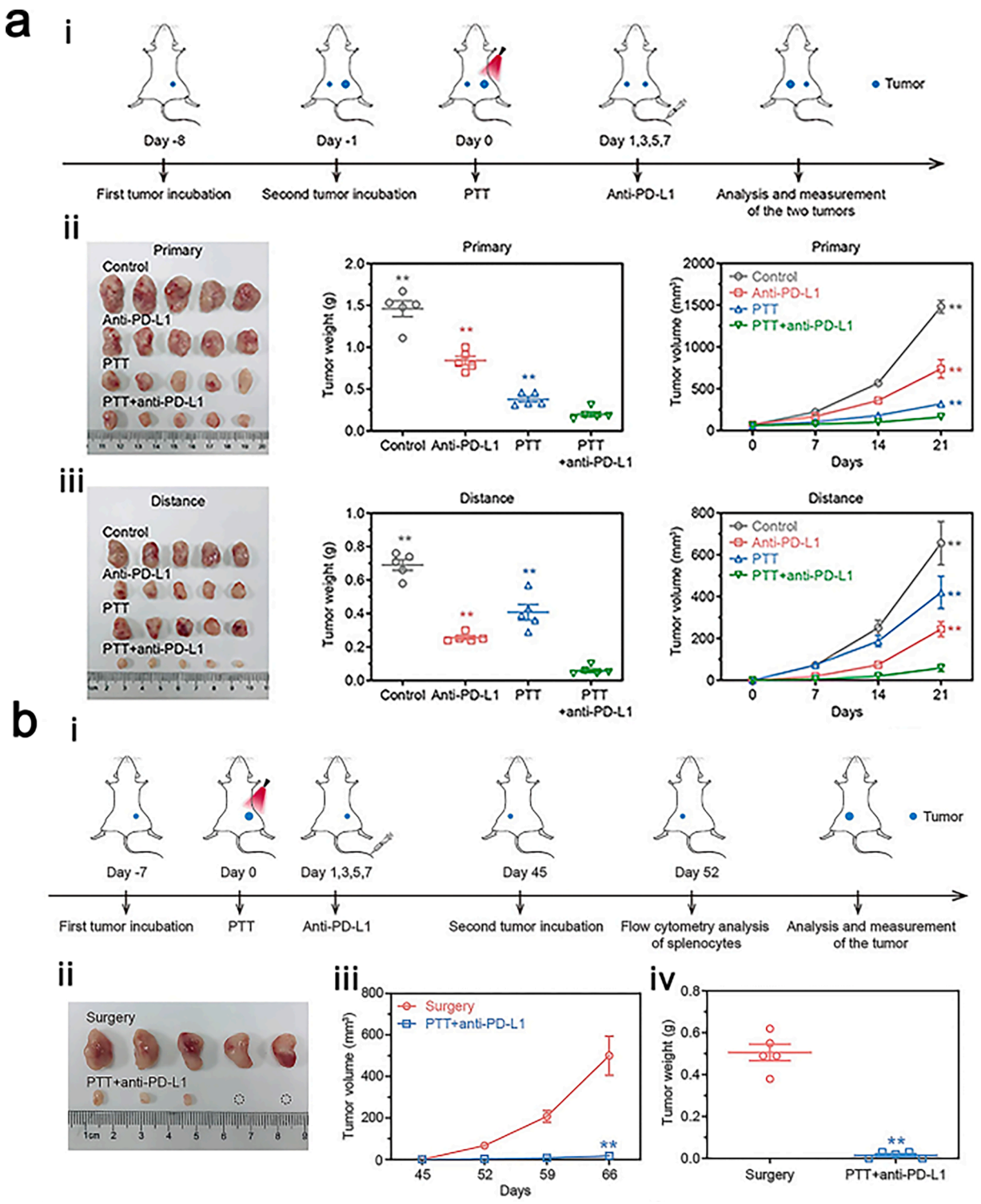

Fig. 26. (a) Effects of anti-PD-L1 immunotherapy combined with BG@NbSiR-scaffold-based PTT against tumours. (i) Schematic of anti-PD-L1 combination treatment including BG@NbSiR-scaffold-based PTT to inhibit tumor growth at the remote orthotopic location. Following the sacrifice of the mice, tumor pictures, weight, and volume diagrams of (ii) the main and (iii) the distant tumours were obtained. (b) Long-term protective effectiveness against tumor recurrence using anti-PD-L1 immunotherapy in conjunction with BG@NbSiR scaffold-based PTT. (i) Schematic representation of anti-PD-L1 combo treatment plus BG@NbSiR-scaffold-based PTT to prevent tumor recurrence (n = 5). Diagrams showing the tumor's (ii) images, (iii) volume, and (iv) weight following the sacrifice of the animals. Reproduced from Ref. [676].

surrounding it [664]. Because tumor cells have poor heat resistance, the photothermal agent can convert near-infrared light into heat energy at the tumor site, resulting in a series of hazards such as protein denaturation, cell lysis, and organelle damage, ultimately killing cancer cells [665]. The ideal photothermal agent has good selectivity for the target tissue, a wide absorption cross section for optical wavelengths, minimal toxicity, and simple functionalization. MXenes, such as $Ti_3C_2T_x$ [658,666], Nb_2CT_x [667], and $Ta_4C_3T_x$ [90] (Fig. 25), have emerged as new PTT reagents (Fig. 26) for deep tissues due to their high photothermal conversion efficiency and strong absorption in the near-infrared wavelength range, and their use in vivo has been demonstrated. Zong et al. [668] has demonstrated the surface engineering and functionalization of 2D Ti_3C_2 MXene nanosheets using GdW10-based polyoxometalates (POMs). The GdW10@Ti_3C_2 composite nanosheets offer hyperthermal therapy with MR and CT imaging guidance for tumor cells or xenografts. During the monitoring period, the tumor was successfully eliminated and did not return. GdW10 nanoclusters on Ti_3C_2 nanosheets act as a contrast agent for CT and MR imaging, offering potential for tumor hyperthermia nanotherapy diagnostics and monitoring. GdW10@Ti_3C_2 composite nanosheets were shown to be highly biocompatible in vivo, making them suitable for medicinal applications (Fig. 27).

Photodynamic therapy (PDT) is a different highly intriguing light therapy for tumor treatment. Photosensitizers (PSs) play a significant role in determining the efficacy of PDT [669]. PS can be administered systemically or locally and allowed to accumulate at the tumor site. Then, in the presence of appropriate light wavelengths, photosensitizing molecules are activated to generate lethal reactive oxygen species (ROSs) in the existence of endogenous molecular oxygen species, particularly singlet-state oxygen, resulting in cancer cell death [670]. MXene nanosheets are good PDT photosensitizers due to their distinct electrical structure and optoelectronic characteristics. Photosensitizer medicines have low toxicity until they are triggered by external light, hence PDT can considerably minimize side effects and enhance target specificity compared to traditional cancer treatment methods such as radiation and chemotherapy [671].

Immunotherapy, a revolutionary approach of treating tumors, develops a long-lasting anticancer response by strengthening or stimulating the patient's own immune system, allowing for specific tumor treatment, targeted cell death, and prevention of tumor recurrence and metastasis [672]. MXene-based materials are progressively gaining traction in the realm of immunotherapy due to their superior features, such as high specific surface area, biocompatibility, and tumor-targeting accumulation. The benefits of MXene-based materials in the realm of immunotherapy have steadily emerged. For instance, Yan et al.[673], for the first time, reported the use of $Ti_3C_2T_x$ MXene nanosheets as a immunotherapeutic strategy to prevent allograft vasculopathy, which interact with human endothelial cells and reduce the expression of genes associated with alloantigen presentation, thus decreasing the activation of allogeneic lymphocytes. RNA-Seq analysis of lymphocytes revealed that MXene treatment suppressed the transcription of genes involved in transplant-induced T-cell activation, cell-mediated rejection, and allograft vasculopathy. In an in vivo rat model, MXene treatment minimized the lymphocyte infiltration into transplanted aortic allografts and preserved the structural integrity of medial smooth muscle cells. Conclusions These results confirm that $Ti_3C_2T_x$ MXene is a promising active candidate drug for treatment against allograft

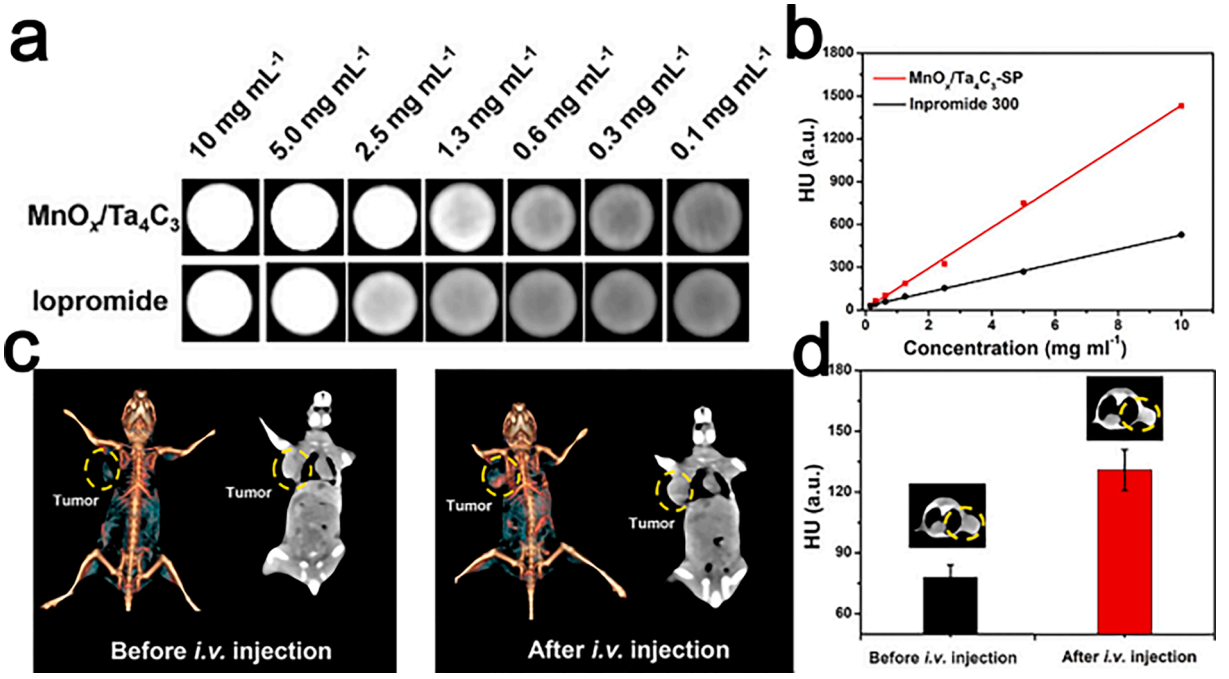

Fig. 27. $MnO_x/Ta_4C_3T_x$-SP composite nanosheet solution in (a) vitro CT images and (b) HU values of iopromide solution with different concentrations (concentration of Ta, I). (c) 3D reconstructed CT (left) and contrast (right) images of mice taken before and after a 2-h intravenous injection of MnOx/$Ta_4C_3T_x$-SP composite nanosheets (20 mg·kg.$^{-1}$, 100 μL). (d) Prior to and following intravenous administration of MnOx/$Ta_4C_3T_x$-SP composite nanosheets, CT comparison of the tumor tissues in vivo. Reprinted with the permission of Ref. [675].

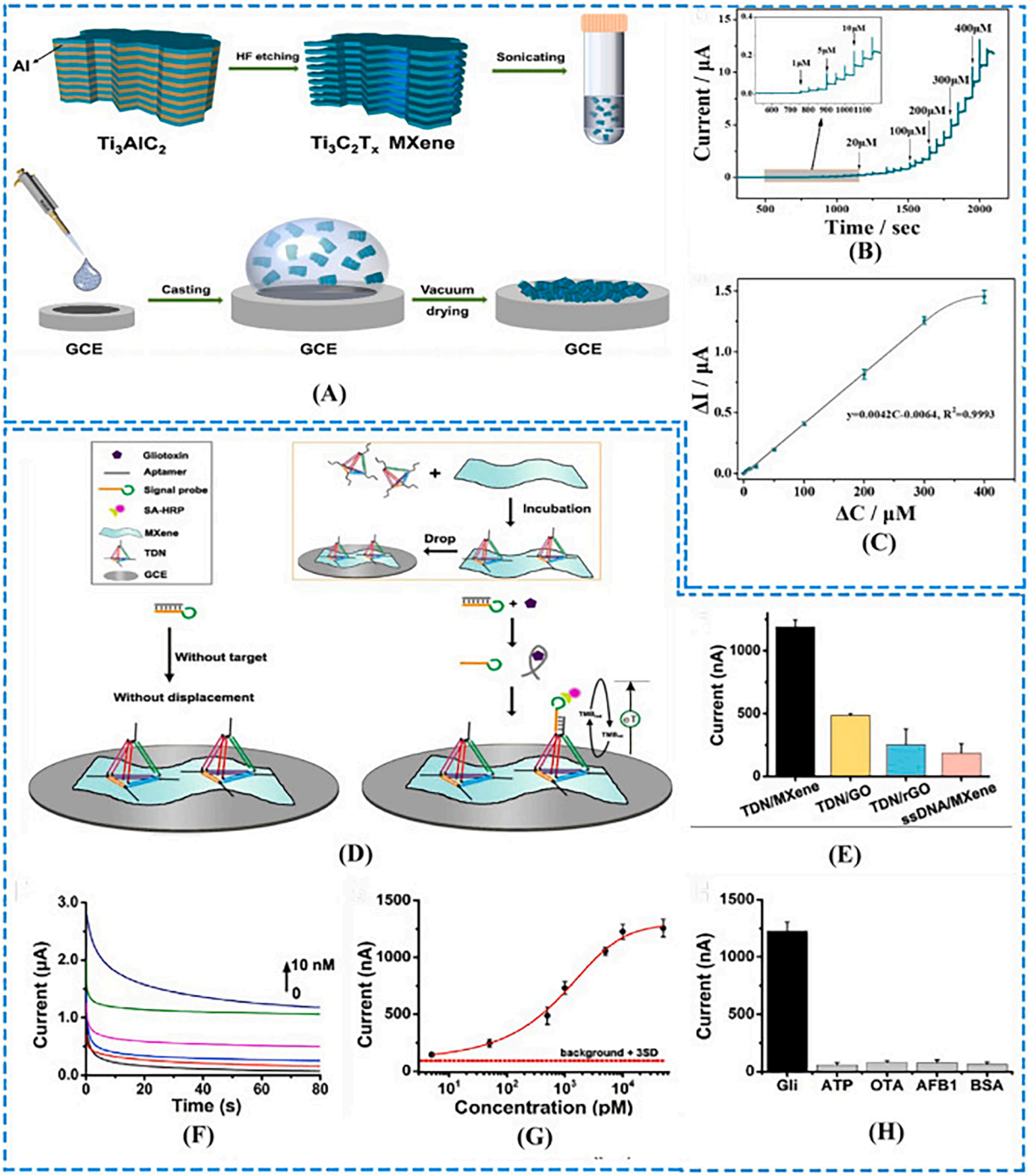

Fig. 28. (A) Schematic of electrode modification and $Ti_3C_2T_x$ synthesis. (B) Current response at varying H_2S concentrations and (C) Calibration curve. Reprinted from the permission of Ref. [682]. (D) The tetrahedral DNA nanostructures (TDN)/MXene gliotoxin electrochemical sensor schematic diagram. (E) TDN/MXene sensor comparison with alternative sensor types. (F) Amperometric curves showing the concentrations at which gliotoxin can be found. (G) Current vs gliotoxin concentration plot. (H) The gliotoxin sensor's selectivity. Reprinted from the permission of Ref. [683].

vasculopathy and other inflammation-related diseases. However, it is typically difficult to get adequate outcomes by immunotherapy alone, thus a combination of immunotherapy with standard non-immunotherapy treatment methods (e.g., chemotherapy, photothermal therapy, and photodynamic therapy) is frequently used [674]. In 2017, Liu et al. [274] created a therapeutic nanoplatform for collaborative PTT/PDT/chemotherapy based on the benefits of $Ti_3C_2T_x$ nanosheets, including tumor-specific accumulation,

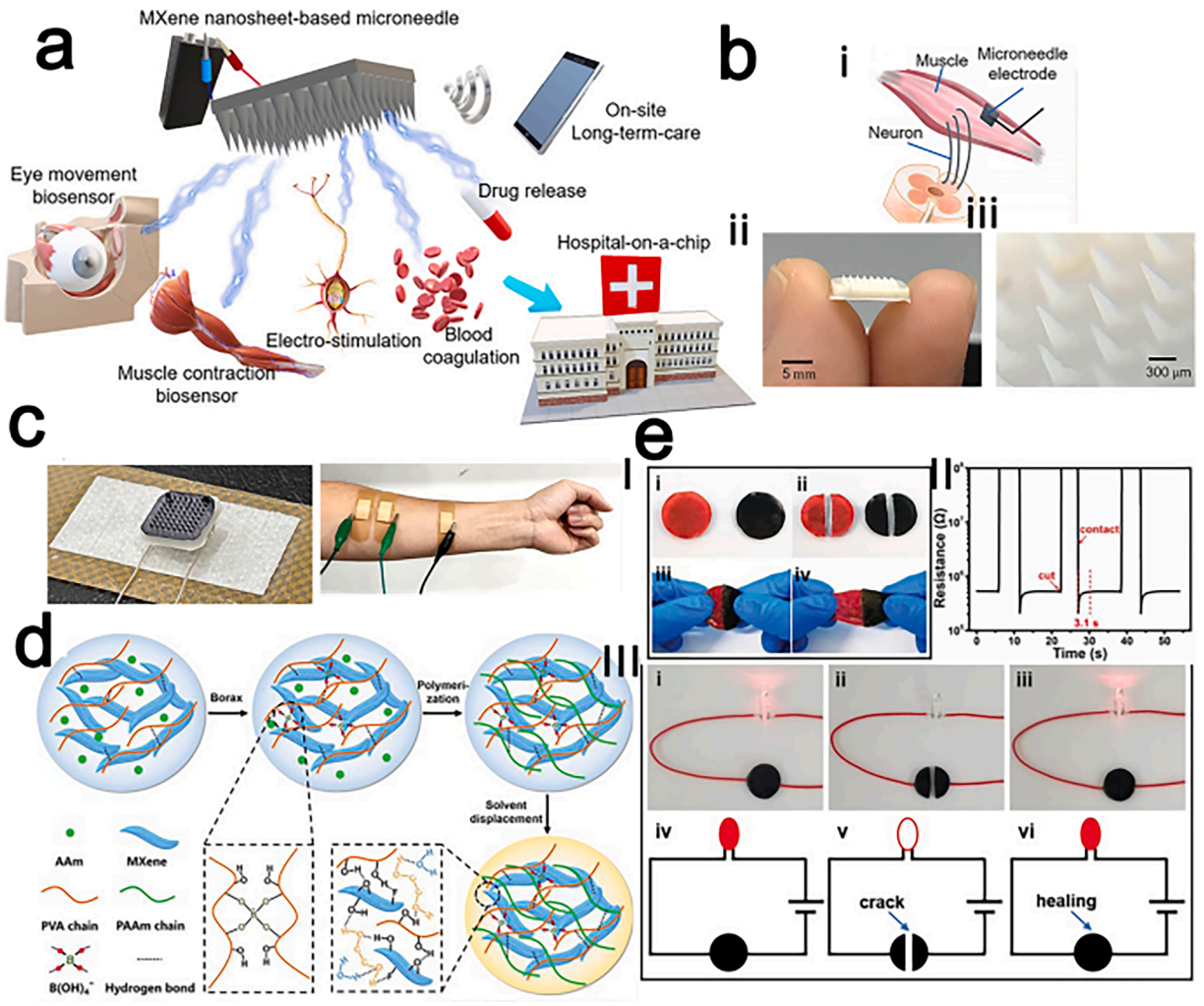

Fig. 29. (a) Diagrammatic representation of the "hospital-on-a-chip" idea. (b) (i) Diagrammatic depiction of the transfer of bioelectric signals from the electrode to the neuron or the other way around. (ii) A picture of a microneedle made of PLA. (iii) A picture showing the tiny needles up close. (c) Images of electrodes for wearing microneedles. Excerpted with permission from Ref. [677]. (d) Schematic depicting the creation of an MXene nanocomposite organohydrogel (MNOH) that is conductive, anti-freezing, and self-healing. (e) The self-healing experiment. (I) The self-healing properties of the rhodamine-dyed MNOH (red) and the original MNOH (black). (II) Real-time resistance measurements to track the healable process' temporal progression for the conductive MNOH. (III) A circuit with a red LED indication and MNOH connected in series: the circuit's (i) original, (ii) fully bifurcated, (iii) self-healing, and (iv–vi) matching schematic designs. Reproduced from Ref. [678].

stimulated-responsive drug dissolution, and excellent biocompatibility, which was shown to have excellent tumor ablation effects in ex vivo experiments and robotic designs (Fig. 28 and Fig. 29).

7.2. Energy Storage

Energy storage Ti_2C, Nb_2C, V_2C, and Sc_2C are among the MXenes with low formula weights that have been discovered to have the most promising theoretical gravimetric capacity, which measures the amount of charge that can be stored per gramme of material [570]. It follows that M_2X electrodes should have greater gravimetric capabilities than M_3X_2 and M_4X_3 electrodes. It is plausible to believe that ions only enter between the MXene sheets since the bonds between M and X are too strong to break readily. Every available experimental data set supports this. Ti_2C and Ti_3C_2, for instance, have the same surface chemistry but differ in that the latter contains one inactive TiC layer. As a result, Ti_2C should have approximately 50% more gravimetric capacitance than Ti_3C_2. Experiments supported this: Ti_2CT_x's gravimetric capacity for Li^+ absorption is approximately 1.5 times more than that of $Ti_3C_2T_x$, which was made in the same manner [679]. It is essential to remember that the weight formula does not fully specify the capacity. For instance, V_2CT_x has the greatest Li^+ capacity of all MXenes evaluated at comparable cycle rates (280 $mAhg^{-1}$ at 1 ℃ and 125 mAh g^{-1} at 10 C) [680]. For example, Zhang et al. [681] presented the fabrication of a few-layer V_2CT_x/carbon nanotubes (CNTs) composite using tetramethylammonium hydroxide (TMAOH) delamination and electrostatic flocculation of NH_4^+ ions. Few-layer V_2CT_x nanosheets with

crimped structures can successfully prevent restacking while ensuring maximum utilization of active surface area. Furthermore, the insertion of CNTs resulted in a developed electrical conductivity network, and CNTs provided structural support for the sheets, further limiting their restacking and assuring their stable structure during the charge and discharge process even at high rates. This resulted in the few-layer V_2CT_x/CNT having a high specific capacitance of 621 mAh/g after 100 cycles at 0.1 A/g and an amazing rate

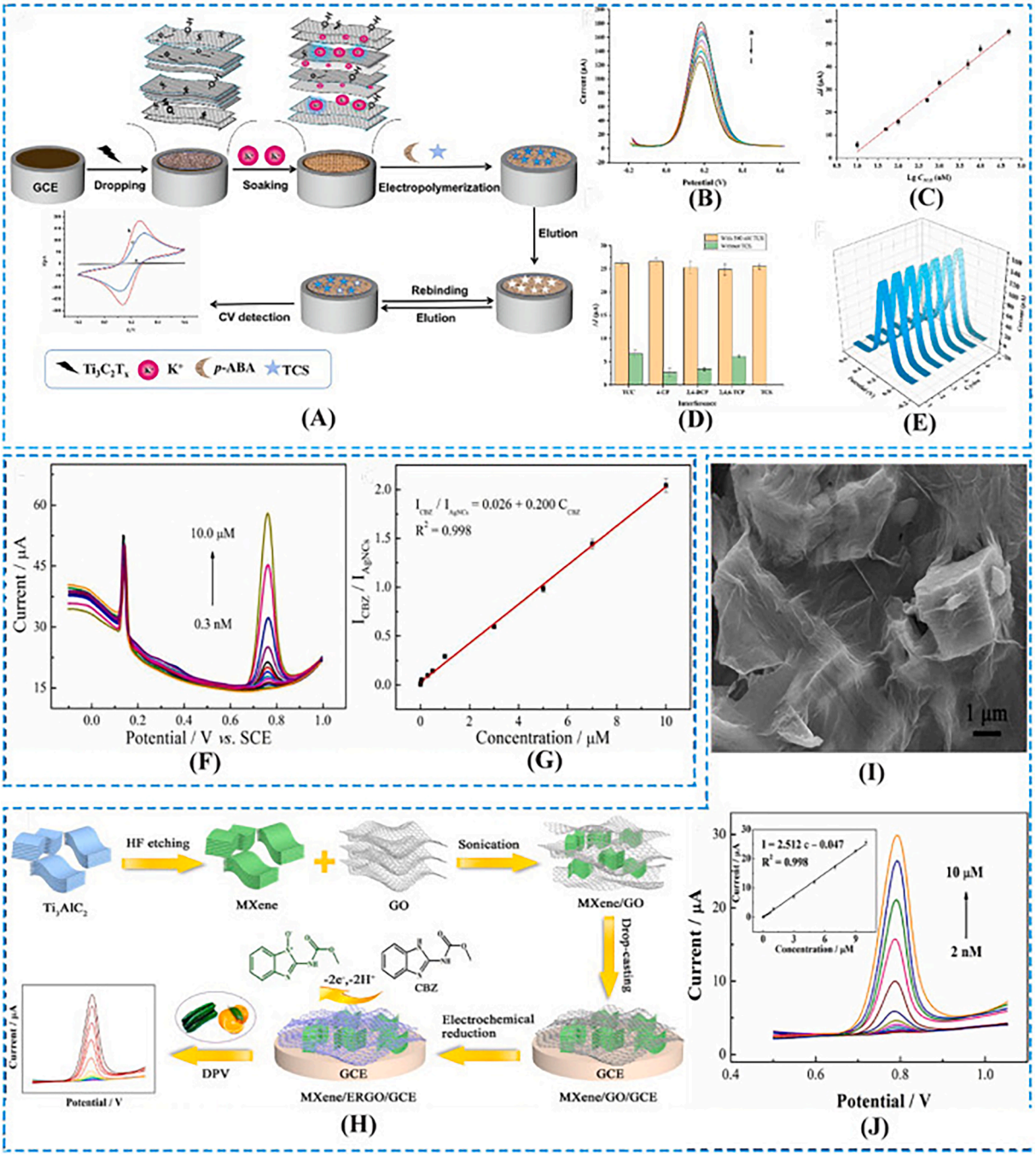

Fig. 30. (A) Schematic preparation for MIP/K^+-$Ti_3C_2T_x$/GCE. The DPV response curves (B), selectivity (D), stability (E), and standard curve of TCS discovered (C) of Molecular imprinting techniques (MIT)-based electrochemical sensors (MIECS) Reprinted from the permission of Ref. [682]. (F) MXene@AgNCs/NH_2-MWCNTs/GCE differential pulse voltammetry curves. (G) ICBZ/IAgNCs and carbendazim (CBZ) concentration have a linear relationship. Reprinted from the permission of Ref. [683]. (H) MXene/electrochemically reduced graphene oxide (ERGO)/ glass carbon electrode (GCE) sensor preparation plan. (I) The MXene/ERGO SEM pictures. (J) The MXene/ERGO/GCE sensor's differential pulse voltammetry plots. Reprinted from the permission of Ref. [684].

performance of 290 mAh/g at 5 A/g. Moreover, the few-layer V_2CT_x/CNT electrode demonstrated exceptional cycling stability, with 82.1% capacitance retention after 2000 cycles at 5 A/g. This indicates that it has tremendous promise for lithium-ion battery applications.

Furthermore, even though Nb atoms are heavier than Ti, Nb_2CT_x has a greater gravimetric capacity (180 mAh g^{-1} compared to 110 mAh g^{-1} of Ti_2CT_x at 1C) than Ti_2CT_x at the same cycle rate [18]. This makes sense in part because of how complicated ion storage is. Theoretical analysis has shown that one specific element that might impact performance is the surface terminations [18]. For instance, oxygen terminations are thought to be the most advantageous, whereas fluorines and hydroxyls reduce capacity and obstruct Li-ion transport [256]. The main characteristics of ion intercalation from organic electrolytes into MXenes have been demonstrated theoretically and verified empirically. For instance, strong technique is devised by Zhao et al. [256] for controlling the functional groups of Nb_2CT_x MXene. The capacity of pristine Nb_2CT_x. MXene was considerably improved by Li^+ intercalation and surface modification. The treated Nb_2CT_x has a specific capacity of up to 448 mAh g^{-1} at 0.05 A g^{-1}, with a high reversible capacity retention rate of 75% after 2000 cycles at a current density of 2 A g^{-1}. These values outperformed the majority of documented pure MXenes (including the most researched $Ti_3C_2T_x$ (Fig. 30)) and carbon-based materials. It revealed that this technique has a significant impact on the electrochemical performance of pure MXene, and the results strengthened MXenes' potential in the use of lithium-ion batteries.

Using in-situ X-ray absorption spectroscopy (XAS) to study the mechanism of Li-ion charge storage in $Ti_3C_2T_x$, it was discovered that during charge and discharge, the transition metal (that is, Ti) oxide state changes continuously up to 0.5 V vs. Li/Li^+ [685]. It's interesting to note that further potential reduction does not result in a shift in oxidation state. Instead, lithium atoms can reversibly create an extra layer because of the 2D structure and conductivity of MXenes. This doubles the capacity boost, and it is anticipated that other MXenes will also be able to use this process. Hybridising porous MXene flakes and optimizing the electrode design allowed for a further rise in capacity. MXenes may hold different-sized ions in between $M_{n+1}X_nT_x$ 2D layers. This qualifies them for use with non-lithium-ion batteries (NLiBs), for which there is currently a restricted range of electrode materials [686]. The capacity would double as a result of the projected creation of an extra metal layer for Na^+ and other ions [687]. Furthermore, various MXenes can offer a variety of working potentials due to their chemical and structural diversity as and their surface chemistry tunability. As a result, some of them are appropriate as anodes and others as cathodes [688].

Theoretical investigations demonstrate low diffusion barriers for Li+ [655,656] and other ions [657,658] in MXenes. This is consistent with the experimentally found very high-rate performance for several MXenes. Typically, MXene-based electrodes have capacities between 50 and 200 mAh g^{-1} at speeds higher than 10C or a 6-minute charging period. As a result, unlike supercapacitors, the MXenes in metal-ion batteries do not exhibit a plateau zone in the galvanostatic charge-discharge patterns. Composite electrodes based on mXene show especially great promise for high-rate, high-performance batteries. For instance, Li et al. [689] presented a three-dimensional (3D) conducting nitrogen-doped carbon foam endorsed electrostatic self-assembled MXene-ammonium polyphosphate (NCF-MXene-APP) layer that serves as a heat-resistant, thermally insulated, flame-retardant, and freestanding host for Li-S batteries using a simple and cost-effective synthesis method. The use of NCF-MXene-APP hosted that firmly anchor polysulfides results in outstanding electrochemical properties for Li-S batteries, including a high beginning discharge capacity of 1191.6 mA h g^{-1}, excellent rate capacity of 755.0 mA h g^{-1} at 1 C, and long-term stability during cycling with an extremely low-capacity decay rate of 0.12% per cycle at 2 C. More crucially, these batteries can function successfully in high temperature or flame attack settings. As a result, this work offers important insights into the design of safe, high-performance Li-S batteries. Moreover, the strong interaction of polysulfide species with MXene functional groups led to significantly increased cyclability and stability when Ti_2CT_x or $Ti_3C_2T_x$ were employed as conductive sulfur hosts in Li–S batteries. Comparably, encasing Sn nanoparticles in layers of $Ti_3C_2T_x$ leads to consistent performance (Fig. 26) and an improved volumetric capacity that approaches 2000 mAh g^{-1} [690]. Applying a hybridization strategy to co-integration with MXenes might significantly enhance the cycle life and rate capability of other high-capacity electrode materials that undergo a notable volume change during intercalation. According to this method, MXenes offer a conductive matrix that permits particle expansion and contraction while preserving electrical and structural integrity. Also, Lithium-sulfur (Lisingle bond) batteries have gained popularity because of their inexpensive cost and high energy density. However, the sluggish electrochemical response and shuttle effect limit the practical viability of Lisingle bondS batteries. NMM (NiS_2-MoS_2@MXene) heterostructures with many defects were effectively constructed by Zhu et al. [691] to give additional active sites for polysulfide catalysis and adsorption. The battery's electrochemical performance was excellent due to 20 wt% (NMM-20) conductive agent MXene being employed. After 800 cycles at 0.5C, the NMM-20 battery demonstrated good rate performance and a reversible capacity of 767.3 mAh g^{-1}. This study broadens the scope of heterogeneous material preparation and sheds light on the ideal quantities of conductive agents to add to heterostructures.

7.3. Catalysis

Structural features of transition metal carbides (TMCs) in the context of catalysis reveal a drawback in their limited specific surface area (SSA), as exemplified by TiC with an SSA of 4.7 m^2 g^{-1} [692]. However, $Ti_3C_2T_x$, part of the MXene class, exhibits an impressive SSA of 40.5 m^2 g^{-1} [693]. Despite their potential, both MXenes and early TMC-based catalysts face challenges due to their high oxophilicity, promoting oxide formation. Nonetheless, the surface functionalization of MXenes with oxygen proves less critical for catalytic processes and can even enhance their catalytic activity [20]. MXenes are derived from layered ternary carbide precursors known as MAX phases, combining an early transition metal, an element from groups 13 or 14, and carbon or nitrogen [694].

The focus then shifts to the promise of MXenes in catalysis, particularly their potential in CO_2 activation [695]. Experimental evidence indicates that Ti_3C_2 [696] and V_2C [697] MXenes are promising sorbent materials for CO_2 capture [698,699]. A comparison of CO_2 adsorption energy between MXenes and three-dimensional TMCs underscores the advantageous reactivity of MXenes. The text emphasizes the geometric equivalence of the highly reactive but challenging-to-synthesize TMC(111)-M surfaces and easily generated

MXene(0001) surfaces [700,701]. This equivalence highlights the potential of MXenes in catalysis, facilitated by their ease of formation and sizeable reactive surface area. The Perspective concludes by emphasizing the need for joint experimental−theoretical studies to understand further and develop the application of MXenes in chemical engineering, energy, and environmental science.

A balance between selectivity towards the desired reaction product, catalytic activity, and stability under reaction conditions must be struck in the design of novel catalysts. Suppose a material meets these requirements and is composed of elements that are readily available on Earth. In that case, it can serve as a substitute for the pricey noble metal catalysts used in industrial processes. Several of these requirements are met by MXenes, making them attractive options for catalytic uses. The state of the art for MXenes as catalysts in traditional heterogeneous catalysis [702] and electrocatalysis [703] will be evaluated, and a summary of current ground-breaking research from computational or experimental perspectives will be included. However, given that this is a young topic, we acknowledge that our collection of citations can hardly be considered exhaustive. For example, Yan et al. [704] mentioned an in-depth analysis of the elaboration and unstacking of Pt or Pd-loaded $Ti_3C_2T_x$ MXenes for gas phase catalysis experiments. Specifically, the effect of the MXene production technique (HF vs. LiF-HCl etchants) on surface structure/composition and metal dispersion/oxidation state was explained, and he reported on the catalytic hydrogenation performance of low-loaded Pt/MXene single-atom catalysts, highlighting their activity, selectivity, and resistance to sintering. They exhibited good selectivity for 2-butene without butane production in butadiene hydrogenation, a model reaction of importance in the petrochemical sector. Also, according to Meng et al.[705] single-atom catalysts (SACs) offers a chance to better understand the catalytic mechanism of complicated processes in heterogeneous catalysis. The low-temperature water-gas shift (WGS) reaction is a key industrial method for producing high purity hydrogen. In his paper, Meng et al. [705] used density functional theory (DFT) to investigate the catalytic activity of Pt1@$Ti_3C_2T_2$ (T = O, S) SACs, in which one subsurface Ti atom with three T vacancies in the functionalized $Ti_3C_2T_2$ (T = O, S) MXene is replaced by one Pt atom for the low-temperature WGS process. The results demonstrated that Pt1@ $Ti_3C_2T_2$ provides an ideal platform for the water–gas shift (WGS) reaction because of the bowl-shaped vacancy formed by the Pt1 single atom and three T defects around it. Pt1@$Ti_3C_2S_2$ SAC, in particular, offered a superior catalytic performance for the WGS process due to the S atom's lower electronegativity than the O atom, which greatly lowers the energy barrier of H* migration in the WGS reaction, which is frequently the rate-determining step. In the most favorable redox mechanism of the WGS reaction on Pt1@ $Ti_3C_2S_2$, the rate-determining step is the dissociation of OH* into O* and H*, with an energy barrier as low as 1.12 eV. These findings show that Pt1@ $Ti_3C_2S_2$ has promise for the use of MXenes in low-temperature WGS processes.

In the context of several processes, including as CO oxidation, CO_2 activation and conversion, water-gas shift (WGS) [706], nitrogen fixation [707], direct dehydrogenation (DDH) [708], and hydrodeoxygenation (HDO) [709], MXenes' catalytic properties are essential. MXenes are studied via many methods in CO oxidation; theoretical studies show that single-atom catalysts (SACs) based on MXenes have the potential to be more effective than certain conventional catalysts in CO oxidation [710]. According to screening investigations, MXenes show stability and activity for CO oxidation when supporting different metal atoms, with Zn@$Mo_2CO_2-\delta$ emerging as a possible catalyst [711]. Moving to CO_2 activation and conversion, MXenes are explored as materials for carbon capture and storage (CCS). Computational studies predict MXenes as effective substrates for CO_2 adsorption, and experimental evidence supports this, with MXenes like $Ti_3C_2T_x$ showing high CO_2 uptake. The catalytic conversion of CO_2 into valuable chemicals is also explored, with MXenes serving as catalysts for the N-formylation reaction, demonstrating the potential for industrial applications. Water-gas shift (WGS) reaction, where MXenes, including functionalized Mo_2CT_x [712] and Pt@Nb_2CT_x [713] exhibit catalytic activity and stability is another approach of catalysis usage. MXenes are proposed as potential catalysts for high-temperature heterogeneous catalytic processes, showing promise for applications in WGS. Additionally, MXenes are considered in the context of nitrogen fixation, displaying outstanding capabilities for N_2 activation and providing a potentially efficient and practical route for ammonia synthesis [142]. For example, Liu et al.[714] presented a high-performance Ru@Ti_3C_2 MXene catalyst for ambient electrocatalytic

Table 9
Outline of HER performance of MXene hybrid composite structures.

Author, Ref. - Year	Catalyst	Electrolyte	Overpotential (mV)@10 mA cm^{-2}	Tafel slope (mV dec^{-1})	Scan rate (mV s^{-1})
Chen et al.,[718]-2022	Ru/Mo_2CT_x	0.5 M H_2SO_4	64	57	5
Luo et al., [719] -2021	$Ti_3C_2T_x$: Co	1 M KOH	103.6	103.3	10
Chen et al., [718] -2022	Co-MoS_2/V_2C@CC	1 M KOH	70.1	98.6	10
Wang et al., [720] -2023	CoBDC/MXene	1 M KOH	29	46	5
Fan et al., [713] - 2021	Pt/Nb_2CT_x-600	0.5 M H_2SO_4	5	34.6	—
Jiang et al., [721] - 2022	Ti_3CNCl_2@CoS_2	0.5 M H_2SO_4	175	89	—
Yan et al., [722] - 2023	Rh-Co-Ni LDH/$Ti_3C_2T_x$	1 M KOH	74.6	43.9	5
Shen et al., [723] - 2022	LDH (60%)/MXene-RGO	1 M KOH	326	100	—
Ma et al., [724] - 2022	MoS_2/Ti_3C_2@CNFs	0.5 M H_2SO_4	142	113	5
Ma et al., [725] - 2023	(MIL-100)/$Ti_3C_2T_x$	0.5 M H_2SO_4	107	61	—
Zhang et al., [726] - 2023	Co-NCNT/$Ti_3C_2T_x$	1 M KOH	190	78	5
Reghunath et al., [727] - 2023	$BiFeO_3$/Cr_2CT_x	1 M KOH	128	53.3	5
Ma et al., [728] - 2024	COF/$Ti_3C_2T_x$	0.5 M H_2SO_4	72	50	—
Hussain et al., [729] - 2023	WS_2@MXene/GO	0.5 M H_2SO_4	42	45	10
		1 M KOH	43	58	10
Yin et al., [730] - 2023	MXene@$CoSnO_3$	1 M KOH	45	51	5

nitrogen reduction nreaction. The Ru@MXene catalyst produced 2.3 μmol h^{-1} cm^{-2} of NH_3 in a 0.1 M KOH electrolyte. It also had a Faraday efficiency of 13.13% at -0.4 V (vs. RHE). Lastly, MXenes were evaluated in direct dehydrogenation (DDH) and hydrodeoxygenation reactions, crucial for gasoline and biofuel production. MXenes, such as $Ti_3C_2T_x$ and Pt@MXenes, showed high selectivity in DDH reactions, with promising results in light alkane dehydrogenation. MXenes also exhibit potential in HDO reactions, with $Ti_3C_2T_x$ nanosheets showing capability in converting biomass-model molecules.

Electrodes containing noble metals are a major component of electrocatalysis at the moment, but they are also quite costly and far less common in the Earth's crust than elements like Ti and C. The research of MXenes, including Ti, C, Mo, Sc, V, Nb, Zr, and Ta, results from the demand for new electrocatalysts based on plentiful elements as shown in Table 8 [715]. These materials can potentially help with the vital energy and environmental problems of the twenty-first century. In simulating MXene electrocatalysts, DFT is commonly employed, often using the computational hydrogen electrode model. However, challenges include the neglect of adsorbate solvation in computational studies, potential gas-phase errors, and the importance of accurately simulating MXene terminations under electrochemical conditions. MXenes have shown potential in various electrochemical reactions, including the Hydrogen Evolution Reaction (HER), where they offer cost-effective alternatives to Pt [716]. The simulations focus on hydrogen adsorption-free energy, and MXenes, particularly Ti_2C and Mo-based MXenes, have demonstrated HER activity. Additionally, MXenes can be used as support for other catalyst materials, such as single-atom Pt catalysts. For the Carbon Dioxide Reduction Reaction (CO_2RR), MXenes have been computationally analyzed, and Ti_2CO_2 and W_2CO_2 were identified as active catalysts for CO_2RR with low limiting potentials to CH_4. The Oxygen Reduction Reaction (ORR) and Oxygen Evolution Reaction (OER) are also explored, with MXenes acting as conductive supports for other active materials [717]. MXenes have potential in the Nitrogen Reduction Reaction (N_2RR), with promising results for $Ti_3C_2T_x$ and W_2CH_2 as electrocatalysts. However, challenges remain in achieving high efficiency and stability under N_2RR conditions. For more information, Table 9 shows a comprehensive outline on HER performance of MXene hybrid composite structures.

In summary, the text underscores MXenes' emerging role as catalysts in various heterogeneous catalytic processes, showcasing their unique properties and potential applications across different chemical reactions. While the $Ti_3C_2T_x$ MXene is the most studied member, the overall findings suggest that MXenes could pave the way for innovative catalysts and supports with unprecedented performance, inspiring further experimental exploration. MXenes hold promise as electrocatalysts for various reactions, offering alternatives to noble-metal-containing electrodes. However, challenges in simulation methods and achieving optimal catalytic performance still need to be addressed for widespread practical applications.

7.4. Purification and Environmental Remediation

The MXene family has sparked significant attention for various environmental concerns based on adsorption and degradation. One ecological promising environmental restoration technique is photocatalytic destruction of organic contaminants. Several photoactive semiconductors, including TiO_2 [731], g-C_3N_4 [732], and CdS [733] have demonstrated encouraging activity toward the photodegradation of several organic contaminants to date. To obtain improved sensitivity and selectivity, MXene might also be easily

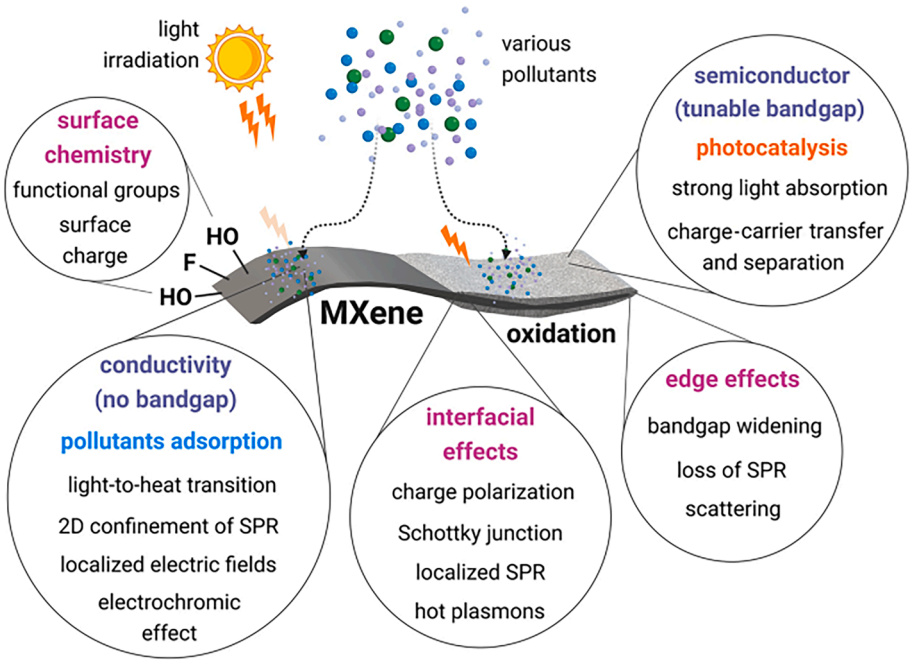

Fig. 31. Visual depiction of the functional properties and interfacial interactions of native and oxidised versions of MXene used for photocatalytic breakdown and organic pollutant adsorption. Reprinted with the permission of Ref. [747].

decorated or hybridized with other active ingredients including metallic nanoparticles and carbon-based compounds [734,735]. The use of 2D MXene layers in redox-based catalytic methods to identify bromate ions was discovered by Rasheed et al. [736] in relation to hazardous ions. According to the spectroscopic investigation, bromate ions adsorbed on MXene sheets caused partial oxidation of MXenes and bromate to be reduced simultaneously. Within the operating window of 50 nM-5 μM, the built-in sensor demonstrated a strong sensitivity with a detection limit of 41 nM. The work offered proof that redox-based sensor systems might directly employ MXene sheets.

Cationic dyes have mainly been researched as organic pollutants due to their widespread usage in the printing, textile, and paper industries, as well as their discharge into aquatic habitats [737]. This difficulty may be handled by using a cutting-edge MXene that effectively eliminates cationic dyes. As shown in Fig. 31, a variety of techniques may be used to efficiently remove pollutants. A composite construction can improve MXene's adsorption effectiveness [738]. Magnetic MXene@Fe_3O_4 systems show strong MB adsorption at various temperatures, including 55 °C [739,740]. The MB clearance rate (11.68 mg/g) was related to Langmuir isotherm processes The adsorption is pH-sensitive, with best results at pH 3 or 11. Aside from hydrogen bonding, electrostatic attraction is the principal mechanism behind MXene's adsorptive behavior. A workable method for treating wastewater and desalination is membrane separation technology. High flux, high selectivity, stability, resistance to fouling and compounds that resemble chlorine, and stability are all desirable qualities in membranes used in desalination and water treatment [741]. Additionally, the membrane needs to be sufficiently thin and mechanically stable to optimize water permeability while maintaining a steady salt rejection rate. Currently, materials with molecular and ionic sieving capabilities that are 2D carbon nanomaterials, including graphene and GO, show great promise. The decreasing interlayer spacing when compressed causes GO membranes to have a relatively limited flux, notwithstanding their suitability for a wide range of applications.

Furthermore, the $Ti_3C_2T_x$-SO_3H composite demonstrated 111.11 mg/g capacity for MB adsorption via electrostatic attraction [742]. MXenes synthesized using hydrothermal etching often show stronger cationic dye adsorption than those synthesized via normal HF etching due to their larger BET-specific surface area [743]. In this regard, the Al-based MOF can remove both MB and anionic dye (AB) from model wastewater [744]. Once again, the PZC took the lead. At pH 3, the MB removal capacity was 190 mg/g. The AB elimination capability was 200 mg/g. When two adsorbents were combined, MXene demonstrated little selectivity. Pressure-assisted membrane technology can be used to address poor selectivities, such as in the instance of an MXene@CNT membrane synthesized via a thermal crosslinking approach [745]. The membranes exhibited good adsorption behavior towards methyl orange, Congo red, and rhodamine B throughout 50 h of operation, as well as anti-swelling features and high efficiency. Within 1.2 V of the applied voltage, the p-MX/SWCNTs demonstrated a high capacity for MB (1068.8 mg/g) [746]. Even at different pH levels, the electrodes were more sensitive to cationic dyes than anionic ones.

MXenes have the potential to demonstrate their efficiency in the burgeoning field of pharmaceutical removal (as illustrated in Fig. 32) due to its antibacterial properties. Wastewaters, particularly those containing active chemicals, are hazardous to the environment because they create irreversible changes in organisms. Thus, adding effective catalysts as MXenes substantially improves medication removal [751]. Previous research has shown that MXenes are effective materials for decomposing numerous medications

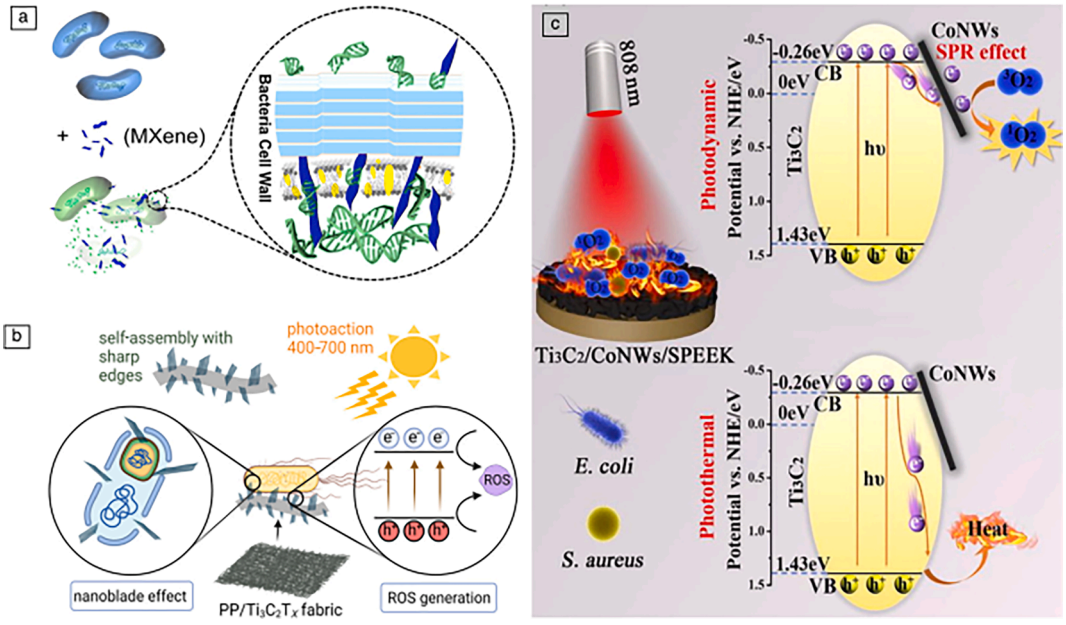

Fig. 32. (a) Schematic representation of colloidal $Ti_3C_2T_x$ MXene nanosheets' antibacterial mechanism of action. Reprinted from Ref. [748]. (b) Polypropylene fabric covered with bristling $Ti_3C_2T_x$ MXene flakes exhibits tunable antibacterial activity by connecting the nanoblade effect with the formation of reactive oxygen species (ROS). Reprinted from Ref. [749]. (c) A schematic representation of the antibacterial properties of MXenes, photothermal, and photodynamic cobalt nanowires (CoNWs) is shown. Reprinted from Ref. [750].

such as amitriptyline (AMT) [752], verapamil [753], carbamazepine [754], 17 α-ethinyl estradiol [755], ibuprofen [756], and diclofenac [757]. $Ti_3C_2T_x$ has an adsorption capability of 58.7 mg/g for AMT due to electrostatic interaction between negatively charged MXene and positively charged medicinal compounds [758]. For example, a 2D/2D Bi_2WO_6/Ti_3C_2 MXene heterostructure was employed to extract the most commonly used antibiotic, amoxicillin. Interestingly, the elimination of compounds was seen after less than 40 minutes of photocatalysis, owing to the production of reactive oxygen species [759]. A nanocellulose-intercalated MXene membrane demonstrated about 99.0% azithromycin breakdown. Furthermore, the membrane demonstrated anti-swelling capabilities in water for up to 76 h, as well as pure water permeance (about 26.0 L m^{-2} h^{-1} bar).

Researchers might employ MXenes' great qualities to treat polluted or deteriorated soil [760]. For this reason, they might use MXenes' aqueous solution, which has good adsorption and nonselective oxidation [761]. For example, MXenes grafted with salt-resistant polyelectrolytes (PEs) demonstrated long-term colloidal stability over six months when kept at severe salinity (ionic strength of 2 M with 182.2 mM Ca^{2+}) [762]. The results showed an adequate adsorption capability of approximately 68 mg g^{-1} for methylene blue, a model pollutant [763]. MXenes in the aqueous phase would allow for a wide range of remediation strategies including various types of soil flushing, both in situ and ex situ. Employing a material with adsorption-oxidation capabilities makes remediation procedures more appealing by partially reducing the difficulties associated with huge amounts of polluted washings.

Pioneering research on MXenes activity against bacteria has shown the physicochemical antibacterial mode of action of colloidal $Ti_3C_2T_x$ [764]. Further research demonstrated that MXene flakes combine the nanoblade effect with ROS generation[765]. Gram-positive Escherichia coli bacteria were injected into selected MXene-based nanocomposites, as were Gram-negative Bacillus sp., Sarcina lutea, and Staphylococcus aureus [766]. Their efficiency was assessed using growth inhibition zones that encircled nanocomposite samples. Researchers found that combining ceramic oxide and noble metal nanoparticles as Al_2O_3/Ag, SiO_2/Ag, and SiO_2/Pd might improve MXene's antibacterial efficiency [767]. Additionally, partial oxidation of the $Ti_3C_2T_x$ coating to TiO_2 increased bactericidal activity [768]. However, the oxidation cannot be significant, reducing the $Ti_3C_2T_x$ MXene to just TiO_2. Preventing MXene oxidation using antioxidants and maintaining it moderate increases bandgap tunability, ensuring effective light activation [769]. More sophisticated heterostructures can address this issue while ensuring near-infrared (NIR) activation. For example, consider a one-dimensional (1D)/2D heterostructure composed of 1D cobalt nanowires (CoNWs) and MXenes [750]. Under 808-nm NIR illumination, the 1D CoNWs captured the electrons photogenerated by the 2D $Ti_3C_2T_x$ MXene, further preventing hot electron-hole recombination. The effective transfer of charge carriers increased reactive oxygen species (ROS) generation. As a result, further heat increased antibacterial effectiveness by more than 90% within 20 minutes.

Heavy metals are common and harmful pollutants because they are non-biodegradable and accumulate in the food chain [770]. Adsorption is the most ensuring approach for removing inorganic impurities from water since it is straightforward, inexpensive, and effective. MXenes can help the adsorption process by exhibiting electrostatic attraction, complexation of the surfaces, and ion exchange [771]. An alkalized (alk) MXene demonstrated that surface -OH groups are active sites for the adsorption of lead (Pb^{2+}) ions via an ionic exchange process [772]. Pb^{2+} adsorption was similarly impacted by pH variations, with 5-7 being the optimal range. Because of the high absorption kinetics per unit mass of material, $Ti_2C(OH)_2$ exhibited an adsorption capacity of 2560 mg/g for Pb^{2+} [773]. DFT simulations on $Ti_3C_2(OH)_xF_2-x$ indicated that -OH groups are necessary for heavy-metal ion removal, whereas -F does not help with Pb^{2+} removal owing to differing binding energies towards metal ions. $Zr_2C(OH)_2$ and $Sc_2C(OH)_2$ are the only $M_2C(OH)_2$ carbide MXenes and nitride MXenes with reversible affinity to Pb^{2+} due to their positive or low formation energies [774]. V_2CT_x has a high affinity for Pb^{2+}, but its instability and production of hazardous vanadium oxides limit its practical usage. MXenes absorb metal ions such as Pb^{2+}, cadmium (Cd^{2+}) [775], copper (Cu^{2+}) [776], and zinc (Zn^{2+}) [777] more efficiently than activated carbons due to their highly negative surface charge. XPS and FTIR investigations demonstrated the process of metal ion adsorption for electrostatic forces, ion exchange, and the development of inner-sphere complexes. MXene-based magnetic nanocomposites produced by a hydrothermal procedure were further investigated for removing mercury (Hg^{2+}) ions. The elimination of Hg^{2+} with an absorption capacity of 1128.41 mg/g was proven throughout a wide pH range, as well as regeneration and reuse [778].

In this case, MXenes are quite useful due to their adjustable surface chemistry and controllable interlayer spacing. Ren et al. published the first report on the MXene-based water purification membrane [779]. The membrane was created by assembling 2D $Ti_3C_2T_x$ MXene nanosheets into a freestanding membrane using vacuum assistance in filtering. The strong hydrophilicity of $Ti_3C_2T_x$, in contrast to graphene or GO, permits the existence of interlayer H_2O, which facilitates ultrafast water flow. The resulting membrane demonstrated high selectivity for positively charged metal cations (such as Li^+, Na^+, K^+, Mg^{2+}, Ca^{2+}, Ni^{2+}, and Al^{3+}) and methylthioninium$^+$ (MB^+) dye cations and was impermeable to cations with hydration radii bigger than the MXene interlayer spacing (~6 Å). The suggested micrometre-thick membrane has the potential to achieve 37.4 L m^{-2} h^{-1} bar^{-1} water flow, with varying sieving capacities according to the charge and hydration radius of the target ions. The utilization of porous MXene membrane, made by vacuum filtration utilising $Fe(OH)_3$ nanoparticles as a template, was described by Ding et al. [780]. With a rejection rate of over 90% for molecules bigger than 2.5 nm, the produced MXene membrane supported on an anodic aluminium oxide substrate demonstrated outstanding water permeance of more than 1000 L m^{-2} h^{-1} bar^{-1}. Compared to other membranes with a comparable rejection rate, the MXene-based membrane performed better.

7.5. Thermal Management

The discipline of thermal management, or TM, has garnered a lot of interest lately because of its importance in several areas, including energy storage and of its significance in several areas, including energy storage, conversion and recovery, technological devices, and personal health. There is no question about it: the TM materials play a significant role in determining the TM efficiency. Because of their distinctive 2D nanostructure, adaptable surface chemistry, high electrical and thermal conductivity, excellent light

absorptivity, and low infrared emissivity, MXenes, a family of transition metal carbides and nitrides, have seen a rise in the TM field in recent years. The current developments in MXene materials, including 0D quantum dots, 1D nanoribbons, 2D nanosheets, and 3D assemblies in the thermodynamics area, are outlined in this study from the perspectives of thermal energy conversion, storage, conduction, and radiation. In particular, their applications in different thermo-mechanical (TM) scenarios, such as thermal conduction, phase change thermal storage, solar conversion, thermotherapy, Joule heaters, thermal electric, thermal camouflage, and passive radiative heating, have become popular. Furthermore, there is a chance and a challenge for MXene-based TM materials to advance their practical use and further scientific research for effective thermal energy utilization. Khazaei et al. [781] anticipated in 2014 that functionalized Mo_2C MXene would be thermoelectric. Subsequently, different MXene materials have been used to progressively explore the theoretical and experimental aspects of a variety of thermal functional performances of MXenes, including thermal conduction, photothermal transformation, electrothermal transformation, phase change storage of heat, thermal camouflage (IR stealth), radiative heating, etc. In addition to introducing MXenes into the intriguing realm of thermodynamics, the past few years have also held promise for the exceptionally effective control and utilization of thermal energy by using MXene materials. The current state of research and development for 0D/1D/2D/3D MXene-based thermoelectric materials is reviewed in this review, along with their functional applications in a variety of thermoelectric and solar conversion applications, as well as thermotherapy, thermoelectric, thermal conduction, phase change thermal storage, radiative heating, and thermal camouflage (IR stealth).

For MXenes phase change materials (PCM) to be used in thermal applications, their thermal conductivity must be improved. Many techniques, including nanoparticles (nanopowders, nanowires, and nanotubes), impregnation, and blade modification, can be used to

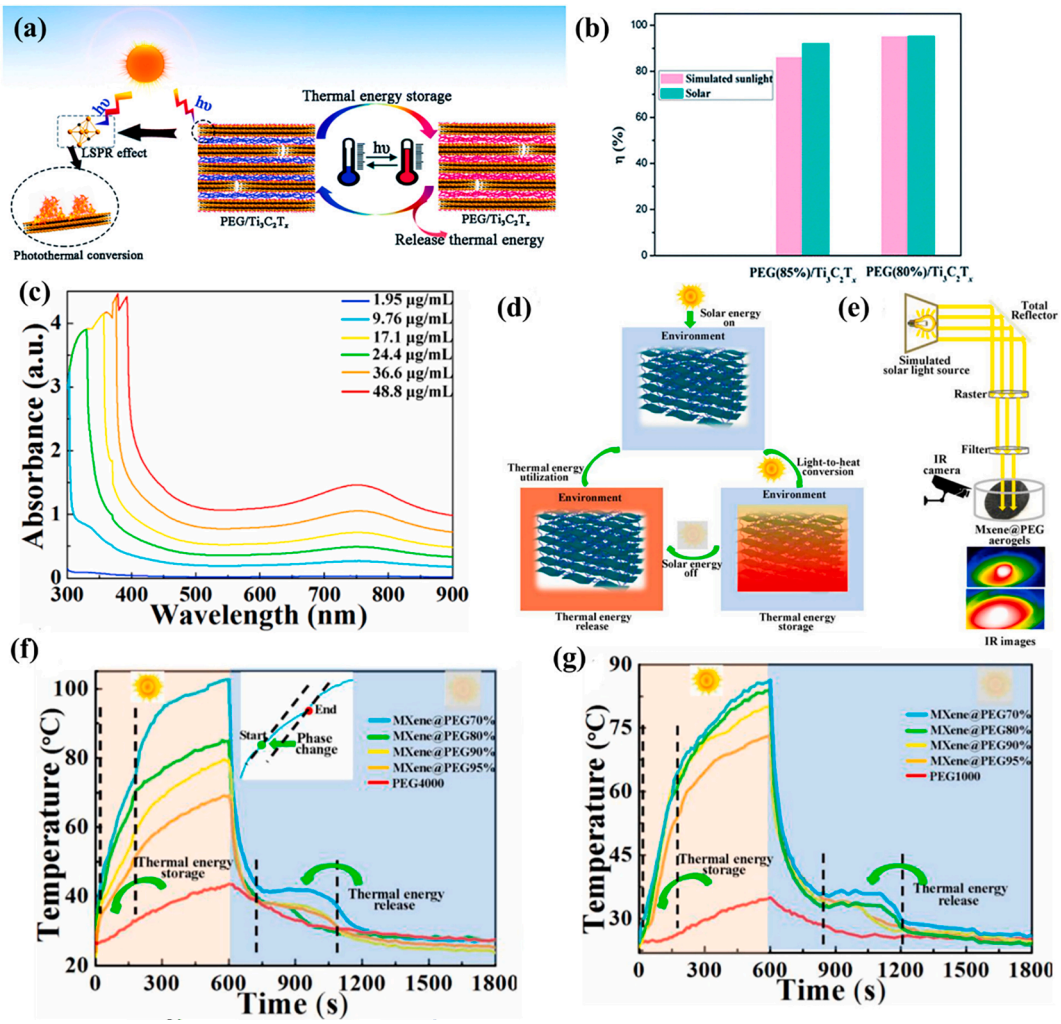

Fig. 33. (a,b) Schematic diagram showing the PTE and storage process of PEG- and MXene-based $Ti_3C_2T_x$ composites and the PTE efficiencies of the manufactured composites under both artificial and actual solar radiation. Reprinted with the permission of Ref. [782]. (c) At room temperature, the UV–Vis–NIR absorption spectra of MXene colloids at different concentrations. (d–g) The light-to-heat conversion and storage of created aerogels is schematically diagrammed, with the photothermal effect driving both processes. Set up experimentally for manufactured materials. Temperature calculation curves at (PEG4000 and PEG10000) for MXene@PEG and bare PEG aerogels, respectively. Reprinted with the permission of Ref. [783].

increase the thermal conductivity of basic PCMs [784]. This is important because a rise in thermal conductivity will accelerate the PCM's melting rate. Convective heat transmission is impacted by the inclusion of nanoparticles, which also raises the PCM's dynamic density [785]. The selection of nanoparticles is influenced by several variables, such as thermal conductivity, particle size, cost, volume fraction, and kind of base fluid [421]. The dispersion of the base PCM is improved when particle size is reduced to the nanoscale because it improves surface area about volume. As a result, a key element in determining the system's thermal conductivity is particle size. According to experimental evidence, improvements in heat conductivity and particle size reduction are positively correlated. In addition, mixes of high concentration nanoparticles melt more slowly than mixtures of low concentration nanoparticles or pure PCMs. This may be explained by the fact that the concentration of nanoparticles has increased, leading to an increase in dynamic viscosity. Decreased buoyancy-driven natural convection, the primary heat transfer mechanism during melting, is the outcome of the increased dynamic viscosity. This slows down the rate of melting overall, highlighting the significance of particle size in affecting the thermal performance of PCMs based on nanoparticles. As a result, MXene materials have a variety of characteristics including structural, optical, and electrical qualities as well as, in some situations, large thermal energy storage capacities. Because of these characteristics, MXenes may be used in a variety of ways, with thermal energy storage receiving special attention. Moreover, MXenes can store solar thermal energy due to the presence of hydrophilic functional groups [786].

Using reduced graphene oxide/MXene hybrid aerogels (rGO/MXene) to act as the supporting matrix and encasing stearic acid as the PCM, Wang et al.[787] created a vertically oriented network composite PCM. It was discovered that the composite had a thermal conductivity that was 317.24% greater than that of stearic acid. In a similar recent study by Qiao et al.[788] exhibited low density (0.023 g/cm^3), flame retardancy, strong mechanical characteristics (longitudinal and transverse compressive modulus of 450.9 kPa and 79.9 kPa at 90% strain, respectively), and 80% compressive elasticity in the optimized MXene/RGO/AuCu NPs aerogels. The malleable porous structure allowed it to respond to pressure, which has been demonstrated in pulse and human respiration monitoring applications. Aerogels feature heat resistance, flame retardancy, good electrothermal (may increase to 245.2 °C in 6 s at 7 V driving voltage) and photothermal qualities (109 °C in 10 s at 1sun sunlight intensity). Its outstanding thermal management capabilities and pressure sensing properties made it a promising candidate for wearable flexible heaters and artificial skin.

A high-performance phase change composite material was created by Liu et al. [789] by enclosing MXene in a phase PCM that had stabilized in shape. This combination improved heat conductivity and electromagnetic interference shielding (EMI) at the same time. The MXene/PCM composite was found to have an enhanced thermal conductivity of 0.74 W/mK and an EMI of 64.7 dB in the X-band. Melamine foam (MF) and MXene were combined using a polydopamine (PDA) technique by Du et al. [790] to create composite PCMs. These materials were then utilized to encapsulate polyethylene glycol (PEG) to create a composite PCM (CPCM). According to the study's findings, the suggested PEG/MPMF CPCM (PEG@MPMF), which has a melting enthalpy of 186.2 J/g—99.5% of the value of pure PEG displayed acceptable thermal energy storage capabilities. A simple method for creating MXene-decorated non-PCM emulsions (NPCMEs) with high thermal conductivity, low supercooling, and excellent stability was described by Wang et al. [791]. This was accomplished by MXene nanosheets self-assembling at the PCM/water interface. The results showed that the average droplet diameters, stability, and thermophysical characteristics of the NPCMEs were significantly influenced by the MXene content. With a 15.5% improvement over water, the 10 wt% n-tetradecane/water NPCME MXene's thermal conductivity was 0.693 W m^{-1} K^{-1}. A new bio-based pomelo peel foam (PPF)/PEG composite PCM was created by Sheng et al. [792] using a straightforward impregnation procedure. To improve the resultant PCM's thermal conductivity, thermal energy storage capacity, and optical-to-thermal energy conversion efficiency, a low concentration of MXene nanosheets was added. Additionally, the obtained PPF@MXene/PEG FCPCMs' thermal conductivity was enhanced (from 0.25 to 0.42 W/mK). Also, PEG MXene composites can be utilized for thermal management by photothermal conversion in solar cells, as shown in Fig. 33. Titania and MXene-based PCM for thermal energy storage was described by Khan et al. [793]. To create nano-enhanced phase change material (NEPCM), paraffin wax (PW82) was treated with NPs that were created and incorporated using the direct synthesis method. A study was conducted to assess the hybrid nano-enhanced PCM in PW82 using TiO_2 and MXene wt%age ratios of 0.1, 0.2, and 0.3. Through the doping of titania and MXene, the PCM's specific heat capacity was increased. A 0.3 wt% doping of TiO_2-Ti_3C_2 resulted in an increase in specific heat of 41.3%. When TiO_2-Ti_3C_2 was doped at 0.3 wt %, a maximum increase in thermal conductivity of 15.6% was found. With a weight fraction of 0.3 wt%, the generated NEPCM's dissociation temperature increased by around 6%. The findings of this work showed that doping TiO_2 and Ti_3C_2 with PW82 to create a unique class of NEPCMs has a substantial potential to increase the heat storage capacity of organic paraffin.

Work by Luo et al.[794], stearyl alcohol (SAL) was chemically modified with a phosphorus-containing molecule to synthesize a flame-retardant PCM effectively. The form-stable phase change composite was produced through a vacuum impregnation process, using an MXene with a porous structure serving as the PCM's supporting backbone. Due to the high aspect ratiosizeable, large capillary force of the MXene aerogel, and the interfacial contact between the PCM molecule and the MXene, the MXene-based PCMs showed a considerable thermal conductivity of 0.486 W m^{-1} K^{-1}. MF was used as a template by Cheng et al. to create a continuous thermal/conductive network by dip-coating it with magnetized nickel (Ni)/MXene (NiM). The porous NiM/MF hybrid sponge was then filled with PEG using a vacuum impregnation method. Due to the synergistic impact of highly conductive MXene and magnetic Ni chains, the resultant NiM/PCM displayed outstanding EMI shielding efficacy (34.6 dB) and desirable thermal conductivity (0.39 W/mK) with electrical conductivity (76.3 S/m) [795]. By mixing PEG with MXene-coated melamine foam (MF@MXene), Shao et al. [796] created innovative PCM composites. Excellent encapsulation qualities and improved solar-to-thermal conversion efficiency, including shape memory capability, were demonstrated by the resultant PCM composites. According to Gao et al. [797], paraffin was used as the PCM combined with MXene to provide flame retardancy and self-healing for thermal applications, while the olefin block copolymer served as the polymer substrate. They found that double-coupling encapsulation of PA was accomplished by the OBC-dependent polymer network and MXene-based layered porous structure. This resulted in a PA/OBC/MXene CPCM with excellent relative enthalpy efficiency (97%), as well as enhanced thermal stability.

8. Computational studies in MXene Filled Composites

Computational studies play a pivotal role in advancing the understanding and development of MXene-based composites. By leveraging powerful tools such as machine learning and density functional theory (DFT), researchers can predict and analyze the properties of MXene composites with remarkable precision. Machine learning algorithms facilitate the identification of key material parameters and trends, accelerating the discovery of optimal composite configurations. Meanwhile, DFT simulations provide deep insights into the electronic structure, surface interactions, and charge transport mechanisms within these materials. Together, these approaches form a comprehensive framework to guide experimental efforts, enabling the design of high-performance MXene composites for a variety of advanced applications. Machine learning algorithms have emerged as a tool for enhancing the synthesis and processing of MXene-loaded composites by identification of correlations between synthesis parameters and material properties. In the synthesizing stage, Machine learning models incorporating decision trees, random forests, and neural networks examine complex datasets, comprising conditions of etching, intercalation agents, and exfoliation techniques [41]. This is where Machine learning processes the data to predict optimal synthesis pathways to reach desired properties, which may include nanosheet thickness, surface functionality, and dispersibility. For example, some supervised learning models can connect precursor composition and reaction conditions to the quality of exfoliation. In doing this, it leads the researchers to minimize defects and thus improve the yield. In addition, reinforcement learning has been implemented with the aim of automation of experimental workflows, greatly reducing trial-and-error that usually characterizes composite material synthesis [50].

This enables the optimization of filler dispersion, interfacial bonding, and matrix compatibility in the processing of MXene composites. Guided by image analysis and spectroscopy data, machine learning algorithms can assess the homogeneity of distribution of MXenes within the polymers or ceramics. Specifically, CNNs have been used in the image analysis conducted via microscopy methods, showing the ability to detect the aggregation of nanosheets inside composite matrices and allowing refinement in the methodologies of mixing or casting techniques. Machine learning-driven optimization models go further in predicting how different modifications-such as surface functionalization or solvent selection-affect the interaction between MXene/MBene fillers and a host matrix to attain their target properties of either improved mechanical strength, electrical conductivity, or thermal stability[798].

Machine learning methodology helped in accelerating the process of discovering the structure-property relationship and predictive modeling in specific applications involving performance evaluation of MXene- composites. For instance, the microstructural parameters-aspect ratio and orientation-of MXene fillers have been coupled with the macroscopic properties of tensile strength or electromagnetic interference shielding efficiency using SVMs and gradient-boosting algorithms [39]. Machine learning also allows for virtual screening of composite formulations for target functionalities including high dielectric permittivity or heat dissipation. In this respect, machine learning can allow for actionable insight into guiding material design by integrating experimental data with computational simulations to enable the engineering of composites with optimized performances at lower dependences on expensive and time-consuming experimental protocols.

The paradigm of science encompasses four main approaches: Experimental science involves conducting controlled experiments in a laboratory setting to observe and analyze outcomes. Theoretical science focuses on constructing models, theories, and frameworks to explain natural phenomena based on existing knowledge and principles. Computational science utilizes computers and algorithms to simulate and model scientific processes that may be challenging to study experimentally, relying on computational methods to analyze data and solve complex equations. Data-driven science, also known as data science, leverages large datasets and advanced analytics techniques to extract meaningful insights, patterns, and trends [799]. Each approach is crucial in advancing scientific knowledge, addressing research questions, and shaping our understanding of the natural world [800]. Integrating these paradigms leads to

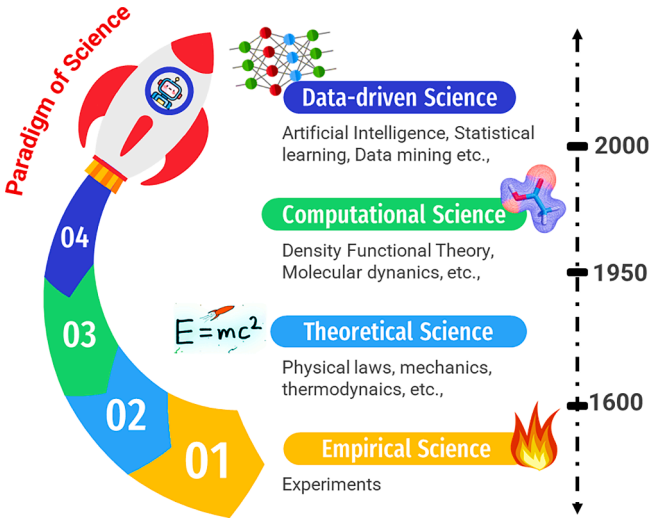

Fig. 34. A chronology of the shifting paradigm of science.

interdisciplinary innovations that drive scientific progress as shown in Fig. 34. This review section will explain the DFT and Data-driven aspects of MXene and MXene-based composites.

8.1. First Principles studies of MXene-based materials

The first investigations conducted on MXene have yielded significant knowledge on the synthesis, structure, characteristics, and potential uses of this promising material for energy storage [801]. The research conducted by Liu et al. [802] has provided a clearer understanding of the fundamental processes and interactions at the atomic level that lead to the improved electrochemical performance of MXenes. In addition, initial investigations have also enabled the logical development and enhancement of MXene-based materials for specific energy storage uses, resulting in enhanced effectiveness and durability. Moreover, these investigations have established the groundwork for subsequent investigation and progress in MXene-based energy storage devices, facilitating future developments in this technology. The extensive examination conducted via primary investigations in MXene has substantially contributed to our comprehension of the material's properties and possibilities in MXene-based energy storage devices, facilitating forthcoming advancements in this technology.

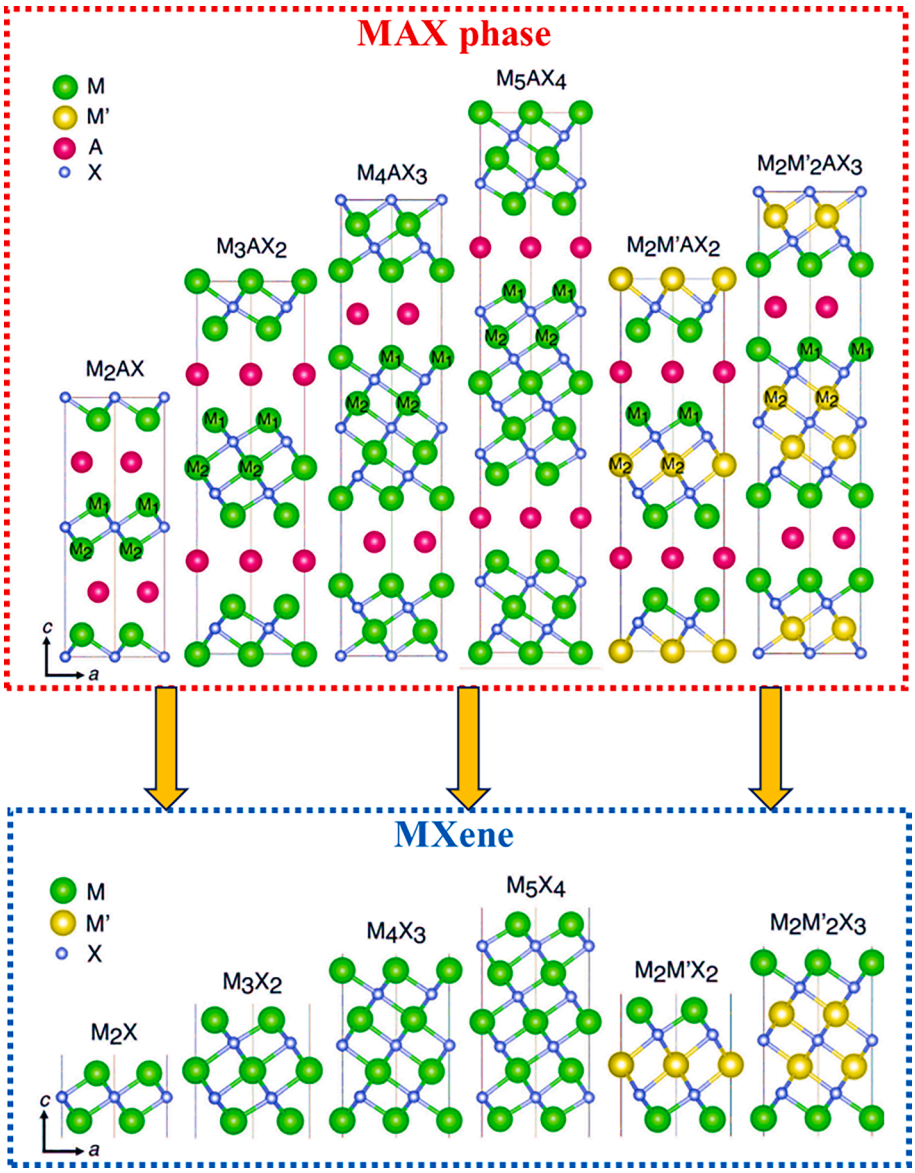

Fig. 35. Atomistic structures of six different crystalline MAX phases and MXenes. The a and c axes are common to all structures—reprint with permission [804].

8.2. MAX phase to MXene with DFT

It is widely recognized that the MAX phases have proven to be a valuable resource for creating innovative 2D systems. With the wide range of compositional options in MAX phases, we can anticipate the emergence of numerous 2D MXenes with remarkable properties. At this point, it is crucial to determine which MAX phases show potential for successful exfoliation into 2D materials. Through the examination of tensile and shear stresses, researchers have explored the process of mechanically exfoliating different M_2AlC MAX phases (M = Ti, Zr, Hf, V, Nb, Ta, Cr, Mo, and W) into 2D M_2C MXenes [803]. Through experimentation, researchers discovered that subjecting the material to significant tensile strain could break the bonds between the M and Al layers, causing the M_2C and Al layers to separate. The atomic structures of six distinct crystalline MAX phases are shown in Fig. 35.

Nevertheless, the chemical exfoliation process is a highly intricate and challenging dynamic process that cannot be accurately modelled and simulated. However, valuable insights can be obtained by examining the strength of bonds and the energy required for exfoliation. This is because MAX phases with weaker M-A bonds hold potential as favorable candidates for successful exfoliation. This paper studies the electronic structures, static exfoliation energies, force constants, and bond strengths of 82 crystalline MAX phases. The investigation uses a set of first-principles calculations based on DFT. There is a strong correlation between the force constant and the bond strength. It has been observed that, apart from the MAX phases containing the A elements S or P, there is a greater likelihood of exfoliation into 2D MXenes for the MAX phases containing other types of A elements. In addition, we investigate how charge injection impacts the bond strength of the MAX phases. When MAX phases have a negative charge, the M-A bonds become elongated and weaker when they receive electrons. This makes the exfoliation process easier. However, the exfoliation process becomes more challenging for MAX phases with a positive charge.

First-principles calculations based on DFT have emerged as a reliable method for predicting a wide range of physical and chemical phenomena on the atomic scale. Therefore, DFT calculations are utilized to optimize the nuclear structures and explore the electronic structures of the MAX phases. The Vienna ab initio simulation package (VASP) code is used for all calculations. Here is an overview of the section on the MAX phase to MXene. The exchange-correlation energy is computed using the Perdew-Burke-Ernzerhof (PBE) functional, part of the generalized gradient approximation (GGA).It is interesting to note that most MAX phases display nonmagnetic properties, except for a small number of Cr-based MAX phases that demonstrate a weak magnetic effect. We evaluate the total energies of all optimized MXenes using spin-polarized calculations. The force constants vs bond length of the MAX phase is shown in Fig. 36.

The force constants of the M1-M2 bonds have similar magnitudes to the M1-A bonds, but they are smaller than the force constants for the M1-X bonds. It can be inferred that the M1-M2 bonds exhibit a lower strength or flexibility than the M1-X bonds, aligning with chemical intuition. Nevertheless, the bonds between M1 and A and M1 and M2 retain enough strength to play a significant role in maintaining the stability of MAX phases. Due to the regular arrangement of the structure, the M1-M1, A-A, and X-X bonds have the same length as the lattice parameter a, which is greater than the lengths of the M1-X, M1-A, or M1-M2 bonds. Considering the X–X interatomic distances are significantly larger than the atomic radii of X elements, it can be inferred that the orbital overlap between the X atoms in the X–X bonds is likely weak.

Additionally, the atomic radii of A or M atoms are twice as large as the A–A or M1-M1 bond lengths, indicating a significant orbital overlap in the A–A or M1-M1 bonds compared to X–X bonds. It is worth noting that the total force constants of an X or M atom are considerably greater than those of an A atom. This clarifies why, during the exfoliation process, the bonds between M and A atoms are usually broken instead of the bonds between M and X atoms.

8.2.1. Structural and Mechanical properties studies with DFT

Yorulmaz et al. [805] examined the dynamic and mechanical stability of certain MXene phases in their original and surface-terminated states. Our research has shown that all the carbides and nitrides of Scandium (Sc), Titanium (Ti), Zirconium (Zr), Molybdenum (Mo), and Hafnium (Hf), except for Mo_2N, exhibit metallic properties. Conversely, whereas most of the wholly terminated structures of carbide-based MXenes are dynamically and mechanically stable, this is not true for nitride-based MXenes. Furthermore, this study presented the Raman active modes of several MXene phases for the first time. These modes are essential for the experimental

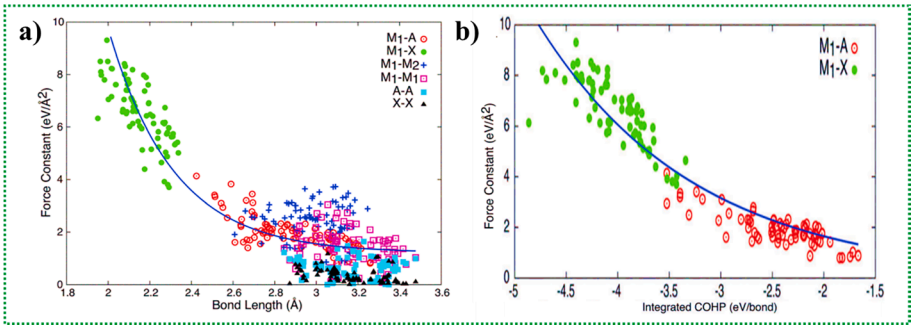

Fig. 36. a) Calculated force constants of different bonds versus the corresponding bond lengths for the 82 experimentally synthesized MAX phases. b) Bond strength versus force constant for the M1-A and M1-X bonds for various experimentally synthesized MAX phases. Reprinted with permission [804].

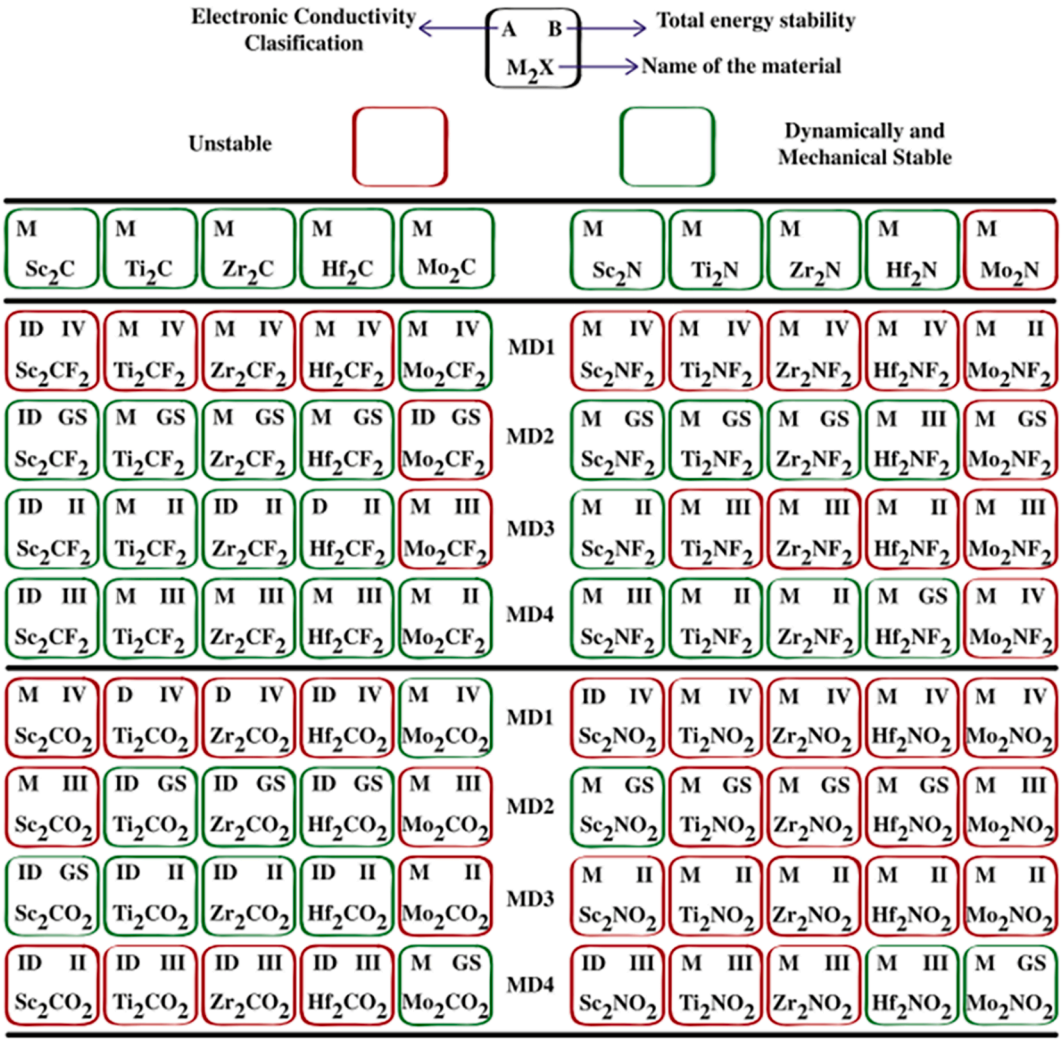

Fig. 37. Dynamical, mechanical stability characteristics and electronic properties illustrate MXenes structures. M, ID, and D refer to metal, indirect bandgap semiconductor, and direct bandgap semiconductor—reprint with permission [805].

identification of MXene phases. In addition, the structural, electrical, vibrational, and mechanical characteristics of the chosen MXene phases in both their original and completely surface-terminated states. The study successfully showed electronic band gaps in some MXenes, which depends on the specific system (whether it is carbide or nitride) and the functional components present. Research has shown that MXene phases exhibit significant changes in their electrical and mechanical characteristics depending on the specific early transition metal, X atom, and surface functional group used. The stability predictions and Raman measurements presented in this study show great potential for synthesizing and developing novel MXene materials. The Illustration of stable MXenes structures is shown in Fig. 37.

In the first phase of our computations, we examine ten structures, out of which nine, namely S_2C, Ti_2C, Zr_2C, Mo_2C, Hf_2C, S_2N, Ti_2N, Zr_2N, and Hf_2N, are determined to be dynamically stable. The only exception is Mo2N. In Fig. 4, stable structures are represented by green frame lines, whereas red frame lines represent unstable structures. The mechanical stability of these systems is evaluated based on the Born criterion. For 2D hexagonal crystals to be mechanically stable, they must satisfy the following conditions: C11 must be more than 0, C44 must be greater than 0 (with 2C44 equal to C11 minus C12), and C11 must be greater than the absolute value of C12 [806,807]. Based on the Born criteria, all of the original phases meet the requirements for mechanical stability. Only Mo_2C has a harmful C12 component, indicating that when the crystal is crushed in the y direction, the Pxx stress component is tensile rather than compressive. This phenomenon is uncommon but feasible in materials like intermediate valence systems [808,809]. Recent investigations CVD have shown the ability to produce MXenes without functional groups [810]. Thus, the experimental findings and our dynamical stability analysis indicate the potential for significant development in several pure MXenes structures.

Moreover, it would be advantageous to explore the stability of the synthesized phases using experimental fingerprints and insights from theoretical studies. This would help us comprehend the significance of synthesizing pure MXenes in connection to our stability

data. Currently, there is no known monolayer MXene made from nitride. Naguib et al.[141] have suggested that the inability of the liquid exfoliation approach to synthesize nitride-based monolayers may be due to the dissolution of $Ti_{n+1}N_n$ in HF solutions. Shein et al. [811] subsequently showed theoretically that nitrides have lower cohesive energy than carbides. The formation energy of $Ti_{n+1}N_n$ derived from $Ti_{n+1}AlN_n$ is greater than that of $Ti_{n+1}C_n$ derived from $Ti_{n+1}AlC_n$.

Nevertheless, our phonon dispersion calculations indicate the absence of complex frequencies in the 2D Ti_2N crystal. This might be seen as a sign of potential expansion in Ti_2N (and other structurally stable layers) using a mechanism distinct from liquid exfoliation, such as chemical vapor deposition (CVD). Indeed, synthesizing pure few-layer MXene crystals using a liquid exfoliation approach is quite complex because of the intrinsic surface functionalization.

8.2.2. Surface terminations with DFT

We investigate the impact of surface functionalization on the behavior of bilayer $Ti_3C_2T_2$ (T = F, O and OH) MXene towards intercalating ions through DFT calculations. When anions and cations are introduced, the interlayer spacing (d) of pristine MXene increases. After the surface functionalization, the systems response to intercalating ions undergoes significant changes. Anions cause an increase in interlayer spacing, while cation intercalation leads to the contraction of d. The interplanar distance decreases even more

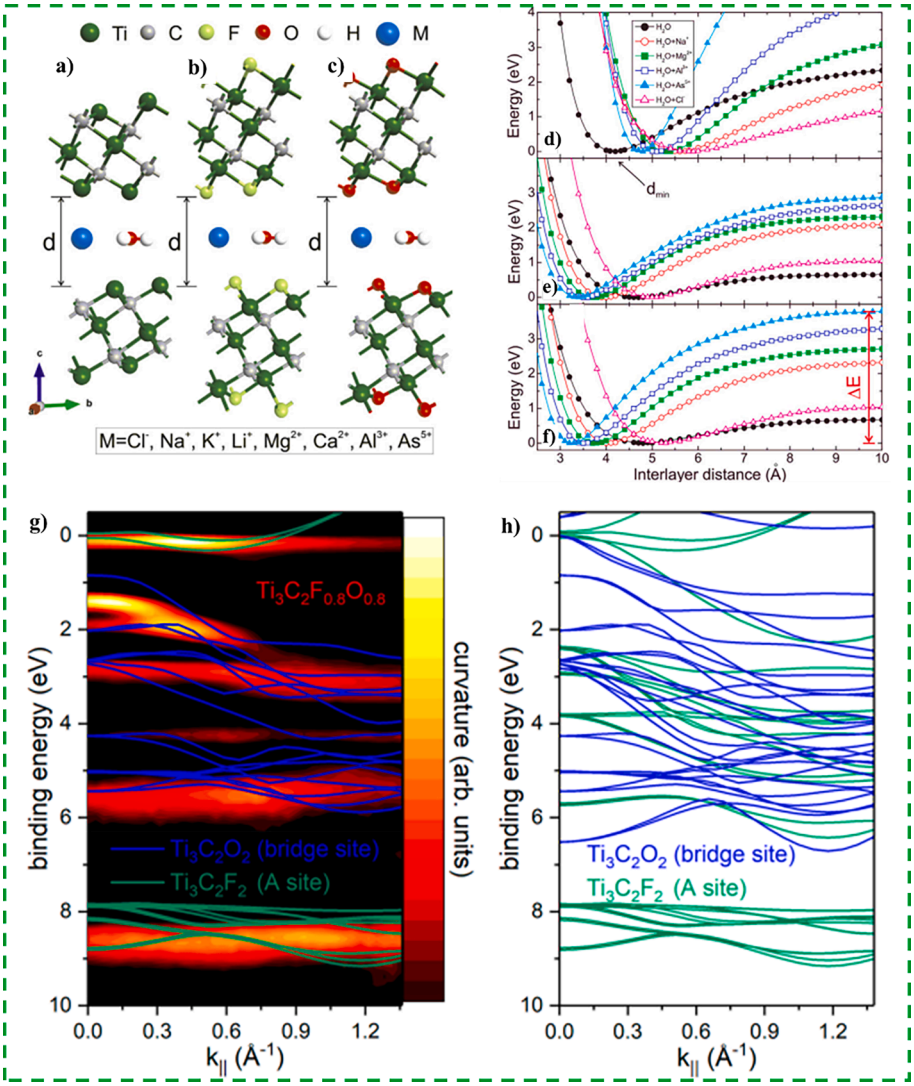

Fig. 38. Model systems: a bilayer of Ti_3C_2 (a), $Ti_3C_2F_2$ (b) and $Ti_3C_2O_2$ (c) with a single water molecule and an ion M. Total energy of Ti_3C_2 (d), $Ti_3C_2F_2$ (e) and $Ti_3C_2O_2$ (f) systems as a function of interlayer distance d for different ions (a-f) Reprinted with permission of Ref. [812]. The minimum energy is taken as reference point in each case (g) Measured ARPES curvature spectrum of $Ti_3C_2F_{0.8}O_{0.8}$ (yellow-red), including a selected part of the calculated band structures of the high-symmetry Γ−K and Γ−M directions for $Ti_3C_2O_2$ with O adsorbed only on the bridge site (blue) and for $Ti_3C_2F_2$ with F adsorbed only on the A site (green). (h)Full calculated band structures of the high-symmetry Γ−K and Γ−M directions for $Ti_3C_2O_2$ with O adsorbed only on the bridge site (blue) and for $Ti_3C_2F_2$ with F adsorbed only on the A site (green)[g,h] [813].

as the charge state of the cations increases, especially with $Ti_3C_2O_2$. The system's dynamic response to the intercalating ions is confirmed in DFT, and the results highlight the significance of surface functionalization in MXene water applications [812] The Ti-based MXenes with F and O terminal groups are shown in Fig. 38.

The model system we used comprised a bilayer of $Ti_3C_2T_2$ (T = non, F, O and OH) MXene with a single ion and a water molecule positioned between the layers (refer to Fig. 38). Initially, we conducted separate DFT calculations on each MXene layer to optimize them. These calculations were performed using the generalized gradient approximation of Perdew–Burke–Ernzerhof (PBE) to accurately describe the exchange-correlation energy [779]. Each simulation unit cell in every instance comprises six titanium atoms and four carbon atoms. A gap of almost 10 angstroms was created perpendicular to the layers of MXene, leaving a vacuum space. The

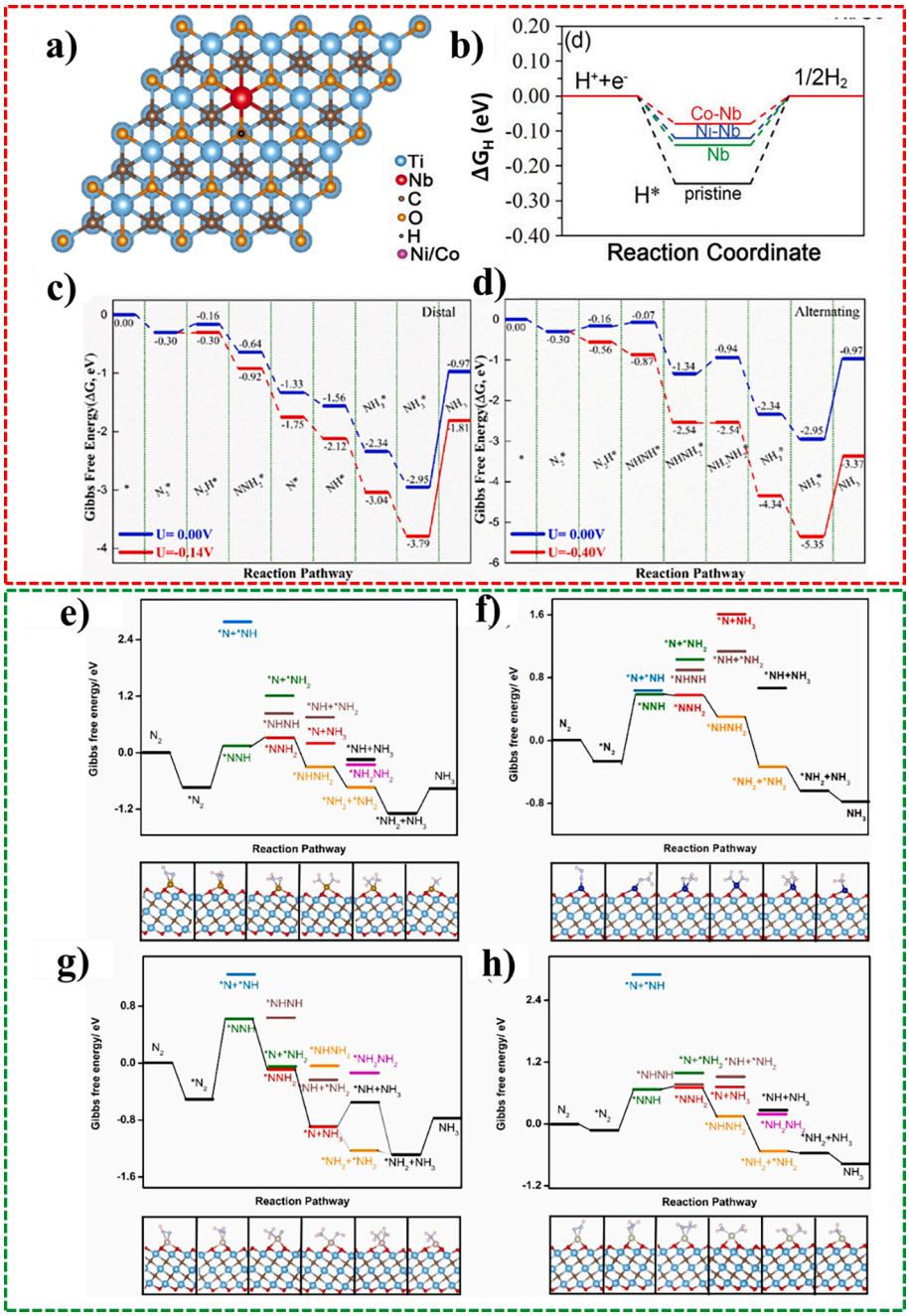

Fig. 39. a) The crystal structure of Ti and Nb-based MXenes, b) Free energy profile of Co and Ni doped Nb MXene, c,d) The NRR free energy profiles on C-doped Nb_2CO_2 nanosheet via distal and alternate paths at zero and applied potentials. Reprinted with permission [825]. ΔG diagrams of e) Fe/MXene, f)Co/MXene, g)Ru/MXene, and h) Rh/MXene. Reprinted with permission [826].

Brillouin zone was discretized using an 8 × 8 × 8 grid of k-points, as described in reference [814]. The electrostatic potentials were computed using a real-space grid with a mesh cutoff energy of 150 Ry. Local numerical orbitals with double-zeta-polarized basis sets were used for all atoms. Grimme's empirical dispersion adjustment was used in the PBE method to account for van der Waals interactions [815]. The convergence conditions for the total energy and Hellman-Feynman forces were set at 10^{-4} eV and 0.01 eV/Å, respectively. The computed parameters of the computational cell are a = 3.145 Å, b = 5.457 Å, and c = 20 Å. He used the optimized structures to create a bilayer of MXene and further optimized the arrangement of the layers. The simulations were conducted using the Atomistix toolset, a computational software based on first-principles calculations. The charge state of the ions was regulated by adjusting the electrostatic potential by introducing a "compensation" charge that was localized to the ions. The compensating charge is implicitly neutralized by the additional carriers supplied by the reservoir [816].

Fig. 38g. displays a curvature map derived from observed ARPES data using the technique outlined by Zhang et al. [817] for a $Ti_3C_2F_{0.8}O_{0.8}$ sample. The presence of nondispersive bands at around 5.5 and 9 eV may be seen, which can be attributed to the surface terminations of oxygen and fluorine, respectively, as previously mentioned. There are visible bands with a wide range of dispersion, spanning from about 1.5 eV to 3 eV in binding energy, as one moves from $k|| = 0Å^{-1}$ to $k|| = 1.2\ Å^{-1}$. Fig. 38g includes chosen bands from the computed band structure of $Ti_3C_2F_2$ with fluorine adsorbed at the A site and $Ti_3C_2O_2$ with oxygen adsorbed at the bridge site for comparison. The full band computations may be seen in Fig. 38h. The computed energy bands for the $Ti_3C_2F_2$ termination exhibit a high degree of agreement with the nondispersive characteristic at around 9 eV and the dispersive characteristic near the Fermi level [813].

The research aims to analyze the behaviour of bilayer $Ti_3C_2T_2$ (T = non, F, O and OH) MXene in the presence of various ions between the layers using DFT calculations. The study revealed that surface functionalization significantly influences the system's reaction to intercalating ions. The system reacts to the ions by contacting them or increasing the distance between the layers. This behavior is not seen in the case of the original Ti_3C_2 MXene. The system reaction to the intercalating ions is more noticeable in the O-terminated sample compared to the F-terminated sample. The DFT simulations successfully achieved the dynamic response of functionalized MXene to intercalating ions. The MXene layers exhibit dynamic behaviour due to their charged nature, as our simulations show by introducing external charges to the O-terminated MXene layers.

8.3. MXene-based materials for Electrocatalytic application with DFT

Due to the distinctive electrical characteristics and extensive chemical and structural modification possibilities of MXene. DFT can assist in the development of MXenes catalysts for many processes, including hydrogen evolution reactions (HER), oxygen evolution reactions (OER) [818], nitrogen reduction reactions (N_2RR), CO_2RR [819], and oxygen reduction reactions (ORR) [820]. DFT computations are used to analyze mechanisms, design materials, and analyze reaction mechanisms. Due to their large surface area and efficient conductivity, MXenes may serve as catalyst carriers, allowing for better dispersion and more active sites. This ultimately leads to improved activity and selectivity of the catalysts.

8.3.1. Hydrogen Evolution Reaction(HER) Catalysis

HER has always been seen as an environmentally friendly and emission-free process. 2D MXenes are well recognized as effective and stable electrocatalysts for the hydrogen evolution reaction (HER). MXenes, with their chemically stable structure under acidic environments, have great potential as a catalyst for HER [821].

Ong et al. [822] documented that the presence of nitrogen (N), boron (B), phosphorus (P), and sulfur (S) has a doping effect on the HER of MXenes, regardless of whether they are functionalized with oxygen (-O) or not. The MXenes doped with X demonstrate superior HER performance compared to the original, unmodified MXene. The X-doped Mo_2CO_2 and Ti_2CO_2 MXenes exhibited superior HER performance compared to the X-doped M_2C.

The Free energy profile of Co and Ni-doped Nb MXene is shown in Fig. 39 (a-d). The NRR free energy profiles on C-doped Nb_2CO_2 nanosheet via distal and alternate paths at zero and applied potentials. Furthermore, the change in Gibbs free energy (ΔGH) indicates that the N-doped Ti_2CO_2 displayed superior performance compared to Pt (1 1 1). Consequently, the process of N-doping may improve the HER efficiency of MXenes. Du et al. [823] described synthesizing a nanohybrid material consisting of Nb-doped $Ti_3C_2T_x$ with surface transition metal (TM) alloy modification. The doping of Nb in the conduction band, as shown by DFT calculation in Fig. 39a, may shift the Fermi level.

Additionally, the surface modification of Ni/Co can reduce the surface affinity of M − H, leading to an enhancement in the performance of the HER. The DFT analysis revealed that this catalyst had exceptional HER catalytic activity in a 1 M KOH solution, requiring only a 43.4 mV overpotential to reach a current density of 10 mA cm^{-2}.

Furthermore, it showed a remarkable level of stability. Both the doping and alloy modification methods offered design concepts for enhancing the MXenes catalyzed HER reaction. Kuznetsov et al. [824] introduced cobalt atoms into the MXenes material by single-site replacement. Co-doping enhances the catalytic efficiency of the HER. DFT simulations demonstrate that substituting Mo with Co in Mo_2CT_x results in a more favourable hydrogen binding on the –O MXenes surface. The outcome offers a method for synthesizing mid-to-late transition metal MXene compounds.

8.3.2. NRR Catalysis

MXenes possess inherent nanoscale layered structures, exceptional mechanical and electrical conductivity, remarkable specific surface area, and favourable hydrophilicity, making them promising candidates for high-performance NRR catalysts or carriers [827]. Banu et al.[630] examined the efficiency of 2D MXenes as catalysts for NH_3 production by DFT calculations. A total of sixty-five

MXenes, both unfunctionalized and functionalized, were analyzed. The free energy spectra of fifty-five $M_{2X}T_x$ MXenes, where M represents Ti, V, Zr, Nb, Mo, Ta, and W, and X represents C or N, were determined for NRR. The free energy spectra of metallic and nonmetallic components in unfunctionalized and functionalized MXenes were also analyzed. The research examined 10 MXenes with $M_3X_2T_x$ structure or different functional groups (T = S, F, Cl) to identify methods for enhancing the catalytic NRR performance of MXenes. Gao et al. [826] used DFT calculations to analyze the Gibbs free energy of $Ti_3C_2O_2$ loaded with various transition metal single-atom catalysts. This analysis is shown in Fig. 39 e. The N_2 adsorption in an end-on orientation is very advantageous, and the Fe with a ΔG of -0.75 eV demonstrates excellent capabilities for activating N_2. The necessary energy for N_2 reduction varies depending on the transition metals used. Fe/$Ti_3C_2O_2$ is 0.92 eV; for Co/$Ti_3C_2O_2$, it is 0.89 eV. For Ru/$Ti_3C_2O_2$, it is 1.16 eV, and for Rh/$Ti_3C_2O_2$ it is 0.84 eV. The calculations indicate that there are two possible phases that might restrict the reaction:

(i) $N_2+H^+ \rightarrow NNH$ and

(ii) $NH_2+H^+ \rightarrow NH_3$

(see Fig. 39f). Gao et al.'s research [826] presents a novel approach to producing N_2RR catalysts. Li et al. [825] evaluated the potential of C-doped $NbCO_2$, WCO_2, and $MoCO_2$ as catalysts for N_2RR by analyzing the free energy diagrams of several N_2RR catalyst candidates. These catalysts have a high catalytic activity for NRR good selectivity and may be further explained by adjusting the filling degree of Pz orbitals of the individual carbon atoms. Hence, the particular catalyst consisting of a single carbon atom may be used as a highly efficient catalyst for N_2RR by carefully choosing an appropriate substrate. In addition to their excellent stability, metal-electron band structure, and electronic properties, 2D transition metal borides (MBenes) exhibit catalytic activity for N_2RR (Fig. 39g) and effectively block the HER with excellent selectivity (Fig. 39h). Zhao et al. [828] conducted DFT calculations to evaluate the catalytic potential of four MBenes (TiB, YB, ZrB, and MoB) using their respective limiting super potentials. The results suggested that these MBenes had promising nitrogen reduction reaction (NRR) catalysis possibilities. These papers provide practical approaches for designing effective electrocatalysts based on MXenes.

9. Artificial Intelligence and Data-driven approaches for MXene-based composites

MXene is a promising category of 2D nanomaterials that has gained significant attention due to its unique properties and potential applications in various fields [406]. To fully exploit the potential of MXene-based composites, it is essential to understand the data collection, training, and testing processes involved in developing these advanced materials. This section aims to provide a comprehensive overview of artificial intelligence and data-driven approaches in MXene-based composites, focusing specifically on the data collection, training, and testing processes. The data collection process for MXene-based composites involves gathering relevant information about the properties and characteristics of MXene nanomaterials and their interactions with other components in the composite [829,830]. This information can be obtained from various sources, such as experimental studies, computational simulations, and literature reviews. The collected data is then used to train artificial intelligence models, which can be supervised or unsupervised, to analyze and predict the behavior of MXene-based composites. Supervised learning algorithms, such as regression and classification models, are trained using labelled data to predict the composites' specific properties or performance metrics.

Data-driven approaches leverage the information available on MXene-based materials, encompassing synthesis parameters, structural characteristics, and performance metrics. By harnessing this data, researchers can uncover insightful relationships between MXene compositions, processing methods, and the resulting composite properties. This knowledge is a valuable foundation for guiding the development of next-generation MXene composites with tailored functionalities. Integrating AI and data-driven methodologies into exploring MXene-based composites holds tremendous potential for streamlining the material development cycle, accelerating

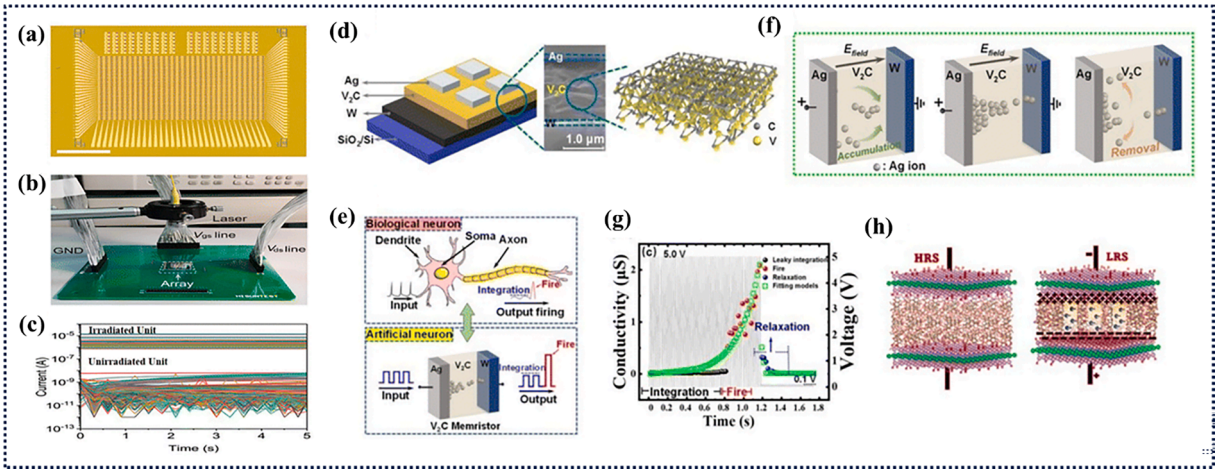

Fig. 40. (a) Array of sensors (scale bar of: 3.25 mm) (b) Circuit diagram of a sensor array (c) Output current signals measurement. Reprinted with permission of Ref. [831] (d) Ag/V2C/W memristor (e) artificial synaptic neuron with the memristor (f) Fitting model of a memristor (g) Fitting model of a memristor (h) Conductive mechanism of memristor. Reprinted with permission of Ref. [832].

innovation, and uncovering new paradigms in materials design. This synergy between advanced computational techniques and materials science offers an exciting frontier for achieving unprecedented advances in composite materials research and development.

9.1. AI based Approaches for MXene-Based Composites in various applications

Recent advancements in artificial intelligence (AI) have established it as a transformative technology in materials science, engineering, and biomedical applications due to its high precision, efficiency, and ability to uncover complex patterns in large datasets. This section explores the role of AI in advancing MXene-based composites, emphasizing its impact on both practical applications. AI-driven techniques, such as deep learning modeling, have revolutionized the design and synthesis of MXenes by predicting optimal synthesis pathways and overcoming traditional trial-and-error approaches. These methods have significantly enhanced the efficiency and scalability of MXene production while identifying their limitations, such as data dependency, that require further refinement.

AI-based modeling tools have also played a pivotal role in optimizing MXene-based devices, particularly in energy storage systems, sensors, and memristors. Machine learning algorithms have been employed to predict material performance, while deep learning approaches have modeled nonlinear dynamic behaviors in memristive systems. Additionally, AI-driven simulations have facilitated the design of adaptive and intelligent MXene-based materials for applications in smart systems. Expanding beyond device optimization, MXenes have demonstrated potential in AI-driven applications, including adaptive systems, dynamic response interfaces, and soft robotics, where their unique electrical, thermal, and mechanical properties are particularly advantageous.

Fig. 40 showcases the integration of MXene-based materials into advanced devices, emphasizing their multifunctionality in sensor arrays and memristive systems. Panel (a) displays an array of sensors with a scale bar of 3.25 mm, highlighting their compact design suitable for precise sensing applications. The corresponding circuit diagram in panel (b) illustrates the connectivity of the sensor array, enabling efficient signal processing and data acquisition. Panel (c) presents the measured output current signals, validating the array's responsiveness under operational conditions [831]. (d) focuses on the Ag/V_2C/W memristor, a key component with exceptional electrical properties. This memristor is further demonstrated in panel (e) as an artificial synaptic neuron, showcasing its potential for neuromorphic computing and brain-inspired applications. Panels (f) and (g) detail the fitting models of the memristor, providing critical insights into its electrical response and functional characteristics. Finally, panel (h) explains the conductive mechanism of the memristor, shedding light on its charge transport pathways and operational principles [832]. Collectively, it underscores the versatility and potential of MXene-based composites in advancing next-generation sensing and computing technologies. This integrated perspective provides a comprehensive understanding of the evolving intersection between AI and MXene composites, positioning them as key players in the development of next-generation intelligent systems

9.2. ML & DL - a generalized approach

Machine learning (ML) techniques offer a broad and robust framework for enhancing the performance and properties of MXene-based composites. These composites, consisting of MXene sheets dispersed within a matrix, exhibit exceptional mechanical, electrical, and electrochemical properties, making them highly attractive for various applications. Leveraging machine learning to develop and optimize these composites can significantly accelerate the discovery of novel materials with tailored properties. Deep learning (DL) enables multi-layered models to learn data representations by processing them in their raw form, which is not feasible in traditional

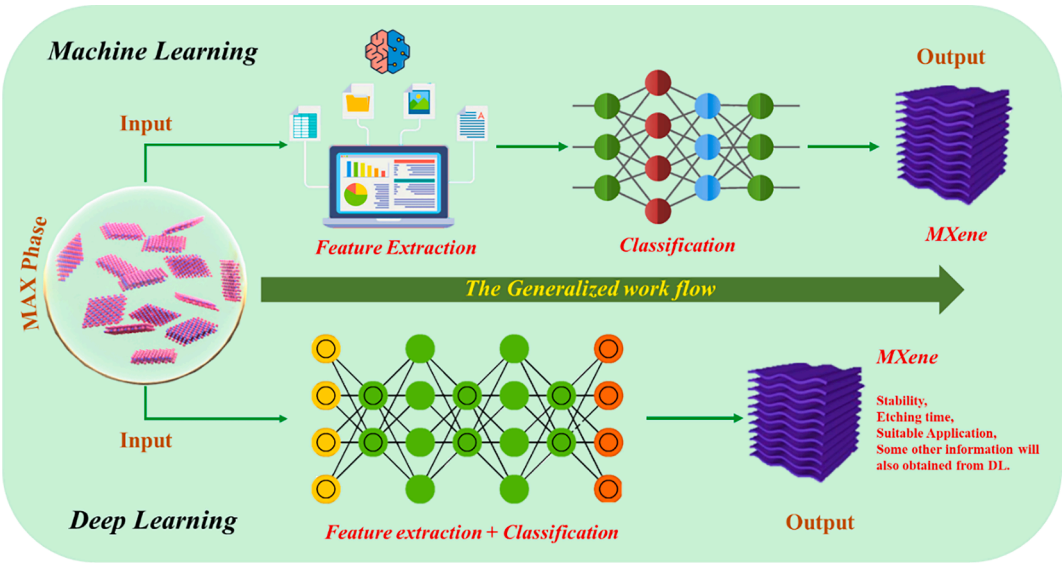

Fig. 41. Generalized workflow of Machine learning and Deep learning algorithms.

Table 10
Comparison of Machine learning with Deep learning in various aspects

Aspect	Machine Learning	Deep Learning
Network Depth	Shallow networks with limited layers	Deep neural networks with multiple layers
Feature Engineering	Manual feature extraction and selection	Automated feature learning from raw data
Training Data Size	Performs well with small to medium data	Requires large amounts of data for training
Computation Power	Less computationally intensive	Highly compute-intensive, often requiring GPUs
Interpretability	It is more accessible to interpret model predictions	Complex models that are often harder to interpret
Use Cases	Adequate for more straightforward tasks and datasets	Excels in complex tasks like image and speech recognition

machine learning. The generalized workflow of the ML and DL is shown in Fig. 41. These approaches significantly enhanced the precision in diverse image processing areas, including voice recognition, face identification, object detection, and biomedical applications [833]. The comparison of Machine learning and Deep learning is given in Table 10.

9.3. Data collection and processing

Data selection is a detailed process of examining the data's kind, quality, and format. High-quality data may help avoid including inaccurate, incomplete, or unnecessary information; hence, researchers should get data from reliable sources. In 2011, the United States introduced the Materials Genome Initiative to emphasize the significance of extensive data in advancing materials research. This initiative aggressively advocated for the creation of a material database. Computational materials research has historically used several material databases, including the Inorganic Crystal Structure Database, Material Project, Open Quantum Material Database, AFLOWLIB, Computational Materials Repository, and Harvard Clean Energy Project. [834-836]. Furthermore, text-mining technology has been used to extract pertinent literature on items to enhance current databases. Raccuglia et al.[837] suggested using machine learning to train a model using failure data from unsuccessful experiments to apply data processing in materials science. The researchers used empirical data from unsuccessful or less effective hydrothermal synthesis operations to build a machine-learning algorithm to forecast the formation of template vanadium selenite crystals. This approach surpasses conventional manual analysis and has an accuracy rate of 89% in predicting the formation circumstances of novel organic template inorganic compounds.

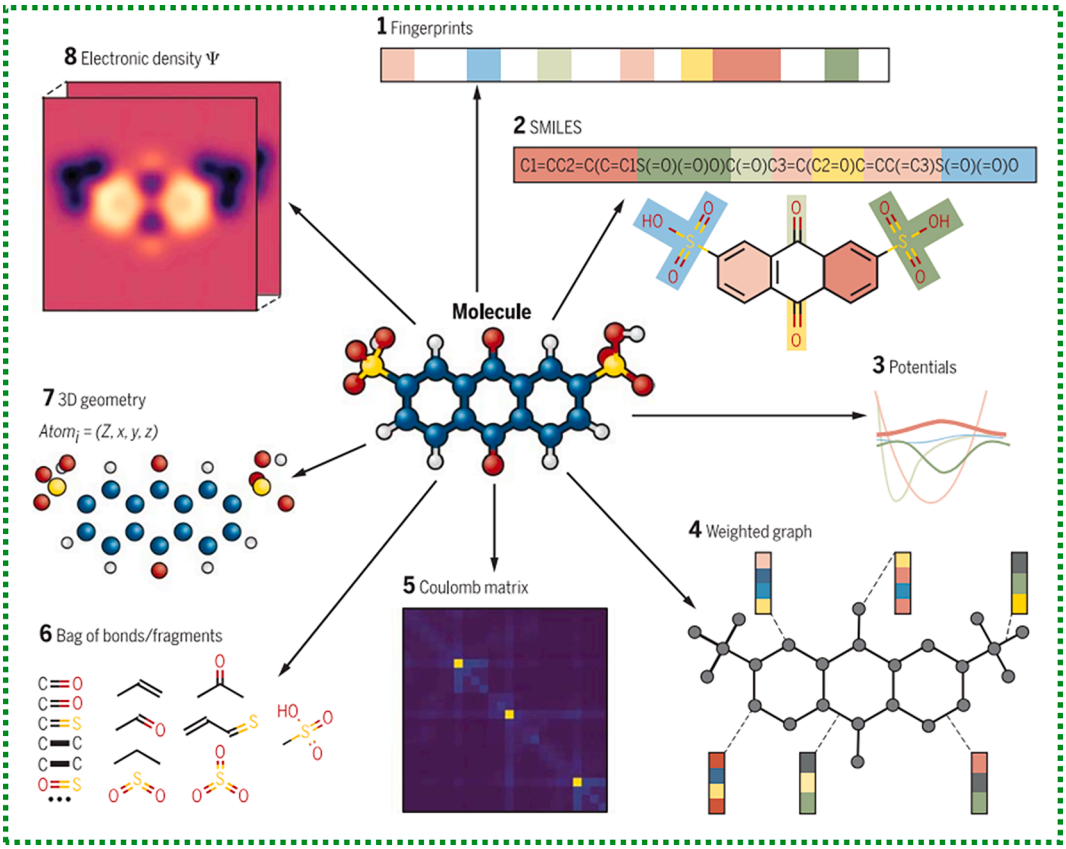

Fig. 42. Representations of a chemical structure in Machine learning. Reprinted with permission [838].

There are currently four primary categories into which materials science data can be divided: data from chemical reactions (such as rates of reaction and temperatures), data from images (such as scanning electron microscope images and photos of material surfaces), data from testing and simulated property measurements (such as chemical, thermodynamic, structural, physical, and dynamic properties), and information from published sources. The data can be classified as discrete (words), continuous (vectors and tensors), or weighted graphs. Combining data from numerous databases and formats is difficult due to diverse data storing methods. Furthermore, the proper data format is determined by the individual machine-learning method. As a result, it is critical to standardise the data format and select an appropriate data model for algorithmic machine learning during data processing. Data formats include SMILES, Coulomb matrix, fingerprint, and the weighted graph. [838-842]. Fig. 42 depicts several visualizations of a molecule.

Rong et al. [39] partitioned the whole dataset into a training set and a test set, maintaining a ratio of 4:1. Three different models were trained using the training set to predict the mechanical characteristics of MXene/nano-cellulose hybrid aerogels. Subsequently,

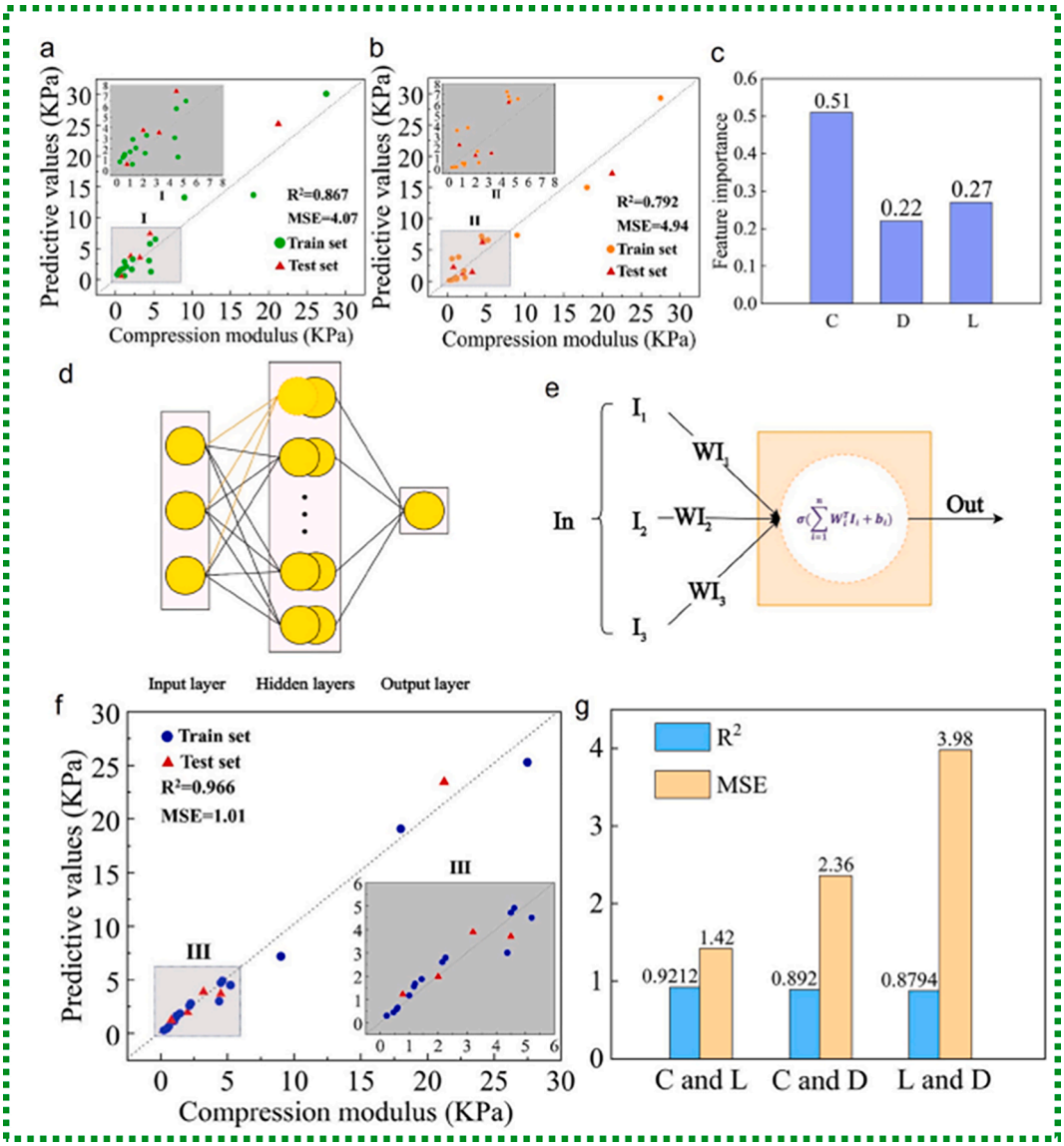

Fig. 43. Machine learning models such as Random Forests, SVM, and ANN provide prediction values. (a) Prediction values of SVM. Predictive values of the Random Forest model (b). (c) The importance of the random forest model's input attributes. (d) Structure of artificial neural networks. (e) Singular neurones are located in the subsurface layer. (f) Synthetic neural network mode predictive values. (g) The performance of the model trained using two input parameters was chosen at random. The quantities C, D, and L, respectively represent the average diameter, average length, and average carbon fibre content. Reprinted with authorization. Reprinted with the permission of the ref.R[39]. Nevertheless, manual feature engineering is not an optimal option. The constraints imposed by human experience make it challenging to identify the most significant characteristics for predicting the target. Furthermore, manually designing features necessitates a more substantial expenditure of both labour and computing resources

they employed the data to validate the accuracy of these models. Initially, they began the training process of a Support Vector Machine (SVM) model. SVM uses a kernel function to convert nonlinear data into a high-dimensional space so that it can be separated linearly. Turning the regression problems into a group of linear formulas for resolution leads to faster training and better accuracy. [843] They employed the kernel function of the Gaussian distribution to create an SVM regression approach to anticipate the aerogel mechanical characteristics. The model's score for R^2 of 0.867 indicates a good match. The mean square error (MSE) was 4.07, which was the mean squared difference between anticipated and actual values. These findings suggested a considerable relationship of input and outcome. They analysed the three input attributes using a random forest regression model. The mechanical properties of aerogels were estimated using random forests. Several training sets were used to train a large number of decision trees. The mean output value for all decision tree elements was then determined. [844]. Because the regression decision tree's output is discontinuous, it is often used when there is a need for poor accuracy. The prediction results of the Random Forests model are shown in Fig. 43 b. The model's R^2 score is 0.79, and its MSE is 4.94. Furthermore, the random forest model can also determine the significance of each input characteristic based on the priority assigned to distinct leaf nodes (Fig. 43 c). The relevance of the $Ti_3C_2T_x$ amount, average carbon fibre length and diameter is 0.51, 0.27, and 0.22, respectively.

To improve the accuracy of forecasting the mechanical properties of hybrid aerogel and evaluate the feature significance conclusions obtained from the RF model, an ANN model was created (Fig. 43 d-e). Three hidden layers, an input and an output, make up the ANN model. A neuron was found in every buried stratum. Layers may be activated using the Sigmoid function, and training requied an average learning rate of 0.005. A set of weight parameters was used to transmit the input properties to the concealed layer neurones. The model's output is then sent to the hidden layer neurones by feature transfer and nonlinear transformation. Fig. 43 f displys the model's results. The ANN model finely adjusted the connection between each neuron via numerous nonlinear layers and many weight parameters. This allows the ANN to adapt to different nonlinear input characteristics effectively. Thus, the Artificial Neural Network (ANN) model outperforms the SVM and random forest models. To examine the significance of various characteristics, they chose two distinct properties as the input for training the artificial neural network. Fig. 43 g displays the findings. Compared to the other two examples, the model performance was superior when using $Ti_3C_2T_x$ content and average carbon fibre length as inputs. This conclusion aligns with the feature significance provided by the random forest model.

The advent of deep neural networks has eliminated the necessity for human feature development, which might eventually become standard procedures in materials research machine learning.

9.4. Training and testing the data with ML/DL algorithms

The learning model is constructed using the provided band gap data set {X, y}, where the expected GW band gap is represented by y, while the input set of capabilities is denoted by X. Please refer to schematic Fig. 44. for a visual representation of the work flow of a model. $X = \{x_i\}$; $i = 1$ to n comprises n distinct characteristics ($n = 47$). These key characteristics are calculated properties of the MXene, including the mean and standard deviation (std) of elemental values.

Data preprocessing standardizes the values of various variables to address significant variation. This results in a standardized X with a mean of 0 and a variance of 1. Statistically significant outliers are data points with substantial residual or high leverage that might negatively impact model fitting.

$$L(\beta) = ||y - X\beta||_2^2 + \alpha||\beta||_1$$

To achieve a quicker and more efficient model, it is preferable to have a lower number of features. Therefore, we aim to identify a smaller collection of essential characteristics. Feature reduction is achieved using Lasso, a regression approach for regularization and feature selection. The task entails minimizing the L2 norm, the sum of the squared differences and regularizing the L1 norm, which is the sum of the mean-absolute discrepancies, on the coefficients (β). The L1 and L2 norms are represented by $||...||_1$ and $||...||_2^2$,

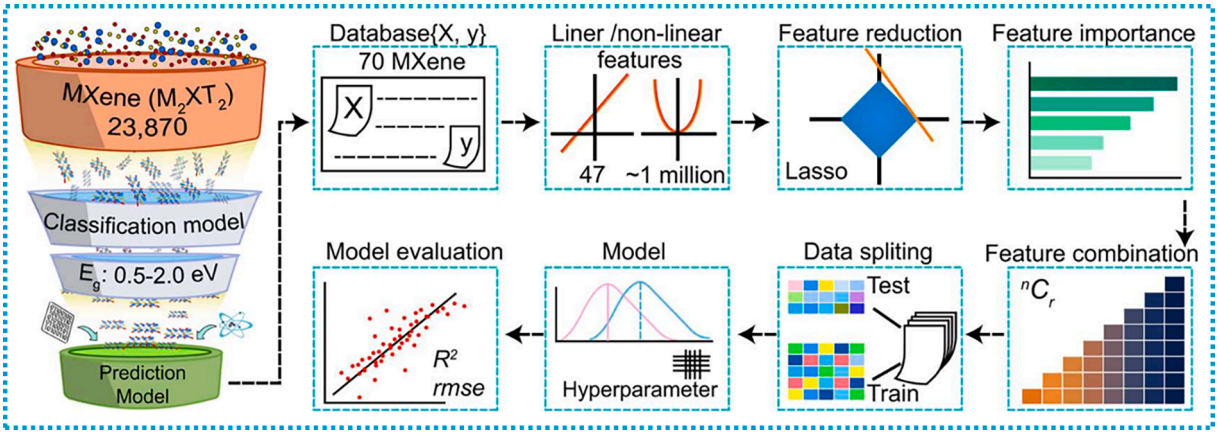

Fig. 44. Work flow: A diagram showing how to select semiconductors using the MXene dataset and feed the machine-learning algorithm with a subset of those results. Reprinted with permission [798].

respectively, and the amount of shrinkage is controlled by α.

Concisely, we have created machine-learning algorithms that can accurately estimate the band gap of MXene. We produce 23,870 MXene structures, then randomly choose 7,200 to form a database that includes computed optimized structural and electrical attributes. Based on the distinction between metal and semiconductor materials, a classification model was constructed and achieved an accuracy rate of 94%. A total of 76 semiconducting MXenes were chosen to build a predictive model.

9.5. Process and property optimization

Particle Swarm Optimization (PSO) is a well-known metaheuristic optimisation method that draws inspiration from social behaviour in nature, including fish schools or flocks of birds. When applied to the field of materials science, specifically for optimizing MXene materials, it can play a crucial role in enhancing the properties and performance of MXenes. Here is a detailed breakdown of how PSO can be leveraged for optimizing MXene properties:

1 Objective Function Definition:

Define the objective function that needs to be optimized based on the specific properties of MXenes you aim to enhance.

Parameters like synthesis temperature, precursor ratios, post-treatment conditions, etc., can be part of the objective function.

2 Particle Representation:

Each particle in the swarm represents a potential solution.

In the context of MXene optimization, each particle could encode different experimental conditions or parameters.

3 Initialization:

Initialize the swarm with a set of random solutions within the search space defined by the parameters for MXene synthesis and properties.

4 Fitness Evaluation:

Evaluate the fitness of each particle based on how well it performs according to the defined objective function.

Simulate MXene properties corresponding to each particle's solution.

5 Velocity and Position Update:

Depending on its ideal position and the best location obtained by any single particle in the swarm, update the velocity and position of each individual particle. This helps particles converge towards better solutions over iterations.

6 Iterative Optimization:

Run multiple iterations where particles adjust their positions iteratively, searching for improved solutions.

These iterations simulate the optimization of MXene properties over successive experimental trials.

7 Convergence and Solution Extraction:

Monitor convergence criteria to stop the algorithm when a satisfactory solution is obtained.

Extract the best solution found by the swarm as the optimized set of parameters for enhancing MXene properties.

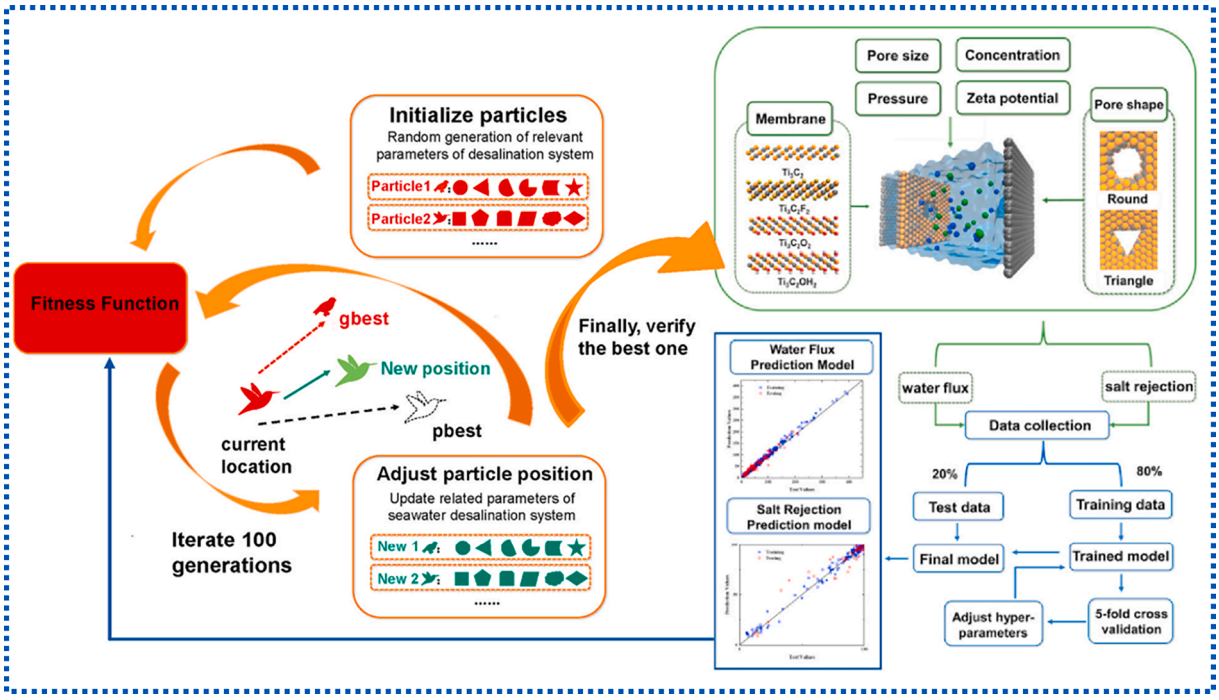

Fig. 45. Optimal system screening using machine learning and optimization algorithm. Reprinted with permission [845].

8 Experimental Validation:

Implement the optimized conditions in actual MXene synthesis experiments to validate the improvements in properties achieved through PSO optimization.

Applying PSO to optimize MXene properties can significantly enhance the efficiency and effectiveness of material design processes, leading to tailored MXene materials with improved characteristics for various applications. Fig. 45 shows the schematic of the optimization algorithm.

To assess the performance of each particle and determine whether they satisfy our desired purpose, the function associated with fitness is presented in this paper. Section 2.2 discussed a machine learning-based model for prediction that was used to obtain the values of the fitness function. Fig. 45 illustrates the steps involved in creating the screening framework for the MXene single nanopore barrier saltwater decontamination system utilising the PSO technique.

1 Initialisation of the population entails specifying the size of the population, the range of parameters, the range of speeds, and the maximum number of repetitions. An arbitrary starting the particle population is formed, and each particle is assigned a random position and speed. The membrane material determines several factors, including the placement of the particles, driving pressure, pore area concentration, hole shape, and charge value of the coefficient. The corresponding ranges of these factors are presented in the given information. The starting velocity value is a randomly generated integer from 0 to 1.

2 Each particle's capacity value is calculated, and its ideal position and value are then modified. The XGBoost model is used to evaluate the flow rate of water and the rejection of the salt rate of the new particle. Multiplying the salt rejection rating by 0.5 and the water flow value yields the new particle's fitness function value. [846].

3 The global optimal location is updated by selecting the ideal place from the collection of all particles' best positions. 4. Every particle's position and speed are altered. The iteration process is carried out repeatedly until the set maximum amount of iterations is reached.

9.6. *Integrating DFT with ML and DL*

Integrating Density Functional Theory (DFT) with Machine Learning (ML) to studying MXene and MXene-based composites presents a significant opportunity to enhance the understanding and predictive capabilities in material science. DFT offers precise electronic structure information, while ML techniques can analyze the data obtained from DFT simulations to uncover complex patterns and correlations, enabling the discovery of new material properties and accelerating materials design and optimization processes. The integration of these two approaches can lead to the creation of forecasting models for different material characteristics, providing deeper insights into the structure-property relationships of MXene and its composites. This multi-faceted approach has the potential to revolutionize the discovery and design of complex materials, which facilitates the production of electrical parts, catalysts, and cutting-edge energy storage devices that use MXene along with its composites. [847,848].

The ML and DFT integrated framework is shown in Fig. 46.

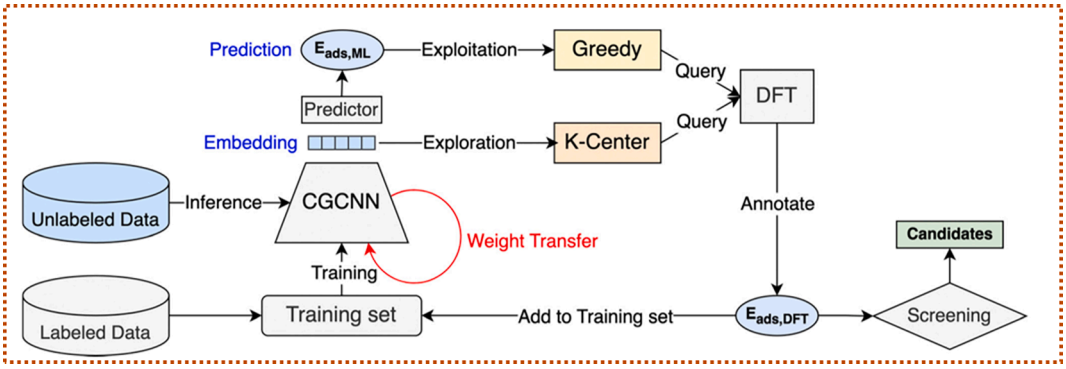

Fig. 46. Schematic representation of DFT integrated ML framework. Reprinted with permission [849]. Boonpalit et al. [849] demonstrate how to effectively screen transition-metal coated MXene for possible use in CO sensing systems by combining active learning with density functional theory examination methods. The process of analysing and processing data using artificial intelligence (AI) techniques and algorithms to create intelligent platforms and applications is known as the AL pipeline. The MXene screening procedure is completed much more quickly, and the amount of effort involved in DFT annotation duties is reduced when a crystal network convolutional neural network is used as a surrogate model. We highlight that the costs related to high-throughput screening can be reduced by active learning. This may be achieved by closely observing the model's behaviour and making informed decisions about whether to explore or exploit the search space. The research identified $Y@Zr_3C_2O_2$ and $Sc@Zr_3C_2O_2$ as the most suitable MXene candidates for detecting carbon monoxide (CO). These individuals perform exceptionally well regarding stability, recovery time, and CO sensitivity. The proposed AL framework extends the possible uses beyond MXene and CO detection by offering a versatile tool for optimising characteristics in the combinatorial chemical space. This technique is a new approach to improving the creation of materials and optimization's efficacy and efficiency in many scientific and commercial uses.

9.6.1. Physics-Informed Neural Networks (PINNs) for MXene-based composite

Physics-informed neural networks (PINNs) have emerged as a robust framework for tackling complex physical phenomena, including those found in MXene-based composites. By integrating domain-specific knowledge and physics-based constraints into neural network architectures, PINNs offer a unique approach for efficiently modelling and optimizing the properties of these materials [850,851].

9.6.1.1. Advantages of PINNs in MXene-Based Composites:. 1 Incorporating Physics Constraints:

PINNs enable the encoding of known physical principles and relationships into the neural network's training process. For MXene-based composites, this allows the inclusion of material properties, interfacial interactions, and mechanical behaviours within the model.

2 Data-Efficient Learning:

PINNs can effectively learn from limited and noisy data, making them suitable for scenarios where experimental data on MXene composites may be scarce or incomplete.

3 Uncertainty Quantification:

PINNs provide a framework for estimating and quantifying uncertainties in the predictions, which is crucial for assessing the reliability of composite property predictions in the presence of limited or noisy data.

4 Interpretability:

Physics-informed constraints in PINNs can lead to more interpretable models, allowing for insights into the underlying physical mechanisms governing the behaviour of MXene-based composites.

9.6.1.2. Application of PINNs in MXene-Based Composites:.

1. Modelling Mechanical Properties:

By incorporating mechanical constraints and material behaviour laws into the model, PINNs can predict mechanical characteristics such as fracture behaviour, Young's modulus, and tensile strength.

2. Optimization of Processing Parameters:

PINNs enable the optimization of processing parameters for MXene composites by considering physical constraints during the training process. This can lead to more efficient and tailored manufacturing processes.

3. Predicting Electrical and Electrochemical Behavior:

PINNs can capture the complex interplay of electrical and electrochemical properties in MXene-based composites, facilitating the creation of substances for electrocatalysis and applications that store energy.

4. Material Property Design and Discovery:

By integrating physics-based constraints, PINNs can aid in rapidly designing and exploring new MXene-based composite formulations with targeted properties, accelerating the materials discovery process.

9.7. Enhanced Understanding and Development:

By using physics-informed artificial neural networks, researchers can gain deeper insights into the complex physics that regulate the behaviour of MXene-based hybrids. This approach contributes to developing accurate predictive models and provides a platform for optimizing composite properties while considering the underlying physical principles. As a result, PINNs hold substantial promise for advancing the design, optimization, and understanding of MXene-based composites across various applications [851].

10. Materials Discovery and Design

10.1. High-Throughput Screening (HTC)

MXenes are perfect candidates for HTC and machine learning approaches because of their well-defined structures and, vast configurational and compositional space. This is especially true when solid solutions and nonstoichiometric MXenes are considered. While precise and quantitative forecasts are ideal, synthesis attempts might be aided by identifying consistent patterns in the properties of trustworthy materials. Tan et al. [852] used the cluster expansion approach in conjunction with first-principles DFT to conduct HTC of the structural stability of binary MXene alloys [852,853]. They discovered that Mo often occupies the external sheets of Mo-rich MXenes $(M_{1-x}Mo_x)_3C_2$ and that the anticipated ordering is stable even at high temperatures. The ideal Ti position in the Ti-combined MXenes hangs on the alloying metals.

As computing technology and software have advanced, high-throughput computation, or HTC, has become a potent tool for investigating the chemical space of various materials. It does this by creating massive datasets, which may then be filtered for certain desired qualities. These two procedures can be used in a guided optimization for specific situations when the desired attribute is known. Numerous computational additional material resources have recently been added. to the previously experimentally oriented materials databases, such as the Crystallography Open Database (COD) [854] and the Inorganic Crystal Structure Database (ISCD) [855]. These consist of the AFLOW database [44], the Materials Project (MP) database [856], and the Open Quantum Materials Database (OQMD) [857]. After the databases are put together, content is screened for specific issues. For example, Zhang et al. used the band-edge locations and stability as criteria for an HTC screening of two-dimensional intersections in the MP record for photocatalytic splitting of water [858]. To investigate new inorganic phosphors for light-emission, Cheng et al.[859] carried out a computational screening, which was then verified empirically. Machine learning based on neural networks has recently been using computational materials databases. Interatomic potentials and other energy-related characteristics have been predicted using artificial neural networks (ANN).

HTC has additionally been utilised to find MXene, which shows promise as a catalytic material. Chen et al. [860] conducted the HTC assessment on the M_2CO_2 single- and double-metal MXenes' HER activities. After discovering that a new descriptor—the electron number gained by the outermost O atom- could accurately assess the HER operation, $TiVCO_2$ was expected to be an intriguing HER catalyst. As shown in Fig. 47, Rajan et al. [798] proposed an ML algorithm to predict bandgaps of functionalized MXenes accurately. Among 23,870 MXene candidates in the database, 76 semiconducting MXenes were selected to establish the predictive model via the supervised ML [57].

More complicated structures or a more enormousmore extensive variety of compositions may be explored because ofof the ANN's quicker assessment than a total quantum mechanical computation. The prediction of materials with certain traits or attributes is another everyday use for shrinkage and decision tree approaches [861]. The minimum extreme shrinking and selection algorithm (LASSO) or its improved version is used for feature regularisation and dimensional reduction. To avoid the high computational expense of accessing high-dimensional descriptors [862]. Goldsmith et al. [863], offered a practical example of applying machine learning-

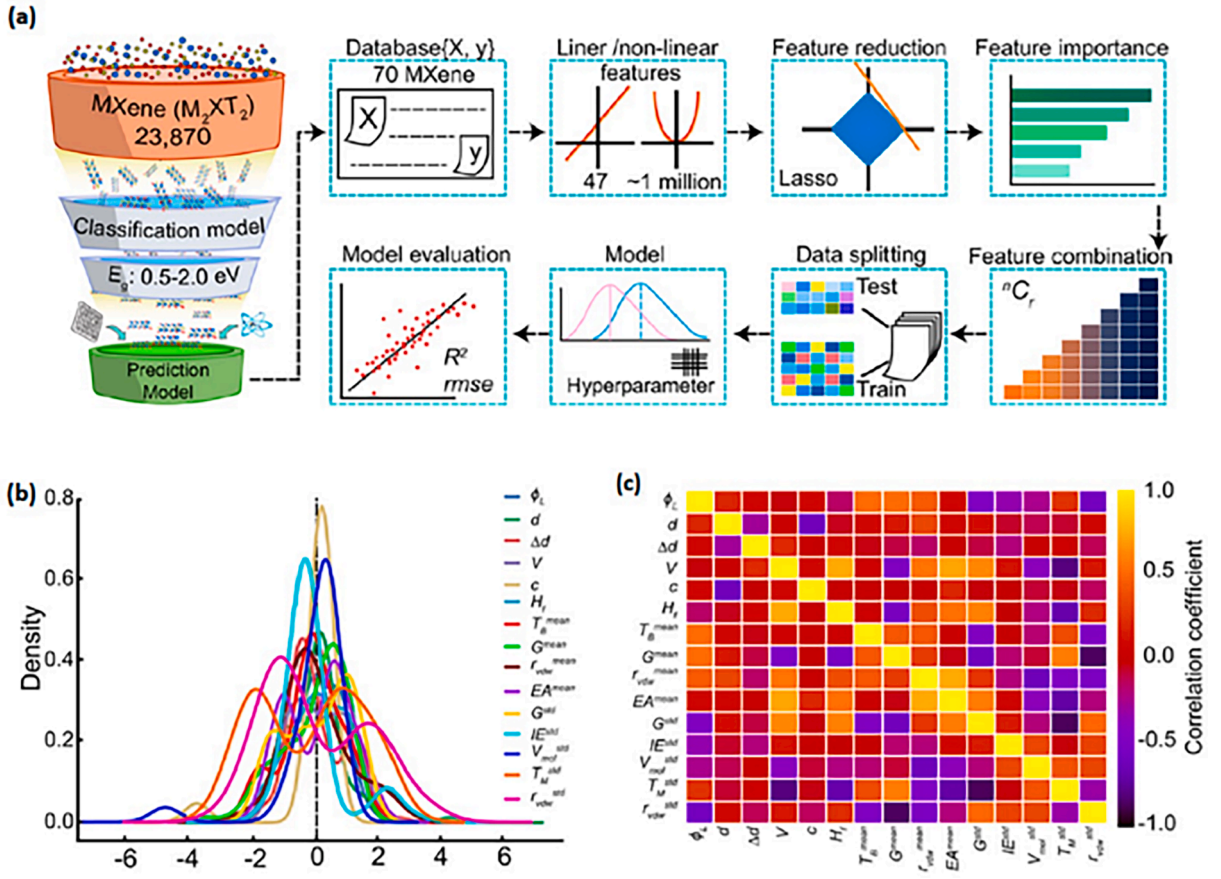

Fig. 47. (a) Workflow: selecting semiconductors fed into machine learning from the databasealgorithms of MXene with a selection of those semiconductors. (b) The density plot variance was used in the machine learning preprocessing for the unit variance, and zero mean standardised data collection. (c) A statistical heat map that illustrates how different key characteristics relate to one another. Reproduced with permission from Ref [798].

based descriptors to forecast the composition and power of rocksalts. Using the ML approach, Heracleous et al. [864] examined the stability of monolayer metal oxides (MMOs) that are both balanced and nonstoichiometric.

HTC was also used to find MXene, which possesses, attractive catalytic qualities. the Chen et al. [822] carried out the HTC screening about M_2CO_2 solitary and dual metal MXenes' HER activities. $TiVCO_2$ was subsequently anticipated to be a viable HER catalyst after it was shown that a new descriptor, the electron number obtained by the surface O atom, could accurately assess the HER activity [827]. Rajan et al.[806] presented an ML approach to precisely forecast the bandgaps of functionalized MXenes.

Approximately, 76 semi-conducting MXenes were chosen among 23870 MXene candidates in the database to use supervised machine learning to create the prediction model. Eventually, fifteen key characteristics were produced by the LASTOSO approach, which ironically did not contain the thermodynamic or DFT bandgap inputs. Pearson's correlation coefficients show that there isn't much of a link between these qualities.

Four techniquesand are bootstrap aggregating (bagging), support vector (SVR), kernel ridge (KRR), and Gaussian process (GPR), and are now often employed to train machine learning models [865]. When predicting MXenes' band gaps, KRR and SVR were shown to be more practicable and promising than other approaches because of their comparatively low root-mean-squared error (rmse) (Fig. 48). The mean boiling point and volume/atom were initiated to be more dependable than the others for learning models and to have a strong positive correlation with band gaps in GW [798].

Although it is easy to predict that HTC and ML will continue to grow in the MXenes domain, since most straight calculations are impossible due to complex processes and a wide range of important length scales, their application is likely to be particularly important for qualities like capacitive efficiency and electrocatalysis. For example, good rate performance requires optimizing ionic diffusivity, yet diffusivity is difficult and challenging to determine directly using sophisticated techniques.

10.2. Materials Informatics

MXene material informatics specifically refers to leveraging machine learning techniques to analyze and predict the properties and applications of MXene materials, a novel and highly promising class of 2D materials. While "machine learning" is a broad field encompassing various algorithms applicable across diverse domains, materials informatics for MXene research remains relatively underexplored. More or less, MXene material informatics and the machine learning of MXene refer to the same domain, emphasizing data-driven methodologies tailored to MXene materials. Including this section aims to provide insights into the emerging intersection of MXene and material informatics, offering a foundation for further advancements in this area [39,845,866].

Recent studies have demonstrated the potential of integrating MXenes into material databases, employing machine learning-driven approaches for property prediction, structural optimization, and application exploration. For example, machine learning models have been applied to screen MXene compositions for energy storage, catalysis, and electronic applications, revealing new opportunities for functional material design. Additionally, multiscale modeling techniques have been used to bridge theoretical predictions with experimental validations, further enhancing the utility of MXene in practical applications. In materials informatics, computers are actively used to analyze large amounts of complicated material data, uncover PSPP linkages, and hasten the creation of novel materials. It usually relates to the interdisciplinary nature of materials science and machine learning. In the early years of the twenty-first

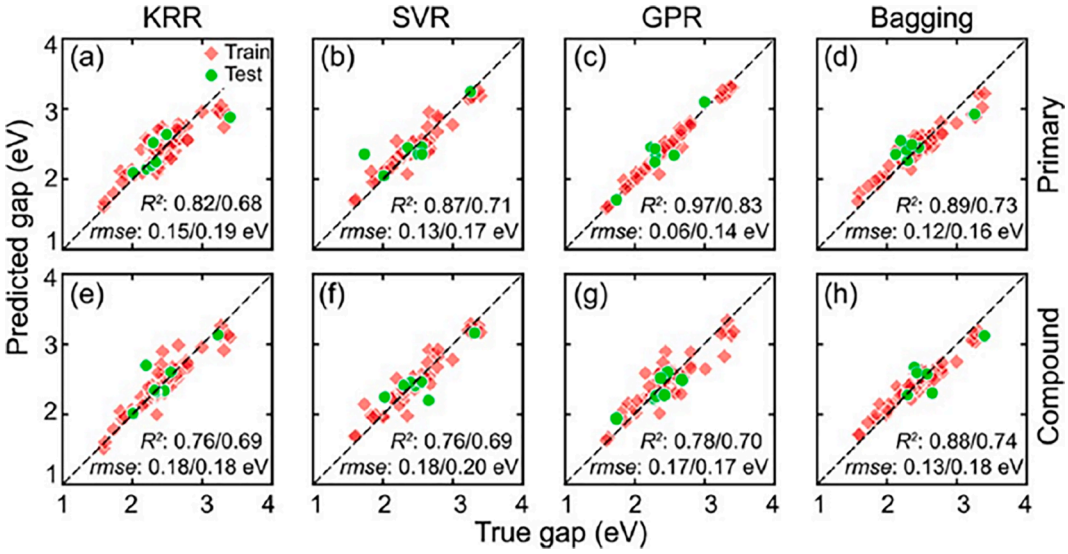

Fig. 48. MXene's band gap predictions. Scatter plots compare band gap forecasts to true (i.e., GW) gaps of essential basic (top panel) and compounded (bottom panel) feature configurations. The best model predictions are shown using R2 and rmse (train/test) of the (a,e) KRR, (b,f) SVR, (c, g) GPR, and (d,h) bagging data, which correspond to 90% training (coloured red) and 10% testing (coloured green). Reproduced figures are authorized from Ref [798].

century, the idea of materials informatics was put out. It comprised the rapid and reliable gathering, organizing, sharing, and data analysis. The objective was to lower the cost and development cycle of novel materials while gaining a more thorough and accurate understanding of materials. Over the last twenty years, machine learning has demonstrated a strong potential for use in materials science [867]. Research has validated the excellent performance of several candidate materials, and machine learning (ML) offers a sufficient supply of acceptable materials in the data-rich materials sector [867]. ML has aided in the advancement of materials research in recent years by using a variety of data types [868-870] without regard to property restrictions. ML in materials science is still relatively new and has several challenges. For instance, ML models built on tiny databases do not always have optimal accuracy [871]. Furthermore, the choice of data is still primarily based on the researchers' intuition30, and how the data is represented has a significant impact on how well the finished model performs. However, the majority of relevant reviews concentrate on applying machine learning to a particular class of materials [872-874], while other reviews that include in-depth explorations of fundamental concepts have established a, robust framework for the advancement of materials informatics [875]. Based on various algorithms, materials, and research orientations, those works offer chances for a more methodical and thorough description of materials informatics.

10.3. Predictive Analytics for Applications:

The development of databases and machine learning techniques has made it possible to conduct high-throughput searches for specific electrical characteristics of a variety of various materials [876-878]. For example, the thermodynamic, structural, and electrical characteristics of materials such as MXenes are stored in databases such as the Computational 2D Materials Database (C2DB) [879] and 2DMatPedia [880]. Additionally, these databases can serve as training sets for machine learning models used to develop electrical characteristic estimations [830], which are otherwise ascertained using DFT calculations. For example, Hashimoto et al. [881] trained a Gaussian Process Regression model using bulk attributes from the Materials Project database. Based on the Fermi level's depth, this model approximated the work function in a short amount of time. Even though the work function was only approximated, the speed at which it was measured allowed for the immediate detection of bulk compositions with high work function values. A collection of properties characterizing MXenes was regressed to the electronic band gap by Rajan et al. [798] These characteristics included bond lengths, atomic radii, and boiling/melting temperatures. The power of regression models, such as the ones covered above, increases when the feature set can be created without the need for extra DFT computations. The physico-chemical characteristics of the constituent components and a material's structural details are two examples of such attributes. The aforementioned characteristics may be instantly ascertained from a database for any novel content that is not part of the first training batch. Thus, by adding these characteristics to the machine learning model, the electrical properties may be directly calculated for the new material [882]. In addition to predicting different characteristics of materials essential to applications in energy, catalysis, and electronic devices, regression-based machine learning models also offer physical insights through feature significance evaluations [44,883,884]. Lamoureux et al. employed a genetic algorithm in conjunction with a feature significance analysis to investigate how the attributes characterizing catalytic nanoparticle stability change as the diameter of the particles does [885,886]. They demonstrated that the most significant characteristics found by the machine learning model are similar to those employed by a linear model based on physics in the limit of big nanoparticles [887]. According to Rajan et al., the volume per atom and mean boiling point of the constituent elements are the most crucial characteristics for determining the electrical band gap of MXenes.

Although databases listing MXenes' electrical characteristics are already common, there are still no predictive algorithms that can calculate the work function of any generic MXene using pre-tabulated information. Furthermore, we still don't fully grasp which physico-chemical characteristics of MXenes result in their precisely adjustable work function. Building a computational framework that not only forecasts the work function of MXenes but also explains how changes in the MXene composition affect the work function is required to close these knowledge gaps. When building MXenes for various catalytic and renewable energy applications, where the work function is a crucial performance indicator, such a framework might be a useful tool.

10.4. Data Integration and Fusion

A growing trend in the development of soft robotics is integration, miniaturization, and multi-functionalization. This trend is also seen in the increasing integration of many types of devices, such as sensors, power sources, actuators, and so on. The most popular approach is to incorporate a sensor with several characteristics [888]. A bimodal tactile sensor free from interference, for instance, that can quickly and independently sense temperature and pressure without any crosstalk has been demonstrated by Ma et al. [845]. Furthermore, systems that combine sensing and energy storage capabilities provide fresh concepts for the creation of soft robots [889]. A MXene hydrogel pressure sensor, Lithium-ion microbatteries based on MXene, and silicon solar cells make up Zheng et al.'s [890] all-flexible, self-powered, integrated system based on MXene. Actuation modules are essential in addition to energy storage units that provide electricity and sensors that pick up external stimuli. Robots frequently have to do a variety of basic tasks for their jobs, such walk, transfer, catch, and so on, all of which typically need actuators.

Parallel computing inspired by the brain One of the most promising technologies for effectively managing massive volumes of data is "neuromorphic computing," which runs on an architecture of hardware-neural network made up of many synthetic synapses and neurons. In order to overcome the von Neumann bottleneck and Moore's law constraints, memristors—artificial synapses with low power consumption, fast speed, and tremendous scalability have been produced for neuromorphic and data storage technologies based on a variety of 2D materials. Because of their extremely high conductivity, quick response of charge, high hydrophilicity and great stacking density, 2D MXenes have a lot of potential applications in memristors.

11. MXene-based composite in soft robotics

Adjusting the MXene composition and structure allows the mechanical features to be customized to meet specific requirements. When creating flexible conductive films or aerogels, these 2D materials are the perfect choice. They can easily be combined with other materials to achieve the desired results. Designing flexible electronics, like wearable sensors and strain sensors, requires materials with exceptional elasticity and flexibility. MXenes, with their unique properties, hold great potential for applications in this field.

Soft robotics is an emerging discipline that creates robots using pliable and adaptable materials [891]. Soft robots, unlike conventional robots composed of rigid materials, possess more adaptability and can execute challenging or unattainable tasks for their inflexible counterparts [892]. Soft robotics can fundamentally transform several sectors, such as manufacturing, transportation, and healthcare. Scientists are now investigating novel structures to fabricate pliable robots that imitate the motions and functionalities of live beings.

The area of soft robotics is now in its nascent phase, although it harbors immense potential about robots and automation in the future. Recently, there has been research on MXenes with high electrical conductivity and hydrophilicity. These MXenes have shown great promise in soft electronics and robotics due to their ability to absorb light and their photo-/electrothermal characteristics [893]. Various applications of MXene-based materials are tabulated below in Table 11.

Stimuli-responsive behavior may be achieved by designing soft actuators using multifunctional MXene-based materials. The numbers provided are [895,899-901]. Bilayer actuators were created by combining MXenes ($Ti_3C_2T_x$) with low-density polyethene (LDPE). These actuators have programmable configurations and exhibit biomimetic behaviors. The design uses the remarkable light absorption and electrothermal and photothermal features of MXenes (Fig. 49) [893]. These bilayer actuators may be controlled by adjusting the temperature of the thermal regulating. By combining numerous actuation units, biomimetic activities can be achieved in many applications, such as mimicking the flight of birds, constructing a synthetic iris and using robotic arms. In addition, the created actuators demonstrated untethered mobility, including crawling, sailing, and rolling. The first MXene-based soft robots showed the ability to move on the ground in different configurations. Additionally, they could navigate on the water in any specified direction and perform surface freight transportation. This was achieved using a near-infrared laser to drive the robots via the Marangoni effects that are photothermal [893]. MXene is ideal for this purpose because of its exceptional light absorption and photothermal and electrothermal properties, outstanding electrical conductivity, photothermal solid conversion capacity, and surface hydrophilicity. MXene-based materials' photothermal effects may be harnessed by soft robotic systems for a variety of uses thanks to theirflexibility, thermal conductivity, tunability and self-healing properties. These soft robotic systems include actuation, sensing, and manipulation. Localized heat was used to cause these systems to alter form, respond, or move in a regulated way. [902,903].

Due to its exceptional ability to deform upon light stimulation, the MXene film has excellent potential as a critical element in developing efficient photo actuators powered by natural sunshine. Fig. 50 a. illustrates the composition of the actuator, which consists of an MXene/polyethene (PE) bimorph structure. In this case, a bimorph structure is used because of its ability to produce bending motion via the two layers' mismatched deformation. This mismatch allows for the optimal performance of the MXene film in actuator. Commercial polymer materials include PEwith a significant thermal expansion coefficient, measuring around 500×10^{-6} /°C. Also, the bimorph actuator is created by connecting the PE film to the lower surface of the MXene film, resulting in the supreme deformation of bending of the output. When exposed to light, the MXene film undergoes bending deformation caused by contraction. Simultaneously, it converts light into heat energy by capturing it, which raises the PE film's temperature, resulting in its thermal expansion. This actuator may accomplish a significant bending deformation due to its bimorph construction. The bimorph actuator demonstrates exceptional performance in actuation when powered by sunlight. Fig. 50 b indicates that when the actuator is in direct sunlight (80

Table 11
Prominent applications of MXene-based materials in the field of soft robotics

MXene materials	Applications	Advantages	References
V_2CT_x cathode and Ti_3C_2 with Zn decorated anode	Stretchable Zn-ion hybrid batteries and flexible robotics that are magnetically actuated	Significant deformability, Ultrathin apparatus, exceedingly low self-discharge rate (0.7 mV h^{-1}), and reduced areal weight (E20 mg cm^{-2}). Superior elasticity, exceptional cycling capabilities, and strain-resistant specific capacities.	[894]
Composites of MXene ($Ti_3C_2T_x$), polydopamine, cellulose nanofibres	Soft actuators	Outstanding flexibility and mechanical properties, as well as actuation capabilities, Outstanding durability, ultrahigh tensile strength, and high modulus of elasticity; strong hydrogen bonding interaction	[895]
Integrating GO, montmorillonite, and MXene into hydrogels	Soft robots resembling batoids and robots that walk like origami	Strain sensing, thermoregulation, stretchability, and threat protection Integration at a high level of skin -mimicking capabilities	[891]
Fluoride-polyvinylidene MXene ($Ti_3C_2T_x$) actuators	Flexible solar trackers	Outstanding optical and thermal capabilities for flexible robotics, superior mechanical durability and strength. There was no discernible decline in actuator performance after 41,000 cycles.	[896]
MXene ($Ti_3C_2T_x$)-graphene oxide films	Actuators and sensors that are powered by moisture respond to humidity changes.	This material exhibited a significant bending angle and may undergo reversible deformation. It can bend at a pace of up to 32 degrees per second and has durable longevity, excellent riding endurance, and linear susceptibility to changes in humidity. The material exhibited excellent biocompatibility and flexibility.	[897]
Metal-organic framework (MOF)-MXene nano architecture	Artificial muscles	Electrodes that were both electro-ionically active and mechanically flexible. Outstanding electrochemical and electrical efficacy.	[898]

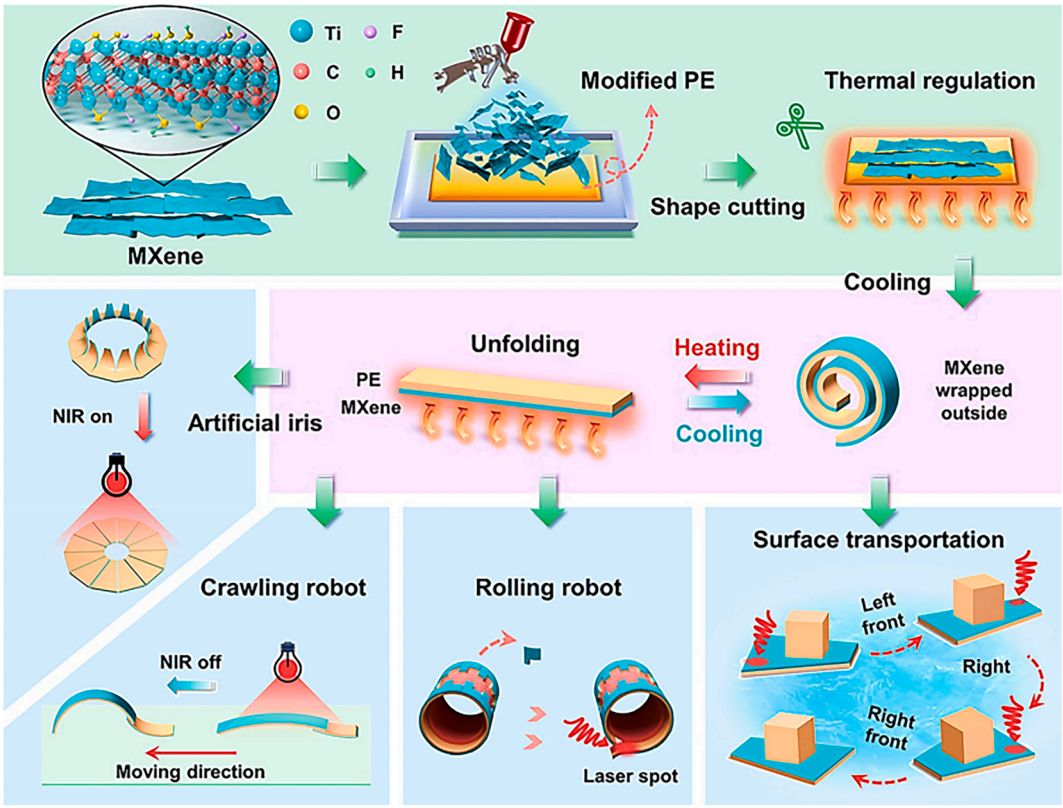

Fig. 49. MXene/LDPE bilayer actuators with many functions and configurable settings [893].

mW/cm^2) in its natural environment, it produces bending deformation with a maximum bending angle of 346°. In addition, a more authentic biomimetic robot, designed to resemble an actual inchworm, has been created. This robot can crawl on a fallen leaf in its natural habitat using solar energy as its power source (Fig. 50 d). Notably, while the "inchworm" crawls, as an ant on the leaf. The ant may be lured towards the "inchworm, " moving towards it by crawling, and establishing physical contact with it.

Using a conformal covering of MXene nanosheet frameworks on polymer chains composed of polyacrylamide and sodium alginate grafted with dopamine/phenylboronic acid, MXene-based nanocomposite hydrogels were created. For 10 days, the nanocomposite hydrogels showed remarkable self-adhesion and sustained moisture retention. These people worked on creating wearable epidermal sensors with outstanding stability to detect different types of human motions. These movements include significant deformations such as finger and wrist bending and subtle deformations like eating, pulse, and breathing [889].

Ma et al. [905] discovered that MXenes (Ti_3C_2) may form a uniform self-healing structure. They also observed that MXenes and graphene oxide can create a mixed self-healing structure when exposed to moisture treatment (Fig. 51). The hydration-induced expansion of MXenes and graphene oxide, along with the reunion of hydrogen-bond networks following the removal of water, were identified as the causes of the self-healing behaviour. Hydration significantly increased the MXenes and graphene oxide interlayer spacing, making it easier for MXene and GO sheets to intercalate at the damaged parts. After moisture treatment, the self-healing MXenes demonstrated impressive tractability and mechanical robustness by recovering their mechanical characteristics and conductivity to 487% of their original value. The grouping of MXenes and graphene oxide in multiform heterostructures can be used in the construction of freestanding soft electronics, such as temperature sensors or pressure sensors, as well as soft robotics. These heterostructures exhibit remarkable self-healing characteristics [905].

11.1. Actuation mechanism types

MXenes in soft robotics fall into numerous kinds dependent on their actuation method, which are briefly explained here. Hybrid systems may be created by combining or customizing actuation mechanisms for MXene soft robots, improving performance and capabilities. The following table lists the various actuation types and their advantages. Multiple kinds of actuation and its advantages are given in Table 12.

11.2. Influencing factors and considerations

The stability of MXenes is a crucial issue that must be resolved for their practical use. Various elements, including the chemical

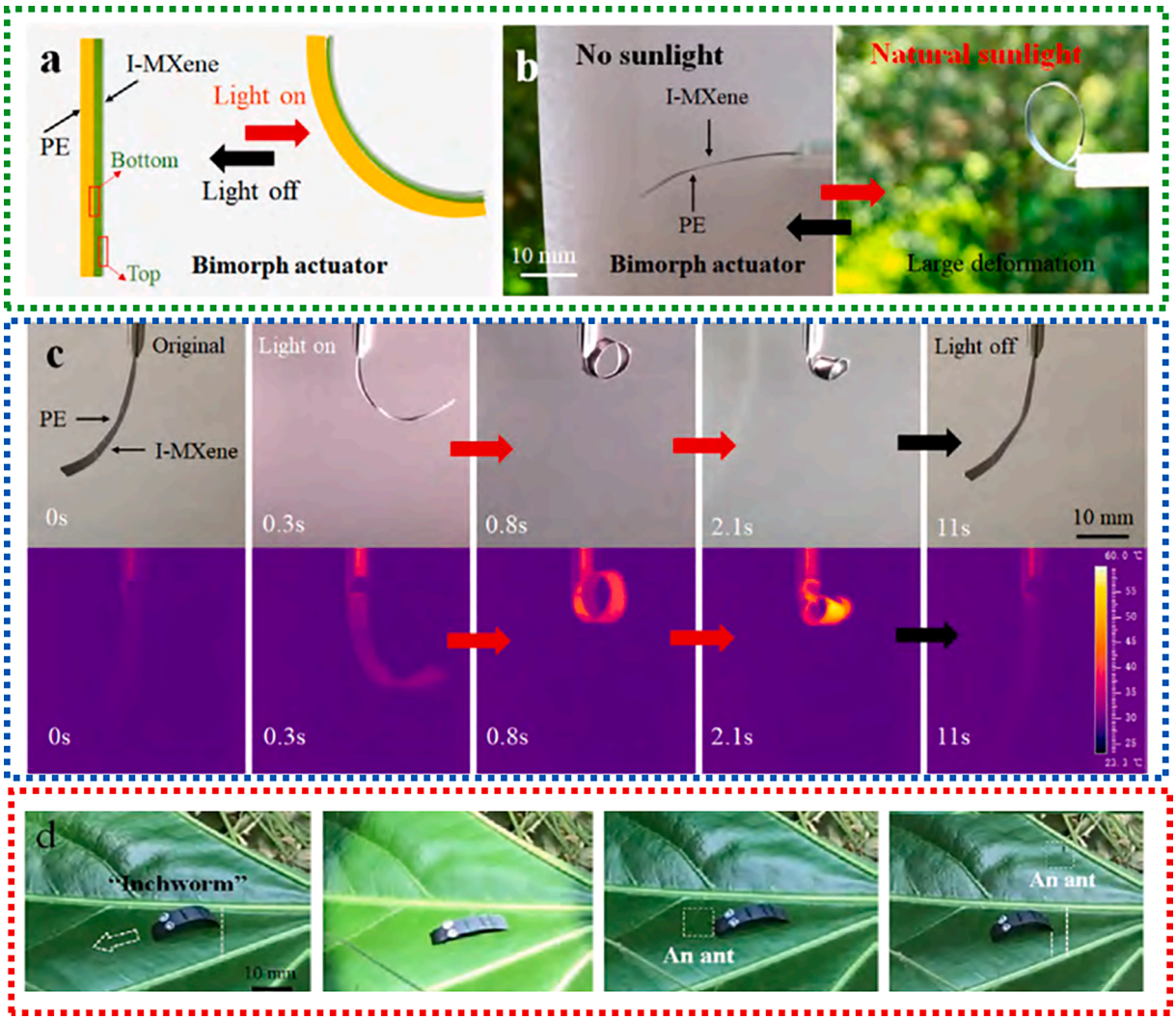

Fig. 50. Bimorph actuator operating due to solar radiation. (a) Diagrammatic illustration of the I-MXene/PE bimorph actuator. (b) Optical pictures show the bimorph actuator's reversible bending deformation under sunshine. (c) Photographic and IR thermal diagrams of the bimorph actuator's light-driven operation (d) Natural sunlight drives a biomimetic "inchworm" automaton to crawl in a specific route on a fallen leaf in its natural habitat. As the "inchworm" crawls over this leaf, an ant arrives and makes contact with it—reprint with permission [904].

environment and inherent qualities, as well as factors such as atmospheric conditions, temperature, chemical composition, microscopic structure, and the presence of water, might impact the structural integrity of MXenes.

Furthermore, much research has been conducted on utilizing graphene and its derivatives in developing electrostatic, electrothermal, and ionic actuators. The next step in this subject is comparative research to analyze the performance and features of these materials alongside MXenes. MXene-based materials have demonstrated significant promise for application in soft robotics owing to their distinctive characteristics, including mechanical robustness, electrical conductivity, and adjustability. However, certain drawbacks, obstacles, and restrictions are still associated with their properties and utilization that must be addressed, as elaborated in Table 13.

12. Challenges and Future Works

MXene-filled composite structures present a cutting-edge frontier in materials science, integrating the unique properties of MXenes, two-dimensional transition metal carbides or nitrides, with composite materials. The synthesis of these advanced structures poses multifaceted challenges, as achieving uniform dispersion and bonding between MXene layers and the composite matrix requires precision [479,919,920]. Controlling the loading levels of MXenes is crucial for optimizing mechanical, electrical, and thermal properties [531]. Achieving homogeneity and avoiding agglomeration during synthesis is a persistent challenge, demanding innovative techniques and methodologies [921,938]. Furthermore, the inherent reactivity of MXenes demands meticulous handling to

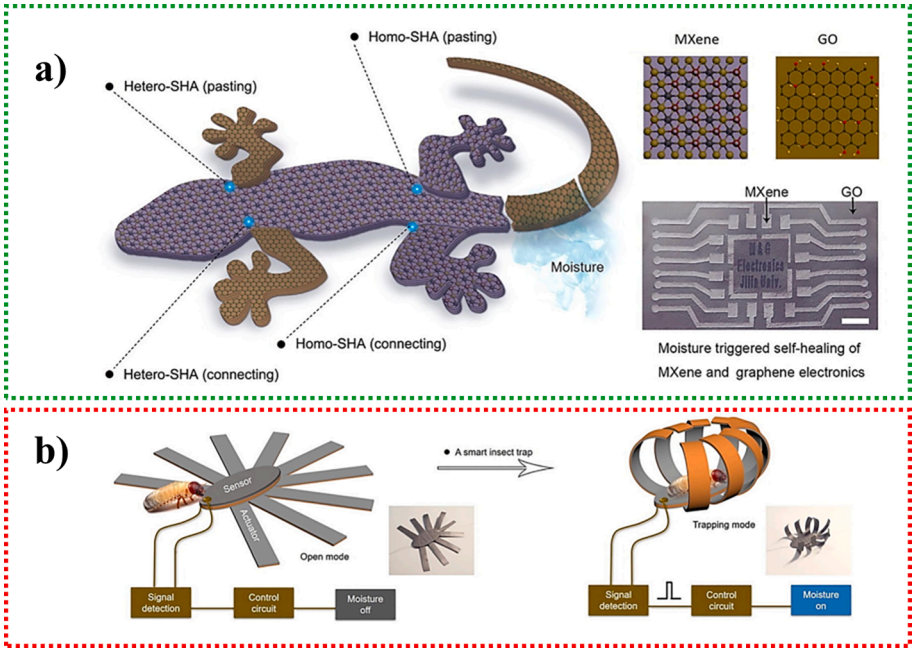

Fig. 51. (a) Strategies for self-healing assemblies (SHA). The MXene circuit with a graphene oxide (GO) layer was created via hetero-SHA. (b) MXene and GO hetero-SHA created smart insect traps and robots with integrated sensing and actuation capabilities—reprint with permission [47].

Table 12
Different actuation types and their advantages.

Actuation type	Description and advantages	References
Electrochemical actuation	- In the presence of various stimulis, MXene act as an actuator.- When an electrical stimulus is applied, electroactive polymers can change their shape or size.- These polymers can be used in soft robotic structures for precise and controlled movements.- These materials can be manipulated to achieve desired motions with the application of electric fields.- MXene bahve like a functional filler in an actuator made of electroactive polymers- The study also involved a MXene-Nafion composite actuator.	[906]
Pneumatic actuation	- Pneumatic actuation allows for flexibility and controllability in robot motion.- Pressurised air or other gases are used to drive the movement of MXene soft robots.- Robotic systems usually include soft and inflatable structures that can change shape or volume by pumping air in or out of them.	[907,908]
Shape memory actuation	Shape-memory alloys and polymers are certain actuator materials that can revert to their original shape after being distorted, often by applying heat or electrical stimuli. Soft robots using MXene may undergo form changes or be induced to move by applying heat or cold to the shape-memory alloys/polymers, enabling programmed movements.	[895,909]
Magnetic actuation	Magnetic fields may activate soft robots made from MXene materials. By integrating magnetic materials or composites containing MXene with magnetic particles, these robotic systems may be regulated and maneuvered utilizing an external magnetic field. An example of a dual-mode biomimetic soft actuator was created utilizing MXene film. This actuator has both electrothermal and magneto-responsive capabilities. It may be incorporated into the wings of a biomimetic dragonfly when exposed to a magnetic field.	[909,910]
Ionic actuation	Ionic actuation utilizes ionic fluids or gels as actuators in soft robotics. Hence, when an electric field is provided, ions within the liquid or gel undergo migration, leading to the actuator's expansion, contraction, or bending, ultimately resulting in the robot's movement.	[910]
Photo responsive actuators	Photothermal actuators use the formation of heat by light to initiate mechanical motion or actuation. This is achieved by using the expansion or contraction caused by the thermal effects to provide the necessary mechanical movement for actuation. The actuation mechanism often uses a material that absorbs light energy and experiences a photothermal effect, resulting in localized heating and subsequent expansion or contraction. Among the materials presented, MXenes stand out due to their distinctive photothermal capabilities. Their unique layered structure and metallic conductivity make them ideal candidates for photothermal actuation. MXenes, when subjected to light, undergo photon absorption and then transform the optical energy into heat via mechanisms including plasmon resonance or inter-band transitions.	[911,912]

prevent oxidation or other chemical transformations during the synthesis process, adding complexity to the production of these materials [922].

Regarding properties, the challenge lies in harnessing the full potential of MXene-filled composites while maintaining structural integrity. Achieving a balance between enhanced mechanical strength, electrical conductivity, and thermal stability requires a nuanced understanding of the interaction between MXene layers and the composite matrix [478,923]. Additionally, the scalability of synthesis processes poses a challenge in realizing large-scale applications [914]. Integrating MXene-filled composite structures into 3D

Table 13
Limitations and considerations of MXene in Soft robotics.

Limitations	Reason	References
Fabrication Complexity	Synthesis and assembly procedures often require aggressive chemicals and specialized equipment, which limits the potential for scaling up and making MXene-based soft robotics more accessible. However, the extent of these limitations may vary depending on the particular applications and desired characteristics.	[895]
Artificial energy requirement	Specific soft actuators based on MXene materials need an external energy input, such as an electric field, to operate. This dependency might impose restrictions on their use in real-world scenarios.	[913]
Multi-stimulus response	Certain soft actuators based on MXene materials have a restricted range of responsiveness, limited to just one specific stimulus, such as heat or light. This lack of variety hinders their adaptability and flexibility. Therefore, it is crucial to build soft actuators based on MXene that can respond to many stimuli, such as natural sunlight, human touch, and other sources.	[913]
Flexibility	MXene-based materials have excellent mechanical capabilities, but their flexibility must be enhanced to be effectively used in soft robotics applications. These materials often have less stretchability than soft materials widely used in soft robotics, such as elastomers or hydrogels. The limited extensibility of soft robotic systems may impede their capacity to achieve a wide range of motion or deformation.	[900]
Cost and scalability	The primary economic issue for MXenes is the expense involved with its manufacturing. Manufacturing MXene-based products on a wide scale may be expensive and require significant resources owing to the intricate and multi-step synthesis and processing involved. Furthermore, the cost of MXenes may be influenced by the raw materials needed, namely the MAX phase precursors. Specific precursors, such as titanium, tantalum, and niobium, are comparatively costly.	[914]
Conductivity	MXenes exhibit high electrical conductivity, although moisture absorption or tension may influence their electrical characteristics. Ensuring stable and dependable electrical conductivity in soft robotics systems based on MXene may be difficult, particularly when exposed to deformation or environmental changes.	[477]
Thermal stability	MXene compositions may have a limited capacity to withstand high temperatures, which may restrict the circumstances in which MXene-based soft robotic devices can operate. This is particularly true when the devices are exposed to excessive temperatures or undergo thermal cycling.	[915]
Actuation capability	MXene-based materials have restricted inherent actuation capabilities, implying that they may not inherently demonstrate a substantial change in form or motion in response to external stimuli. MXene-based soft robotic systems may need additional actuation mechanisms or integration with other materials to achieve the necessary actuation.	[47]
Biocompatibility	Despite attempts to enhance the biocompatibility of MXenes/derivatives, several MXenes still demonstrate cytotoxicity or negative responses in biological systems. The constraint presents difficulties for MXene-based soft robots designed for biomedical applications.	[312]
Complexity in integration	Integrating MXene-based materials with other components or structures in soft robotics might be difficult. The distinct mechanical characteristics, adhesion challenges, and compatibility concerns between MXenes and other materials may require specific bonding methods or interface engineering tactics.	[916]
Environmental factors	MXenes/derivatives may require chemicals and energy-intensive procedures, resulting in environmental consequences if not well controlled.	[917,918]

printing methodologies introduces challenges related to printability, layer adhesion, and post-processing techniques [33]. Moreover, the effective integration of machine learning in the design and optimization of these materials demands the development of robust algorithms capable of navigating the complex parameter space associated with MXene-filled composites [924]. As researchers strive to unlock the full potential of these materials, addressing these challenges will be pivotal in advancing their synthesis, understanding their properties, and unlocking their diverse applications across various industries.

1. **Synthesis Challenges**:
   - o Achieving uniform dispersion and bonding between MXene layers and the composite matrix remains a complex task, requiring precise methodologies.
   - o Controlling MXene loading levels is critical to optimizing mechanical, electrical, and thermal properties, but achieving homogeneity without agglomeration is a persistent challenge.
   - o Preventing oxidation and other chemical transformations during MXene synthesis demands meticulous handling and advanced stabilization techniques.
2. **Property Optimization Challenges**:
   - o Balancing enhanced mechanical strength, electrical conductivity, and thermal stability requires a nuanced understanding of the MXene-matrix interaction.
   - o Maintaining structural integrity while harnessing MXene properties is critical for large-scale applications.
3. **Scalability and Integration Challenges**:
   - o Scaling up synthesis processes to industrial levels while maintaining cost-effectiveness and reproducibility remains a major obstacle.
   - o Incorporating MXene-filled composites into 3D printing processes introduces challenges in printability, layer adhesion, and post-processing optimization.
   - o Developing robust machine learning algorithms to navigate the complex parameter space of MXene-filled composites for design and optimization is still in its infancy.

The future of MXene-filled composite structures promises a dynamic landscape of research and innovation across multiple fronts. In the realm of synthesis, efforts will be directed towards refining existing methods and developing novel approaches to enhance the

scalability [925], reproducibility [926], and cost-effectiveness of production [927]. Researchers will explore advanced techniques to achieve precise control over MXene loading levels and distribution within the composite matrix, ensuring optimal synergy between the two components [928,929]. Additionally, strategies to mitigate challenges related to the reactivity of MXenes during synthesis will be a focal point, with the aim of expanding the range of applicable composite materials [930].

In terms of properties, future work will delve deeper into understanding the intricate relationships between MXene composition [571], orientation [161], and the resulting mechanical, electrical, and thermal characteristics of the composites [931]. This knowledge will inform the design of tailored MXene-filled materials with optimized properties for specific applications. Furthermore, the integration of MXene-filled composites into 3D printing methodologies [616,932] will witness advancements as researchers explore new printing techniques [933], optimized formulations [934], and post-processing methods to enhance printability and overall structural integrity [40,939]. The synergy between machine learning and MXene-filled composite structures will be a key area of exploration, with the development of sophisticated algorithms capable of predicting material behavior, guiding synthesis parameters, and optimizing performance across diverse applications [38,935-937]. The collaborative efforts of material scientists, engineers, and data scientists will drive the evolution of MXene-filled composite structures, unlocking their full potential and paving the way for transformative applications in areas such as energy storage, flexible electronics, and advanced structural materials.

1. **Advances in Synthesis Techniques**:
   - o Refining existing synthesis methods and developing novel approaches to enhance scalability, reproducibility, and cost efficiency.
   - o Exploring advanced techniques to precisely control MXene loading levels and achieve uniform distribution in the composite matrix.
   - o Developing strategies to mitigate the reactivity of MXenes during synthesis to expand their compatibility with a wider range of composite materials.
2. **Deepening Property Understanding**:
   - o Investigating the relationships between MXene composition, orientation, and the resulting mechanical, electrical, and thermal properties to design tailored materials for specific applications.
3. **Enhancing 3D Printing Integration**:
   - o Advancing 3D and 4D printing methodologies by exploring new techniques, optimized formulations, and post-processing methods to improve printability and structural integrity.
4. **Synergy with Machine Learning**:
   - o Developing sophisticated algorithms to predict material behavior, guide synthesis parameters, and optimize performance across diverse applications [33,895-897].
5. **Broadening Applications**:
   - o Expanding the use of MXene-filled composites in transformative fields, including energy storage, flexible electronics, and advanced structural materials, with a focus on real-world applications.

13. Conclusions

This paper has given an extensive overview of MXene-filled composite structures, including their synthesis, characteristics, uses, and integration with cutting-edge manufacturing processes like 3D and 4D printing. MXenes are extremely promising materials for a variety of applications, such as energy storage, sensing, electromagnetic interference shielding, and biomedical devices, due to their flexibility and tunability. Additionally, the synthesis and design of materials based on MXene have the potential to be revolutionized by integrating AI and machine learning approaches, opening the door to creating sophisticated functional composites with customized features. MXene-filled composite structures are predicted to become more commonplace in various sectors as this field of study progresses, providing creative answers to urgent technical problems. More research and development is necessary to fully use MXenes' potential and to optimize their influence across a variety of application areas.

- MXene-filled composites exhibit exceptional mechanical, electrical, and thermal properties, making them highly versatile for applications in energy storage, aerospace, biomedical, and environmental fields.
- Advanced synthesis methods, including chemical etching, intercalation, and functionalization, enable fine-tuning of MXene properties, significantly enhancing their compatibility and performance in various matrices.
- Integration of MXene composites into 3D/4D printing technologies provides unparalleled design flexibility, enabling the fabrication of complex structures with high precision and tailored functionalities.
- The role of machine learning in MXene research is transformative, accelerating material discovery, optimizing synthesis protocols, and predicting properties with high accuracy (>90%), offering a data-driven approach to material innovation.
- This review presents a multidisciplinary perspective, bridging material science, additive manufacturing, and artificial intelligence, to pave the way for next-generation MXene applications and inspire advancements in sustainable technologies.

However, several challenges remain unresolved, including understanding long-term stability, overcoming synthesis scalability issues, and addressing environmental concerns related to MXene production and degradation. Future efforts should focus on addressing these gaps by developing robust fabrication techniques and leveraging advanced computational tools to predict and optimize composite behavior. Overall, this review emphasizes the importance of MXene-filled composite materials and draws attention to the fascinating prospects for more study and advancement in this quickly developing area.

CRediT authorship contribution statement

Vimukthi Dananjaya: Writing – review & editing, Writing – original draft, Validation, Software, Resources, Methodology, Investigation, Formal analysis, Data curation, Conceptualization. **Nethmi Hansika:** Writing – review & editing, Writing – original draft, Software, Methodology, Investigation, Formal analysis, Data curation. **Sathish Marimuthu:** Writing – review & editing, Writing – original draft, Software, Resources, Investigation. **Venkata Chevali:** Writing – review & editing, Writing – original draft, Software, Resources, Investigation. **Yogendra Kumar Mishra:** Writing – review & editing, Writing – original draft. **Andrews Nirmala Grace:** Writing – review & editing, Writing – original draft, Conceptualization. **Nisa Salim:** Writing – review & editing, Writing – original draft, Visualization, Validation, Supervision, Resources, Formal analysis, Conceptualization. **Chamil Abeykoon:** Writing – review & editing, Writing – original draft, Visualization, Validation, Supervision, Software, Resources, Project administration, Methodology, Conceptualization.

Declaration of competing interest

The authors declare that they have no known competing financial interests or personal relationships that could have appeared to influence the work reported in this paper.

Data availability

No data was used for the research described in the article.

References

[1] Hong W, Wyatt BC, Nemani SK, Anasori B. Double transition-metal MXenes: Atomistic design of two-dimensional carbides and nitrides. MRS Bull 2020;45:850–61. https://doi.org/10.1557/mrs.2020.251.
[2] Dananjaya SAV, Priyanka UMS, Somarathna YR, Karunanayake L, Siriwardena S. A comparative study on mica waste-filled natural rubber foam composites made out of creamed and centrifuged latex. Journal of Vinyl and Additive Technology 2022;28:907–19. https://doi.org/10.1002/vnl.21937.
[3] Dananjaya SAV, Somarathna YR, Karunanayake L, Siriwardena S. Physical properties of natural rubber latex foams produced with processed mica waste powder and creamed natural rubber latex. Journal of the Rubber Research Institute of Sri Lanka 2022;102:1–10. https://doi.org/10.4038/jrrisl.v102i1.1908.
[4] Yuan Y, Abeykoon C, Mirihanage W, Fernando A, Kao YC, Harings JAW. Prediction of temperature and crystal growth evolution during 3D printing of polymeric materials via extrusion. Mater Des 2020;196:109121. https://doi.org/10.1016/j.matdes.2020.109121.
[5] Abeykoon C, Zhu C, Fernando A. The Effect of Process Settings and Materials Properties on Mechanical Properties of 3D Printed Structures. 2022.
[6] Dananjaya V, Somarathna Y, Siriwardena S, Sirimuthu N, Karunanayake L, Abeykoon C. Effects of Latex Type and Processed-Mica Waste Loading on the Structural and Thermo-Physical Properties of Natural Rubber Latex Foam Composites. International Journal of Lightweight Materials and Manufacture 2023. https://doi.org/10.1016/j.ijlmm.2023.12.002.
[7] Dananjaya V, Marimuthu S, Yang (Chunhui) R, Grace AN, Abeykoon C. Synthesis, properties, applications, 3D printing and machine learning of graphene quantum dots in polymer nanocomposites. Prog Mater Sci 2024;144:101282. https://doi.org/10.1016/j.pmatsci.2024.101282.
[8] Sariga BAM, Kumar S, Rajeev R, Thadathil DA, Varghese A. New Horizons in the Synthesis, Properties, and Applications of MXene Quantum Dots. Adv Mater Interfaces 2023;10:2202139. https://doi.org/10.1002/admi.202202139.
[9] Vahidifar A, Nouri Khorasani S, Park CB, Naguib HE, Khonakdar HA. Fabrication and Characterization of Closed-Cell Rubber Foams Based on Natural Rubber/Carbon Black by One-Step Foam Processing. Ind Eng Chem Res 2016;55:2407–16. https://doi.org/10.1021/acs.iecr.5b04448.
[10] Soomro RA, Zhang P, Fan B, Wei Y, Xu B. Progression in the Oxidation Stability of MXenes. Nanomicro Lett 2023;15:108. https://doi.org/10.1007/s40820-023-01069-7.
[11] Bae S, Kang YG, Khazaei M, Ohno K, Kim YH, Han MJ, et al. Electronic and magnetic properties of carbide MXenes—the role of electron correlations. Mater Today Adv 2021;9:100118. https://doi.org/10.1016/j.mtadv.2020.100118.
[12] Li G, Lian S, Wang J, Xie G, Zhang N, Xie X. Surface chemistry engineering and the applications of MXenes. Journal of Materiomics 2023;9:1160–84. https://doi.org/10.1016/j.jmat.2023.08.003.
[13] Kosnan MA, Azam MA, Safie NE, Munawar RF, Takasaki A. Recent Progress of Electrode Architecture for MXene/MoS2 Supercapacitor: Preparation Methods and Characterizations. Micromachines (Basel) 2022;13. https://doi.org/10.3390/mi13111837.
[14] Irfan MS, Ali MA, Khan T, Anwer S, Liao K, Umer R. MXene and graphene coated multifunctional fiber reinforced aerospace composites with sensing and EMI shielding abilities. Compos Part A Appl Sci Manuf 2023;165:107351. https://doi.org/10.1016/j.compositesa.2022.107351.
[15] Garg R, Vitale F. Latest advances on MXenes in biomedical research and health care. MRS Bull 2023;48:283–90. https://doi.org/10.1557/s43577-023-00480-0.
[16] Sun Y, Li Y. Potential environmental applications of MXenes: A critical review. Chemosphere 2021;271:129578. https://doi.org/10.1016/j.chemosphere.2021.129578.
[17] Yu Z, Feng W, Lu W, Li B, Yao H, Zeng K, et al. MXenes with tunable work functions and their application as electron- and hole-transport materials in non-fullerene organic solar cells. J Mater Chem A Mater 2019;7:11160–9. https://doi.org/10.1039/c9ta01195a.
[18] Guan G, Guo F. A Review of Nb2CTx MXene: Synthesis, Properties and Applications. Batteries 2023;9. https://doi.org/10.3390/batteries9040235.
[19] Zhu Q, Li J, Simon P, Xu B. Two-dimensional MXenes for electrochemical capacitor applications: Progress, challenges and perspectives. Energy Storage Mater 2021;35:630–60. https://doi.org/10.1016/j.ensm.2020.11.035.
[20] Sun Y, Dall'Agnese C, Zhang C, Yang L, Jin X, Dall'Agnese Y, et al. Applications of MXenes and their composites in catalysis and photoelectrocatalysis. In: Sadasivuni KK, Deshmukh K, Pasha SKK, Kovářík TBT-M and their C, editors. MXenes and their Composites: Synthesis, Properties and Potential Applications, Elsevier; 2021, p. 449–98. doi: 10.1016/B978-0-12-823361-0.00007-1.
[21] Xie K, Wang J, Xu S, Hao W, Zhao L, Huang L, et al. Application of Two-Dimensional MXene materials in sensors. Mater Des 2023;228:111867. https://doi.org/10.1016/j.matdes.2023.111867.
[22] Sana SS, Santhamoorthy M, Haldar R, Raorane CJ, Iravani S, Varma RS, et al. Recent advances on MXene-based hydrogels for antibacterial and drug delivery applications. Process Biochemistry 2023;132:200–20. https://doi.org/10.1016/j.procbio.2023.06.022.
[23] Iravani S, Varma RS. MXenes and MXene-based materials for tissue engineering and regenerative medicine: Recent advances. Mater Adv 2021;2:2906–17. https://doi.org/10.1039/d1ma00189b.
[24] Huang M, Gu Z, Zhang J, Zhang D, Zhang H, Yang Z, et al. MXene and black phosphorus based 2D nanomaterials in bioimaging and biosensing: progress and perspectives. J Mater Chem B 2021;9:5195–220. https://doi.org/10.1039/d1tb00410g.

[25] Dananjaya SAV, Somarathna YR, Karunanayake L, Siriwardena S. Waste mica as filler for natural rubber latex foam composites. Journal of Polymer Research 2022;29:71. https://doi.org/10.1007/s10965-022-02930-w.
[26] Dananjaya SAV, Chevali VS, Dear JP, Potluri P, Abeykoon C. 3D printing of biodegradable polymers and their composites – Current state-of-the-art, properties, applications, and machine learning for potential future applications. Prog Mater Sci 2024;146:101336. https://doi.org/10.1016/j.pmatsci.2024.101336.
[27] Salas A, Pazniak H, Gonzalez-Julian J, Bianco S, Amici J, Ouisse T, et al. Development of polymeric/MXenes composites towards 3D printable electronics. Compos B Eng 2023;263:110854. https://doi.org/10.1016/j.compositesb.2023.110854.
[28] Redondo E, Pumera M. MXene-functionalised 3D-printed electrodes for electrochemical capacitors. Electrochem Commun 2021;124:106920. https://doi.org/10.1016/j.elecom.2021.106920.
[29] Zhou G, Li MC, Liu C, Wu Q, Mei C. 3D Printed Ti3C2Tx MXene/Cellulose Nanofiber Architectures for Solid-State Supercapacitors: Ink Rheology, 3D Printability, and Electrochemical Performance. Adv Funct Mater 2022;32:2109593. https://doi.org/10.1002/adfm.202109593.
[30] Orangi J, Hamade F, Davis VA, Beidaghi M. 3D Printing of Additive-Free 2D Ti3C2Tx (MXene) Ink for Fabrication of Micro-Supercapacitors with Ultra-High Energy Densities. ACS Nano 2020;14:640–50. https://doi.org/10.1021/acsnano.9b07325.
[31] Huang X, Huang J, Yang D, Wu P. A Multi-Scale Structural Engineering Strategy for High-Performance MXene Hydrogel Supercapacitor Electrode. Advanced Science 2021;8. https://doi.org/10.1002/advs.202101664.
[32] Li K, Zhao J, Zhussupbekova A, Shuck CE, Hughes L, Dong Y, et al. 4D printing of MXene hydrogels for high-efficiency pseudocapacitive energy storage. Nat Commun 2022;13:6884. https://doi.org/10.1038/s41467-022-34583-0.
[33] Osman A, Liu H, Lu J. Sacrificial 3D printing to fabricate MXene-based wearable sensors with tunable performance. Chemical Engineering Journal 2024;484:149461. https://doi.org/10.1016/j.cej.2024.149461.
[34] Vertina EW, Aaron Deskins N, Sutherland E, Mangoubi O. Predicting MXene Properties via Machine Learning. Proceedings - 21st IEEE International Conference on Machine Learning and Applications, ICMLA 2022 2022:1573–8. doi: 10.1109/ICMLA55696.2022.00278.
[35] Tian S, Zhou K, Huang CQ, Qian C, Gao Z, Liu Y. Investigation and understanding of the mechanical properties of MXene by high-throughput computations and interpretable machine learning. Extreme Mech Lett 2022;57:101921. https://doi.org/10.1016/j.eml.2022.101921.
[36] Ajmal Z, Hayat A, Qadeer A, Zhao Y, Ibrahim EH, Haq M ul, et al. Advancements in MXene-based frameworks towards photocatalytic hydrogen production, carbon dioxide reduction and pollutant degradation: Current challenges and future prospects. Coord Chem Rev 2025;523:216226. doi: 10.1016/J.CCR.2024.216226.
[37] Hayat A, Bashir T, Ahmed AM, Ajmal Z, Alghamdi MM, El-Zahhar AA, et al. Novel 2D MBenes-synthesis, structure, properties with excellent performance in energy conversion and storage: A review. Materials Science and Engineering: R: Reports 2024;159:100796. https://doi.org/10.1016/J.MSER.2024.100796.
[38] Li S, Barnard AS. Multi-target neural network predictions of MXenes as high-capacity energy storage materials in a Rashomon set. Cell Rep Phys Sci 2023;4:101675. https://doi.org/10.1016/j.xcrp.2023.101675.
[39] Rong C, Zhou L, Zhang B, Xuan FZ. Machine learning for mechanics prediction of 2D MXene-based aerogels. Composites Communications 2023;38:101474. https://doi.org/10.1016/j.coco.2022.101474.
[40] Tang H, Wang R, Shi L, Sheremet E, Rodriguez RD, Sun J. Post-processing strategies for improving the electrical and mechanical properties of MXenes. Chemical Engineering Journal 2021;425:131472. https://doi.org/10.1016/j.cej.2021.131472.
[41] Khatri Y, Atpadkar V, Agarwal A, Kashyap A. Magnetic MXene: A Machine-Learning Model With Small Data. IEEE Trans Magn 2023;59:1–5. https://doi.org/10.1109/TMAG.2023.3287988.
[42] Diedkova K, Pogrebnjak AD, Kyrylenko S, Smyrnova K, Buranich VV, Horodek P, et al. Polycaprolactone-Mxene nanofibrous scaffolds for tissue engineering. ACS Appl Mater Interfaces 2023;15:14033–47. https://doi.org/10.1021/acsami.2c22780.
[43] Driscoll N, Erickson B, Murphy BB, Richardson AG, Robbins G, Apollo NV, et al. MXene-infused bioelectronic interfaces for multiscale electrophysiology and stimulation. Sci Transl Med 2021;13. https://doi.org/10.1126/scitranslmed.abf8629.
[44] He M, Zhang L. Machine learning and symbolic regression investigation on stability of MXene materials. Comput Mater Sci 2021;196:110578. https://doi.org/10.1016/j.commatsci.2021.110578.
[45] Yang H, Li J, Xiao X, Wang J, Li Y, Li K, et al. Topographic design in wearable MXene sensors with in-sensor machine learning for full-body avatar reconstruction. Nat Commun 2022;13:5311. https://doi.org/10.1038/s41467-022-33021-5.
[46] Wang Y, Guo T, Tian Z, Shi L, Barman SC, Alshareef HN. MXenes for soft robotics. Matter 2023;6:2807–33. https://doi.org/10.1016/j.matt.2023.07.013.
[47] Iravani S. Role of MXenes in advancing soft robotics. Soft Matter 2023;19:6196–212. https://doi.org/10.1039/d3sm00756a.
[48] Pang J, Peng S, Hou C, Wang X, Wang T, Cao Y, et al. Applications of MXenes in human-like sensors and actuators. Nano Res 2023;16:5767–95. https://doi.org/10.1007/s12274-022-5272-8.
[49] Yang H, Wu W. A review: Machine learning for strain sensor-integrated soft robots. Frontiers in Electronic Materials 2022;2:1–8. https://doi.org/10.3389/femat.2022.1000781.
[50] Duan S, Lin Y, Zhang C, Li Y, Zhu D, Wu J, et al. Machine-learned, waterproof MXene fiber-based glove platform for underwater interactivities. Nano Energy 2022;91:106650. https://doi.org/10.1016/j.nanoen.2021.106650.
[51] Garg R, Patra NR, Samal S, Babbar S, Parida K. A review on accelerated development of skin-like MXene electrodes: from experimental to machine learning. Nanoscale 2023;15:8110–33. https://doi.org/10.1039/d2nr05969j.
[52] Li X, Huang Z, Shuck CE, Liang G, Gogotsi Y, Zhi C. MXene chemistry, electrochemistry and energy storage applications. Nature Reviews Chemistry 2022 6:6 2022;6:389–404. doi: 10.1038/s41570-022-00384-8.
[53] Maleki A, Ghomi M, Nikfarjam N, Akbari M, Sharifi E, Shahbazi MA, et al. Biomedical Applications of MXene-Integrated Composites: Regenerative Medicine, Infection Therapy, Cancer Treatment, and Biosensing. Adv Funct Mater 2022;32:2203430. https://doi.org/10.1002/ADFM.202203430.
[54] Yang W, Yang J, Byun JJ, Moissinac FP, Xu J, Haigh SJ, et al. 3D Printing of Freestanding MXene Architectures for Current-Collector-Free Supercapacitors. Advanced Materials 2019;31:1902725. https://doi.org/10.1002/ADMA.201902725.
[55] Qian C, Sun K, Bao W. Recent advance on machine learning of MXenes for energy storage and conversion. Int J Energy Res 2022;46:21511–22. https://doi.org/10.1002/ER.7833.
[56] Hassani N, Neek-Amal M. Simulative Molecular Modelling of MXene. Engineering Materials 2022:109–38. https://doi.org/10.1007/978-3-031-05006-0_6.
[57] Zhan C, Sun W, Xie Y, Jiang DE, Kent PRC. Computational Discovery and Design of MXenes for Energy Applications: Status, Successes, and Opportunities. ACS Appl Mater Interfaces 2019;11:24885–905. https://doi.org/10.1021/acsami.9b00439.
[58] Wu T, Jiang DE. Computational studies of MXenes. MRS Bull 2023;48:253–60. https://doi.org/10.1557/s43577-023-00499-3.
[59] Venkateshalu S, Tomboc GM, Kim B, Li J, Lee K. Ordered Double Transition Metal MXenes. ChemNanoMat 2022;8:e202200320. https://doi.org/10.1002/cnma.202200320.
[60] Abbasi NM, Xiao Y, Peng L, Duo Y, Wang L, Zhang L, et al. Recent Advancement for the Synthesis of MXene Derivatives and Their Sensing Protocol. Adv Mater Technol 2021;6. doi: 10.1002/admt.202001197.
[61] Guerrero-Sanchez J, Muñoz-Pizza DM, Moreno-Armenta MG, Takeuchi N. Atomic-scale understanding of the Na and Cl trapping on the Mo1.33C(OH)2-MXene. Sci Rep 2022;12:1.. https://doi.org/10.1038/s41598-022-12177-6.
[62] Meshkian R, Lind H, Halim J, El Ghazaly A, Thörnberg J, Tao Q, et al. Theoretical Analysis, Synthesis, and Characterization of 2D W1.33C (MXene) with Ordered Vacancies. ACS Appl Nano Mater 2019;2:6209–19. https://doi.org/10.1021/acsanm.9b01107.
[63] Meshkian R, Dahlqvist M, Lu J, Wickman B, Halim J, Thörnberg J, et al. W-Based Atomic Laminates and Their 2D Derivative W1.33C MXene with Vacancy Ordering. Advanced Materials 2018;30. https://doi.org/10.1002/adma.201706409.
[64] Mostafaei A, Abbasnejad M. Computational studies on the structural, electronic and optical properties of M2CT2 (M=Y, Sc and T=F, Cl) MXene monolayer. J Alloys Compd 2021;857:157982. https://doi.org/10.1016/j.jallcom.2020.157982.
[65] Hadler-Jacobsen J, Fagerli FH, Kaland H, Schnell SK. Stacking Sequence, Interlayer Bonding, Termination Group Stability and Li/Na/Mg Diffusion in MXenes. ACS Mater Lett 2021;3:1369–76. https://doi.org/10.1021/acsmaterialslett.1c00316.

[66] Wang L, Han M, Shuck CE, Wang X, Gogotsi Y. Adjustable electrochemical properties of solid-solution MXenes. Nano Energy 2021;88:106308. https://doi.org/10.1016/j.nanoen.2021.106308.

[67] Gao Z. Preparation of MXene and its application and research progress in supercapacitors. MATEC Web of Conferences 2023;382:01027. https://doi.org/10.1051/matecconf/202338201027.

[68] Zhou C, Zhao X, Xiong Y, Tang Y, Ma X, Tao Q, et al. A review of etching methods of MXene and applications of MXene conductive hydrogels. Eur Polym J 2022;167:111063. https://doi.org/10.1016/j.eurpolymj.2022.111063.

[69] Zhou J, Tao Q, Ahmed B, Palisaitis J, Persson I, Halim J, et al. High-Entropy Laminate Metal Carbide (MAX Phase) and Its Two-Dimensional Derivative MXene. Chemistry of Materials 2022;34:2098–106. https://doi.org/10.1021/acs.chemmater.1c03348.

[70] Mohseni-Salehi MS, Taheri-Nassaj E, Babaei A, Ghazvini AS, Soleimanzade M. Effect of temperature and atmosphere on V2AlC etching for V2CTx MXenes synthesis used as anode for Li-ion storage systems. J Energy Storage 2023;66:107462. https://doi.org/10.1016/j.est.2023.107462.

[71] Zhou J, Zha X, Zhou X, Chen F, Gao G, Wang S, et al. Synthesis and Electrochemical Properties of Two-Dimensional Hafnium Carbide. ACS Nano 2017;11:3841–50. https://doi.org/10.1021/acsnano.7b00030.

[72] Kumar S, Park HM, Singh T, Kumar M, Seo Y. Long-Term Stability Studies and Applications of Ti3C2Tx MXene. Int J Energy Res 2023;2023:5275439. https://doi.org/10.1155/2023/5275439.

[73] Halim J, Cook KM, Naguib M, Eklund P, Gogotsi Y, Rosen J, et al. X-ray photoelectron spectroscopy of select multi-layered transition metal carbides (MXenes). Applied Surface Science 2016;362:406–17. https://doi.org/10.1016/j.apsusc.2015.11.089.

[74] Bashir T, Ismail SA, Wang J, Zhu W, Zhao J, Gao L. MXene terminating groups [dbnd]O, –F or –OH, –F or [dbnd]O, –OH, –F, or [dbnd]O, –OH, –Cl? Journal of Energy Chemistry 2023;76:90–104. https://doi.org/10.1016/j.jechem.2022.08.032.

[75] Zhou H, Chen Z, Kountoupi E, Tsoukalou A, Abdala PM, Florian P, et al. Two-dimensional molybdenum carbide 2D-Mo2C as a superior catalyst for CO2 hydrogenation. Nat Commun 2021;12:5510. https://doi.org/10.1038/s41467-021-25784-0.

[76] Vovusha H, Bae H, Lee S, Park J, Raza A, Kotmool K, et al. Density Functional Theory Studies of MXene-Based Nanosensors for Detecting Volatile Organic Compounds in Meat Spoilage Assessment. ACS Appl Nano Mater 2023;6:18592–601. https://doi.org/10.1021/acsanm.3c03846.

[77] Naguib M, Barsoum M, Gogotsi Y. Ten Years of Progress in the Synthesis and Development of MXenes. Advanced Materials 2021;33:2103393. https://doi.org/10.1002/adma.202103393.

[78] Naguib M, Kurtoglu M, Presser V, Lu J, Niu J, Heon M, et al. Two-dimensional nanocrystals produced by exfoliation of Ti3ALC2. MXenes: From Discovery to Applications of Two-Dimensional Metal Carbides and Nitrides 2023;23:15–29. https://doi.org/10.1201/9781003306511-4.

[79] Pei Y, Zhang X, Hui Z, Zhou J, Huang X, Sun G, et al. Ti3C2TXMXene for Sensing Applications: Recent Progress, Design Principles, and Future Perspectives. ACS Nano 2021;15:3996–4017. https://doi.org/10.1021/acsnano.1c00248.

[80] Luo JQ, Zhao S, Zhang H Bin, Deng Z, Li L, Yu ZZ. Flexible, stretchable and electrically conductive MXene/natural rubber nanocomposite films for efficient electromagnetic interference shielding. Compos Sci Technol 2019;182:107754. doi:10.1016/j.compscitech.2019.107754.

[81] Wang Z, Cheng Z, Xie L, Hou X, Fang C. Flexible and lightweight Ti3C2Tx MXene/Fe3O4@PANI composite films for high-performance electromagnetic interference shielding. Ceram Int 2021;47:5747–57. https://doi.org/10.1016/j.ceramint.2020.10.161.

[82] Huang B, Zhou Z, Wei L, Song Q, Yu W, Zhou Y, et al. Ti3C2Tx MXene as a novel functional photo blocker for stereolithographic 3D printing of multifunctional gels via Continuous Liquid Interface Production. Compos B Eng 2021;225. https://doi.org/10.1016/j.compositesb.2021.109261.

[83] Li X, Bai Y, Shi X, Su N, Nie G, Zhang R, et al. Applications of MXene (Ti3C2T: X) in photocatalysis: A review. Mater Adv 2021;2:1570–94. https://doi.org/10.1039/d0ma00938e.

[84] Li X, Yin X, Liang S, Li M, Cheng L, Zhang L. 2D carbide MXene Ti 2 CT X as a novel high-performance electromagnetic interference shielding material. Carbon N Y 2019;146:210–7. https://doi.org/10.1016/j.carbon.2019.02.003.

[85] Xue N, Li X, Han L, Zhu H, Zhao X, Zhuang J, et al. Fluorine-free synthesis of ambient-stable delaminated Ti2CTx (MXene). J Mater Chem A Mater 2022;10:7960–7. https://doi.org/10.1039/d1ta09981g.

[86] Liu G, Shen J, Ji Y, Liu Q, Liu G, Yang J, et al. Two-dimensional Ti2CT: X MXene membranes with integrated and ordered nanochannels for efficient solvent dehydration. J Mater Chem A Mater 2019;7:12095–104. https://doi.org/10.1039/c9ta01507h.

[87] Yang Z, Yang Q, Tian Y, Ren X, Li C, Zu Y, et al. Few-layer Ti3CN MXene for ultrafast photonics applications in visible band. Journal of Materiomics 2023;9:44–55. https://doi.org/10.1016/j.jmat.2022.09.004.

[88] Li G, Du W, Sun S, Chen Z, Liu H, Lu Q, et al. Nanometer-Thin Stacks of MXenes (Ti3C2Txand Ta4C3Tx) for Applications as Nonlinear Photonic Devices. ACS Appl Nano Mater 2023;6:856–66. https://doi.org/10.1021/acsanm.2c04004.

[89] Liu M, Wu J, Wang C, Sun Z, Fan Z, Xin C. Asymmetric janus functionalities induced changes in structural, electronic, optical characteristics of MXenes Ta4C3Tx. Solid State Commun 2022;341:114585. https://doi.org/10.1016/j.ssc.2021.114585.

[90] Rafieerad A, Yan W, Alagarsamy KN, Srivastava A, Sareen N, Arora RC, et al. Fabrication of Smart Tantalum Carbide MXene Quantum Dots with Intrinsic Immunomodulatory Properties for Treatment of Allograft Vasculopathy. Adv Funct Mater 2021;31. doi: 10.1002/adfm.202106786.

[91] Rafieerad A, Amiri A, Sequiera GL, Yan W, Chen Y, Polycarpou AA, et al. Development of Fluorine-Free Tantalum Carbide MXene Hybrid Structure as a Biocompatible Material for Supercapacitor Electrodes. Adv Funct Mater 2021;31. https://doi.org/10.1002/adfm.202100015.

[92] Zhao S, Luo X, Cheng Y, Shi Z, Huang T, Yang S, et al. A flexible zinc ion hybrid capacitor integrated system with layers-dependent V2CTx MXene. Chemical Engineering Journal 2023;454. doi: 10.1016/j.cej.2022.140360.

[93] Yu T, Li S, Zhang L, Li F, Wang J, Pan H, et al. In situ growth of ZIF-67-derived nickel-cobalt-manganese hydroxides on 2D V2CTx MXene for dual-functional orientation as high-performance asymmetric supercapacitor and electrochemical hydroquinone sensor. J Colloid Interface Sci 2023;629:546–58. https://doi.org/10.1016/j.jcis.2022.09.107.

[94] Ye M, Shen J, Zhu X, Cao Z, Wang W, Li H, et al. Superior-performance aqueous zinc-ion batteries based on the in situ growth of mno2 nanosheets on V2CTX MXene. ACS Nano 2021;15:2971–83. https://doi.org/10.1021/acsnano.0c09205.

[95] Sha D, Lu C, He W, Ding J, Zhang H, Bao Z, et al. Surface Selenization Strategy for V2CTx MXene toward Superior Zn-Ion Storage. ACS Nano 2022;16:2711–20. https://doi.org/10.1021/acsnano.1c09639.

[96] Wang Z, Huang Z, Wang H, Li W, Wang B, Xu J, et al. 3D-Printed Sodiophilic V2CTx/rGO-CNT MXene Microgrid Aerogel for Stable Na Metal Anode with High Areal Capacity. ACS Nano 2022;16:9105–16. https://doi.org/10.1021/acsnano.2c01186.

[97] Yang L, Yang T, Chen Y, Zheng Y, Wang E, Du Z, et al. FeNi LDH/V2CTx/NF as Self-Supported Bifunctional Electrocatalyst for Highly Effective Overall Water Splitting. Nanomaterials 2022;12. https://doi.org/10.3390/nano12152640.

[98] Yuan Z, Wang L, Li D, Cao J, Han W. Carbon-Reinforced Nb2CTxMXene/MoS2Nanosheets as a Superior Rate and High-Capacity Anode for Sodium-Ion Batteries. ACS Nano 2021;15:7439–50. https://doi.org/10.1021/acsnano.1c00849.

[99] Huang J, Tao J, Liu G, Lu L, Tang H, Qiao G. In situ construction of 1D CdS/2D Nb2CTx MXene Schottky heterojunction for enhanced photocatalytic hydrogen production activity. Appl Surf Sci 2022;573. https://doi.org/10.1016/j.apsusc.2021.151491.

[100] Makola LC, Moeno S, Ouma CNM, Sharma A, Vo DVN, Dlamini LN. Facile fabrication of a metal-free 2D–2D Nb2CTx@g-C3N4 MXene-based Schottky-heterojunction with the potential application in photocatalytic processes. J Alloys Compd 2022;916. https://doi.org/10.1016/j.jallcom.2022.165459.

[101] Zhao Q, Jiang Y, Duan Z, Yuan Z, Zha J, Wu Z, et al. A Nb2CTx/sodium alginate-based composite film with neuron-like network for self-powered humidity sensing. Chemical Engineering Journal 2022;438. https://doi.org/10.1016/j.cej.2022.135588.

[102] Liu Z, El-Demellawi JK, Bakr OM, Ooi BS, Alshareef HN. Plasmonic Nb2C TxMXene-MAPbI3Heterostructure for Self-Powered Visible-NIR Photodiodes. ACS Nano 2022. https://doi.org/10.1021/acsnano.2c00558.

[103] Lipatov A, Loes MJ, Vorobeva NS, Bagheri S, Abourahma J, Chen H, et al. High Breakdown Current Density in Monolayer Nb4C3TxMXene. ACS Mater Lett 2021;3:1088–94. https://doi.org/10.1021/acsmaterialslett.1c00324.

[104] Zhao S, Chen C, Zhao X, Chu X, Du F, Chen G, et al. Flexible Nb4C3Tx Film with Large Interlayer Spacing for High-Performance Supercapacitors. Adv Funct Mater 2020;30. https://doi.org/10.1002/adfm.202000815.

[105] Wu F, Xu C, Yang X, Yang L, Yin S. S-doped multilayer niobium carbide (Nb4C3Tx) electrocatalyst for efficient hydrogen evolution in alkaline solutions. Int J Hydrogen Energy 2022;47:17233–40. https://doi.org/10.1016/j.ijhydene.2022.03.227.
[106] Tan Y, Zhu Z, Zhang X, Zhang J, Zhou Y, Li H, et al. Nb4C3Tx (MXene) as a new stable catalyst for the hydrogen evolution reaction. Int J Hydrogen Energy 2021;46:1955–66. https://doi.org/10.1016/j.ijhydene.2020.10.046.
[107] Arjun AM, Shabana N, Ankitha M, Rasheed PA. Electrochemical Deposition of Prussian Blue on Nb4c3tx Mxene Modified Carbon Cloth For the Non-Enzymatic Electrochemical Detection of Hydrogen Peroxide. SSRN Electronic Journal 2022. https://doi.org/10.2139/ssrn.4165888.
[108] Shabana N, Arjun AM, Rasheed PA. Exploring the catalytic activity of Nb4C3Tx MXene towards the degradation of nitro compounds and organic dyes by in situ decoration of palladium nanoparticles. New Journal of Chemistry 2022;46:13622–8. https://doi.org/10.1039/d2nj02315f.
[109] Thomas T, Kozhiparambil Chandran S, Kumar Y, Ramos Ramón JA, Agarwal V, Álvarez Méndez A, et al. Highly Stable, Fast Responsive Mo2ctx Mxene Sensors for Room Temperature Carbon Dioxide Detection. SSRN Electronic Journal 2022. https://doi.org/10.2139/ssrn.4022311.
[110] Zhou H, Chen Z, López AV, López ED, Lam E, Tsoukalou A, et al. Engineering the Cu/Mo2CTx (MXene) interface to drive CO2 hydrogenation to methanol. Nat Catal 2021;4:860–71. https://doi.org/10.1038/s41929-021-00684-0.
[111] Choi J, Chacon B, Park H, Hantanasirisakul K, Kim T, Shevchuk K, et al. N-p-Conductor Transition of Gas Sensing Behaviors in Mo2CTxMXene. ACS Sens 2022;7:2225–34. https://doi.org/10.1021/acssensors.2c00658.
[112] Yi M, Hu S, Li N, Wang H, Zhang J. Selenium vacancy-rich and heteroatom-doped CoSe/Mo2CTx MXene prepared using ionic liquid dopants for pH-universal hydrogen evolution and flexible supercapacitors. Journal of Energy Chemistry 2022;72:453–64. https://doi.org/10.1016/j.jechem.2022.05.040.
[113] Wang J, Liu Z, Zhang H, Wang J. Tailoring Magnetic Properties of MAX Phases, a Theoretical Investigation of (Cr2Ti)AlC2 and Cr2AlC. Journal of the American Ceramic Society 2016;99:3371–5. https://doi.org/10.1111/jace.14358.
[114] Anasori B, Dahlqvist M, Halim J, Moon EJ, Lu J, Hosler BC, et al. Experimental and theoretical characterization of ordered MAX phases Mo2TiAlC2 and Mo2Ti2AlC3. J Appl Phys 2015;118. https://doi.org/10.1063/1.4929640.
[115] Zhou J, Zha X, Chen FY, Ye Q, Eklund P, Du S, et al. A Two-Dimensional Zirconium Carbide by Selective Etching of Al3C3 from Nanolaminated Zr3Al3C5. Angewandte Chemie - International Edition 2016;55:5008–13. https://doi.org/10.1002/anie.201510432.
[116] Guo Y, Zhang X, Jin S, Xia Q, Chang Y, Wang L, et al. Synthesis of Mo2C MXene with high electrochemical performance by alkali hydrothermal etching. Journal of Advanced Ceramics 2023;12:1889–901. https://doi.org/10.26599/JAC.2023.9220795.
[117] Eliardsson P, Stenumgaard P. Artificial Intelligence for Automatic Classification of Unintentional Electromagnetic Interference in Air Traffic Control Communications. In: EMC Europe 2019–2019 International Symposium on Electromagnetic Compatibility; 2019. p. 896–901. https://doi.org/10.1109/EMCEurope.2019.8872082.
[118] Urbankowski P, Anasori B, Makaryan T, Er D, Kota S, Walsh PL, et al. Synthesis of two-dimensional titanium nitride Ti4N3 (MXene). Nanoscale 2016;8:11385–91. https://doi.org/10.1039/c6nr02253g.
[119] Djire A, Zhang H, Liu J, Miller EM, Neale NR. Electrocatalytic and Optoelectronic Characteristics of the Two-Dimensional Titanium Nitride Ti 4 N 3 T x MXene. ACS Appl Mater Interfaces 2019;11:11812–23. https://doi.org/10.1021/acsami.9b01150.
[120] Li G, Li T, Qiao W, Feng T, Feng C, Zhao J, et al. Passively Q-switched Er:Lu 2 O 3 laser with MXene material Ti 4 N 3 T x (T = F, O, or OH) as a saturable absorber. Opt Lett 2020;45:4256. https://doi.org/10.1364/ol.399317.
[121] Li T, Xiang C, Zou Y, Xu F, Sun L. Synthesis of highly stable cobalt nanorods anchored on a Ti4N3Tx MXene composite for the hydrolysis of sodium borohydride. J Alloys Compd 2021;885. https://doi.org/10.1016/j.jallcom.2021.160991.
[122] Pazniak H, Varezhnikov AS, Kolosov DA, Plugin IA, Di VA, Glukhova OE, et al. 2D Molybdenum Carbide MXenes for Enhanced Selective Detection of Humidity in Air. Advanced Materials 2021;33. https://doi.org/10.1002/adma.202104878.
[123] Urbankowski P, Anasori B, Hantanasirisakul K, Yang L, Zhang L, Haines B, et al. 2D molybdenum and vanadium nitrides synthesized by ammoniation of 2D transition metal carbides (MXenes). Nanoscale 2017;9:17722–30. https://doi.org/10.1039/c7nr06721f.
[124] Venkateshalu S, Cherusseri J, Karnan M, Kumar KS, Kollu P, Sathish M, et al. New Method for the Synthesis of 2D Vanadium Nitride (MXene) and Its Application as a Supercapacitor Electrode. ACS Omega 2020;5:17983–92. https://doi.org/10.1021/acsomega.0c01215.
[125] Mehta V, Srivastava S, Tankeshwar K, Saini HS. First principles study of Mo2N monolayer as potential anode material for na-ion batteries. AIP Conf Proc 2020;2265. https://doi.org/10.1063/5.0017690.
[126] Yin XZ, Wang H, Wang QH, Jiao N, Ni MY, Zheng MM, et al. Superconductivity Modulated by Carbonization and Hydrogenation in Two-Dimensional MXenes M 2N (M = Mo, W). Chinese Physics Letters 2023;40. https://doi.org/10.1088/0256-307X/40/9/097404.
[127] Khan S, Kumar N, Hussain T, Tit N. Functionalized Hf3C2 and Zr3C2 MXenes for suppression of shuttle effect to enhance the performance of sodium–sulfur batteries. J Power Sources 2023;580:233298. https://doi.org/10.1016/j.jpowsour.2023.233298.
[128] Ulbrich LM, Balbinot G de S, Brotto GL, Leitune VCB, Soares RMD, Collares FM, et al. 3D printing of poly(butylene adipate-co-terephthalate) (PBAT)/niobium containing bioactive glasses (BAGNb) scaffolds: Characterization of composites, in vitro bioactivity, and in vivo bone repair. J Tissue Eng Regen Med 2022;16:267–78. https://doi.org/10.1002/term.3276.
[129] Rasheed PA, Pandey RP, Banat F, Hasan SW. Recent advances in niobium MXenes: Synthesis, properties, and emerging applications. Matter 2022;5:546–72. https://doi.org/10.1016/j.matt.2021.12.021.
[130] Tran MH, Schäfer T, Shahraei A, Dürrschnabel M, Molina-Luna L, Kramm UI, et al. Adding a New Member to the MXene Family: Synthesis, Structure, and Electrocatalytic Activity for the Hydrogen Evolution Reaction of V4C3Tx. ACS Appl Energy Mater 2018;1:3908–14. https://doi.org/10.1021/acsaem.8b00652.
[131] Yu X, Yang Y, Si L, Cai J, Lu X, Sun Z. V4C3TX MXene: First-principles computational and separator modification study on immobilization and catalytic conversion of polysulfide in Li-S batteries. J Colloid Interface Sci 2022;627:992–1002. https://doi.org/10.1016/j.jcis.2022.07.082.
[132] Du CF, Yang L, Tang K, Fang W, Zhao X, Liang Q, et al. Ni nanoparticles/V4C3TxMXene heterostructures for electrocatalytic nitrogen fixation. Mater Chem Front 2021;5:2338–46. https://doi.org/10.1039/d0qm00898b.
[133] Du CF, Sun X, Yu H, Fang W, Jing Y, Wang Y, et al. V4C3Tx MXene: A promising active substrate for reactive surface modification and the enhanced electrocatalytic oxygen evolution activity. InfoMat 2020;2:950–9. https://doi.org/10.1002/inf2.12078.
[134] Bilibana MP. Electrochemical properties of MXenes and applications. Advanced Sensor and Energy Materials 2023;2:100080. https://doi.org/10.1016/j.asems.2023.100080.
[135] Lailatul Mufidah KT. No 主観的健康感を中心とした在宅高齢者における 健康関連指標に関する共分散構造分析Title 2021;7:6.
[136] Rahman UU, Humayun M, Ghani U, Usman M, Ullah H, Khan A, et al. MXenes as Emerging Materials: Synthesis, Properties, and Applications. Molecules 2022;27. https://doi.org/10.3390/molecules27154909.
[137] Noor U, Mughal MF, Ahmed T, Farid MF, Ammar M, Kulsum U, et al. Synthesis and applications of MXene-based composites: a review. Nanotechnology 2023;34. https://doi.org/10.1088/1361-6528/acc7a8.
[138] Natu V, Pai R, Sokol M, Carey M, Kalra V, Barsoum MW. 2D Ti3C2Tz MXene Synthesized by Water-free Etching of Ti3AlC2 in Polar Organic Solvents. Chem 2020;6:616–30. https://doi.org/10.1016/j.chempr.2020.01.019.
[139] Xu C, Chen L, Liu Z, Cheng HM, Ren W. Bottom-up synthesis of 2D transition metal carbides and nitrides. In: Anasori B, Gogotsi Y, editors. 2D Metal Carbides and Nitrides (MXenes): Structure, Properties and Applications. Cham: Springer International Publishing; 2019. p. 89–109. https://doi.org/10.1007/978-3-030-19026-2_6.
[140] Maleski K, Alhabeb M. Top-down MXene synthesis (selective etching). In: Anasori B, Gogotsi Y, editors. 2D Metal Carbides and Nitrides (MXenes): Structure, Properties and Applications. Cham: Springer International Publishing; 2019. p. 69–87. https://doi.org/10.1007/978-3-030-19026-2_5.
[141] Naguib M, Mochalin VN, Barsoum MW, Gogotsi Y. 25th anniversary article: MXenes: A new family of two-dimensional materials. Advanced Materials 2014;26:992–1005. https://doi.org/10.1002/adma.201304138.
[142] Amrillah T, Hermawan A, Alviani VN, Seh ZW, Yin S. MXenes and their derivatives as nitrogen reduction reaction catalysts: recent progress and perspectives. Mater Today Energy 2021;22:100864. https://doi.org/10.1016/j.mtener.2021.100864.

[143] Goossens N, Tunca B, Lapauw T, Lambrinou K, Vleugels J. MAX Phases, Structure, Processing, and Properties. Encyclopedia of Materials: Technical Ceramics and Glasses: Volume 1-3, vol. 2, 2021, p. V2-182-V2-199. doi: 10.1016/B978-0-12-818542-1.00015-1.
[144] Zhang Z, Duan X, Jia D, Zhou Y, van der Zwaag S. On the formation mechanisms and properties of MAX phases: A review. J Eur Ceram Soc 2021;41:3851–78. https://doi.org/10.1016/j.jeurceramsoc.2021.02.002.
[145] Aydinyan S. Combustion Synthesis of MAX Phases: Microstructure and Properties Inherited from the Processing Pathway. Crystals (Basel) 2023;13. https://doi.org/10.3390/cryst13071143.
[146] Nashim A, Parida K. A Glimpse on the plethora of applications of prodigious material MXene. Sustainable Materials and Technologies 2022;32:e00439. https://doi.org/10.1016/j.susmat.2022.e00439.
[147] Jun BM, Kim S, Heo J, Park CM, Her N, Jang M, et al. Review of MXenes as new nanomaterials for energy storage/delivery and selected environmental applications. Nano Res 2019;12:471–87. https://doi.org/10.1007/s12274-018-2225-3.
[148] Dahlqvist M, Barsoum MW, Rosen J. MAX phases – Past, present, and future. Materials Today 2024;72:1–24. https://doi.org/10.1016/j.mattod.2023.11.010.
[149] Mane RB, Haribabu A, Panigrahi BB. Synthesis and sintering of Ti3GeC2 MAX phase powders. Ceram Int 2018;44:890–3. https://doi.org/10.1016/j.ceramint.2017.10.017.
[150] Lamiel C, Hussain I, Warner JH, Zhang K. Beyond Ti-based MXenes: A review of emerging non-Ti based metal-MXene structure, properties, and applications. Materials Today 2023;63:313–38. https://doi.org/10.1016/j.mattod.2023.01.020.
[151] Kubitza N, Büchner C, Sinclair J, Snyder RM, Birkel CS. Extending the Chemistry of Layered Solids and Nanosheets: Chemistry and Structure of MAX Phases, MAB Phases and MXenes. Chempluschem 2023;88:e202300214. https://doi.org/10.1002/cplu.202300214.
[152] Gogotsi Y. The Future of MXenes. Chemistry of Materials 2023;35:8767–70. https://doi.org/10.1021/acs.chemmater.3c02491.
[153] Sokol M, Natu V, Kota S, Barsoum MW. On the Chemical Diversity of the MAX Phases. Trends Chem 2019;1:210–23. https://doi.org/10.1016/j.trechm.2019.02.016.
[154] Uddin MN, Ishtiaq AKMN, Islam S, Rana MR, Ali MA, Hoque K. Prediction of new 212 M2AB2 borides as a promising candidate for future engineering: DFT calculations. Mater Today Commun 2024;39:108536. https://doi.org/10.1016/j.mtcomm.2024.108536.
[155] Miao N, Wang J, Gong Y, Wu J, Niu H, Wang S, et al. Computational prediction of boron-based MAX phases and MXene derivatives. Chemistry of Materials 2020;32:6947–57. https://doi.org/10.1021/acs.chemmater.0c02139.
[156] Carlsson A, Rosen J, Dahlqvist M. Theoretical predictions of phase stability for orthorhombic and hexagonal ternary MAB phases. Physical Chemistry Chemical Physics 2022:11249–58. https://doi.org/10.1039/d1cp05750b.
[157] Adam Carlsson. Phase stability and mechanical properties of M4AlB4 (M = Cr, Hf, Mo, Nb, Ta, Ti, V, W, Zr) from first principles 2019;4:70.
[158] Dahlqvist M, Rosen J. Chemical order or disorder - a theoretical stability expose for expanding the compositional space of quaternary metal borides. Mater Adv 2022;3:2908–17. https://doi.org/10.1039/d1ma01076j.
[159] Koutná N, Hultman L, Mayrhofer PH, Sangiovanni DG. Phase stability and mechanical property trends for MAB phases by high-throughput ab initio calculations. Materials & Design 2024. https://doi.org/10.1016/j.matdes.2024.112959.
[160] Shi C, Beidaghi M, Naguib M, Mashtalir O, Gogotsi Y, Billinge SJL. Structure of nanocrystalline Ti3 C2 MXene using atomic pair distribution function. PhysRevLett 2013;112:125501. https://doi.org/10.1103/PhysRevLett.112.125501.
[161] Anasori B, Gogotsi Y. MXenes: trends, growth, and future directions. Graphene and 2D Materials 2022;7:75–9. doi: 10.1007/s41127-022-00053-z.
[162] Rosen J, Dahlqvist M, Tao Q, Hultman L. In-and out-of-plane ordered MAX phases and their MXene derivatives. 2D Metal Carbides and Nitrides (MXenes): Structure, Properties and Applications 2019:37–52. https://doi.org/10.1007/978-3-030-19026-2_3.
[163] Gandla D, Zhuang Z, Jadhav VV, Tan DQ. Lewis acid molten salt method for 2D MXene synthesis and energy storage applications: A review. Energy Storage Mater 2023;63:102977. https://doi.org/10.1016/j.ensm.2023.102977.
[164] Mei J, Ayoko GA, Hu C, Sun Z. Thermal reduction of sulfur-containing MAX phase for MXene production. Chemical Engineering Journal 2020;395:125111. https://doi.org/10.1016/j.cej.2020.125111.
[165] Yang J, Liu R, Jia N, Wu K, Fu X, Wang Q, et al. Novel W-based in-plane chemically ordered (W2/3R1/3)2AlC (R = Gd, Tb, Dy, Ho, Er, Tm and Lu). Carbon N Y 2021;183:76–83. https://doi.org/10.1016/j.carbon.2021.07.010.
[166] Lapauw T, Tunca B, Cabioc'H T, Lu J, Persson POÅ, Lambrinou K, et al. Synthesis of MAX Phases in the Hf-Al-C System. Inorg Chem 2016;55:10922–7. https://doi.org/10.1021/acs.inorgchem.6b01398.
[167] Lapauw T, Lambrinou K, Cabioc'h T, Halim J, Lu J, Pesach A, et al. Synthesis of the new MAX phase Zr2AlC. J Eur Ceram Soc 2016;36:1847–53. https://doi.org/10.1016/j.jeurceramsoc.2016.02.044.
[168] Aleksanyan AG, Dolukhanyan SK, Mayilyan DG, Muradyan GN, Ter-Galstyan OP, Mnatsakanyan NL. Formation of Ti2AlNx MAX phase by "Hydride Cycle" and SHS methods. Ceram Int 2023;49:24229–34. https://doi.org/10.1016/j.ceramint.2022.11.350.
[169] Shuck CE, Han M, Maleski K, Hantanasirisakul K, Kim SJ, Choi J, et al. Effect of Ti3AlC2 MAX Phase on Structure and Properties of Resultant Ti3C2Tx MXene. ACS Appl Nano Mater 2019;2:3368–76. https://doi.org/10.1021/acsanm.9b00286.
[170] Lapauw T, Halim J, Lu J, Cabioc'h T, Hultman L, Barsoum MW, et al. Synthesis of the novel Zr3AlC2 MAX phase. J Eur Ceram Soc 2016;36:943–7. https://doi.org/10.1016/j.jeurceramsoc.2015.10.011.
[171] Etzkorn J, Ade M, Hillebrecht H. Ta3AlC2 and Ta4AlC3 - Single-crystal investigations of two new ternary carbides of tantalum synthesized by the molten metal technique. Inorg Chem 2007;46:1410–8. https://doi.org/10.1021/ic062231y.
[172] Mehrabi-Kalajahi S, Orooji Y, Arefi-Oskoui S, Varfolomeev MA, Khasanova NM, Yoon Y, et al. Preparasion of layered V4AlC3 MAX phase for highly selective and efficient solvent-free aerobic oxidation of toluene to benzaldehyde. Molecular Catalysis 2022;529:112545. https://doi.org/10.1016/j.mcat.2022.112545.
[173] Mishra A, Srivastava P, Mizuseki H, Lee KR, Singh AK. Isolation of pristine MXene from Nb4AlC3 MAX phase: A first-principles study. Physical Chemistry Chemical Physics 2016;18:11073–80. https://doi.org/10.1039/c5cp07609a.
[174] Griseri M, Tunca B, Lapauw T, Huang S, Popescu L, Barsoum MW, et al. Synthesis, properties and thermal decomposition of the Ta 4 AlC 3 MAX phase. J Eur Ceram Soc 2019;39:2973–81. https://doi.org/10.1016/j.jeurceramsoc.2019.04.021.
[175] Liu X, Li Y, Ding H, Chen L, Du S, Chai Z, et al. Topotactic transition of Ti4AlN3 MAX phase in Lewis acid molten salt. Journal of Materiomics 2023;9:1032–8. https://doi.org/10.1016/j.jmat.2023.03.012.
[176] Lane NJ, Naguib M, Lu J, Hultman L, Barsoum MW. Structure of a new bulk Ti 5Al 2C 3 MAX phase produced by the topotactic transformation of Ti 2AlC. J Eur Ceram Soc 2012;32:3485–91. https://doi.org/10.1016/j.jeurceramsoc.2012.03.035.
[177] Palmquist JP, Li S, Persson POÅ, Emmerlich J, Wilhelmsson O, Högberg H, et al. Mn+1AXn phases in the Ti-Si-C system studied by thin-film synthesis and ab initio calculations [74]. Phys Rev B Condens Matter Mater Phys 2004;70:1–13. https://doi.org/10.1103/PhysRevB.70.165401.
[178] Usha Kiran N, Das P, Chatterjee S, Besra L. Effect of 'Ti' particle size in the synthesis of highly pure Ti3SiC2 MAX phase. Nano-Structures and Nano-Objects 2022;30:100849. https://doi.org/10.1016/j.nanoso.2022.100849.
[179] Sinclair J, Siebert JP, Juelsholt M, Shen C, Zhang H, Birkel CS. Sol Gel-Based Synthesis of the Phosphorus-Containing MAX Phase V2PC. Inorg Chem 2022;61:16976–80. https://doi.org/10.1021/acs.inorgchem.2c02880.
[180] Nasir MT, Islam AKMA. MAX phases Nb 2AC (A = S, Sn): An ab initio study. Comput Mater Sci 2012;65:365–71. https://doi.org/10.1016/j.commatsci.2012.08.003.
[181] Hasegawa G, Kawahara K, Shima K, Inada M, Enomoto N, Hayashi K. Characterization of an AX Compound Derived from Ti2SC MAX Phase. Eur J Inorg Chem 2019;2019:2312–7. https://doi.org/10.1002/ejic.201900311.
[182] Opeka M, Zaykoski J, Talmy I, Causey S. Synthesis and characterization of Zr2SC ceramics. Materials Science and Engineering: A 2011;528:1994–2001. https://doi.org/10.1016/j.msea.2010.10.084.
[183] Mitro SK, Hadi MA, Parvin F, Majumder R, Naqib SH, Islama AKMA. Effect of boron incorporation into the carbon-site in Nb2SC MAX phase: Insights from DFT. Journal of Materials Research and Technology 2021;11:1969–81. https://doi.org/10.1016/j.jmrt.2021.02.031.

[184] Xiong K, Sun Z, Zhang S, Wang Y, Li W, You L, et al. A comparative study the structural, mechanical, and electronic properties of medium-entropy MAX phase (TiZrHf)2SC with Ti2SC, Zr2SC, Hf2SC via first-principles. Journal of Materials Research and Technology 2022;19:2717–29. https://doi.org/10.1016/j.jmrt.2022.06.040.
[185] Rackl T, Johrendt D. The MAX phase borides Zr2SB and Hf2SB. Solid State Sci 2020;106:106316. https://doi.org/10.1016/j.solidstatesciences.2020.106316.
[186] Qin Y, Zhou Y, Fan L, Feng Q, Grasso S, Hu C. Synthesis and characterization of ternary layered Nb2SB ceramics fabricated by spark plasma sintering. J Alloys Compd 2021;878:160344. https://doi.org/10.1016/j.jallcom.2021.160344.
[187] Li Y, Liang J, Ding H, Lu J, Mu X, Yan P, et al. Near-Room-Temperature Ferromagnetic Behavior of Single-Atom-Thick 2D Iron in Nanolaminated Ternary MAX Phases. (arXiv:2105.06139v1 [cond-mat.mtrl-sci]). ArXiv Materials Science n.d.:1–27.
[188] Li Y, Zhu S, Wu E, Ding H, Lu J, Mu X, et al. Nanolaminated Ternary Transition Metal Carbide (MAX Phase)-Derived Core-Shell Structure Electrocatalysts for Hydrogen Evolution and Oxygen Evolution Reactions in Alkaline Electrolytes. Journal of Physical Chemistry Letters 2023;14:481–8. https://doi.org/10.1021/acs.jpclett.2c03230.
[189] Ding H, Li Y, Li M, Chen K, Liang K, Chen G, et al. Chemical scissor-mediated structural editing of layered transition metal carbides. vol. 379. 2023. doi: 10.1126/science.add5901.
[190] Hadi MA, Kelaidis N, Naqib SH, Islam AKMA, Chroneos A, Vovk RV. Insights into the physical properties of a new 211 MAX phase Nb2CuC. Journal of Physics and Chemistry of Solids 2021;149:109759. https://doi.org/10.1016/j.jpcs.2020.109759.
[191] Zhang Y, Xu Y, Huang Q, Du S, Li M, Li Y, et al. Structure maps for MAX phases formability revisited. Ceram Int 2024;50:2855–63. https://doi.org/10.1016/j.ceramint.2023.11.009.
[192] Das P, Jahan N, Ali MA. DFT insights into Nb-based 211 MAX phase carbides: Nb2AC (A = Ga, Ge, Tl, Zn, P, In, and Cd). RSC Adv 2023;13:5538–56. https://doi.org/10.1039/d2ra07468k.
[193] Qureshi MW, Ali MA, Ma X, Tang G, Javed MU, Paudyal D. Verification of stability and unraveling the electronic and physical properties of bulk and (001)-surfaces of newly synthesized Ti2ZnX (X = C, N) MAX phases. vol. 31. 2022. doi: 10.1016/j.surfin.2022.102032.
[194] Etzkorn J, Ade M, Kotzott D, Kleczek M, Hillebrecht H. Ti2GaC, Ti4GaC3 and Cr2GaC-Synthesis, crystal growth and structure analysis of Ga-containing MAX-phases Mn+1GaCn with M=Ti, Cr and n=1, 3. J Solid State Chem 2009;182:995–1002. https://doi.org/10.1016/j.jssc.2009.01.003.
[195] Thore A, Dahlqvist M, Alling B, Rosen J. Phase stability of the nanolaminates V2Ga2C and (Mo1-: XVx)2Ga2C from first-principles calculations. Physical Chemistry Chemical Physics 2016;18:12682–8. https://doi.org/10.1039/c6cp00802j.
[196] Dey J, Wójcik M, Jędryka E, Kalvig R, Wiedwald U, Salikhov R, et al. Non-collinear magnetic structure of the MAX phase Mn2GaC epitaxial films inferred from zero-field NMR study (CE-5:L05). Ceram Int 2023;49:24235–8. https://doi.org/10.1016/j.ceramint.2022.11.265.
[197] Nadeem M, Haseeb M, Hussain A, Javed A, Rafiq MA, Ramzan M, et al. Structural stability, electronic structure, mechanical and optical properties of MAX phase ternary Mo2Ga2C, Mo2GaC and Mo3GaC2 carbides. Journal of Materials Research and Technology 2021;14:521–32. https://doi.org/10.1016/j.jmrt.2021.06.079.
[198] Petruhins A. Synthesis and characterization of Ga-containing MAX phase thin films. Linköping University Electronic Press 2014. https://doi.org/10.3384/lic.diva-110764.
[199] Faraoun HI, Abderrahim FZ, Esling C. First principle calculations of MAX ceramics Cr2GeC, V 2GeC and their substitutional solid solutions. Comput Mater Sci 2013;74:40–9. https://doi.org/10.1016/j.commatsci.2013.03.005.
[200] Shein IR, Ivanovskii AL. Structural, elastic, and electronic properties of new 211 MAX phase Nb 2GeC from first-principles calculations. Physica B Condens Matter 2013;410:42–8. https://doi.org/10.1016/j.physb.2012.10.036.
[201] Hussein DR, Abbas KK, Al-Ghaban AMHA. Overview of structural, electronic, elastic, thermal, optical, and nuclear properties of Zr2AC (A= Al, Si, P, S, Ge, As, Se In, Sn, Tl, and Pb) MAX phases: A brief review. Heliyon 2023;9:e18303. https://doi.org/10.1016/j.heliyon.2023.e18303.
[202] Ansarian Z, Khataee A, Orooji Y, Khataee A, Arefi-Oskoui S, Ghasali E. Titanium germanium carbide MAX phase electrocatalysts for supercapacitors and alkaline water electrolysis processes. Mater Today Chem 2023;33:101714. https://doi.org/10.1016/j.mtchem.2023.101714.
[203] Högberg H, Eklund P, Emmerlich J, Birch J, Hultman L. Epitaxial Ti2GeC, Ti3GeC2, and Ti4GeC3 MAX-phase thin films grown by magnetron sputtering. J Mater Res 2005;20:779–82. https://doi.org/10.1557/JMR.2005.0105.
[204] Kumar RS, Rekhi S, Cornelius AL, Barsoum MW. Compressibility of Nb 2AsC to 41 GPa. Appl Phys Lett 2005;86:1–3. https://doi.org/10.1063/1.1884261.
[205] Ali MA, Qureshi MW. Newly synthesized MAX phase Zr2SeC: DFT insights into physical properties towards possible applications. RSC Adv 2021;11:16892–905. https://doi.org/10.1039/d1ra02345d.
[206] Ali MA, Qureshi MW. DFT insights into the new Hf-based chalcogenide MAX phase Hf2SeC. Vacuum 2022;201:111072. https://doi.org/10.1016/j.vacuum.2022.111072.
[207] Zhang Q, Zhou Y, San X, Li W, Bao Y, Feng Q, et al. Zr2SeB and Hf2SeB: Two new MAB phase compounds with the Cr2AlC-type MAX phase (211 phase) crystal structures. vol. 11. 2022. doi: 10.1007/s40145-022-0646-7.
[208] Roknuzzaman M, Hadi MA, Abden MJ, Nasir MT, Islam AKMA, Ali MS, et al. Physical properties of predicted Ti2CdN versus existing Ti2CDC MAX phase: An ab initio study. Comput Mater Sci 2016;113:148–53. https://doi.org/10.1016/j.commatsci.2015.11.039.
[209] Shahzad A, Nawaz M, Moztahida M, Tahir K, Kim J, Lim Y, et al. Exfoliation of Titanium Aluminum Carbide (211 MAX Phase) to Form Nanofibers and Two-Dimensional Nanosheets and Their Application in Aqueous-Phase Cadmium Sequestration. ACS Appl Mater Interfaces 2019;11:19156–66. https://doi.org/10.1021/acsami.9b03899.
[210] Xu X, Sha D, Tian Z, Wu F, Zheng W, Yang L, et al. Lithium storage performance and mechanism of nano-sized Ti2InC MAX phase. Nanoscale Horiz 2022;8:331–7. https://doi.org/10.1039/d2nh00489e.
[211] Brik MG, Avram NM, Avram CN. Ab initio calculations of the electronic, structural and elastic properties of Nb 2InC. Comput Mater Sci 2012;63:227–31. https://doi.org/10.1016/j.commatsci.2012.06.027.
[212] Zhang Q, Luo J, Wen B, Zhou Y, Chu L, Feng Q, et al. Determination of New α-312 MAX phases of Zr3InC2 and Hf3InC2. J Eur Ceram Soc 2023;43:7228–33. https://doi.org/10.1016/j.jeurceramsoc.2023.07.015.
[213] Cuskelly DT, Richards ER, Kisi EH, Keast VJ. Ti3GaC2 and Ti3InC2: First bulk synthesis, DFT stability calculations and structural systematics. J Solid State Chem 2015;230:418–25. https://doi.org/10.1016/j.jssc.2015.07.028.
[214] Khediri R, Hammoutène D, Kassali K, Rodríguez-Hernández P, Muñoz A. High-pressure structural, elastic, vibrational, and thermodynamic study of MAX-phase Ti2InN. vol. 36. 2023. doi: 10.1016/j.cocom.2023.e00829.
[215] Ali E, Hussein SA, Karim MM, Abdulwahid AS, Omran AA, Hameed SM, et al. Ti2SnC MAX Phase Directly Synthesized by High-Temperature Ball Milling. Transactions of the Indian Institute of Metals 2024. https://doi.org/10.1007/s12666-024-03273-4.
[216] Li Y, Qin Y, Chen K, Chen L, Zhang X, Ding H, et al. Molten Salt Synthesis of Nanolaminated Sc2SnC MAX Phase. vol. 36. 2021. doi: 10.15541/jim20200529.
[217] Hadi MA, Dahlqvist M, Christopoulos SRG, Naqib SH, Chroneos A, Islam AKMA. Chemically stable new MAX phase V2SnC: A damage and radiation tolerant TBC material. RSC Adv 2020;10:43783–98. https://doi.org/10.1039/d0ra07730e.
[218] Zhao S, Dall'Agnese Y, Chu X, Zhao X, Gogotsi Y, Gao Y. Electrochemical Interaction of Sn-Containing MAX Phase (Nb2SnC) with Li-Ions. ACS Energy Lett 2019;4:2452–7. https://doi.org/10.1021/acsenergylett.9b01580.
[219] Lapauw T, Tunca B, Cabioc'h T, Vleugels J, Lambrinou K. Reactive spark plasma sintering of Ti3SnC2, Zr3SnC2 and Hf3SnC2 using Fe, Co or Ni additives. J Eur Ceram Soc 2017;37:4539–45. https://doi.org/10.1016/j.jeurceramsoc.2017.06.041.
[220] Dai X, Du ZY, Sun Y, Chen P, Duan X, Zhang J, et al. Enhancing Green Ammonia Electrosynthesis Through Tuning Sn Vacancies in Sn-Based MXene/MAX Hybrids. Nanomicro Lett 2024;16:89. https://doi.org/10.1007/s40820-023-01303-2.
[221] Roumili A, Medkour Y, Maouche D. Elastic and electronic properties of hf2sncand hf2snn. Int J Mod Phys B 2009;23:5155–61. https://doi.org/10.1142/S0217979209053370.
[222] Li S, Yang Z, Khaledialidusti R, Lin S, Yu J, Khazaei M, et al. High-throughput study and machine learning on MAX and MAB phases: new materials and fingerprints of superior lattice thermal conductivities. Acta Mater 2023;254. https://doi.org/10.1016/j.actamat.2023.119001.

[223] Music D, Sun Z, Schneider JM. Structure and bonding of M 2SbP (M=Ti,Zr,Hf). Phys Rev B Condens Matter Mater Phys 2005;71. https://doi.org/10.1103/PhysRevB.71.092102.
[224] Zhang Q, Zhou Y, San X, Wan D, Bao Y, Feng Q, et al. Thermal explosion synthesis of first Te-containing layered ternary Hf2TeB MAX phase. J Eur Ceram Soc 2023;43:173–6. https://doi.org/10.1016/j.jeurceramsoc.2022.09.051.
[225] Fashandi H, Dahlqvist M, Lu J, Palisaitis J, Simak SI, Abrikosov IA, et al. Synthesis of Ti3AuC2, Ti3Au2C2 and Ti3IrC2 by noble metal substitution reaction in Ti3SiC2 for high-temperature-stable Ohmic contacts to SiC. Nat Mater 2017;16:814–8. https://doi.org/10.1038/nmat4896.
[226] Fashandi H, Lai CC, Dahlqvist M, Lu J, Rosen J, Hultman L, et al. Ti2Au2C and Ti3Au2C2 formed by solid state reaction of gold with Ti2AlC and Ti3AlC2. Chemical Communications 2017;53:9554–7. https://doi.org/10.1039/c7cc04701k.
[227] Lai C, Fashandi H, Lu J, Palisaitis J, Persson POA, Hultman L, et al. Nanoscale 2017;2:17681–7. https://doi.org/10.1039/C7NR03663A.Volume.
[228] Shi Y, Kashiwaya S, Helmer P, Lu J, Andersson M, Petruhins A, et al. Synthesis of Cr2AuC via thermal substitution reaction in Au-covered Cr2GaC and Cr2GeC thin films. Results in Materials 2023;18:100403. https://doi.org/10.1016/j.rinma.2023.100403.
[229] Kashiwaya S, Lai CC, Lu J, Petruhins A, Rosen J, Hultman L. Formation of Ti2AuN from Au-Covered Ti2AlN Thin Films: A General Strategy to Thermally Induce Intercalation of Noble Metals into MAX Phases. Cryst Growth Des 2020;20:4077–81. https://doi.org/10.1021/acs.cgd.0c00355.
[230] Sohel M, Uddin MM, Ali MA, Hossain MM, Islam AKMA, Naqib SH. Impact of M atomic species on physical properties of M2TlC (M = Ti, Zr, Hf): A first principles calculation. AIP Adv 2023;13. https://doi.org/10.1063/5.0150252.
[231] Khatun R, Rahman MA, Hossain KM, Hasan MZ, Rasheduzzaman M, Sarker S. Physical properties of MAX phase Zr2PbC under pressure: Investigation via DFT scheme. Physica B Condens Matter 2021;620:413258. https://doi.org/10.1016/j.physb.2021.413258.
[232] Zhang Q, Wen B, Luo J, Zhou Y, San X, Bao Y, et al. Synthesis of new rare earth containing ternary laminar Sc2PbC ceramic. J Eur Ceram Soc 2023;43:1735–9. https://doi.org/10.1016/j.jeurceramsoc.2022.11.056.
[233] Ling C, Tian WB, Zhang P, Zheng W, Zhang YM, Sun ZM. Synthesis and formation mechanism of titanium lead carbide. Journal of Advanced Ceramics 2018;7:178–83. https://doi.org/10.1007/s40145-018-0269-1.
[234] Zhang Q, Wen B, Luo J, Zhou Y, San X, Bao Y, et al. Synthesis of new lead-containing MAX phases of Zr3PbC2 and Hf3PbC2. Journal of the American Ceramic Society 2023;106:6390–7. https://doi.org/10.1111/jace.19332.
[235] Saita E, Iwata M, Shibata Y, Matsunaga Y, Suizu R, Awaga K, et al. Exfoliation of Al-Residual Multilayer MXene Using Tetramethylammonium Bases for Conductive Film Applications. Front Chem 2022;10. https://doi.org/10.3389/fchem.2022.841313.
[236] Natu V, Barsoum MW. MXene Surface Terminations: A Perspective. The Journal of Physical Chemistry C 2023;127:20197–206. https://doi.org/10.1021/acs.jpcc.3c04324.
[237] Liu Y, Tang Q, Xu M, Ren J, Guo C, Chen C, et al. Efficient mechanical exfoliation of MXene nanosheets. Chemical Engineering Journal 2023;468:143439. https://doi.org/10.1016/j.cej.2023.143439.
[238] Sun W, Shah SA, Chen Y, Tan Z, Gao H, Habib T, et al. Electrochemical etching of Ti2AlC to Ti2CT:X (MXene) in low-concentration hydrochloric acid solution. J Mater Chem A Mater 2017;5:21663–8. https://doi.org/10.1039/c7ta05574a.
[239] Singh KK, Pushpan S, Loredo SL, Cerdán-Pasarán A, Hernández-Magallanes JA, Sanal KC. Safe Etching Route of Nb2SnC for the Synthesis of Two-Dimensional Nb2CTx MXene: An Electrode Material with Improved Electrochemical Performance. Materials 2023;16. https://doi.org/10.3390/ma16093488.
[240] Wang F, Jin S, Du Y, Xia Q, Wang L, Zhou A. Preparation of Mo2CTx MXene as co-catalyst for H2 production by etching of pure/mixed HBr solution. Diam Relat Mater 2023;136:109922. https://doi.org/10.1016/j.diamond.2023.109922.
[241] Zong H, Qi R, Yu K, Zhu Z. Ultrathin Ti2NTx MXene-wrapped MOF-derived CoP frameworks towards hydrogen evolution and water oxidation. Electrochim Acta 2021;393:139068. https://doi.org/10.1016/j.electacta.2021.139068.
[242] Zhang Y, Bin LW, Zhou JP, Sun DQ, Li HM. The multiple synthesis of layered V2CTx-MXene composites with enhanced electrochemical properties. J Alloys Compd 2022;929:167276. https://doi.org/10.1016/j.jallcom.2022.167276.
[243] Chen N, Zhou Y, Zhang S, Huang H, Zhang C, (John),Zheng X, et al. Tailoring Ti3CNTx MXene via an acid molecular scissor. Nano Energy 2021;85:106007. https://doi.org/10.1016/j.nanoen.2021.106007.
[244] Ince JC, Peerzada M, Mathews LD, Pai AR, Al-qatatsheh A, Abbasi S, et al. Overview of emerging hybrid and composite materials for space applications. Adv Compos Hybrid Mater 2023;6:130. https://doi.org/10.1007/s42114-023-00678-5.
[245] Halim J, Palisaitis J, Lu J, Thörnberg J, Moon EJ, Precner M, et al. Synthesis of two-dimensional nb1.33c (mxene) with randomly distributed vacancies by etching of the quaternary solid solution (nb2/3sc1/3)2alc max phase. ACS Appl Nano Mater 2018;1:2455–60. https://doi.org/10.1021/acsanm.8b00332.
[246] Kong D, Huang P, Qin F, Liu J, Lin J, Lin Y, et al. Exploring monolayer Ta4C3Tx MXene for quick ammonia detection at room temperature. Mater Lett 2024;363:136250. https://doi.org/10.1016/j.matlet.2024.136250.
[247] Liu S, Liu L, Liu J, Xiang Y, Gao L, Fu F, et al. Mo2TiC2Tx MXene-Supported Ru/Ni-NiO as an Electrocatalyst for the pH-Universal Hydrogen Evolution Reaction. ACS Appl Nano Mater 2023;6:22192–201. https://doi.org/10.1021/acsanm.3c04420.
[248] Guo X, Wang S, Yan P, Wang J, Yu L, Liu W, et al. High Modulation Depth Enabled by Mo2Ti2C3Tx MXene for Q-Switched Pulse Generation in a Mid-Infrared Fiber Laser. Nanomaterials 2022;12. https://doi.org/10.3390/nano12081343.
[249] Tang Q, Wang Y, Chen N, Pu B, Qing Y, Zhang M, et al. Ultra-Efficient Synthesis of Nb4C3Tx MXene via H2O-Assisted Supercritical Etching for Li-Ion Battery. Small Methods 2024;8:2300836. https://doi.org/10.1002/smtd.202300836.
[250] Wang L, Liu D, Lian W, Hu Q, Liu X, Zhou A. The preparation of V2CTx by facile hydrothermal-assisted etching processing and its performance in lithium-ion battery. Journal of Materials Research and Technology 2020;9:984–93. https://doi.org/10.1016/j.jmrt.2019.11.038.
[251] Wang S, Liu Y, Liu Y, Hu W. Effect of HF etching on titanium carbide (Ti3C2Tx) microstructure and its capacitive properties. Chemical Engineering Journal 2023;452:139512. https://doi.org/10.1016/j.cej.2022.139512.
[252] Wang C, Shou H, Chen S, Wei S, Lin Y, Zhang P, et al. HCl-Based Hydrothermal Etching Strategy toward Fluoride-Free MXenes. Advanced Materials 2021;33:2101015. https://doi.org/10.1002/adma.202101015.
[253] Lu G, Sun S, Wu M, Zhao X, Ma L. Two-dimensional Ti2CTx with expanded interlayer spacing for Na-ion storage. Mater Lett 2022;324:132754. https://doi.org/10.1016/j.matlet.2022.132754.
[254] Zhang B, Ju Z, Xie Q, Luo J, Du L, Zhang C, et al. Ti3CNTx MXene/rGO scaffolds directing the formation of a robust, layered SEI toward high-rate and long-cycle lithium metal batteries. Energy Storage Mater 2023;58:322–31. https://doi.org/10.1016/j.ensm.2023.03.030.
[255] Chaturvedi K, Hada V, Paul S, Sarma B, Malvi D, Dhangar M, et al. The Rise of MXene: A Wonder 2D Material, from Its Synthesis and Properties to Its Versatile Applications—A Comprehensive Review. Top Curr Chem 2023;381:11. https://doi.org/10.1007/s41061-023-00420-1.
[256] Xiao J, Zhao J, Ma X, Li L, Su H, Zhang X, et al. One-step synthesis Nb2CTx MXene with excellent lithium-ion storage capacity. J Alloys Compd 2022;889:161542. https://doi.org/10.1016/j.jallcom.2021.161542.
[257] Feng A, Yu Y, Jiang F, Wang Y, Mi L, Yu Y, et al. Fabrication and thermal stability of NH4HF2-etched Ti3C2 MXene. Ceram Int 2017;43:6322–8. https://doi.org/10.1016/j.ceramint.2017.02.039.
[258] Yoon J, Kim S, Park KH, Lee S, Kim SJ, Lee H, et al. Biocompatible and Oxidation-Resistant Ti3C2Tx MXene with Halogen-Free Surface Terminations. Small Methods 2023;7:1–11. https://doi.org/10.1002/smtd.202201579.
[259] Thomas T, Pushpan S, Aguilar Martínez JA, Torres Castro A, Pineda Aguilar N, Álvarez-Méndez A, et al. UV-assisted safe etching route for the synthesis of Mo2CTx MXene from Mo–In–C non-MAX phase. vol. 47. 2021. doi: 10.1016/j.ceramint.2021.08.342.
[260] Gavriel B, Shpigel N, Malchik F, Bergman G, Turgeman M, Levi MD, et al. Enhanced Performance of Ti3C2Tx (MXene) Electrodes in Concentrated ZnCl2 Solutions: A Combined Electrochemical and EQCM-D Study. Energy Storage Mater 2021;38:535–41. https://doi.org/10.1016/j.ensm.2021.03.027.
[261] Liu L, Zschiesche H, Antonietti M, Daffos B, Tarakina NV, Gibilaro M, et al. Tuning the Surface Chemistry of MXene to Improve Energy Storage: Example of Nitrification by Salt Melt. Adv Energy Mater 2023;13:2202709. https://doi.org/10.1002/aenm.202202709.
[262] Li Y, Shao H, Lin Z, Lu J, Liu L, Duployer B, et al. A general Lewis acidic etching route for preparing MXenes with enhanced electrochemical performance in non-aqueous electrolyte. Nat Mater 2020;19:894–9. https://doi.org/10.1038/s41563-020-0657-0.

[263] Sunderiya S, Suragtkhuu S, Purevdorj S, Ochirkhuyag T, Bat-Erdene M, Myagmarsereejid P, et al. Understanding the oxidation chemistry of Ti3C2Tx (MXene) sheets and their catalytic performances. Journal of Energy Chemistry 2024;88:437–45. https://doi.org/10.1016/j.jechem.2023.09.037.
[264] Chen J, Jin Q, Li Y, Shao H, Liu P, Liu Y, et al. Molten Salt-Shielded Synthesis (MS3) of MXenes in Air. Energy and Environmental Materials 2023;6. https://doi.org/10.1002/eem2.12328.
[265] Mokrushin AS, Nagornov IA, Gorobtsov PY, Averin AA, Simonenko TL, Simonenko NP, et al. Effect of Ti2CTx MXene Oxidation on Its Gas-Sensitive Properties. Chemosensors 2023;11. https://doi.org/10.3390/chemosensors11010013.
[266] Hantanasirisakul K, Alhabeb M, Lipatov A, Maleski K, Anasori B, Salles P, et al. Effects of Synthesis and Processing on Optoelectronic Properties of Titanium Carbonitride MXene. Chemistry of Materials 2019;31:2941–51. https://doi.org/10.1021/acs.chemmater.9b00401.
[267] Purbayanto MAK, Bury D, Chandel M, Shahrak ZD, Mochalin VN, Wójcik A, et al. Ambient Processed rGO/Ti3CNTx MXene Thin Film with High Oxidation Stability, Photosensitivity, and Self-Cleaning Potential. ACS Appl Mater Interfaces 2023;15:44075–86. https://doi.org/10.1021/acsami.3c07972.
[268] Mokhtari F, Hasanzadeh M, Mokhtarzadeh A, Shadjou N. Electrochemical determination of malondialdehyde biomarker in exhaled breath condensate using poly arginine functionalized by graphene quantum dots and chitosan. Medical Journal of Tabriz University of Medical Sciences and Health Services 2019;41:85–94. https://doi.org/10.34172/mj.2019.037.
[269] Xiao Z, Xiao X, Kong LB, Dong H, Li X, He B, et al. Preparation of MXene-based hybrids and their application in neuromorphic devices. International Journal of Extreme Manufacturing 2024;6. https://doi.org/10.1088/2631-7990/ad1573.
[270] Gentile A, Marchionna S, Balordi M, Pagot G, Ferrara C, Di Noto V, et al. Critical Analysis of MXene Production with In-Situ HF Forming Agents for Sustainable Manufacturing. ChemElectroChem 2022;9:e202200891. https://doi.org/10.1002/celc.202200891.
[271] Alhabeb M, Maleski K, Anasori B, Lelyukh P, Clark L, Sin S, et al. Guidelines for Synthesis and Processing of Two-Dimensional Titanium Carbide (Ti3C2Tx MXene). Chemistry of Materials 2017;29:7633–44. https://doi.org/10.1021/acs.chemmater.7b02847.
[272] Vaia RA, Jawaid A, Hassan A, Neher G, Nepal D, Pachter R, et al. Halogen etch of Ti3AlC2 MAX phase for mxene fabrication. ACS Nano 2021;15:2771–7. https://doi.org/10.1021/acsnano.0c08630.
[273] Cho I, Selvaraj AR, Bak J, Kim H, Prabakar K. Mechanochemical Pretreated Mn+1AXn (MAX) Phase to Synthesize 2D-Ti3C2Tx MXene Sheets for High-Performance Supercapacitors. Nanomaterials 2023;13:1741. https://doi.org/10.3390/NANO13111741/S1.
[274] Liu F, Zhou A, Chen J, Jia J, Zhou W, Wang L, et al. Preparation of Ti 3 C 2 and Ti 2 C MXenes by fluoride salts etching and methane adsorptive properties. Appl Surf Sci 2017;416:781–9. https://doi.org/10.1016/j.apsusc.2017.04.239.
[275] Khan U, Luo Y, Kong LB, Que W. Synthesis of fluorine free MXene through lewis acidic etching for application as electrode of proton supercapacitors. J Alloys Compd 2022;926:166903. https://doi.org/10.1016/j.jallcom.2022.166903.
[276] Cockreham CB, Zhang X, Li H, Hammond-Pereira E, Sun J, Saunders SR, et al. Inhibition of AlF3·3H2O Impurity Formation in Ti3C2Tx MXene Synthesis under a Unique CoFx/HCl Etching Environment. ACS Appl Energy Mater 2019;2:8145–52. https://doi.org/10.1021/acsaem.9b01618.
[277] Choi S, Cheong Y, Lee GJ, Park HK. Effect of fluoride pretreatment on primary and permanent tooth surfaces by acid-etching. Scanning 2010;32:375–82. https://doi.org/10.1002/sca.20211.
[278] Ghidiu M, Lukatskaya MR, Zhao MQ, Gogotsi Y, Barsoum MW. Conductive two-dimensional titanium carbide "Clay" with high volumetric capacitance. MXenes: From Discovery to Applications of Two-Dimensional. Metal Carbides and Nitrides 2023:379–99. https://doi.org/10.1201/9781003306511-19.
[279] Liu L, Raymundo-Piñero E, Taberna PL, Simon P. Electrochemical characterization of Ti3C2Tx MXene prepared via a molten salt etching route in an acetonitrile-based electrolyte. Electrochem Commun 2023;148:107453. https://doi.org/10.1016/j.elecom.2023.107453.
[280] Bao Z, Lu C, Cao X, Zhang P, Yang L, Zhang H, et al. Role of MXene surface terminations in electrochemical energy storage: A review. Chinese Chemical Letters 2021;32:2648–58. https://doi.org/10.1016/j.cclet.2021.02.012.
[281] Fagerli FH, Wang Z, Grande T, Kaland H, Selbach SM, Wagner NP, et al. Removing Fluoride-Terminations from Multilayered V2C TxMXene by Gas Hydrolyzation. ACS Omega 2022;7:23790–9. https://doi.org/10.1021/acsomega.2c02441.
[282] Xu J, You J, Wang L, Wang Z, Zhang H. MXenes serving aqueous supercapacitors: Preparation, energy storage mechanism and electrochemical performance enhancement. Sustainable Materials and Technologies 2022;33:e00490. https://doi.org/10.1016/j.susmat.2022.e00490.
[283] Li T, Yao L, Liu Q, Gu J, Luo R, Li J, et al. Fluorine-Free Synthesis of High-Purity Ti3C2Tx (T=OH, O) via Alkali Treatment. Angewandte Chemie - International Edition 2018;57:6115–9. https://doi.org/10.1002/anie.201800887.
[284] Chen J, Chen M, Zhou W, Xu X, Liu B, Zhang W, et al. Simplified Synthesis of Fluoride-Free Ti3C2Tx via Electrochemical Etching toward High-Performance Electrochemical Capacitors. ACS Nano 2022;16:2461–70. https://doi.org/10.1021/acsnano.1c09004.
[285] Khan U, Gao B, Kong LB, Chen Z, Que W. Green synthesis of fluorine-free MXene via hydrothermal process: A sustainable approach for proton supercapacitor electrodes. Electrochim Acta 2024;475:143651. https://doi.org/10.1016/j.electacta.2023.143651.
[286] Wang Z, Kochat V, Pandey P, Kashyap S, Chattopadhyay S, Samanta A, et al. Metal Immiscibility Route to Synthesis of Ultrathin Carbides, Borides, and Nitrides. Advanced Materials 2017;29:1700364. https://doi.org/10.1002/ADMA.201700364.
[287] Wang D, Zhou C, Filatov AS, Cho W, Lagunas F, Wang M, et al. Direct synthesis and chemical vapor deposition of 2D carbide and nitride MXenes. Science 1979;2023(379):1242–7. https://doi.org/10.1126/SCIENCE.ADD9204/SUPPL_FILE/SCIENCE.ADD9204_SM.PDF.
[288] Robertson DD, Tolbert SH. A direct and clean route to MXenes. Science 1979;2023(379):1189–90. https://doi.org/10.1126/SCIENCE.ADE9914.
[289] Boyd DA, Lin WH, Hsu CC, Teague ML, Chen CC, Lo YY, et al. Single-step deposition of high-mobility graphene at reduced temperatures. Nature Communications 2015 6:1 2015;6:1–8. doi: 10.1038/ncomms7620.
[290] Zhang F, Zhang Z, Wang H, Chan CH, Chan NY, Chen XX, et al. Plasma-enhanced pulsed-laser deposition of single-crystalline M o2 C ultrathin superconducting films. Phys Rev Mater 2017;1. https://doi.org/10.1103/PHYSREVMATERIALS.1.034002/FIGURES/5/THUMBNAIL.
[291] Druffel DL, Lanetti MG, Sundberg JD, Pawlik JT, Stark MS, Donley CL, et al. Synthesis and Electronic Structure of a 3D Crystalline Stack of MXene-Like Sheets. Chemistry of Materials 2019;31:9788–96. https://doi.org/10.1021/ACS.CHEMMATER.9B03722/SUPPL_FILE/CM9B03722_SI_001.PDF.
[292] Xiao X, Yu H, Jin H, Wu M, Fang Y, Sun J, et al. Salt-Templated Synthesis of 2D Metallic MoN and Other Nitrides. ACS Nano 2017;11:2180–6. https://doi.org/10.1021/ACSNANO.6B08534/SUPPL_FILE/NN6B08534_SI_001.PDF.
[293] Ding W, Feng Z, Andreu-Perez J, Pedrycz W. Derived Multi-population Genetic Algorithm for Adaptive Fuzzy C-Means Clustering. Neural Process Lett 2023;55:2023–47. https://doi.org/10.1007/S11063-022-10876-9/FIGURES/11.
[294] Li N, Peng J, Ong WJ, Ma T, Arramel ZP, et al. MXenes: An Emerging Platform for Wearable Electronics and Looking Beyond. Matter 2021;4:377–407. https://doi.org/10.1016/J.MATT.2020.10.024.
[295] Chouhan RS, Shah M, Prakashan D, Ramya PR, Kolhe P, Gandhi S. Emerging Trends and Recent Progress of MXene as a Promising 2D Material for Point of Care (POC) Diagnostics. Diagnostics 2023;13. https://doi.org/10.3390/diagnostics13040697.
[296] Han Y, Chen Y, Wang N, He Z. Magnesium doped carbon quantum dots synthesized by mechanical ball milling and displayed Fe 3+ sensing. Materials Technology 2019;34:336–42. https://doi.org/10.1080/10667857.2018.1556469.
[297] Zhou Z, Li L, Liu X, Lei H, Wang W, Yang Y, et al. An efficient water-assisted liquid exfoliation of layered MXene (Ti3C2Tx) by rationally matching Hansen solubility parameter and surface tension. J Mol Liq 2021;324:115116. https://doi.org/10.1016/j.molliq.2020.115116.
[298] Mohanty B, Giri L, Jena BK. MXene-Derived Quantum Dots for Energy Conversion and Storage Applications. Energy and Fuels 2021;35:14304–24. https://doi.org/10.1021/acs.energyfuels.1c01923.
[299] Xu Y, Wang X, Zhang WL, Lv F, Guo S. Recent progress in two-dimensional inorganic quantum dots. Chem Soc Rev 2018;47:586–625. https://doi.org/10.1039/c7cs00500h.
[300] Yang X, Jia Q, Duan F, Hu B, Wang M, He L, et al. Multiwall carbon nanotubes loaded with MoS 2 quantum dots and MXene quantum dots: Non–Pt bifunctional catalyst for the methanol oxidation and oxygen reduction reactions in alkaline solution. Appl Surf Sci 2019;464:78–87. https://doi.org/10.1016/j.apsusc.2018.09.069.
[301] Shao B, Liu Z, Zeng G, Wang H, Liang Q, He Q, et al. Two-dimensional transition metal carbide and nitride (MXene) derived quantum dots (QDs): Synthesis, properties, applications and prospects. J Mater Chem A Mater 2020;8:7508–35. https://doi.org/10.1039/d0ta01552k.

[302] Xue Q, Zhang H, Zhu M, Pei Z, Li H, Wang Z, et al. Photoluminescent Ti3C2 MXene Quantum Dots for Multicolor Cellular Imaging. Advanced Materials 2017; 29:1604847. https://doi.org/10.1002/adma.201604847.
[303] Wang J, Zhang Z, Yan X, Zhang S, Wu Z, Zhuang Z, et al. Rational Design of Porous N-Ti3C2 MXene@CNT Microspheres for High Cycling Stability in Li–S Battery. Nanomicro Lett 2020;12:1–14. https://doi.org/10.1007/s40820-019-0341-6.
[304] Storage E, Of S, Flexible B, Materials E. Ti 3 C 2 T x MXene 基柔性电极材料的制备及电 化学储能研究 PREPARATION AND ELECTROCHEMICAL ENERGY STORAGE STUDY OF TI 3 C 2 T X MXENE Ti 3 C 2 T x MXene 基柔性电极材料的制备及 电化学储能研究. N. Nanoscale 2022;10:1–14.
[305] Guan Q, Ma J, Yang W, Zhang R, Zhang X, Dong X, et al. Highly fluorescent Ti3C2 MXene quantum dots for macrophage labeling and Cu2+ ion sensing. Nanoscale 2019;11:14123–33. https://doi.org/10.1039/c9nr04421c.
[306] Xu Q, Ma J, Khan W, Zeng X, Li N, Cao Y, et al. Highly green fluorescent Nb2C MXene quantum dots. Chemical Communications 2020;56:6648–51. https://doi.org/10.1039/d0cc02131h.
[307] Peng C, Wei P, Chen X, Zhang Y, Zhu F, Cao Y, et al. A hydrothermal etching route to synthesis of 2D MXene (Ti3C2, Nb2C): Enhanced exfoliation and improved adsorption performance. Ceram Int 2018;44:18886–93. https://doi.org/10.1016/j.ceramint.2018.07.124.
[308] Grause G, Buekens A, Sakata Y, Okuwaki A, Yoshioka T. Feedstock recycling of waste polymeric material. J Mater Cycles Waste Manag 2011;13:265–82. https://doi.org/10.1007/s10163-011-0031-z.
[309] Jin Z, Liu C, Liu Z, Han J, Fang Y, Han Y, et al. Rational Design of Hydroxyl-Rich Ti3C2Tx MXene Quantum Dots for High-Performance Electrochemical N2 Reduction. Adv Energy Mater 2020;10:2000797. https://doi.org/10.1002/aenm.202000797.
[310] Iravani S, Varma RS. Smart MXene Quantum Dot-Based Nanosystems for Biomedical Applications. Nanomaterials 2022;12:1200. https://doi.org/10.3390/nano12071200.
[311] Abdelsalam H, Zhang QF. Properties and applications of quantum dots derived from two-dimensional materials. Adv Phys X 2022;7:2048966. https://doi.org/10.1080/23746149.2022.2048966.
[312] Lim GP, Soon CF, Ma NL, Morsin M, Nayan N, Ahmad MK, et al. Cytotoxicity of MXene-based nanomaterials for biomedical applications: A mini review. Environ Res 2021;201:111592. https://doi.org/10.1016/j.envres.2021.111592.
[313] Cheng Y, Jiang B, Chaemchuen S, Verpoort F, Kou Z. Advances and challenges in designing MXene quantum dots for sensors. Carbon Neutralization 2023;2: 213–34. https://doi.org/10.1002/cnl2.47.
[314] Ginterseder M, Franke D, Perkinson CF, Wang L, Hansen EC, Bawendi MG. Scalable Synthesis of InAs Quantum Dots Mediated through Indium Redox Chemistry. J Am Chem Soc 2020;142:4088–92. https://doi.org/10.1021/jacs.9b12350.
[315] Rambabu D, Bhattacharyya S, Singh T, M. L. C, Maji TK. Stabilization of MAPbBr3 Perovskite Quantum Dots on Perovskite MOFs by a One-Step Mechanochemical Synthesis. Inorg Chem 2020;59:1436–43. https://doi.org/10.1021/acs.inorgchem.9b03183.
[316] Lu S, Sui L, Liu Y, Yong X, Xiao G, Yuan K, et al. White Photoluminescent Ti 3 C 2 MXene Quantum Dots with Two-Photon Fluorescence. Advanced Science 2019;6:1801470. https://doi.org/10.1002/advs.201801470.
[317] Zhu Y, Feng L, Zhao R, Liu B, Yang P. Review of MXene-Derived Quantum Dots for Cancer Theranostics. ACS Appl Nano Mater 2024;7:2546–74. https://doi.org/10.1021/acsanm.3c05675.
[318] Vénosová B, Karlický F. Modeling size and edge functionalization of MXene-based quantum dots and their effect on electronic and magnetic properties. Nanoscale Adv 2023;5:7067–76. https://doi.org/10.1039/d3na00474k.
[319] Ramírez R, Melillo A, Osella S, Asiri AM, Garcia H, Primo A. Green, HF-Free Synthesis of MXene Quantum Dots and their Photocatalytic Activity for Hydrogen Evolution. Small Methods 2023;7:2300063. https://doi.org/10.1002/smtd.202300063.
[320] Safaei M, Shishehbore MR. Energy conversion and optical applications of MXene quantum dots. J Mater Sci 2021;56:17942–78. https://doi.org/10.1007/s10853-021-06428-6.
[321] Xu Q, Yang W, Wen Y, Liu S, Liu Z, Ong WJ, et al. Hydrochromic full-color MXene quantum dots through hydrogen bonding toward ultrahigh-efficiency white light-emitting diodes. Appl Mater Today 2019;16:90–101. https://doi.org/10.1016/j.apmt.2019.05.001.
[322] Rafieerad A, Yan W, Sequiera GL, Sareen N, Abu-El-Rub E, Moudgil M, et al. Application of Ti3C2 MXene Quantum Dots for Immunomodulation and Regenerative Medicine. Adv Healthc Mater 2019;8:1970067. https://doi.org/10.1002/adhm.201900569.
[323] Liu F, Wang C, Sui X, Riaz MA, Xu M, Wei L, et al. Synthesis of graphene materials by electrochemical exfoliation: Recent progress and future potential. Carbon Energy 2019;1:173–99. https://doi.org/10.1002/cey2.14.
[324] Babu AM, Rajeev R, Thadathil DA, Varghese A, Hegde G. Surface modulation and structural engineering of graphitic carbon nitride for electrochemical sensing applications. J Nanostructure Chem 2022;12:765–807. https://doi.org/10.1007/s40097-021-00459-w.
[325] Zhang Q, Sun Y, Liu M, Liu Y. Selective detection of Fe3+ ions based on fluorescence MXene quantum dots via a mechanism integrating electron transfer and inner filter effect. Nanoscale 2020;12:1826–32. https://doi.org/10.1039/c9nr08794j.
[326] Yang F, Ge Y, Yin T, Guo J, Zhang F, Tang X, et al. Ti3C2T xMXene Quantum Dots with Enhanced Stability for Ultrafast Photonics. ACS Appl Nano Mater 2020; 3:11850–60. https://doi.org/10.1021/acsanm.0c02369.
[327] Sinha A, Dhanjai ZH, Huang Y, Lu X, Chen J, et al. MXene: An emerging material for sensing and biosensing. TrAC - T. Trends in Analytical Chemistry 2018; 105:424–35. https://doi.org/10.1016/j.trac.2018.05.021.
[328] Chen X, Sun X, Xu W, Pan G, Zhou D, Zhu J, et al. Ratiometric photoluminescence sensing based on Ti3C2 MXene quantum dots as an intracellular pH sensor. Nanoscale 2018;10:1111–8. https://doi.org/10.1039/c7nr06958h.
[329] Yu H, Wang Y, Jing Y, Ma J, Du CF, Yan Q. Surface Modified MXene-Based Nanocomposites for Electrochemical Energy Conversion and Storage. Small 2019; 15:1901503. https://doi.org/10.1002/smll.201901503.
[330] Li R, Zhang L, Shi L, Wang P. MXene Ti3C2: An Effective 2D Light-to-Heat Conversion Material. ACS Nano 2017;11:3752–9. https://doi.org/10.1021/acsnano.6b08415.
[331] Liu Y, Zhang W, Zheng W. Quantum Dots Compete at the Acme of MXene Family for the Optimal Catalysis. Nanomicro Lett 2022;14:158. https://doi.org/10.1007/s40820-022-00908-3.
[332] Chen X, Li J, Pan G, Xu W, Zhu J, Zhou D, et al. Ti3C2 MXene quantum dots/TiO2 inverse opal heterojunction electrode platform for superior photoelectrochemical biosensing. Sens Actuators B Chem 2019;289:131–7. https://doi.org/10.1016/j.snb.2019.03.052.
[333] Alijani H, Rezk AR, Khosravi Farsani MM, Ahmed H, Halim J, Reineck P, et al. Acoustomicrofluidic Synthesis of Pristine Ultrathin Ti3C2TzMXene Nanosheets and Quantum Dots. ACS Nano 2021;15:12099–108. https://doi.org/10.1021/acsnano.1c03428.
[334] Kong W, Niu Y, Liu M, Zhang K, Xu G, Wang Y, et al. One-step hydrothermal synthesis of fluorescent MXene-like titanium carbonitride quantum dots. Inorg Chem Commun 2019;105:151–7. https://doi.org/10.1016/j.inoche.2019.04.033.
[335] Sui J, Chen X, Li Y, Peng W, Zhang F, Fan X. MXene derivatives: Synthesis and applications in energy convention and storage. RSC Adv 2021;11:16065–82. https://doi.org/10.1039/d0ra10018h.
[336] Wang C, Shou H, Chen S, Wei S, Lin Y, Zhang P, et al. Mxene Synthesis: HCl-Based Hydrothermal Etching Strategy toward Fluoride-Free MXenes (Adv. Mater. 27/2021). Advanced Materials 2021;33. doi: 10.1002/adma.202170209.
[337] Baig N, Kammakakam I, Falath W, Kammakakam I. Nanomaterials: A review of synthesis methods, properties, recent progress, and challenges. Mater Adv 2021;2:1821–71. https://doi.org/10.1039/d0ma00807a.
[338] Zhang C, Cui L, Abdolhosseinzadeh S, Heier J. Two-dimensional MXenes for lithium-sulfur batteries. InfoMat 2020;2:613–38.
[339] Zhao L, Wang Z, Li Y, Wang S, Wang L, Qi Z, et al. Designed synthesis of chlorine and nitrogen co-doped Ti3C2 MXene quantum dots and their outstanding hydroxyl radical scavenging properties. J Mater Sci Technol 2021;78:30–7. https://doi.org/10.1016/j.jmst.2020.10.048.
[340] Liang Q, Liu X, Zeng G, Liu Z, Tang L, Shao B, et al. Surfactant-assisted synthesis of photocatalysts: Mechanism, synthesis, recent advances and environmental application. Chemical Engineering Journal 2019;372:429–51. https://doi.org/10.1016/j.cej.2019.04.168.
[341] Feng Y, Zhou F, Deng Q, Peng C. Solvothermal synthesis of in situ nitrogen-doped Ti3C2 MXene fluorescent quantum dots for selective Cu2+ detection. Ceram Int 2020;46:8320–7. https://doi.org/10.1016/j.ceramint.2019.12.063.

[342] Huang D, Wu Y, Ai F, Zhou X, Zhu G. Fluorescent nitrogen-doped Ti3C2 MXene quantum dots as a unique "on-off-on" nanoprobe for chrominum (VI) and ascorbic acid based on inner filter effect. Sens Actuators B Chem 2021;342:130074. https://doi.org/10.1016/j.snb.2021.130074.
[343] Zhang K, Li D, Cao H, Zhu Q, Trapalis C, Zhu P, et al. Insights into different dimensional MXenes for photocatalysis. Chemical Engineering Journal 2021;424:130340. https://doi.org/10.1016/j.cej.2021.130340.
[344] Lakhe P, Prehn EM, Habib T, Lutkenhaus JL, Radovic M, Mannan MS, et al. Process Safety Analysis for Ti 3 C 2 T x MXene Synthesis and Processing. Ind Eng Chem Res 2019;58:1570–9. https://doi.org/10.1021/acs.iecr.8b05416.
[345] Zhang L, Song W, Liu H, Ding H, Yan Y, Chen R. Influencing Factors on Synthesis and Properties of MXene: A Review. Processes 2022;10. https://doi.org/10.3390/pr10091744.
[346] Shuck CE. MXenes are materials, not chemicals: Synthesis factors that influence MXene properties. MRS Commun 2023;13:957–70. https://doi.org/10.1557/s43579-023-00442-2.
[347] Wu Y, Ding L, Lu Z, Deng J, Wei Y. Two-dimensional MXene membrane for ethanol dehydration. J Memb Sci 2019;590:117300. https://doi.org/10.1016/j.memsci.2019.117300.
[348] Jia L, Zhou S, Ahmed A, Yang Z, Liu S, Wang H, et al. Tuning MXene electrical conductivity towards multifunctionality. Chemical Engineering Journal 2023;475:146361. https://doi.org/10.1016/j.cej.2023.146361.
[349] Kazim S, Huang C, Hemasiri NH, Kulkarni A, Mathur S, Ahmad S. MXene-Based Energy Devices: From Progressive to Prospective. Adv Funct Mater 2024;n/a:2315694. doi: 10.1002/adfm.202315694.
[350] Ibrahim Y, Mohamed A, Abdelgawad AM, Eid K, Abdullah AM, Elzatahry A. The recent advances in the mechanical properties of self-standing two-dimensional MXene-based nanostructures: Deep insights into the supercapacitor. Nanomaterials 2020;10:1–27. https://doi.org/10.3390/nano10101916.
[351] Yu LP, Lu L, Zhou XH, Xu L. Current Understanding of the Wettability of MXenes. Adv Mater Interfaces 2023;10:2201818. https://doi.org/10.1002/admi.202201818.
[352] Zhang B, Wong PW, Guo J, Zhou Y, Wang Y, Sun J, et al. Transforming Ti3C2Tx MXene's intrinsic hydrophilicity into superhydrophobicity for efficient photothermal membrane desalination. Nat Commun 2022;13:3315. https://doi.org/10.1038/s41467-022-31028-6.
[353] Akhtar S, Singh J, Tran TT, Roy S, Lee E, Kim J. Synthesis and optical properties of light-emitting V2N MXene quantum dots. Opt Mater (Amst) 2023;138:113660. https://doi.org/10.1016/j.optmat.2023.113660.
[354] Pang J, Mendes RG, Bachmatiuk A, Zhao L, Ta HQ, Gemming T, et al. Applications of 2D MXenes in energy conversion and storage systems. Chem Soc Rev 2019;48:72–133. https://doi.org/10.1039/c8cs00324f.
[355] Osti NC, Naguib M, Ostadhossein A, Xie Y, Kent PRC, Dyatkin B, et al. Effect of Metal Ion Intercalation on the Structure of MXene and Water Dynamics on its Internal Surfaces. ACS Appl Mater Interfaces 2016;8:8859–63. https://doi.org/10.1021/acsami.6b01490.
[356] Derikvandi Z, Dadsetani M. Electron Energy Loss Spectra of Mo2TMC2O2 (TM = Ti, Zr and Hf) Ordered Double Transition Metals MXenes. J Electron Mater 2023;52:8065–75. https://doi.org/10.1007/s11664-023-10722-1.
[357] Karlsson LH, Birch J, Halim J, Barsoum MW, Persson POÅ. Atomically Resolved Structural and Chemical Investigation of Single MXene Sheets. Nano Lett 2015;15:4955–60. https://doi.org/10.1021/acs.nanolett.5b00737.
[358] Duan T, Wu W, Choy KL. Density-functional-theory simulations of the water and ice adhesion on silicene quantum dots. Sci Rep 2022;12:8537. https://doi.org/10.1038/s41598-022-11943-w.
[359] Yuen ACY, Chen TBY, Lin B, Yang W, Kabir II, De Cachinho Cordeiro IM, et al. Study of structure morphology and layer thickness of Ti3C2 MXene with Small-Angle Neutron Scattering (SANS). Composites Part C: Open Access 2021;5:100155. https://doi.org/10.1016/j.jcomc.2021.100155.
[360] Cheng Y, Xie Y, Cao H, Li L, Liu Z, Yan S, et al. High-strength MXene sheets through interlayer hydrogen bonding for self-healing flexible pressure sensor. Chemical Engineering Journal 2023;453:139823. https://doi.org/10.1016/j.cej.2022.139823.
[361] Zhao W, Peng J, Wang W, Jin B, Chen T, Liu S, et al. Interlayer Hydrogen-Bonded Metal Porphyrin Frameworks/MXene Hybrid Film with High Capacitance for Flexible All-Solid-State Supercapacitors. Small 2019;15:1901351. https://doi.org/10.1002/smll.201901351.
[362] Ruiz-Hitzky E, Ruiz-Garcia C, Wang X. MXenes and Clay Minerals in the Framework of the 2D Organic-Inorganic Hybrid Nanomaterials. Chemistry of Materials 2023;35:10295–315. https://doi.org/10.1021/acs.chemmater.3c01759.
[363] Murugesan RA, Nagamuthu Raja KC. Capacitance performance of Ti3C2Tx MXene nanosheets on alkaline and neutral electrolytes. Mater Res Bull 2023;163:112217. https://doi.org/10.1016/j.materresbull.2023.112217.
[364] Zhang CJ, Kremer MP, Seral-Ascaso A, Park SH, McEvoy N, Anasori B, et al. Stamping of Flexible, Coplanar Micro-Supercapacitors Using MXene Inks. Adv Funct Mater 2018;28:1705506. https://doi.org/10.1002/adfm.201705506.
[365] Liang M, Wang L, Presser V, Dai X, Yu F, Ma J. Combining Battery-Type and Pseudocapacitive Charge Storage in Ag/Ti3C2Tx MXene Electrode for Capturing Chloride Ions with High Capacitance and Fast Ion Transport. Advanced Science 2020;7:2000621. https://doi.org/10.1002/advs.202000621.
[366] Lukatskaya MR, Kota S, Lin Z, Zhao MQ, Shpigel N, Levi MD, et al. Ultra-high-rate pseudocapacitive energy storage in two-dimensional transition metal carbides. MXenes: From Discovery to Applications of Two-Dimensional Metal Carbides and Nitrides 2023;2:723–43. https://doi.org/10.1201/9781003306511-36.
[367] Islam MN, Hossain MM, Maktedar SS, Rahaman M, Rahman MA, Aldalbahi A, et al. Ce-Doped TiO2 Fabricated Glassy Carbon Electrode for Efficient Hydrogen Evolution Reaction in Acidic Medium. Chem Asian J 2024;n/a:e202301143. doi: 10.1002/asia.202301143.
[368] Zehtab Salmasi M, Omidkar A, Nguyen HM, Song H. MXenes as electrocatalysts for hydrogen production through the electrocatalytic water splitting process: A mini review. Energy Reviews 2024;3:100070. https://doi.org/10.1016/j.enrev.2024.100070.
[369] Yang C, Tang Y, Tian Y, Luo Y, Faraz Ud Din M, Yin X, et al. Flexible Nitrogen-Doped 2D Titanium Carbides (MXene) Films Constructed by an Ex Situ Solvothermal Method with Extraordinary Volumetric Capacitance. Adv Energy Mater 2018;8:1802087. doi: 10.1002/aenm.201802087.
[370] Wen J, Huang L, Huang Y, Luo W, Huo H, Wang Z, et al. A lithium-MXene composite anode with high specific capacity and low interfacial resistance for solid-state batteries. Energy Storage Mater 2022;45:934–40. https://doi.org/10.1016/j.ensm.2021.12.033.
[371] Fang L, Lin L, Wu Z, Xu T, Wang X, Chang L, et al. High-Performance Layered CaV4O9-MXene Composite Cathodes for Aqueous Zinc Ion Batteries. Nanomaterials 2023;13. https://doi.org/10.3390/nano13091536.
[372] Peng J, Chen X, Ong WJ, Zhao X, Li N. Surface and Heterointerface Engineering of 2D MXenes and Their Nanocomposites: Insights into Electro- and Photocatalysis. Chem 2019;5:18–50. https://doi.org/10.1016/j.chempr.2018.08.037.
[373] Mostafaei A, Semiromi EH. A tight-binding model for the electronic structure of MXene monolayers. Nanoscale 2022;14:11760–9. https://doi.org/10.1039/d2nr00745b.
[374] Shah NK, Kaphle GC, Karn AL, Limbu Y, Paudyal D. Interplay of electronic structure, magnetism, strain, and defects in carbide MXenes. Vacuum 2022;206:111489. https://doi.org/10.1016/j.vacuum.2022.111489.
[375] Yorulmaz U, Demiroglu I, Çakır D, Gülseren O, Sevik C. A systematical ab-initio review of promising 2D MXene monolayers towards Li-ion battery applications. Journal of Physics: Energy 2020;2:32006. https://doi.org/10.1088/2515-7655/ab9fe3.
[376] Shayesteh Zeraati A, Mirkhani SA, Sun P, Naguib M, Braun PV, Sundararaj U. Improved synthesis of Ti3C2T: XMXenes resulting in exceptional electrical conductivity, high synthesis yield, and enhanced capacitance. Nanoscale 2021;13:3572–80. https://doi.org/10.1039/d0nr06671k.
[377] Yadav S, Kurra N. Diffusion kinetics of ionic charge carriers across Ti3C2Tx MXene-aqueous electrochemical interfaces. Energy Storage Mater 2024;65:103094. https://doi.org/10.1016/j.ensm.2023.103094.
[378] Guo T, Zhou D, Deng S, Jafarpour M, Avaro J, Neels A, et al. Rational Design of Ti3C2Tx MXene Inks for Conductive. Transparent Films. ACS Nano 2023;17:3737–49. https://doi.org/10.1021/acsnano.2c11180.
[379] Qiao C, Wu H, Xu X, Guan Z, Ou-Yang W. Electrical Conductivity Enhancement and Electronic Applications of 2D Ti3C2Tx MXene Materials. Adv Mater Interfaces 2021;8:2100903. https://doi.org/10.1002/admi.202100903.
[380] Geng X, Liu C, Sun Y, Zhao Y, Yi R, Song P, et al. A Ti3C2Tx MXene - carbon nanocage - sulfur cathode with high conductivity for improving the performance of Li-S batteries. J Alloys Compd 2022;895:162586. https://doi.org/10.1016/j.jallcom.2021.162586.

[381] Yang Q, Zhang F, Zhang N, Zhang H. Few-layer MXene Ti 3 C 2 T x (T = F, O, or OH) saturable absorber for visible bulk laser. Opt Mater Express 2019;9:1795. https://doi.org/10.1364/ome.9.001795.
[382] Yi Y, Chen X, Zhao Y, Xu X, Zhang P, Li C. MXene-Based Semiconductor Materials for Various Applications in Photocatalysis Field. Energy Technology 2024;n/a:2301520. doi: 10.1002/ente.202301520.
[383] Lipatov A, Goad A, Loes MJ, Vorobeva NS, Abourahma J, Gogotsi Y, et al. High electrical conductivity and breakdown current density of individual monolayer Ti3C2Tx MXene flakes. Matter 2021;4:1413–27. https://doi.org/10.1016/j.matt.2021.01.021.
[384] Nguyen TP, Tuan Nguyen DM, Tran DL, Le HK, Vo DVN, Lam SS, et al. MXenes: Applications in electrocatalytic, photocatalytic hydrogen evolution reaction and CO2 reduction. Molecular Catalysis 2020;486:110850. https://doi.org/10.1016/j.mcat.2020.110850.
[385] Jiang X, Kuklin AV, Baev A, Ge Y, Ågren H, Zhang H, et al. Two-dimensional MXenes: From morphological to optical, electric, and magnetic properties and applications. Phys Rep 2020;848:1–58. https://doi.org/10.1016/j.physrep.2019.12.006.
[386] Ontiveros D, Viñes F, Sousa C. Bandgap engineering of MXene compounds for water splitting. J Mater Chem A Mater 2023;11:13754–64. https://doi.org/10.1039/d3ta01933k.
[387] Wu YH, Luo JC, Zhang J, He ZC, Lan Y, Huang GF, et al. Tuning the metal–semiconductor contact nature in MXene-based van der Waals heterostructures. Results Phys 2023;54:107047. https://doi.org/10.1016/j.rinp.2023.107047.
[388] Li H, Eddaoudi M, O'Keeffe M, Yaghi OM. Design and synthesis of an exceptionally stable and highly porous metal- organic framework. Nature 1999;402:276–9. https://doi.org/10.1038/46248.
[389] Xu T, Wang Y, Xue Y, Li J, Wang Y. MXenes@metal-organic framework hybrids for energy storage and electrocatalytic application: Insights into recent advances. Chemical Engineering Journal 2023;470:144247. https://doi.org/10.1016/j.cej.2023.144247.
[390] Yang H, Zhang GX, Zhou HJ, Sun YY, Pang H. Metal–Organic Frameworks Meet MXene: New Opportunities for Electrochemical Application. Energy Material. Advances 2023;4. https://doi.org/10.34133/energymatadv.0033.
[391] Borysiuk VN, Mochalin VN, Gogotsi Y. Molecular dynamic study of the mechanical properties of two-dimensional titanium carbides Tin+1Cn (MXenes). Nanotechnology 2015;26:1–10. https://doi.org/10.1088/0957-4484/26/26/265705.
[392] Lipatov A, Lu H, Alhabeb M, Anasori B, Gruverman A, Gogotsi Y, et al. Elastic properties of 2D Ti3C2Tx mxene monolayers and bilayers. MXenes: From Discovery to Applications of Two-Dimensional Metal Carbides and Nitrides 2023;4:207–25. https://doi.org/10.1201/9781003306511-11.
[393] Wang H, Wu Y, Yuan X, Zeng G, Zhou J, Wang X, et al. Clay-Inspired MXene-Based Electrochemical Devices and Photo-Electrocatalyst: State-of-the-Art Progresses and Challenges. Advanced Materials 2018;30:1704561. https://doi.org/10.1002/adma.201704561.
[394] Hu C, Shen F, Zhu D, Zhang H, Xue J, Han X. Characteristics of Ti 3 C 2 X-Chitosan Films with Enhanced Mechanical Properties. Front Energy Res 2017;4:41. https://doi.org/10.3389/fenrg.2016.00041.
[395] Ling Z, Ren CE, Zhao MQ, Yang J, Giammarco JM, Qiu J, et al. Flexible and conductive MXene films and nanocomposites with high capacitance. MXenes: From Discovery to Applications of Two-Dimensional Metal Carbides and Nitrides 2023;111:563–81. doi: 10.1201/9781003306511-28.
[396] Rong C, Su T, Li Z, Chu T, Zhu M, Yan Y, et al. Elastic properties and tensile strength of 2D Ti3C2Tx MXene monolayers. Nat Commun 2024;15:1566. https://doi.org/10.1038/s41467-024-45657-6.
[397] Firestein KL, Von Treifeldt JE, Kvashnin DG, Fernando JFS, Zhang C, Kvashnin AG, et al. Young's Modulus and Tensile Strength of Ti3C2MXene Nanosheets As Revealed by in Situ TEM Probing, AFM Nanomechanical Mapping, and Theoretical Calculations. Nano Lett 2020;20:5900–8. https://doi.org/10.1021/acs.nanolett.0c01861.
[398] Cygan T, Wozniak J, Petrus M, Lachowski A, Pawlak W, Adamczyk-Cieślak B, et al. Microstructure and mechanical properties of alumina composites with addition of structurally modified 2d ti3c2 (Mxene) phase. Materials 2021;14:1–18. https://doi.org/10.3390/ma14040829.
[399] Chen XH, Wang F, Zhang Z, Zhang F. Enhanced mechanical properties of Ti3C2Tx MXene/Al composites with nacre-inspired laminated architecture. J Alloys Compd 2024;987:174180. https://doi.org/10.1016/j.jallcom.2024.174180.
[400] Kim S, Vu CM, Kim S, In I, Lee J. Improved Mechanical Strength of Dicatechol Crosslinked MXene Films for Electromagnetic Interference Shielding Performance. Nanomaterials 2023;13. https://doi.org/10.3390/nano13050787.
[401] Liu Z, Alshareef HN. MXenes for Optoelectronic Devices. Adv Electron Mater 2021;7:2100295. https://doi.org/10.1002/aelm.202100295.
[402] Zhang X, Shao J, Yan C, Qin R, Lu Z, Geng H, et al. A review on optoelectronic device applications of 2D transition metal carbides and nitrides. Mater Des 2021;200:109452. https://doi.org/10.1016/j.matdes.2021.109452.
[403] Younes H, Lou D, Rahman MM, Choi D, Hong H, Zou L. Review on 2D MXene and graphene electrodes in capacitive deionization. Environ Technol Innov 2022;28:102858. https://doi.org/10.1016/j.eti.2022.102858.
[404] Zhang CJ, Anasori B, Seral-Ascaso A, Park SH, McEvoy N, Shmeliov A, et al. Transparent, Flexible, and Conductive 2D Titanium Carbide (MXene) Films with High Volumetric Capacitance. Advanced Materials 2017;29:1702678. https://doi.org/10.1002/adma.201702678.
[405] Dillon AD, Ghidiu MJ, Krick AL, Griggs J, May SJ, Gogotsi Y, et al. Highly Conductive Optical Quality Solution-Processed Films of 2D Titanium Carbide. Adv Funct Mater 2016;26:4162–8. https://doi.org/10.1002/adfm.201600357.
[406] Li X, Ran F, Yang F, Long J, Shao L. Advances in MXene Films: Synthesis, Assembly, and Applications. Transactions of Tianjin University 2021;27:217–47. https://doi.org/10.1007/s12209-021-00282-y.
[407] Ali I, Din FUM, Gu ZG. MXenes Thin Films: From Fabrication to Their Applications. Molecules 2022;27. https://doi.org/10.3390/molecules27154925.
[408] Zhang (John) C, Nicolosi V. Graphene and MXene-based transparent conductive electrodes and supercapacitors. Energy Storage Mater 2019;16:102–25. https://doi.org/10.1016/j.ensm.2018.05.003.
[409] Fan W, Wang Q, Rong K, Shi Y, Peng W, Li H, et al. MXene Enhanced 3D Needled Waste Denim Felt for High-Performance Flexible Supercapacitors. Nanomicro Lett 2024;16:36. https://doi.org/10.1007/s40820-023-01226-y.
[410] Vadakke Neelamana H, Rekha SM, Bhat SV. Ti3C2Tx MXene: A New Promising 2D Material for Optoelectronics. Chemistry of Materials 2023;35:7386–405. https://doi.org/10.1021/acs.chemmater.3c01660.
[411] Ying G, Kota S, Dillon AD, Fafarman AT, Barsoum MW. Conductive transparent V2CTx (MXene) films. FlatChem 2018;8:25–30. https://doi.org/10.1016/j.flatc.2018.03.001.
[412] Ying G, Dillon AD, Fafarman AT, Barsoum MW. Transparent, conductive solution processed spincast 2D Ti2CTx (MXene) films. Mater Res Lett 2017;5:391–8. https://doi.org/10.1080/21663831.2017.1296043.
[413] Hantanasirisakul K, Zhao M-Q, Urbankowski P, Halim J, Anasori B, Kota S, et al. Fabrication of Ti3C2Tx MXene Transparent Thin Films with Tunable Optoelectronic Properties. Adv Electron Mater 2016;2:1600050. https://doi.org/10.1002/aelm.201600050.
[414] Xu J, Shim J, Park J-H, Lee S. MXene Electrode for the Integration of WSe2 and MoS2 Field Effect Transistors. Adv Funct Mater 2016;26:5328–34. https://doi.org/10.1002/adfm.201600771.
[415] Jhon YI, Koo J, Anasori B, Seo M, Lee JH, Gogotsi Y, et al. Metallic MXene Saturable Absorber for Femtosecond Mode-Locked Lasers. Advanced Materials 2017;29:1702496. https://doi.org/10.1002/adma.201702496.
[416] Dong Y, Chertopalov S, Maleski K, Anasori B, Hu L, Bhattacharya S, et al. Saturable Absorption in 2D Ti3C2 MXene Thin Films for Passive Photonic Diodes. Advanced Materials 2018;30:1705714. https://doi.org/10.1002/adma.201705714.
[417] Ma H, Fang H, Xie X, Liu Y, Tian H, Chai Y. Optoelectronic Synapses Based on MXene/Violet Phosphorus van der Waals Heterojunctions for Visual-Olfactory Crossmodal Perception. Nanomicro Lett 2024;16:104. https://doi.org/10.1007/s40820-024-01330-7.
[418] Hadi Z, Yeganeh JK, Zare Y, Munir MT, Rhee KY. Predicting of electrical conductivity for Polymer-MXene nanocomposites. Journal of Materials Research and Technology 2024;28:4229–38. https://doi.org/10.1016/j.jmrt.2024.01.014.
[419] Carey M, Barsoum MW. MXene polymer nanocomposites: a review. Mater Today Adv 2021;9:100120. https://doi.org/10.1016/j.mtadv.2020.100120.
[420] Zheng Z, Zhao Y, Ye Z, Hu J, Wang H. Electrically conductive porous MXene-polymer composites with ultralow percolation threshold via Pickering high internal phase emulsion templating strategy. J Colloid Interface Sci 2022;618:290–9. https://doi.org/10.1016/j.jcis.2022.03.086.

[421] Yu LP, Xu L, Lu L, Alhalili Z, Zhou XH. Thermal Properties of MXenes and Relevant Applications. ChemPhysChem 2022;23:e202200203. https://doi.org/10.1002/cphc.202200203.
[422] Wang K, Zhou Y, Xu W, Huang D, Wang Z, Hong M. Fabrication and thermal stability of two-dimensional carbide Ti3C2 nanosheets. Ceram Int 2016;42:8419–24. https://doi.org/10.1016/j.ceramint.2016.02.059.
[423] Mashtalir O, Lukatskaya MR, Kolesnikov AI, Raymundo-Piñero E, Naguib M, Barsoum MW, et al. The effect of hydrazine intercalation on the structure and capacitance of 2D titanium carbide (MXene). Nanoscale 2016;8:9128–33. https://doi.org/10.1039/c6nr01462c.
[424] Li Z, Wang L, Sun D, Zhang Y, Liu B, Hu Q, et al. Synthesis and thermal stability of two-dimensional carbide MXene Ti3C2. Materials Science and Engineering: B 2015;191:33–40. https://doi.org/10.1016/j.mseb.2014.10.009.
[425] Li R, Ma X, Li J, Cao J, Gao H, Li T, et al. Flexible and high-performance electrochromic devices enabled by self-assembled 2D TiO2/MXene heterostructures. Nat Commun 2021;12:1587. https://doi.org/10.1038/s41467-021-21852-7.
[426] Liu G, Yu R, Liu D, Xia Y, Pei X, Wang W, et al. 3D-printed TiO2-Ti3C2Tx heterojunction/rGO/PDMS composites with gradient pore size for electromagnetic interference shielding and thermal management. Compos Part A Appl Sci Manuf 2022;160:107058. https://doi.org/10.1016/j.compositesa.2022.107058.
[427] Zhou J, Dahlqvist M, Björk J, Rosen J. Atomic Scale Design of MXenes and Their Parent Materials—From Theoretical and Experimental Perspectives. Chem Rev 2023;123:13291–322. https://doi.org/10.1021/acs.chemrev.3c00241.
[428] Ji J, Zhao L, Shen Y, Liu S, Zhang Y. Covalent stabilization and functionalization of MXene via silylation reactions with improved surface properties. FlatChem 2019;17:100128. https://doi.org/10.1016/j.flatc.2019.100128.
[429] Wang S, Du Y, Liao W, Sun Z. Hydrogen adsorption, dissociation and diffusion on two-dimensional Ti2C monolayer. Int J Hydrogen Energy 2017;42:27214–9. https://doi.org/10.1016/j.ijhydene.2017.09.111.
[430] Li XH, Shan-Shan L, Cui HL, Zhang RZ. Pressure-induced modulation of electronic and optical properties of surface o-functionalized ti2c mxene. ACS Omega 2020;5:22248–54. https://doi.org/10.1021/acsomega.0c02435.
[431] Das S, Shamim SUD, Hossain MK, Ahmed F, Hossain MA, Rahman MO. A novel silicon-doped 2D Ti2C MXene monolayer as high capacity stable anode material for lithium ion batteries: Insight from density functional theory study. Appl Surf Sci 2022;600:154173. https://doi.org/10.1016/j.apsusc.2022.154173.
[432] Qiu K, Zhang Y, Wang L, Wu M, Jin J, Shi W. N-Functionalized Ti2C MXene as a High-Performance Adsorbent for Strontium Ions: A First-Principles Study. Journal of Physical Chemistry C 2023;127:11167–75. https://doi.org/10.1021/acs.jpcc.3c00849.
[433] Kang CS, Kim JK, Lee CS, Chang HJ, Cho YH, Prasad C, et al. Facile fabrication and characterization of MXene/cellulose composites for electrical properties, electric heating performance. Fashion and Textiles 2024;11:1. https://doi.org/10.1186/s40691-023-00356-6.
[434] Nguyen VP, Lim M, Kim KS, Kim JH, Park JS, Yuk JM, et al. Drastically increased electrical and thermal conductivities of Pt-infiltrated MXenes. J Mater Chem A Mater 2021;9:10739–46. https://doi.org/10.1039/d1ta00331c.
[435] Wu H, Gu J, Li Z, Liu W, Bao H, Lin H, et al. Characterization of phonon thermal transport of Ti3C2T x MXene thin film. Journal of Physics: Condensed Matter 2022;34:155704.
[436] Yasaei P, Hemmat Z, Foss CJ, Li SJ, Hong L, Behranginia A, et al. Enhanced thermal boundary conductance in few-layer Ti3C2 MXene with encapsulation. Advanced Materials 2018;30:1801629.
[437] Li J, Chi Z, Qin R, Yan L, Lin X, Hu M, et al. Hydrogen bond interaction promotes flash energy transport at MXene-solvent interface. The Journal of Physical Chemistry C 2020;124:10306–14.
[438] Luo Y, Cheng C, Chen H-J, Liu K, Zhou X-L. Systematic investigations of the electron, phonon and elastic properties of monolayer M2C (M= V, Nb, Ta) by first-principles calculations. Journal of Physics: Condensed Matter 2019;31:405703.
[439] Zha XH, Yin J, Zhou Y, Huang Q, Luo K, Lang J, et al. Intrinsic Structural, Electrical, Thermal, and Mechanical Properties of the Promising Conductor Mo2C MXene. Journal of Physical Chemistry C 2016;120:15082–8. https://doi.org/10.1021/acs.jpcc.6b04192.
[440] Karmakar S, Saha-Dasgupta T. First-principles prediction of enhanced thermoelectric properties of double transition metal MXenes: Ti 3− x Mo x C 2 T 2;(x= 0.5, 1, 1.5, 2, 2.5, T=− OH/− O/− F). Phys Rev Mater 2020;4:124007.
[441] Park TH, Yu S, Koo M, Kim H, Kim EH, Park J-E, et al. Shape-adaptable 2D titanium carbide (MXene) heater. ACS Nano 2019;13:6835–44.
[442] Lee Y, Kim SJ, Kim Y-J, Lim Y, Chae Y, Lee B-J, et al. Oxidation-resistant titanium carbide MXene films. J Mater Chem A Mater 2020;8:573–81.
[443] Guo Y, Wang H, Feng X, Zhao Y, Liang C, Yang L, et al. 3D MXene microspheres with honeycomb architecture for tumor photothermal/photodynamic/chemo combination therapy. Nanotechnology 2021;32:195701.
[444] Ma S, Zhu S, Liu M, Zhong B, Chen Y, Luo Y, et al. A high-performance, thermal and electrical conductive elastomer composite based on Ti3C2 MXene. Compos Part A Appl Sci Manuf 2021;145:106292. https://doi.org/10.1016/j.compositesa.2021.106292.
[445] Liu Y, Zou W, Zhao N, Xu J. Electrically insulating PBO/MXene film with superior thermal conductivity, mechanical properties, thermal stability, and flame retardancy. Nat Commun 2023;14:5342. https://doi.org/10.1038/s41467-023-40707-x.
[446] Zha XH, Huang Q, He J, He H, Zhai J, Francisco JS, et al. The thermal and electrical properties of the promising semiconductor MXene Hf2CO2. Sci Rep 2016;6:27971. https://doi.org/10.1038/srep27971.
[447] Li Y, Lai M, Hu M, Zhao S, Liu B, Kai JJ. Insights into electronic and magnetic properties of MXenes: From a fundamental perspective. Sustainable Materials and Technologies 2022;34:e00516. https://doi.org/10.1016/j.susmat.2022.e00516.
[448] Frey NC, Price CC, Bandyopadhyay A, Kumar H, Shenoy VB. Predicted magnetic properties of MXenes. In: Anasori B, Gogotsi Y, editors. 2D Metal Carbides and Nitrides (MXenes): Structure, Properties and Applications. Cham: Springer International Publishing; 2019. p. 291–300. https://doi.org/10.1007/978-3-030-19026-2_15.
[449] Tan Z, Fang Z, Li B, Yang Y. First-Principles Study of the Ferromagnetic Properties of Cr2CO2and Cr2NO2MXenes. ACS Omega 2020;5:25848–53. https://doi.org/10.1021/acsomega.0c03176.
[450] Limbu Y, Kaphle GC, Karn AL, Shah NK, Paudyal H, Paudyal D. Electronic structure and magnetism of pristine, defected, and strained Ti2N MXene. J Magn Magn Mater 2022;563:169895. https://doi.org/10.1016/j.jmmm.2022.169895.
[451] Gutierrez-Ojeda SJ, Ponce-Pérez R, Guerrero-Sánchez J, Moreno-Armenta MG. MXene heterostructures based on Cr2C and Cr2N: evidence of strong interfacial interactions that induce an antiferromagnetic alignment. In: Graphene and 2D Materials; 2023. https://doi.org/10.1007/s41127-023-00068-0.
[452] Kozak VV, Fedorova NA, Olshevskaya JS, Kovaleva AV, Shubin AA, Tarasov AS, et al. Nearly flat bands and ferromagnetism in the terminated Mn2C MXene. Computational Condensed Matter 2023;35:e00806. https://doi.org/10.1016/j.cocom.2023.e00806.
[453] Peng M, Dong M, Wei W, Xu H, Liu C, Shen C. The introduction of amino termination on Ti3C2 MXene surface for its flexible film with excellent property. Carbon N Y 2021;179:400–7. https://doi.org/10.1016/j.carbon.2021.04.049.
[454] Lu ZH, Tian Q, Zhou DD, Chen M, Cao YW, Zhuang LY, et al. Magnetic MXene based metal organic frameworks composites: Synthesis, characterization and application. J Environ Chem Eng 2022;10:108037. https://doi.org/10.1016/j.jece.2022.108037.
[455] Dong L, Kumar H, Anasori B, Gogotsi Y, Shenoy VB. Rational Design of Two-Dimensional Metallic and Semiconducting Spintronic Materials Based on Ordered Double-Transition-Metal MXenes. Journal of Physical Chemistry Letters 2017;8:422–8. https://doi.org/10.1021/acs.jpclett.6b02751.
[456] Siriwardane EMD, Çakir D. Strain engineering of electronic and magnetic properties of double-transition metal ferromagnetic semiconductor MXenes. J Appl Phys 2019;125:82527. https://doi.org/10.1063/1.5054131.
[457] Sun W, Xie Y, Kent PRC. Double transition metal MXenes with wide band gaps and novel magnetic properties. Nanoscale 2018;10:11962–8. https://doi.org/10.1039/c8nr00513c.
[458] Gao Q, Zhang H. Magnetic i-MXenes: A new class of multifunctional two-dimensional materials. Nanoscale 2020;12:5995–6001. https://doi.org/10.1039/c9nr10181k.
[459] Zhu J, Chroneos A, Schwingenschlögl U. Nb-based MXenes for Li-ion battery applications. Physica Status Solidi - Rapid Research Letters 2015;9:726–9. https://doi.org/10.1002/pssr.201510358.
[460] Kumar H, Frey NC, Dong L, Anasori B, Gogotsi Y, Shenoy VB. Tunable Magnetism and Transport Properties in Nitride MXenes. ACS Nano 2017;11:7648–55. https://doi.org/10.1021/acsnano.7b02578.

[461] Bandyopadhyay A, Ghosh D, Pati SK. Effects of point defects on the magnetoelectronic structures of MXenes from first principles. Physical Chemistry Chemical Physics 2018;20:4012–9. https://doi.org/10.1039/c7cp07165e.

[462] Scheibe B, Tadyszak K, Jarek M, Michalak N, Kempiński M, Lewandowski M, et al. Study on the magnetic properties of differently functionalized multilayered Ti 3 C 2 T x MXenes and Ti-Al-C carbides. Appl Surf Sci 2019;479:216–24. https://doi.org/10.1016/j.apsusc.2019.02.055.

[463] Sobolev K, Omelyanchik A, Shilov N, Gorshenkov M, Andreev N, Comite A, et al. Iron Oxide Nanoparticle-Assisted Delamination of Ti3C2Tx MXenes: A New Approach to Produce Magnetic MXene-Based Composites. Nanomaterials 2024;14. https://doi.org/10.3390/nano14010097.

[464] Allen-Perry K, Straka W, Keith D, Han S, Reynolds L, Gautam B, et al. Tuning the Magnetic Properties of Two-Dimensional MXenes by Chemical Etching. Materials (Basel) 2021;14. https://doi.org/10.3390/ma14030694.

[465] Tan B, Thomas NL. A review of the water barrier properties of polymer/clay and polymer/graphene nanocomposites. J Memb Sci 2016;514:595–612. https://doi.org/10.1016/j.memsci.2016.05.026.

[466] Sheng X, Li S, Huang H, Zhao Y, Chen Y, Zhang L, et al. Anticorrosive and UV-blocking waterborne polyurethane composite coating containing novel two-dimensional Ti3C2 MXene nanosheets. J Mater Sci 2021;56:4212–24. https://doi.org/10.1007/s10853-020-05525-2.

[467] Carey M, Hinton Z, Sokol M, Alvarez NJ, Barsoum MW. Nylon-6/Ti3C2Tz MXene Nanocomposites Synthesized by in Situ Ring Opening Polymerization of ϵ-Caprolactam and Their Water Transport Properties. ACS Appl Mater Interfaces 2019;11:20425–36. https://doi.org/10.1021/acsami.9b05027.

[468] Carey MS, Sokol M, Palmese GR, Barsoum MW. Water Transport and Thermomechanical Properties of Ti3C2T z MXene Epoxy Nanocomposites. ACS Appl Mater Interfaces 2019;11:39143–9. https://doi.org/10.1021/acsami.9b11448.

[469] Liu G, Liu S, Ma K, Wang H, Wang X, Liu G, et al. Polyelectrolyte functionalized ti2ct x mxene membranes for pervaporation dehydration of isopropanol/water mixtures. Ind Eng Chem Res 2020;59:4732–41. https://doi.org/10.1021/acs.iecr.9b06881.

[470] Shamsabadi AA, Isfahani AP, Salestan SK, Rahimpour A, Ghalei B, Sivaniah E, et al. Pushing Rubbery Polymer Membranes to Be Economic for CO2 Separation: Embedment with Ti3C2Tx MXene Nanosheets. ACS Appl Mater Interfaces 2020;12:3984–92. https://doi.org/10.1021/acsami.9b19960.

[471] Seo OB, Saha S, Kim NH, Lee JH. Preparation of functionalized MXene-stitched-graphene oxide/poly (ethylene-co-acrylic acid) nanocomposite with enhanced hydrogen gas barrier properties. J Memb Sci 2021;640:119839. https://doi.org/10.1016/j.memsci.2021.119839.

[472] Shi K, Meng X, Xiao S, Chen G, Wu H, Zhou C, et al. Mxene coatings: Novel hydrogen permeation barriers for pipe steels. Nanomaterials 2021;11. https://doi.org/10.3390/nano11102737.

[473] Wang X, Li X, Cui L, Liu Y, Fan S. Improvement of Gas Barrier Properties for Biodegradable Poly(butylene adipate-co-terephthalate) Nanocomposites with MXene Nanosheets via Biaxial Stretching. Polymers (Basel) 2022;14. https://doi.org/10.3390/polym14030480.

[474] Zhou Z, Pourhashem S, Wang Z, Sun J, Ji X, Zhai X, et al. Mxene structure: A key parameter in corrosion barrier performance of organic coatings. Journal of Industrial and Engineering Chemistry 2022;116:310–20. https://doi.org/10.1016/j.jiec.2022.09.021.

[475] Wang G, Yang Z, Wu L, Wang J, Liu X. Studies on improved stability and electrochemical activity of titanium carbide MXene-polymer nanocomposites. Journal of Electroanalytical Chemistry 2021;900:115708. https://doi.org/10.1016/j.jelechem.2021.115708.

[476] Kamysbayev V, James NM, Filatov AS, Srivastava V, Anasori B, Jaeger HM, et al. Colloidal gelation in liquid metals enables functional nanocomposites of 2D metal carbides (MXenes) and lightweight metals. MXenes: From Discovery to Applications of Two-Dimensional Metal Carbides and Nitrides 2023;13:625–52. https://doi.org/10.1201/9781003306511-31.

[477] Hart JL, Hantanasirisakul K, Lang AC, Anasori B, Pinto D, Pivak Y, et al. Control of MXenes' electronic properties through termination and intercalation. Nat Commun 2019;10:522.

[478] Liu R, Li W. High-Thermal-Stability and High-Thermal-Conductivity Ti3C2Tx MXene/Poly(vinyl alcohol) (PVA) Composites. ACS Omega 2018;3:2609–17. https://doi.org/10.1021/acsomega.7b02001.

[479] Carey M, Hinton Z, Natu V, Pai R, Sokol M, Alvarez NJ, et al. Dispersion and Stabilization of Alkylated 2D MXene in Nonpolar Solvents and Their Pseudocapacitive Behavior. Cell Rep Phys Sci 2020;1. https://doi.org/10.1016/j.xcrp.2020.100042.

[480] Chen J, Chen K, Tong D, Huang Y, Zhang J, Xue J, et al. CO2 and temperature dual responsive "smart" MXene phases. Chemical Communications 2015;51:314–7. https://doi.org/10.1039/c4cc07220k.

[481] Hao L, Zhang H, Wu X, Zhang J, Wang J, Li Y. Novel thin-film nanocomposite membranes filled with multi-functional Ti3C2Tx nanosheets for task-specific solvent transport. Compos Part A Appl Sci Manuf 2017;100:139–49. https://doi.org/10.1016/j.compositesa.2017.05.003.

[482] Wang R, Shi T, Zhang X, Wang W, Wei J, Lu J, et al. Bipolar Analog Memristors as artificial synapses for neuromorphic computing. Materials 2018;11:2102. https://doi.org/10.3390/ma11112102.

[483] Jiang R, Xiao X, Zheng J, Chen M, Chen L. Remarkable hydrogen absorption/desorption behaviors and mechanism of sodium alanates in-situ doped with Ti-based 2D MXene. Mater Chem Phys 2020;242:122529. https://doi.org/10.1016/j.matchemphys.2019.122529.

[484] Li Z, Zhuang Z, Lv F, Zhu H, Zhou L, Luo M, et al. The Marriage of the FeN4 Moiety and MXene Boosts Oxygen Reduction Catalysis: Fe 3d Electron Delocalization Matters. Advanced Materials 2018;30:1803220. https://doi.org/10.1002/adma.201803220.

[485] Xia Y, Mathis TS, Zhao M-Q, Anasori B, Dang A, Zhou Z, et al. Thickness-independent capacitance of vertically aligned liquid-crystalline MXenes. Nature 2018;557:409–12. https://doi.org/10.1038/s41586-018-0109-z.

[486] Jin Z, Fang Y, Wang X, Xu G, liu M, Wei S, et al. Ultra-efficient electromagnetic wave absorption with ethanol-thermally treated two-dimensional Nb2CTx nanosheets. J Colloid Interface Sci 2019;537:306–15. https://doi.org/10.1016/j.jcis.2018.11.034.

[487] Shahzad F, Alhabeb M, Hatter CB, Anasori B, Man Hong S, Koo CM, et al. Electromagnetic interference shielding with 2D transition metal carbides (MXenes). Science 1979;2016(353):1137–40. https://doi.org/10.1126/science.aag2421.

[488] Boota M, Anasori B, Voigt C, Zhao M-Q, Barsoum MW, Gogotsi Y. Pseudocapacitive Electrodes Produced by Oxidant-Free Polymerization of Pyrrole between the Layers of 2D Titanium Carbide (MXene). Advanced Materials 2016;28:1517–22. https://doi.org/10.1002/adma.201504705.

[489] Sun R, Zhang H-B, Liu J, Xie X, Yang R, Li Y, et al. Highly Conductive Transition Metal Carbide/Carbonitride(MXene)@polystyrene Nanocomposites Fabricated by Electrostatic Assembly for Highly Efficient Electromagnetic Interference Shielding. Adv Funct Mater 2017;27:1702807. https://doi.org/10.1002/adfm.201702807.

[490] Ling Z, Ren CE, Zhao M-Q, Yang J, Giammarco JM, Qiu J, et al. Flexible and conductive MXene films and nanocomposites with high capacitance. Proceedings of the National Academy of Sciences 2014;111:16676–81. https://doi.org/10.1073/pnas.1414215111.

[491] Gao Z-W, Zheng W, Lee LYS. Highly Enhanced Pseudocapacitive Performance of Vanadium-Doped MXenes in Neutral Electrolytes. Small 2019;15:1902649. https://doi.org/10.1002/smll.201902649.

[492] Liang X, Garsuch A, Nazar LF. Sulfur cathodes based on conductive MXene nanosheets for high-performance lithium-sulfur batteries. Angewandte Chemie - International Edition 2015;54:3907–11. https://doi.org/10.1002/anie.201410174.

[493] Zhao M, Li X, Zhang DZ, Zhai W. Design, mechanical properties and optimization of lattice structures with hollow prismatic struts 2022. doi: 10.1016/J.IJMECSCI.2022.107842.

[494] Bao W, Shuck CE, Zhang W, Guo X, Gogotsi Y, Wang G. Boosting Performance of Na–S Batteries Using Sulfur-Doped Ti3C2Tx MXene Nanosheets with a Strong Affinity to Sodium Polysulfides. ACS Nano 2019;13:11500–9. https://doi.org/10.1021/acsnano.9b04977.

[495] Liu R, Cao W, Han D, Mo Y, Zeng H, Yang H, et al. Nitrogen-doped Nb2CTx MXene as anode materials for lithium ion batteries. J Alloys Compd 2019;793:505–11. https://doi.org/10.1016/j.jallcom.2019.03.209.

[496] Yoon Y, Tiwari AP, Choi M, Novak TG, Song W, Chang H, et al. Precious-Metal-Free Electrocatalysts for Activation of Hydrogen Evolution with Nonmetallic Electron Donor: Chemical Composition Controllable Phosphorous Doped Vanadium Carbide MXene. Adv Funct Mater 2019;29:1903443. https://doi.org/10.1002/adfm.201903443.

[497] Chen K, Chen Y, Deng Q, Jeong SH, Jang TS, Du S, et al. Strong and biocompatible poly(lactic acid) membrane enhanced by Ti3C2Tz (MXene) nanosheets for Guided bone regeneration. Mater Lett 2018;229:114–7. https://doi.org/10.1016/j.matlet.2018.06.063.

[498] Si JY, Tawiah B, Sun WL, Lin B, Wang C, Yuen ACY, et al. Functionalization of MXene nanosheets for polystyrene towards high thermal stability and flame retardant properties. Polymers (Basel) 2019;11. https://doi.org/10.3390/polym11060976.

[499] Wei L, Wang JW, Gao XH, Wang HQ, Wang XZ, Ren H. Enhanced dielectric properties of poly(dimethyl siloxane) bimodal network percolative composite with chemically modified graphene. Polym Test 2020;91:16805–14. https://doi.org/10.1016/j.polymertesting.2020.106824.
[500] Lee JT, Wyatt BC, Davis GA, Masterson AN, Pagan AL, Shah A, et al. Covalent Surface Modification of Ti3C2TxMXene with Chemically Active Polymeric Ligands Producing Highly Conductive and Ordered Microstructure Films. ACS Nano 2021;15:19600–12. https://doi.org/10.1021/acsnano.1c06670.
[501] Khan MU, Du L, Fu S, Wan D, Bao Y, Feng Q, et al. Preparations and Applications of MXene–Metal Composites: A Review. Coatings 2022;12. https://doi.org/10.3390/coatings12040516.
[502] Parajuli D, Samatha K. MXene as Topological Insulator. Jetir 2019;6:689–706. https://doi.org/10.5281/zenodo.5766016.
[503] Wang K, Shen L, Zhu Q, Bo R, Lu R, Lu X, et al. Construction of modified MXene with "organic–inorganic" structure to enhance the interfacial and mechanical properties of UHMWPE fiber-reinforced epoxy composite. Chemical Engineering Journal 2023;452:139156. https://doi.org/10.1016/j.cej.2022.139156.
[504] Chen ZH, Zhang ZN, Zhang HQ, Hu D, Bin YZ, Zhang Y, et al. Modification of Ti3C2 MXene nanosheets with tunable properties using a post-processing method. Rare Metals 2022;41:3100–6. https://doi.org/10.1007/s12598-022-02017-x.
[505] Ma Y, Sheng H, Dou W, Su Q, Zhou J, Xie E, et al. Fe2O3Nanoparticles Anchored on the Ti3C2TxMXene Paper for Flexible Supercapacitors with Ultrahigh Volumetric Capacitance. ACS Appl Mater Interfaces 2020;12:41410–8. https://doi.org/10.1021/acsami.0c11034.
[506] Cheng W, Lin Z, Zhao L, Fan N, Bai H, Cheng W, et al. CeO2/MXene heterojunction-based ultrasensitive electrochemiluminescence biosensing for BCR-ABL fusion gene detection combined with dual-toehold strand displacement reaction for signal amplification. Biosens Bioelectron 2022;210:114287. https://doi.org/10.1016/j.bios.2022.114287.
[507] Mahmood M, Zulfiqar S, Warsi MF, Aadil M, Shakir I, Haider S, et al. Nanostructured V2O5 and its nanohybrid with MXene as an efficient electrode material for electrochemical capacitor applications. Ceram Int 2022;48:2345–54. https://doi.org/10.1016/j.ceramint.2021.10.014.
[508] Chae A, Doo S, Kim D, Ko TY, Oh T, Kim SJ, et al. Tunable Ti3C2TxMXene-Derived TiO2Nanocrystals at Controlled pH and Temperature. Langmuir 2022;38:12657–65. https://doi.org/10.1021/acs.langmuir.2c02110.
[509] Guo L, Zhang Y, Zhang G, Wang Q, Wang T. MXene-Al2O3 synergize to reduce friction and wear on epoxy-steel contacts lubricated with ultra-low sulfur diesel. Tribol Int 2021;153:106588. https://doi.org/10.1016/j.triboint.2020.106588.
[510] Zhou C, Wang D, Lagunas F, Atterberry B, Lei M, Hu H, et al. Hybrid organic–inorganic two-dimensional metal carbide MXenes with amido- and imido-terminated surfaces. Nat Chem 2023;15:1722–9. https://doi.org/10.1038/s41557-023-01288-w.
[511] Tekalgne MA, Do HH, Van NT, Van LQ, Hong SH, Ahn SH, et al. MXene Hybrid Nanosheet of WS2/Ti3C2 for Electrocatalytic Hydrogen Evolution Reaction. ACS Omega 2023;8:41802–8. https://doi.org/10.1021/acsomega.3c06403.
[512] Aldhaher A, Rabiee N, Iravani S. Exploring the synergistic potential of MXene-MOF hybrid composites: A perspective on synthesis, properties, and applications. Hybrid Advances 2024;5:100131. https://doi.org/10.1016/j.hybadv.2023.100131.
[513] Naguib M, Saito T, Lai S, Rager MS, Aytug T, Paranthaman MP, et al. Ti 3 C 2 T x (MXene)–polyacrylamide nanocomposite films. RSC Adv 2016;6:72069–73.
[514] Wang D, Lin Y, Hu D, Jiang P, Huang X. Multifunctional 3D-MXene/PDMS nanocomposites for electrical, thermal and triboelectric applications. Compos Part A Appl Sci Manuf 2020;130:105754. https://doi.org/10.1016/j.compositesa.2019.105754.
[515] Yang JB, Wang JW, Zhuang GC, Wang XZ, Wang HQ, Ma YJ, et al. High dielectric constant acrylic resin based percolative composite with acidified carbon nanotubes intercalation of MXene. Eur Polym J 2023;190:112006. https://doi.org/10.1016/j.eurpolymj.2023.112006.
[516] Jin X, Wang J, Dai L, Liu X, Li L, Yang Y, et al. Flame-retardant poly(vinyl alcohol)/MXene multilayered films with outstanding electromagnetic interference shielding and thermal conductive performances. Chemical Engineering Journal 2020;380:122475. https://doi.org/10.1016/j.cej.2019.122475.
[517] Lipton J, Weng GM, Alhabeb M, Maleski K, Antonio F, Kong J, et al. Mechanically strong and electrically conductive multilayer MXene nanocomposites. Nanoscale 2019;11:20295–300. https://doi.org/10.1039/c9nr06015d.
[518] Li L, Liu X, Wang J, Yang Y, Cao Y, Wang W. New application of MXene in polymer composites toward remarkable anti-dripping performance for flame retardancy. Compos Part A Appl Sci Manuf 2019;127:105649. https://doi.org/10.1016/j.compositesa.2019.105649.
[519] Mirkhani SA, Shayesteh Zeraati A, Aliabadian E, Naguib M, Sundararaj U. High Dielectric Constant and Low Dielectric Loss via Poly(vinyl alcohol)/Ti3C2Tx MXene Nanocomposites. ACS Appl Mater Interfaces 2019;11:18599–608. https://doi.org/10.1021/acsami.9b00393.
[520] Xu H, Yin X, Li X, Li M, Liang S, Zhang L, et al. Lightweight Ti 2 CT x MXene/Poly(vinyl alcohol) Composite Foams for Electromagnetic Wave Shielding with Absorption-Dominated Feature. ACS Appl Mater Interfaces 2019;11:10198–207. https://doi.org/10.1021/acsami.8b21671.
[521] Zhang W, Ma J, Zhang W, Zhang P, He W, Chen J, et al. A multidimensional nanostructural design towards electrochemically stable and mechanically strong hydrogel electrodes. Nanoscale 2020;12:6637–43. https://doi.org/10.1039/d0nr01414a.
[522] Zhao S, Bin ZH, Luo JQ, Wang QW, Xu B, Hong S, et al. Highly Electrically Conductive Three-Dimensional Ti3C2Tx MXene/Reduced Graphene Oxide Hybrid Aerogels with Excellent Electromagnetic Interference Shielding Performances. ACS Nano 2018;12:11193–202. https://doi.org/10.1021/acsnano.8b05739.
[523] Wan W, Tao M, Cao H, Zhao Y, Luo J, Yang J, et al. Enhanced dielectric properties of homogeneous Ti3C2Tx MXene@SiO2/polyvinyl alcohol composite films. Ceram Int 2020;46:13862–8. https://doi.org/10.1016/j.ceramint.2020.02.179.
[524] Carey MS. On the Synthesis & Characterization of Ti3C2Tx MXene Polymer Composites. Thesis 2017:1–53.
[525] Mayerberger EA, Urbanek O, McDaniel RM, Street RM, Barsoum MW, Schauer CL. Preparation and characterization of polymer-Ti3C2Tx (MXene) composite nanofibers produced via electrospinning. J Appl Polym Sci 2017;134:45295. https://doi.org/10.1002/app.45295.
[526] Zhou B, Zhang Z, Li Y, Han G, Feng Y, Wang B, et al. Flexible, Robust, and Multifunctional Electromagnetic Interference Shielding Film with Alternating Cellulose Nanofiber and MXene Layers. ACS Appl Mater Interfaces 2020;12:4895–905. https://doi.org/10.1021/acsami.9b19768.
[527] Shi Y, Liu C, Liu L, Fu L, Yu B, Lv Y, et al. Strengthening, toughing and thermally stable ultra-thin MXene nanosheets/polypropylene nanocomposites via nanoconfinement. Chemical Engineering Journal 2019;378:122267. https://doi.org/10.1016/j.cej.2019.122267.
[528] Tanvir A, Sobolčiak P, Popelka A, Mrlik M, Spitalsky Z, Micusik M, et al. Electrically conductive, transparent polymeric nanocomposites modified by 2D 2019;11. https://doi.org/10.3390/polym11081272.
[529] Wang L, Qiu H, Song P, Zhang Y, Lu Y, Liang C, et al. 3D Ti3C2Tx MXene/C hybrid foam/epoxy nanocomposites with superior electromagnetic interference shielding performances and robust mechanical properties. Compos Part A Appl Sci Manuf 2019;123:293–300. https://doi.org/10.1016/j.compositesa.2019.05.030.
[530] Naguib M, Saito T, Lai S, Rager MS, Aytug T, Parans Paranthaman M, et al. Ti3C2TX (MXene)-polyacrylamide nanocomposite films. RSC Adv 2016;6:72069–73. https://doi.org/10.1039/c6ra10384g.
[531] Seyedin S, Uzun S, Levitt A, Anasori B, Dion G, Gogotsi Y, et al. MXene Composite and Coaxial Fibers with High Stretchability and Conductivity for Wearable Strain Sensing Textiles. Adv Funct Mater 2020;30:1910504. https://doi.org/10.1002/adfm.201910504.
[532] Wei H, Dong J, Fang X, Zheng W, Sun Y, Qian Y, et al. Ti3C2Tx MXene/polyaniline (PANI) sandwich intercalation structure composites constructed for microwave absorption. Compos Sci Technol 2019;169:52–9. https://doi.org/10.1016/j.compscitech.2018.10.016.
[533] Seroka NS, Mamo MA. Application of functionalised MXene-carbon nanoparticle-polymer composites in resistive hydrostatic pressure sensors. SN Appl Sci 2020;2:413. https://doi.org/10.1007/s42452-020-2166-9.
[534] Wang X, Sun K, Li K, Li X, Gogotsi Y. Ti3C2Tx/PEDOT:PSS hybrid materials for room-temperature methanol sensor. Chinese Chemical Letters 2020;31:1018–21. https://doi.org/10.1016/j.cclet.2019.11.031.
[535] Feng Y, Deng Q, Peng C, Hu J, Li Y, Wu Q, et al. An ultrahigh discharged energy density achieved in an inhomogeneous PVDF dielectric composite filled with 2D MXene nanosheets: Via interface engineering. J Mater Chem C Mater 2018;6:13283–92. https://doi.org/10.1039/c8tc05180a.
[536] Gong L, Young RJ, Kinloch IA, Riaz I, Jalil R, Novoselov KS. Optimizing the reinforcement of polymer-based nanocomposites by graphene. ACS Nano 2012;6:2086–95. https://doi.org/10.1021/nn203917d.
[537] Zhou W, Zhou Z, Fan Y, Nomura N. Significant strengthening effect in few-layered MXene-reinforced Al matrix composites. Mater Res Lett 2021;9:148–54. https://doi.org/10.1080/21663831.2020.1861120.
[538] Hu J, Li S, Zhang J, Chang Q, Yu W, Zhou Y. Mechanical properties and frictional resistance of Al composites reinforced with Ti3C2Tx MXene. Chinese Chemical Letters 2020;31:996–9. https://doi.org/10.1016/j.cclet.2019.09.004.

[539] Zhang J, Li S, Hu S, Zhou Y. Chemical stability of Ti3C2 MXene with Al in the temperature range 500-700°C. Materials 2018;11. https://doi.org/10.3390/ma11101979.
[540] Si XY, Chen FY, Deng QH, Du SY, Huang Q. Preparation and property of mxene/copper alloy composites. Wuji Cailiao Xuebao/Journal of Inorganic Materials 2018;33:603–8. https://doi.org/10.15541/jim20170297.
[541] Li M, Wang S, Wang Q, Ren F, Wang Y. Microstructure and tensile properties of Ni nano particles modified MXene reinforced copper matrix composites. Materials Science and Engineering: A 2021;808:140932. https://doi.org/10.1016/j.msea.2021.140932.
[542] Liu T, Wang Q, Yuan J, Zhao X, Gao G. Highly Dispersed Bimetallic Nanoparticles Supported on Titanium Carbides for Remarkable Hydrogen Release from Hydrous Hydrazine. ChemCatChem 2018;10:2200–4. https://doi.org/10.1002/cctc.201701633.
[543] Wu M, Fan X, Zhang W, Chen B, Ye T, Zhang Q, et al. Highly dispersed Ru nanospecies on N-doped carbon/MXene composite for highly efficient alkaline hydrogen evolution. Chinese Chemical Letters 2024;35:109258. https://doi.org/10.1016/j.cclet.2023.109258.
[544] Li N, Xie X, Lu H, Fan B, Wang X, Zhao B, et al. Novel two-dimensional Ti3C2TX/Ni-spheres hybrids with enhanced microwave absorption properties. Ceram Int 2019;45:22880–8. https://doi.org/10.1016/j.ceramint.2019.07.331.
[545] Gothandapani K, Tamil Selvi G, Sofia Jennifer R, Velmurugan V, Pandiaraj S, Muthuramamoorthy M, et al. Ni-Ti3C2 MXene composite derived from Ni-metal organic framework for electrochemical hydrogen evolution reaction in acidic and alkaline medium. Int J Hydrogen Energy 2024;52:1164–71. https://doi.org/10.1016/j.ijhydene.2023.10.022.
[546] Zheng J, Wang B, Ding A, Weng B, Chen J. Synthesis of MXene/DNA/Pd/Pt nanocomposite for sensitive detection of dopamine. Journal of Electroanalytical Chemistry 2018;816:189–94. https://doi.org/10.1016/j.jelechem.2018.03.056.
[547] Karataş Y, Çetin T, Akinay Y, Gülcan M. Synthesis and characterization of Pd doped MXene for hydrogen production from the hydrolysis of methylamine borane: Effect of cryogenic treatment. Journal of the Energy Institute 2023;109:101310. https://doi.org/10.1016/j.joei.2023.101310.
[548] Yin J, Zhan F, Jiao T, Wang W, Zhang G, Jiao J, et al. Facile preparation of self-assembled MXene@Au@CdS nanocomposite with enhanced photocatalytic hydrogen production activity. Sci China Mater 2020;63:2228–38. https://doi.org/10.1007/s40843-020-1299-4.
[549] Rakhi RB, Nayuk P, Xia C, Alshareef HN. Novel amperometric glucose biosensor based on MXene nanocomposite. Sci Rep 2016;6:36422. https://doi.org/10.1038/srep36422.
[550] Shin SE, Choi HJ, Shin JH, Bae DH. Strengthening behavior of few-layered graphene/aluminum composites. Carbon N Y 2015;82:143–51. https://doi.org/10.1016/j.carbon.2014.10.044.
[551] Wyatt BC, Nemani SK, Desai K, Kaur H, Zhang B, Anasori B. High-temperature stability and phase transformations of titanium carbide (Ti3C2Tx) MXene. Journal of Physics Condensed Matter 2021;33. https://doi.org/10.1088/1361-648X/abe793.
[552] Mai YJ, Li YG, Li SL, Zhang LY, Liu CS, Jie XH. Self-lubricating Ti3C2 nanosheets/copper composite coatings. J Alloys Compd 2019;770:1–5. https://doi.org/10.1016/j.jallcom.2018.08.100.
[553] Zhang CJ, Pinilla S, McEvoy N, Cullen CP, Anasori B, Long E, et al. Oxidation Stability of Colloidal Two-Dimensional Titanium Carbides (MXenes). Chemistry of Materials 2017;29:4848–56. https://doi.org/10.1021/acs.chemmater.7b00745.
[554] Li K, Jiao T, Xing R, Zou G, Zhou J, Zhang L, et al. Fabrication of tunable hierarchical MXene@AuNPs nanocomposites constructed by self-reduction reactions with enhanced catalytic performances. Sci China Mater 2018;61:728–36. https://doi.org/10.1007/s40843-017-9196-8.
[555] Wu Y, Wu L, Yao W, Jiang B, Wu J, Chen Y, et al. Improved corrosion resistance of AZ31 Mg alloy coated with MXenes/MgAl-LDHs composite layer modified with yttrium. Electrochim Acta 2021;374:137913. https://doi.org/10.1016/j.electacta.2021.137913.
[556] Zhu X, Liu P, Xue T, Ge Y, Ai S, Sheng Y, et al. A novel graphene-like titanium carbide MXene/Au–Ag nanoshuttles bifunctional nanosensor for electrochemical and SERS intelligent analysis of ultra-trace carbendazim coupled with machine learning. Ceram Int 2021;47:173–84. https://doi.org/10.1016/j.ceramint.2020.08.121.
[557] Song D, Jiang X, Li Y, Lu X, Luan S, Wang Y, et al. Metal−organic frameworks-derived MnO2/Mn3O4 microcuboids with hierarchically ordered nanosheets and Ti3C2 MXene/Au NPs composites for electrochemical pesticide detection. J Hazard Mater 2019;373:367–76. https://doi.org/10.1016/j.jhazmat.2019.03.083.
[558] Zou G, Zhang Z, Guo J, Liu B, Zhang Q, Fernandez C, et al. Synthesis of MXene/Ag Composites for Extraordinary Long Cycle Lifetime Lithium Storage at High Rates. ACS Appl Mater Interfaces 2016;8:22280–6. https://doi.org/10.1021/acsami.6b08089.
[559] Liu P, Yao Z, Ng VMH, Zhou J, Kong LB. Novel multilayer-like structure of Ti 3 C 2 T x /CNZF composites for low-frequency electromagnetic absorption. Mater Lett 2019;248:214–7. https://doi.org/10.1016/j.matlet.2019.04.042.
[560] Rajavel K, Hu Y, Zhu P, Sun R, Wong C. MXene/metal oxides-Ag ternary nanostructures for electromagnetic interference shielding. Chemical Engineering Journal 2020;399:125791. https://doi.org/10.1016/j.cej.2020.125791.
[561] Zhang Z, Li H, Zou G, Fernandez C, Liu B, Zhang Q, et al. Self-Reduction Synthesis of New MXene/Ag Composites with Unexpected Electrocatalytic Activity. ACS Sustain Chem Eng 2016;4:6763–71. https://doi.org/10.1021/acssuschemeng.6b01698.
[562] He J, Liu X, Deng Y, Peng Y, Deng L, Luo H, et al. Improved magnetic loss and impedance matching of the FeNi-decorated Ti3C2Tx MXene composite toward the broadband microwave absorption performance. J Alloys Compd 2021;862:158684. https://doi.org/10.1016/j.jallcom.2021.158684.
[563] Satheeshkumar E, Makaryan T, Melikyan A, Minassian H, Gogotsi Y, Yoshimura M. One-step Solution Processing of Ag, Au and Pd@MXene Hybrids for SERS. Sci Rep 2016;6:32049. https://doi.org/10.1038/srep32049.
[564] Tian Y, An Y, Wei C, Xi B, Xiong S, Feng J, et al. Flexible and Free-Standing Ti3C2Tx MXene@Zn Paper for Dendrite-Free Aqueous Zinc Metal Batteries and Nonaqueous Lithium Metal Batteries. ACS Nano 2019;13:11676–85. https://doi.org/10.1021/acsnano.9b05599.
[565] Li M, Wang S, Wang Q, Ren F, Wang Y. Microstructure and tensile properties of Ni nano particles modified MXene reinforced copper matrix composites. Materials Science and Engineering: A 2021;808:140699. https://doi.org/10.1016/j.msea.2021.140932.
[566] Tian Y, An Y, Xiong S, Feng J, Qian Y. A general method for constructing robust, flexible and freestanding MXene@metal anodes for high-performance potassium-ion batteries. J Mater Chem A Mater 2019;7:9716–25. https://doi.org/10.1039/c9ta02233c.
[567] Tian Y, An Y, Wei C, Xi B, Xiong S, Feng J, et al. Flexible and free-standing Ti3C2T x MXene@ Zn paper for dendrite-free aqueous zinc metal batteries and nonaqueous lithium metal batteries. ACS Nano 2019;13:11676–85.
[568] Naguib M, Unocic RR, Armstrong BL, Nanda J. Large-scale delamination of multi-layers transition metal carbides and carbonitrides "mXenes. Dalton Transactions 2015;44:9353–8. https://doi.org/10.1039/c5dt01247c.
[569] Porwal H, Grasso S, Reece MJ. Review of graphene-ceramic matrix composites. Advances in Applied Ceramics 2013;112:443–54. https://doi.org/10.1179/174367613X13764308970581.
[570] Anasori B, Lukatskaya MR, Gogotsi Y. 2D metal carbides and nitrides (MXenes) for energy storage. Nat Rev Mater 2017;2:16098. https://doi.org/10.1038/natrevmats.2016.98.
[571] Rahman M, Al Mamun MS. Future prospects of MXenes: synthesis, functionalization, properties, and application in field effect transistors. Nanoscale Adv 2023;6:367–85. https://doi.org/10.1039/d3na00874f.
[572] Sankar BD, Sekar S, Sathish S, Dhanasekaran S, Nirmala R, Kim DY, et al. Recent advancements in MXene with two-dimensional transition metal chalcogenides/oxides nanocomposites for supercapacitor application – A topical review. J Alloys Compd 2024;978:173481. https://doi.org/10.1016/j.jallcom.2024.173481.
[573] Arslanoglu M, Yuan B, Panat R, Ozdoganlar OB. 3D Assembly of MXene Networks using a Ceramic Backbone with Controlled Porosity. Advanced Materials 2023;35:e2304757. https://doi.org/10.1002/adma.202304757.
[574] Fei M, Lin R, Lu Y, Zhang X, Bian R, Cheng J, et al. MXene-reinforced alumina ceramic composites. Ceram Int 2017;43:17206–10. https://doi.org/10.1016/j.ceramint.2017.08.202.
[575] Guo J, Legum B, Anasori B, Wang K, Lelyukh P, Gogotsi Y, et al. Cold Sintered Ceramic Nanocomposites of 2D MXene and Zinc Oxide. Advanced Materials 2018;30:1801846. https://doi.org/10.1002/adma.201801846.
[576] Seredych M, Shuck CE, Pinto D, Alhabeb M, Precetti E, Deysher G, et al. High-Temperature Behavior and Surface Chemistry of Carbide MXenes Studied by Thermal Analysis. Chemistry of Materials 2019;31:3324–32. https://doi.org/10.1021/acs.chemmater.9b00397.

[577] Wozniak J, Petrus M, Cygan T, Lachowski A, Adamczyk-Cieślak B, Moszczyńska D, et al. Influence of mxene (Ti3C2) phase addition on the microstructure and mechanical properties of silicon nitride ceramics. Materials 2020;13:1–11. https://doi.org/10.3390/ma13225221.
[578] Ding J, Chen F, Chen J, Liang J, Kong J. MXene-derived TiC/SiBCN ceramics with excellent electromagnetic absorption and high-temperature resistance. Journal of the American Ceramic Society 2021;104:1772–84. https://doi.org/10.1111/jace.17596.
[579] Wozniak J, Petrus M, Cygan T, Jastrzębska A, Wojciechowski T, Ziemkowska W, et al. Silicon carbide matrix composites reinforced with two-dimensional titanium carbide – Manufacturing and properties. Ceram Int 2019;45:6624–31. https://doi.org/10.1016/j.ceramint.2018.12.149.
[580] Ahmadi Z, Asl MS. Effect of SiC morphology on characteristics of ZrB 2 ceramics fabricated by spark plasma sintering. 2019.
[581] Cheng Y, Zhu W, Lu X, Wang C. Lightweight and flexible MXene/carboxymethyl cellulose aerogel for electromagnetic shielding, energy harvest and self-powered sensing. Nano Energy 2022;98:107229. https://doi.org/10.1016/j.nanoen.2022.107229.
[582] Xia M, Ning J, Feng X, Guo H, Wang D, Zhang J, et al. Ionization-bombardment assisted deposition of MXene/SiC heterostructure for micro-supercapacitor with enhanced sodium storage. Chemical Engineering Journal 2021;428:131114. https://doi.org/10.1016/j.cej.2021.131114.
[583] Cheng Y, An Y, Liu Y, Wei Q, Han W, Zhang X, et al. ZrB2-Based "brick-and-Mortar" Composites Achieving the Synergy of Superior Damage Tolerance and Ablation Resistance. ACS Appl Mater Interfaces 2020;12:33246–55. https://doi.org/10.1021/acsami.0c08206.
[584] Lan D, Cheng T, Qu Y, Zhang X, Yan X, Suzuki T, et al. Tungsten Carbide Nanoparticles as Saturable Absorber for Q-Switched Erbium-Doped Fiber Laser. IEEE Photonics Technology Letters 2022;34:113–6. https://doi.org/10.1109/LPT.2022.3142143.
[585] Kiran GK, Sreekanth TVM, Yoo K, Kim J. Bifunctional electrocatalytic activity of two-dimensional multilayered vanadium carbide (MXene) for ORR and OER. Mater Chem Phys 2023;296:127272. https://doi.org/10.1016/j.matchemphys.2022.127272.
[586] Wang J, Li G, Liu S, Chai J, Wang Y, Cheng G, et al. Nonlinear Absorption Response of Zirconium Carbide Films. ACS Appl Mater Interfaces 2022;15:3317–24. https://doi.org/10.1021/acsami.2c18652.
[587] Fan B, Zhao X, Zhang P, Wei Y, Qiao N, Yang B, et al. Effect of Sodium Dodecyl Sulfate on Stability of MXene Aqueous Dispersion. Advanced Science 2023;10:2300273. https://doi.org/10.1002/advs.202300273.
[588] Huang D, Wang Z, Sheng X, Chen Y. Bio-based MXene hybrid aerogel/paraffin composite phase change materials with superior photo and electrical responses toward solar thermal energy storage. Solar Energy Materials and Solar Cells 2023;251:112124. https://doi.org/10.1016/j.solmat.2022.112124.
[589] Rabiee N, Bagherzadeh M, Jouyandeh M, Zarrintaj P, Saeb MR, Mozafari M, et al. Natural Polymers Decorated MOF-MXene Nanocarriers for Co-delivery of Doxorubicin/pCRISPR. ACS Appl Bio Mater 2021;4:5106–21. https://doi.org/10.1021/acsabm.1c00332.
[590] Yang Y, Min J, Xue T, Jiang P, Liu X, Peng R, et al. Complete bio-degradation of poly(butylene adipate-co-terephthalate) via engineered cutinases. Nat Commun 2023;14:1645. https://doi.org/10.1038/s41467-023-37374-3.
[591] Gul I, Sayed M, Saeed T, Rehman F, Naeem A, Gul S, et al. Unveiling cutting-edge progress in the fundamentals of MXene: Synthesis strategies, energy and bio-environmental applications. Coord Chem Rev 2024;511:215870. https://doi.org/10.1016/j.ccr.2024.215870.
[592] Siwal SS, Kaur H, Chauhan G, Thakur VK. MXene-Based Nanomaterials for Biomedical Applications: Healthier Substitute Materials for the Future. Adv Nanobiomed Res 2023;3:2200123. https://doi.org/10.1002/anbr.202200123.
[593] Srivastava P. Fabrication of Mxene Based Flexible Bio-Sensor. 2022. https://doi.org/10.13140/RG.2.2.25909.35049.
[594] Amani AM, Tayebi L, Abbasi M, Vaez A, Kamyab H, Chelliapan S, et al. The Need for Smart Materials in an Expanding Smart World: MXene-Based Wearable Electronics and Their Advantageous Applications. ACS Omega 2023;9:3123–42. https://doi.org/10.1021/acsomega.3c06590.
[595] Park H, Kim S, Kim S, Kim M, Kang Y, Amirthalingam S, et al. Bioactive inorganic compound MXene and its application in tissue engineering and regenerative medicine. Journal of Industrial and Engineering Chemistry 2023;117:38–53. https://doi.org/10.1016/j.jiec.2022.10.014.
[596] Guo R, Hu D, Liu D, Jiang Q, Qiu J. MXene nanomaterials in biomedicine: A bibliometric perspective. Front Bioeng. Biotechnol 2023;11. https://doi.org/10.3389/fbioe.2023.1184275.
[597] Gürbüz B, Ciftci F. Bio-electric-electronics and tissue engineering applications of MXenes wearable materials: A review. Chemical Engineering Journal 2024;489:151230. https://doi.org/10.1016/j.cej.2024.151230.
[598] Amrillah T, Abdullah CAC, Hermawan A, Sari FNI, Alvani VN. Towards Greener and More Sustainable Synthesis of MXenes: A Review. Nanomaterials 2022;12. https://doi.org/10.3390/nano12234280.
[599] Koyappayil A, Chavan SG, Mohammadniaei M, Go A, Hwang SY, Lee M-H. β-Hydroxybutyrate dehydrogenase decorated MXene nanosheets for the amperometric determination of β-hydroxybutyrate. Microchimica Acta 2020;187:277. https://doi.org/10.1007/s00604-020-04258-y.
[600] Mohammadniaei M, Koyappayil A, Sun Y, Min J, Lee M-H. Gold nanoparticle/MXene for multiple and sensitive detection of oncomiRs based on synergetic signal amplification. Biosens Bioelectron 2020;159:112208.
[601] G A, Gupta N, Saha P, Bhattacharya P.. 3D Printing of MXenes-Based Electrodes for Energy Storage Applications. Recent Prog Mater 2023;05:1–23. https://doi.org/10.21926/rpm.2302020.
[602] Dananjaya SA V, Chevali VS, Dear JP, Potluri P, Abeykoon C. 3D printing of biodegradable polymers and their composites – Current state-of-the-art, properties, applications, and machine learning for potential future applications. Prog Mater Sci 2024:101336. doi: doi: 10.1016/j.pmatsci.2024.101336.
[603] Zhou W, Zhou Z, Guo S, Fan Y, Nomura N. Structural evolution mechanism during 3D printing of MXene-reinforced metal matrix composites. Composites Communications 2022;29:101034. https://doi.org/10.1016/j.coco.2021.101034.
[604] Yang W, Yang J, Byun JJ, Moissinac FP, Xu J, Haigh SJ, et al. 3D Printing of Freestanding MXene Architectures for Current-Collector-Free Supercapacitors. Advanced Materials 2019;31. https://doi.org/10.1002/adma.201902725.
[605] Song F, Li G, Zhu Y, Wu Z, Xie X, Zhang N. Rising from the horizon: three-dimensional functional architectures assembled with MXene nanosheets. J Mater Chem A Mater 2020;8:18538–59. https://doi.org/10.1039/d0ta06222g.
[606] Jiang X, Jia H, Chen X, Li J, Chen Y, Jia J, et al. Broadening the Voltage Window of 3D-Printed MXene Micro-Supercapacitors with a Hybridized Electrolyte. Molecules 2024;29. https://doi.org/10.3390/molecules29061393.
[607] Faruk O, Adak B. Recent advances in PEDOT:PSS integrated graphene and MXene-based composites for electrochemical supercapacitor applications. Synth Met 2023;297:117384. https://doi.org/10.1016/j.synthmet.2023.117384.
[608] Li L, Meng J, Bao X, Huang Y, Yan X-P, Qian H-L, et al. Direct-Ink-Write 3D Printing of Programmable Micro-Supercapacitors from MXene-Regulating Conducting Polymer Inks. Adv Energy Mater 2023;13:2203683. https://doi.org/10.1002/aenm.202203683.
[609] Matias ML, Pereira C, Almeida HV, Jana S, Panigrahi S, Menda UD, et al. 3D printed MXene architectures for a plethora of smart applications. Mater Today Adv 2024;23:100512. https://doi.org/10.1016/j.mtadv.2024.100512.
[610] Polychronopoulos ND, Brouzgou A. Direct Ink Writing for Electrochemical Device Fabrication: A Review of 3D-Printed Electrodes and Ink Rheology. Catalysts 2024;14. https://doi.org/10.3390/catal14020110.
[611] Huang H, Yang W. MXene-Based Micro-Supercapacitors: Ink Rheology, Microelectrode Design and Integrated System. ACS Nano 2024;18:4651–82. https://doi.org/10.1021/acsnano.3c10246.
[612] Zhou G, Liu X, Liu C, Li Z, Liu C, Shi X, et al. 3D printed MXene-based films and cellulose nanofiber reinforced hydrogel electrolyte to enable high-performance flexible supercapacitors. J Mater Chem A 2024;12:3734–44. https://doi.org/10.1039/D3TA06925G.
[613] Peng S, Liu C, Tan J, Zhang P, Zou J, Wang Y, et al. Direct Ink Writing of Low-Concentration MXene/Aramid Nanofiber Inks for Tunable Electromagnetic Shielding and Infrared Anticounterfeiting Applications. ACS Appl Mater Interfaces 2024;16:25113–23. https://doi.org/10.1021/acsami.4c02755.
[614] Song Y, Tay R, Li J, Xu C, Min J, Shirzaei E, et al. 3D-printed epifluidic electronic skin for machine learning–powered multimodal health surveillance. Sci Adv 2023;9. https://doi.org/10.1126/sciadv.adi6492.
[615] Li T, Chen T, Shen X, Shi HH, Jabari E, Naguib HE. A binder jet 3D printed MXene composite for strain sensing and energy storage application. Nanoscale Adv 2022;4:916–25. https://doi.org/10.1039/D1NA00698C.
[616] Li Y, Peng S, Kankala RK, Wu L, Chen A-Z, Wang S-B. 3D printing of mechanically robust MXene-encapsulated polyurethane elastomer. Compos Part A Appl Sci Manuf 2022;163:107182. https://doi.org/10.1016/j.compositesa.2022.107182.

[617] Tao X, Zhang L, He X, Fang L, Wang H, Zhang L, et al. Nitrogen-Doped Porous MXene (Ti3C2) for Flexible Supercapacitors with Enhanced Storage Performance. Molecules 2022;27. https://doi.org/10.3390/molecules27154890.
[618] Fan Z, Jin J, Li C, Cai J, Wei C, Shao Y, et al. 3D-Printed Zn-Ion Hybrid Capacitor Enabled by Universal Divalent Cation-Gelated Additive-Free Ti3C2 MXene Ink. ACS Nano 2021;15:3098–107. https://doi.org/10.1021/acsnano.0c09646.
[619] Cao W, Wang Z, Liu X, Zhou Z, Zhang Y, He S, et al. Bioinspired MXene-Based User-Interactive Electronic Skin for Digital and Visual Dual-Channel Sensing. Nanomicro Lett 2022;14:119. https://doi.org/10.1007/s40820-022-00838-0.
[620] Tagliaferri S, Panagiotopoulos A, Mattevi C. Direct ink writing of energy materials. Mater Adv 2021;2:540–63.
[621] Zhang C, McKeon L, Kremer MP, Park S-H, Ronan O, Seral-Ascaso A, et al. Additive-free MXene inks and direct printing of micro-supercapacitors. Nat Commun 2019;10:1795.
[622] Orangi J, Hamade F, Davis VA, Beidaghi M. 3D printing of additive-free 2D Ti3C2T x (MXene) ink for fabrication of micro-supercapacitors with ultra-high energy densities. ACS Nano 2019;14:640–50.
[623] Yu L, Fan Z, Shao Y, Tian Z, Sun J, Liu Z. Versatile N-doped MXene ink for printed electrochemical energy storage application. Adv Energy Mater 2019;9:1901839.
[624] McLellan K, Li T, Sun YC, Jakubinek MB, Naguib HE. 4D Printing of MXene Composites for Deployable Actuating Structures. ACS Appl Polym Mater 2022;4:8774–85. https://doi.org/10.1021/ACSAPM.2C01192/ASSET/IMAGES/LARGE/AP2C01192_0010.JPEG.
[625] Wang Z, Zheng Y, Qiao L, Ma Y, Zeng H, Liang J, et al. 4D-Printed MXene-Based Artificial Nerve Guidance Conduit for Enhanced Regeneration of Peripheral Nerve Injuries. Adv Healthc Mater 2024;13:2401093. https://doi.org/10.1002/ADHM.202401093.
[626] Yang J, Gui Y, Wang Y, He S. NiO/Ti3C2Tx MXene nanocomposites sensor for ammonia gas detection at room temperature. Journal of Industrial and Engineering Chemistry 2023;119:476–84. https://doi.org/10.1016/j.jiec.2022.11.070.
[627] Quan W, Shi J, Luo H, Fan C, Lv W, Chen X, et al. Fully Flexible MXene-based Gas Sensor on Paper for Highly Sensitive Room-Temperature Nitrogen Dioxide Detection. ACS Sens 2023;8:103–13. https://doi.org/10.1021/acssensors.2c01748.
[628] Yuan W, Yang K, Peng H, Li F, Yin F. A flexible VOCs sensor based on a 3D Mxene framework with a high sensing performance. J Mater Chem A Mater 2018;6:18116–24. https://doi.org/10.1039/c8ta06928j.
[629] Mohanadas D, Rohani R, Sulaiman Y, Bakar SA, Mahmoudi E, Zhang LC. Heavy metal detection in water using MXene and its composites: A review. Materials Today Sustainability 2023;22:100411. https://doi.org/10.1016/j.mtsust.2023.100411.
[630] Banu AA, Sinthika S, Premkumar S, Vigneshwaran J, Karazhanov SZ, Jose SP. DFT study of NH3 adsorption on 2D monolayer MXenes (M2C, M = Cr, Fe) via oxygen functionalization: Suitable materials for gas sensors. FlatChem 2022;31:100329. https://doi.org/10.1016/j.flatc.2021.100329.
[631] Yang G, Liu F, Zhao J, Fu L, Gu Y, Qu L, et al. MXenes-based nanomaterials for biosensing and biomedicine. Coord Chem Rev 2023;479:215002. https://doi.org/10.1016/j.ccr.2022.215002.
[632] Sharif A, Khan SM, Tabish TA, Gull N, Zia S. Biosensing Applications of MXene-Based Composites. In: Rizwan K, Khan A, Ahmed Asiri AM, editors., Singapore: Springer Nature Singapore; 2023, p. 325–43. doi: 10.1007/978-981-99-2038-9_19.
[633] Wang Q, Han N, Shen Z, Li X, Chen Z, Cao Y, et al. MXene-based electrochemical (bio) sensors for sustainable applications: Roadmap for future advanced materials. Nano Materials Science 2023;5:39–52. https://doi.org/10.1016/j.nanoms.2022.07.003.
[634] Rhouati A, Berkani M, Vasseghian Y, Golzadeh N. MXene-based electrochemical sensors for detection of environmental pollutants: A comprehensive review. Chemosphere 2022;291:132921. https://doi.org/10.1016/j.chemosphere.2021.132921.
[635] Dhillon A, Singh N, Nair M, Kumar D. Analytical methods to determine and sense heavy metal pollutants using MXene and MXene-based composites: Mechanistic prophecy into sensing properties. Chemosphere 2022;303:135166. https://doi.org/10.1016/j.chemosphere.2022.135166.
[636] Gopalram K, Kapoor A, Kumar PS, Sunil A, Rangasamy G. MXenes and MXene-Based Materials for Removal and Detection of Water Contaminants: A Review. Ind Eng Chem Res 2023;62:6559–83. https://doi.org/10.1021/acs.iecr.3c00595.
[637] Pouramini Z, Mousavi SM, Babapoor A, Hashemi SA, Pynadathu Rumjit N, Garg S, et al. Recent Advances in MXene-Based Nanocomposites for Wastewater Purification and Water Treatment: A Review. Water (Switzerland) 2023;15. doi: 10.3390/w15071267.
[638] Hilal M, Yang W, Hwang Y, Xie W. Tailoring MXene Thickness and Functionalization for Enhanced Room-Temperature Trace NO2 Sensing. Nanomicro Lett 2024;16:84. https://doi.org/10.1007/s40820-023-01316-x.
[639] Majhi SM, Ali A, Greish YE, El-Maghraby HF, Mahmoud ST. V2CTX MXene-based hybrid sensor with high selectivity and ppb-level detection for acetone at room temperature. Sci Rep 2023;13:3114. https://doi.org/10.1038/s41598-023-30002-6.
[640] Chia HL, Mayorga-Martinez CC, Antonatos N, Sofer Z, Gonzalez-Julian JJ, Webster RD, et al. MXene titanium carbide-based biosensor: strong dependence of exfoliation method on performance. Anal Chem 2020;92:2452–9.
[641] Xia T, Liu G, Wang J, Hou S, Hou S. MXene-based enzymatic sensor for highly sensitive and selective detection of cholesterol. Biosens Bioelectron 2021;183:113243. https://doi.org/10.1016/j.bios.2021.113243.
[642] Amara U, Hussain I, Ahmad M, Mahmood K, Zhang K. 2D MXene-Based Biosensing: A Review. Small 2023;19:2205249. https://doi.org/10.1002/smll.202205249.
[643] Aslam M, Ahmad T, Manzoor MH, Laiba VF. MXenes as theranostics: Diagnosis and therapy including in vitro and in vivo applications. Appl Mater Today 2023;35:102002. https://doi.org/10.1016/j.apmt.2023.102002.
[644] Bashandeh K, Amiri A, Rafieerad A, Rahman S, Yan W, Dhingra S, et al. MXene-aromatic thermosetting copolyester nanocomposite as an extremely wear-resistant biocompatible implant material for osteoarthritis applications. Appl Surf Sci 2022;600:154124. https://doi.org/10.1016/j.apsusc.2022.154124.
[645] Ye S, Zhang H, Lai H, Xu J, Yu L, Ye Z, et al. MXene: A wonderful nanomaterial in antibacterial. Front Bioeng. Biotechnol 2024;12. https://doi.org/10.3389/fbioe.2024.1338539.
[646] Sinha A, Dhanjai, Mugo SM, Chen J, Lokesh KS. MXene-based sensors and biosensors: Next-generation detection platforms. In: Mustansar Hussain CBT-H of N in AC, editor. Handbook of Nanomaterials in Analytical Chemistry: Modern Trends in Analysis, Elsevier; 2019, p. 361–72. doi: 10.1016/B978-0-12-816699-4.00014-1.
[647] Goel H, Gupta P, Jha K, Akshita PM, Shruti, et al. Mxene-based nanocomposites for biosensing: Recent developments and future prospects. FlatChem 2023;42:100576. https://doi.org/10.1016/j.flatc.2023.100576.
[648] Jamalipour Soufi G, Iravani P, Hekmatnia A, Mostafavi E, Khatami M, Iravani S. MXenes and MXene-based Materials with Cancer Diagnostic Applications: Challenges and Opportunities. Comments on Inorganic Chemistry 2022;42:174–207. https://doi.org/10.1080/02603594.2021.1990890.
[649] Iravani S, Varma RS. MXenes in Cancer Nanotheranostics. Nanomaterials 2022;12. https://doi.org/10.3390/nano12193360.
[650] Iravani S, Varma RS. MXenes for Cancer Therapy and Diagnosis: Recent Advances and Current Challenges. ACS Biomater Sci Eng 2021;7:1900–13. https://doi.org/10.1021/acsbiomaterials.0c01763.
[651] Xia Z, Chen X, Ci H, Fan Z, Yi Y, Yin W, et al. Designing N-doped graphene/ReSe2/Ti3C2 MXene heterostructure frameworks as promising anodes for high-rate potassium-ion batteries. Journal of Energy Chemistry 2020;53:155–62. https://doi.org/10.1016/j.jechem.2020.04.071.
[652] Kulkarni S, Soman S, Navti PD, Roy AA, Nikam AN, Vineeth P, et al. Nano-Innovations in Cancer Therapy: The Unparalleled Potential of MXene Conjugates. Materials 2024;17. https://doi.org/10.3390/ma17061423.
[653] Su X, You Q, Zhuang L, Chang Z, Ge M, Yang L, et al. Bifunctional electrochemical biosensor based on PB-MXene films for the real-time analysis and detection of living cancer cells. J Pharm Biomed Anal 2023;234:115479. https://doi.org/10.1016/j.jpba.2023.115479.
[654] Bai M, Sutrisno L, Duan J, Wan H, Chen G, Liu X, et al. Rare-earth hydroxide/MXene hybrid: a promising agent for near-infrared photothermy and magnetic resonance imaging. Chem Sci 2023;14:10795–9. https://doi.org/10.1039/d3sc02604c.
[655] Lu B, Hu S, Wu D, Wu C, Zhu Z, Hu L, et al. Ionic liquid exfoliated Ti3C2TxMXene nanosheets for photoacoustic imaging and synergistic photothermal/chemotherapy of cancer. J Mater Chem B 2022;10:1226–35. https://doi.org/10.1039/d1tb01938d.
[656] Yang M, Xu Y, Zhang X, Bisoyi HK, Xue P, Yang Y, et al. Bioinspired Phototropic MXene-Reinforced Soft Tubular Actuators for Omnidirectional Light-Tracking and Adaptive Photovoltaics (Adv. Funct. Mater. 26/2022). Adv Funct Mater 2022;32:2270152. doi: 10.1002/adfm.202270152.

[657] Ranjbari S, Darroudi M, Hatamluyi B, Arefinia R, Aghaee-Bakhtiari SH, Rezayi M, et al. Application of MXene in the diagnosis and treatment of breast cancer: A critical overview. Front Bioeng. Biotechnol 2022;10. https://doi.org/10.3389/fbioe.2022.984336.
[658] Perini G, Rosenkranz A, Friggeri G, Zambrano D, Rosa E, Augello A, et al. Advanced usage of Ti3C2Tx MXenes for photothermal therapy on different 3D breast cancer models. Biomedicine and Pharmacotherapy 2022;153:113496. https://doi.org/10.1016/j.biopha.2022.113496.
[659] Iravani S, Varma RS. MXenes in photomedicine: advances and prospects. Chemical Communications 2022;58:7336–50. https://doi.org/10.1039/d2cc01694j.
[660] Mousavi SM, Kalashgrani MY, Binazadeh M, Mazaheri Y, Omidifar N, Rahmanian V, et al. Recent advancements in smart MXene quantum dot-based nanosystems for immunomodulatory and effective cancer treatment. Mater Today Chem 2024;38:102097. https://doi.org/10.1016/j.mtchem.2024.102097.
[661] Singh B, Bahadur R, Rai D, Srivastava R. Preclinical Toxicity Assessment of Ti-Based MXene Nanomaterials for Advanced Theranostic Applications. Adv Ther (Weinh) 2024;7:2300268. https://doi.org/10.1002/adtp.202300268.
[662] Wang J, Qiao Q, Feng Y, Guo Y, Liao T, Li L, et al. Two-dimensional MXene-based nano-prodrug for synergistic chemo-photothermal therapy on cancer treatment. Mater Today Chem 2024;38:102048. https://doi.org/10.1016/j.mtchem.2024.102048.
[663] Tan EW, Simon SE, Numan A, Khalid M, Tan KO. Impact of UV radiation on Mxene-mediated tubulin dissociation and mitochondrial apoptosis in breast cancer cells. Colloids Surf B Biointerfaces 2024;235:113793. https://doi.org/10.1016/j.colsurfb.2024.113793.
[664] Bai Z, Zhao L, Feng H, Xin Z, Wang C, Liu Z, et al. Aptamer modified Ti3C2 nanosheets application in smart targeted photothermal therapy for cancer. Cancer Nanotechnol 2023;14:35. https://doi.org/10.1186/s12645-023-00189-4.
[665] Li F, Yan Y, Wang Y, Fan Y, Zou H, Liu H, et al. A bifunctional MXene-modified scaffold for photothermal therapy and maxillofacial tissue regeneration. Regen Biomater 2021;8:rbab057. https://doi.org/10.1093/rb/rbab057.
[666] Zhao L, Zhang R, Yang G, Wang Y, Gai S, Zhao X, et al. CeO2 and Glucose Oxidase Co-Enriched Ti3C2Tx MXene for Hyperthermia-Augmented Nanocatalytic Cancer Therapy. ACS Appl Mater Interfaces 2024;16:9968–79. https://doi.org/10.1021/acsami.4c00425.
[667] Ramachandran T, Mourad AHI, ElSayed MSA. Nb2CTx-Based MXenes Most Recent Developments: From Principles to New Applications. Energies (Basel) 2023;16:3520. https://doi.org/10.3390/en16083520.
[668] Zong L, Wu H, Lin H, Chen Y. A polyoxometalate-functionalized two-dimensional titanium carbide composite MXene for effective cancer theranostics. Nano Res 2018;11:4149–68. https://doi.org/10.1007/s12274-018-2002-3.
[669] Deng R, Chang M, Chen Y, Zhou Y. Two-dimensional photonic MXene nanomedicine. Nanophotonics 2022;11:4995–5017. https://doi.org/10.1515/nanoph-2022-0514.
[670] Feng W, Han X, Hu H, Chang M, Ding L, Xiang H, et al. 2D vanadium carbide MXenzyme to alleviate ROS-mediated inflammatory and neurodegenerative diseases. Nat Commun 2021;12:2203. https://doi.org/10.1038/s41467-021-22278-x.
[671] Navitski I, Ramanaviciute A, Ramanavicius S, Pogorielov M, Ramanavicius A. MXene-Based Chemo-Sensors and Other Sensing Devices. Nanomaterials 2024;14. https://doi.org/10.3390/nano14050447.
[672] He J, Zou H, Zhou J, Deng C. Thermoresponsive MXene-based hydrogel for controlled anticancer drug release. J Drug Deliv Sci Technol 2024;91:105207. https://doi.org/10.1016/j.jddst.2023.105207.
[673] Yan W, Rafieerad A, Alagarsamy KN, Saleth LR, Arora RC, Dhingra S. Immunoengineered MXene nanosystem for mitigation of alloantigen presentation and prevention of transplant vasculopathy. Nano Today 2023;48:101706. https://doi.org/10.1016/j.nantod.2022.101706.
[674] Gazzi A, Fusco L, Khan A, Bedognetti D, Zavan B, Vitale F, et al. Photodynamic therapy based on graphene and MXene in cancer theranostics. Front Bioeng Biotechnol 2019;7:295. https://doi.org/10.3389/fbioe.2019.00295.
[675] Dai C, Chen Y, Jing X, Xiang L, Yang D, Lin H, et al. Two-dimensional tantalum carbide (MXenes) composite nanosheets for multiple imaging-guided photothermal tumor ablation. ACS Nano 2017;11:12696–712.
[676] He C, Yu L, Yao H, Chen Y, Hao Y. Combinatorial photothermal 3D-printing scaffold and checkpoint blockade inhibits growth/metastasis of breast cancer to bone and accelerates osteogenesis. Adv Funct Mater 2021;31:2006214.
[677] Yang Y-C, Lin Y-T, Yu J, Chang H-T, Lu T-Y, Huang T-Y, et al. MXene Nanosheet-Based Microneedles for Monitoring Muscle Contraction and Electrostimulation Treatment. ACS Appl Nano Mater 2021;4:7917–24. https://doi.org/10.1021/acsanm.1c01237.
[678] Liao H, Guo X, Wan P, Yu G. Conductive MXene nanocomposite organohydrogel for flexible, healable, low-temperature tolerant strain sensors. Adv Funct Mater 2019;29:1904507.
[679] Pereira P, Ferreira DP, Araújo JC, Ferreira A, Fangueiro R. The potential of graphene nanoplatelets in the development of smart and multifunctional ecocomposites. Polymers (Basel) 2020;12:2189. https://doi.org/10.3390/POLYM12102189.
[680] Zahra SA, Murshed MM, Naeem U, Gesing TM, Rizwan S. Cation-assisted self-assembled pillared V2CTx MXene electrodes for efficient energy storage. Chemical Engineering Journal 2023;474:145526. https://doi.org/10.1016/j.cej.2023.145526.
[681] Zhang X, Zhang T, Xiao J, Jin Q, Wang Z, Zhang C, et al. Highly stable few-layer V2CTx MXene/Carbon nanotube structure with restrained restacking for lithium ion storage. J Colloid Interface Sci 2023;630:502–11. https://doi.org/10.1016/j.jcis.2022.10.038.
[682] Zhang M, Yang Y, Wang Y, Zhang B, Wang H, Fang G, et al. A molecularly imprinted electrochemical sensor based on cationic intercalated two-dimensional titanium carbide nanosheets for sensitive and selective detection of triclosan in food samples. Food Control 2022;132:108532.
[683] Zhong W, Gao F, Zou J, Liu S, Li M, Gao Y, et al. MXene@ Ag-based ratiometric electrochemical sensing strategy for effective detection of carbendazim in vegetable samples. Food Chem 2021;360:130006.
[684] Xie Y, Gao F, Tu X, Ma X, Xu Q, Dai R, et al. Facile synthesis of MXene/electrochemically reduced graphene oxide composites and their application for electrochemical sensing of carbendazim. J Electrochem Soc 2019;166:B1673.
[685] Shetti NP, Mishra A, Basu S, Aminabhavi TM, Alodhayb A, Pandiaraj S. MXenes as Li-Ion Battery Electrodes: Progress and Outlook. Energy and Fuels 2023;37:12541–57. https://doi.org/10.1021/acs.energyfuels.3c01346.
[686] Aslam MK, Niu Y, Xu M. MXenes for Non-Lithium-Ion (Na, K, Ca, Mg, and Al) Batteries and Supercapacitors. Adv Energy Mater 2021;11:2000681. https://doi.org/10.1002/aenm.202000681.
[687] Li J, Liu H, Shi X, Li X, Li W, Guan E, et al. MXene-based anode materials for high performance sodium-ion batteries. J Colloid Interface Sci 2024;658:425–40. https://doi.org/10.1016/j.jcis.2023.12.065.
[688] Zhang L, Chen Y, Yu L, Tao X, Tang L, Ye L, et al. Efficient sulfur atom-doped three-dimensional porous MXene-assisted sodium ion batteries. Dalton Transactions 2024;53:6583–91. https://doi.org/10.1039/d3dt04312f.
[689] Li Y, Zhu YC, Vallem S, Li M, Song S, Chen T, et al. Flame-retardant ammonium polyphosphate/MXene decorated carbon foam materials as polysulfide traps for fire-safe and stable lithium-sulfur batteries. Journal of Energy Chemistry 2024;89:313–23. https://doi.org/10.1016/j.jechem.2023.10.029.
[690] Luo J, Tao X, Zhang J, Xia Y, Huang H, Zhang L, et al. Sn4+ Ion Decorated Highly Conductive Ti3C2 MXene: Promising Lithium-Ion Anodes with Enhanced Volumetric Capacity and Cyclic Performance. ACS Nano 2016;10:2491–9. https://doi.org/10.1021/acsnano.5b07333.
[691] Zhu F, Tao J, Yan M, Huang S, Irshad MS, Mei T, et al. NiS2-MoS2@MXene heterostructures for enhancing polysulfide adsorption and conversion of Li–S battery. Sustainable Materials and Technologies 2024;39:e00868. https://doi.org/10.1016/j.susmat.2024.e00868.
[692] Perminov A, Bartzsch G, Franke A, Biermann H, Volkova O. Manufacturing Fe–TiC Composite Powder via Inert Gas Atomization by Forming Reinforcement Phase In Situ. Adv Eng Mater 2021;23:2000717. https://doi.org/10.1002/adem.202000717.
[693] Xia QX, Fu J, Yun JM, Mane RS, Kim KH. High volumetric energy density annealed-MXene-nickel oxide/MXene asymmetric supercapacitor. RSC Adv 2017;7:11000–11. https://doi.org/10.1039/c6ra27880a.
[694] Li Z, Wu Y. 2D Early Transition Metal Carbides (MXenes) for Catalysis. Small 2019;15:1804736. https://doi.org/10.1002/smll.201804736.
[695] Kadja GTM, Ilmi MM, Azhari NJ, Febrianti A, Siregar JJM, Nurdini N, et al. MXene-based nanocomposite for electrocatalytic reduction of CO2: Experimental and theoretical results. FlatChem 2023;38:100481. https://doi.org/10.1016/j.flatc.2023.100481.
[696] Chen L, Huang K, Xie Q, Lam SM, Sin JC, Su T, et al. The enhancement of photocatalytic CO2reduction by thein situgrowth of TiO2on Ti3C2MXene. Catal Sci Technol 2021;11:1602–14. https://doi.org/10.1039/d0cy02212h.

[697] Zhang F, Zhang X, Hu S, Hu H, Ye J, Wang D. Selective photothermal reduction of CO2 to CH4 via the synergistic effect of Ni-nanoparticle@NiO-nanosheet/V2C-MXene catalyst. Mater Today Energy 2024;39:101470. https://doi.org/10.1016/j.mtener.2023.101470.
[698] Li J, Wang Z, Chen H, Zhang Q, Hu H, Liu L, et al. A surface-alkalinized Ti3C2MXene as an efficient cocatalyst for enhanced photocatalytic CO2reduction over ZnO. Catal Sci Technol 2021;11:4953–61. https://doi.org/10.1039/d1cy00716e.
[699] Wang Z, Al Jitan S, AlNashef I, Tardy BL, Palmisano G. Recent progress of MXene as a cocatalyst in photocatalytic carbon dioxide reduction. Chemical Engineering Journal Advances 2024;18:100593. https://doi.org/10.1016/j.ceja.2024.100593.
[700] Ranjan P, Saptal VB, Bera JK. Recent Advances in Carbon Dioxide Adsorption, Activation and Hydrogenation to Methanol using Transition Metal Carbides. ChemSusChem 2022;15:e202201183. https://doi.org/10.1002/cssc.202201183.
[701] Zhang Q, Pastor-Pérez L, Gu S, Reina TR. Transition metal carbides (TMCS) catalysts for gas phase CO2 upgrading reactions: A comprehensive overview. Catalysts 2020;10. https://doi.org/10.3390/catal10090955.
[702] Wang L, Jiang H, Wang H, Show PL, Ivanets A, Luo D, et al. MXenes as heterogeneous Fenton-like catalysts for removal of organic pollutants: A review. J Environ Chem Eng 2022;10:108954. https://doi.org/10.1016/j.jece.2022.108954.
[703] Rapeyko A, Barjola A, Seva MD, Sahuquillo O, Navalón S, Giménez E, et al. Titanium MXenes as Heterogeneous Catalysts for the Styrene-to-Benzaldehyde Oxidation: Influence of the Etching Conditions. ChemCatChem 2024;16:e202301599. https://doi.org/10.1002/cctc.202301599.
[704] Yan Y, Sall D, Loupias L, Célérier S, Aouine M, Bargiela P, et al. MXene-supported single-atom and nano catalysts for effective gas-phase hydrogenation reactions. Materials Today Catalysis 2023;2:100010. https://doi.org/10.1016/j.mtcata.2023.100010.
[705] Meng Y, Wang H, Liang JX, Zhu C, Li J. Computational Screening of Pt1@Ti3C2T2 (T = O, S) MXene Catalysts for Water-Gas Shift Reaction. Precision Chemistry 2024;2:70–80. https://doi.org/10.1021/prechem.3c00104.
[706] Dolz D, De Armas R, Lozano-Reis P, Morales-García Á, Viñes F, Sayós R, et al. Understanding the Reverse Water Gas Shift Reaction over Mo2C MXene Catalyst: A Holistic Computational Analysis. ChemCatChem 2024;n/a:e202400122. doi: 10.1002/cctc.202400122.
[707] Gouveia JD, Morales-García ángel, Viñes F, Gomes JRB, Illas F.. Facile Heterogeneously Catalyzed Nitrogen Fixation by MXenes. ACS Catal 2020;10:5049–56. https://doi.org/10.1021/acscatal.0c00935.
[708] Diao J, Hu M, Lian Z, Li Z, Zhang H, Huang F, et al. Ti3C2Tx MXene Catalyzed Ethylbenzene Dehydrogenation: Active Sites and Mechanism Exploration from both Experimental and Theoretical Aspects. ACS Catal 2018;8:10051–7. https://doi.org/10.1021/acscatal.8b02002.
[709] Blanco E, Rosenkranz A, Espinoza-González R, Fuenzalida VM, Zhang Z, Suárez S, et al. Catalytic performance of 2D-Mxene nano-sheets for the hydrodeoxygenation (HDO) of lignin-derived model compounds. Catal Commun 2020;133:105833. https://doi.org/10.1016/j.catcom.2019.105833.
[710] Talib SH, Lu Z, Bashir B, Hussain S, Ahmad K, Khan S, et al. CO oxidation on MXene (Mo2CS2) supported single-atom catalyst: A termolecular Eley-Rideal mechanism. Chinese Chemical Letters 2023;34:107412. https://doi.org/10.1016/j.cclet.2022.04.010.
[711] Cheng C, Zhang X, Yang Z, Hermansson K. Identification of High-Performance Single-Atom MXenes Catalysts for Low-Temperature CO Oxidation. Adv Theory Simul 2019;2:1900006. https://doi.org/10.1002/adts.201900006.
[712] Deeva EB, Kurlov A, Abdala PM, Lebedev D, Kim SM, Gordon CP, et al. In Situ XANES/XRD Study of the Structural Stability of Two-Dimensional Molybdenum Carbide Mo2CT x: Implications for the Catalytic Activity in the Water-Gas Shift Reaction. Chemistry of Materials 2019;31:4505–13. https://doi.org/10.1021/acs.chemmater.9b01105.
[713] Fan X, Du P, Ma X, Wang R, Ma J, Wang Y, et al. Mechanochemical synthesis of pt/nb2ctx mxene composites for enhanced electrocatalytic hydrogen evolution. Materials 2021;14. https://doi.org/10.3390/ma14092426.
[714] Liu A, Gao M, Ren X, Meng F, Yang Y, Yang Q, et al. A two-dimensional Ru@MXene catalyst for highly selective ambient electrocatalytic nitrogen reduction. Nanoscale 2020;12:10933–8. https://doi.org/10.1039/d0nr00788a.
[715] Sun Z, Wang R, Matulis VE, Vladimir K. MXene-Based Catalysts 2024.
[716] Sajid IH, Iqbal MZ, Rizwan S. Recent advances in the role of MXene based hybrid architectures as electrocatalysts for water splitting. RSC Adv 2024;14:6823–47. https://doi.org/10.1039/d3ra06725d.
[717] Chen J, Gao X, Li J, Kang Z, Bai J, Wang T, et al. Progress in MXene-based catalysts for oxygen evolution reaction. Electron 2024;2. https://doi.org/10.1002/elt2.17.
[718] Chen Y, Meng G, Yang T, Chen C, Chang Z, Kong F, et al. Interfacial engineering of Co-doped 1T-MoS2 coupled with V2C MXene for efficient electrocatalytic hydrogen evolution. Chemical Engineering Journal 2022;450:138157. https://doi.org/10.1016/j.cej.2022.138157.
[719] Luo R, Li R, Jiang C, Qi R, Liu M, Luo C, et al. Facile synthesis of cobalt modified 2D titanium carbide with enhanced hydrogen evolution performance in alkaline media. Int J Hydrogen Energy 2021;46:32536–45. https://doi.org/10.1016/j.ijhydene.2021.07.110.
[720] Wang L, Song L, Yang Z, Chang YM, Hu F, Li L, et al. Electronic Modulation of Metal–Organic Frameworks by Interfacial Bridging for Efficient pH-Universal Hydrogen Evolution. Adv Funct Mater 2023;33:2210322. https://doi.org/10.1002/adfm.202210322.
[721] Jiang J, Bai S, Yang M, Zou J, Li N, Peng J, et al. Strategic design and fabrication of MXenes-Ti3CNCl2@CoS2 core-shell nanostructure for high-efficiency hydrogen evolution. Nano Res 2022;15:5977–86. https://doi.org/10.1007/s12274-022-4276-8.
[722] Yan L, Song D, Liang J, Li X, Li H, Liu Q. Fabrication of highly efficient Rh-doped cobalt–nickel-layered double hydroxide/MXene-based electrocatalyst with rich oxygen vacancies for hydrogen evolution. J Colloid Interface Sci 2023;640:338–47. https://doi.org/10.1016/j.jcis.2023.02.113.
[723] Shen B, Huang H, Jiang Y, Xue Y, He H. 3D interweaving MXene–graphene network–confined Ni–Fe layered double hydroxide nanosheets for enhanced hydrogen evolution. Electrochim Acta 2022;407:139913. https://doi.org/10.1016/j.electacta.2022.139913.
[724] Ma S, Xu Z, Jia Z, Chen L, Zhu H, Chen Y, et al. Facile fabrication of carbon fiber skeleton structure of MoS2 supported on 2D MXene composite with highly efficient and stable hydrogen evolution reaction. Compos Sci Technol 2022;222:109380. https://doi.org/10.1016/j.compscitech.2022.109380.
[725] Ma C, He H, Qin J, Hao L, Jia L, Yang L, et al. Combining MXene nanosheets with iron-based metal-organic frameworks for enhanced electrocatalytic hydrogen evolution reaction. Mater Today Chem 2023;30:101531. https://doi.org/10.1016/j.mtchem.2023.101531.
[726] Zhang L, Zhao X, Chu Z, Wang Q, Cao Y, Li J, et al. Construction of Co-decorated 3D nitrogen doped-carbon nanotube/Ti3C2Tx-MXene as efficient hydrogen evolution electrocatalyst. Int J Hydrogen Energy 2023;48:15053–64. https://doi.org/10.1016/j.ijhydene.2022.12.028.
[727] Reghunath BS, K R SD, Rajasekaran S, Saravanakumar B, William JJ, Pinheiro D. Hierarchical BiFeO3/Cr2CTx MXene composite as a multifunctional catalyst for hydrogen evolution reaction and as an electrode material for energy storage devices. Electrochim Acta 2023;461:142685. doi: 10.1016/j.electacta.2023.142685.
[728] Ma C, He H, Qin J, Luo L, Lan Y, Zhang J, et al. The Marriage of Hydrazone-Linked Covalent Organic Frameworks and MXene Enables Efficient Electrocatalytic Hydrogen Evolution. Small Struct 2024;5:2300279. https://doi.org/10.1002/sstr.202300279.
[729] Hussain S, Vikraman D, Ali Sheikh Z, Taqi Mehran M, Shahzad F, Mujasam Batoo K, et al. WS2-embedded MXene/GO hybrid nanosheets as electrodes for asymmetric supercapacitors and hydrogen evolution reactions. Chemical Engineering Journal 2023;452:139523. https://doi.org/10.1016/j.cej.2022.139523.
[730] Yin J, Wei K, Bai Y, Liu Y, Zhang Q, Wang J, et al. Integration of amorphous CoSnO3 onto wrinkled MXene nanosheets as efficient electrocatalysts for alkaline hydrogen evolution. Sep Purif Technol 2023;308:122947. https://doi.org/10.1016/j.seppur.2022.122947.
[731] Biswal L, Mohanty R, Nayak S, Parida K. Review on MXene/TiO2 nanohybrids for photocatalytic hydrogen production and pollutant degradations. J Environ Chem Eng 2022;10:107211. https://doi.org/10.1016/j.jece.2022.107211.
[732] Yang C, Tan Q, Li Q, Zhou J, Fan J, Li B, et al. 2D/2D Ti3C2 MXene/g-C3N4 nanosheets heterojunction for high efficient CO2 reduction photocatalyst: Dual effects of urea. Appl Catal B 2020;268:118738. https://doi.org/10.1016/j.apcatb.2020.118738.
[733] Navakoteswara Rao V, Kwon H, Lee Y, Ravi P, Won Ahn C, Kim K, et al. Synergistic integration of MXene nanosheets with CdS@TiO2 core@shell S-scheme photocatalyst for augmented hydrogen generation. Chemical Engineering Journal 2023;471:144490. https://doi.org/10.1016/j.cej.2023.144490.
[734] Jiang J, Li F, Ding L, Zhang C, Arramel LX. MXenes/CNTs-based hybrids: Fabrications, mechanisms, and modification strategies for energy and environmental applications. Nano Res 2024;17:3429–54. https://doi.org/10.1007/s12274-023-6302-x.
[735] Pavithra Siddu NK, Jeong SM, Rout CS. MXene-carbon based hybrid materials for supercapacitor applications. Energy Advances 2024;3:341–65. https://doi.org/10.1039/d3ya00502j.

[736] Rasheed T, Kausar F, Rizwan K, Adeel M, Sher F, Alwadai N, et al. Two dimensional MXenes as emerging paradigm for adsorptive removal of toxic metallic pollutants from wastewater. Chemosphere 2022;287:132319. https://doi.org/10.1016/j.chemosphere.2021.132319.
[737] Ibrahim Y, Meslam M, Eid K, Salah B, Abdullah AM, Ozoemena KI, et al. A review of MXenes as emergent materials for dye removal from wastewater. Sep Purif Technol 2022;282:120083. https://doi.org/10.1016/j.seppur.2021.120083.
[738] Kashif S, Akram S, Murtaza M, Amjad A, Shah SSA, Waseem A. Development of MOF-MXene composite for the removal of dyes and antibiotic. Diam Relat Mater 2023;136:110023. https://doi.org/10.1016/j.diamond.2023.110023.
[739] Rethinasabapathy M, Bhaskaran G, Park B, Shin JY, Kim WS, Ryu J, et al. Iron oxide (Fe3O4)-laden titanium carbide (Ti3C2Tx) MXene stacks for the efficient sequestration of cationic dyes from aqueous solution. Chemosphere 2022;286:131679. https://doi.org/10.1016/j.chemosphere.2021.131679.
[740] Jiang S, Qian K, Yu K, Zhou H, Weng Y, Zhang Z. Controllable synthesis and microwave absorption properties of Fe3O4@f-GNPs nanocomposites. Composites Communications 2020;20:100363. https://doi.org/10.1016/j.coco.2020.100363.
[741] Ma XY, Fan TT, Wang G, Li ZH, Lin JH, Long YZ. High performance GO/MXene/PPS composite filtration membrane for dye wastewater treatment under harsh environmental conditions. Composites Communications 2022;29:101017. https://doi.org/10.1016/j.coco.2021.101017.
[742] My Tran N, Thanh Hoai Ta Q, Sreedhar A, Noh JS. Ti3C2Tx MXene playing as a strong methylene blue adsorbent in wastewater. Appl Surf Sci 2021;537:148006. https://doi.org/10.1016/j.apsusc.2020.148006.
[743] Lim S, Kim JH, Park H, Kwak C, Yang J, Kim J, et al. Role of electrostatic interactions in the adsorption of dye molecules by Ti3C2-MXenes. RSC Adv 2021;11:6201–11. https://doi.org/10.1039/d0ra10876f.
[744] Jun BM, Heo J, Taheri-Qazvini N, Park CM, Yoon Y. Adsorption of selected dyes on Ti3C2Tx MXene and Al-based metal-organic framework. Ceram Int 2020;46:2960–8. https://doi.org/10.1016/j.ceramint.2019.09.293.
[745] Lu J, Dai C, Li S, Zou D, Sun Y, Jing W. Ultraefficient Li+/Mg2+ separation with MXene/CNT membranes under electric field assistance. Sep Purif Technol 2024;338:126508. https://doi.org/10.1016/j.seppur.2024.126508.
[746] Van der Bruggen B. The Separation Power of Nanotubes in Membranes: A Review. ISRN Nanotechnology 2012;2012:1–17. https://doi.org/10.5402/2012/693485.
[747] Bury D, Jakubczak M, Kumar R, Ścieżyńska D, Bogacki J, Marcinowski P, et al. Cleaning the environment with MXenes. MRS Bull 2023;48:271–82. https://doi.org/10.1557/s43577-023-00507-6.
[748] Arabi Shamsabadi A, Sharifian GM, Anasori B, Soroush M. Antimicrobial mode-of-action of colloidal Ti3C2T x MXene nanosheets. ACS Sustain Chem Eng 2018;6:16586–96.
[749] Purbayanto MAK, Jakubczak M, Bury D, Nair VG, Birowska M, Moszczyńska D, et al. Tunable Antibacterial Activity of a Polypropylene Fabric Coated with Bristling Ti3C2T x MXene Flakes Coupling the Nanoblade Effect with ROS Generation. ACS Appl Nano Mater 2022;5:5373–86.
[750] Liu Y, Tian Y, Han Q, Yin J, Zhang J, Yu Y, et al. Synergism of 2D/1D MXene/cobalt nanowire heterojunctions for boosted photo-activated antibacterial application. Chemical Engineering Journal 2021;410:128209. https://doi.org/10.1016/j.cej.2020.128209.
[751] Tawalbeh M, Mohammed S, Al-Othman A, Yusuf M, Mofijur M, Kamyab H. MXenes and MXene-based materials for removal of pharmaceutical compounds from wastewater: Critical review. Environ Res 2023;228:115919. https://doi.org/10.1016/j.envres.2023.115919.
[752] Jeon M, Jun BM, Kim S, Cho J, Park CM, Choong CE, et al. Sonodegradation of amitriptyline and ibuprofen in the presence of Ti3C2Tx MXene. Journal of Hazardous Materials Letters 2021;2:100028. https://doi.org/10.1016/j.hazl.2021.100028.
[753] Kim S, Nam SN, Park CM, Jang M, Taheri-Qazvini N, Yoon Y. Effect of single and multilayered Ti3C2TX MXene as a catalyst and adsorbent on enhanced sonodegradation of diclofenac and verapamil. J Hazard Mater 2022;426:128120. https://doi.org/10.1016/j.jhazmat.2021.128120.
[754] Shahzad A, Rasool K, Nawaz M, Miran W, Jang J, Moztahida M, et al. Heterostructural TiO2/Ti3C2Tx (MXene) for photocatalytic degradation of antiepileptic drug carbamazepine. Chemical Engineering Journal 2018;349:748–55. https://doi.org/10.1016/j.cej.2018.05.148.
[755] Xu M, Huang C, Lu J, Wu Z, Zhu X, Li H, et al. Optimizing adsorption of 17α-ethinylestradiol from water by magnetic mxene using response surface methodology and adsorption kinetics, isotherm, and thermodynamics studies. Molecules 2021;26. https://doi.org/10.3390/molecules26113150.
[756] Grzegórska A, Ofoegbu JC, Cervera-Gabalda L, Gómez-Polo C, Sannino D, Zielińska-Jurek A. Magnetically recyclable TiO2/MXene/MnFe2O4 photocatalyst for enhanced peroxymonosulphate-assisted photocatalytic degradation of carbamazepine and ibuprofen under simulated solar light. J Environ Chem Eng 2023;11:110660. https://doi.org/10.1016/j.jece.2023.110660.
[757] Jang J, Shahzad A, Woo SH, Lee DS. Magnetic Ti3C2Tx (Mxene) for diclofenac degradation via the ultraviolet/chlorine advanced oxidation process. Environ Res 2020;182:108990. https://doi.org/10.1016/j.envres.2019.108990.
[758] Kim S, Gholamirad F, Yu M, Park CM, Jang A, Jang M, et al. Enhanced adsorption performance for selected pharmaceutical compounds by sonicated Ti3C2TX MXene. Chemical Engineering Journal 2021;406:126789. https://doi.org/10.1016/j.cej.2020.126789.
[759] Sharma V, Kumar A, Kumar A, Krishnan V. Enhanced photocatalytic activity of two dimensional ternary nanocomposites of ZnO–Bi2WO6–Ti3C2 MXene under natural sunlight irradiation. Chemosphere 2022;287:132119. https://doi.org/10.1016/j.chemosphere.2021.132119.
[760] Chinnasamy C, Perumal N, Choubey A, Rajendran S. Recent advancements in MXene-based nanocomposites as photocatalysts for hazardous pollutant degradation - A review. Environ Res 2023;233:116459. https://doi.org/10.1016/j.envres.2023.116459.
[761] Mu M, Graham N, Yu W, Sun K, Xu X, Liu T. Optimal cross-linking of MXene-based membranes for high rejection and low adsorption with long-term stability for water treatment. J Memb Sci 2024;701:122738. https://doi.org/10.1016/j.memsci.2024.122738.
[762] Lim S, Park H, Kim JH, Yang J, Kwak C, Kim J, et al. Polyelectrolyte-grafted Ti3C2-MXenes stable in extreme salinity aquatic conditions for remediation of contaminated subsurface environments. RSC Adv 2020;10:25966–78. https://doi.org/10.1039/d0ra04348f.
[763] Zhang ZH, Xu JY, Yang XL. MXene/sodium alginate gel beads for adsorption of methylene blue. Mater Chem Phys 2021;260:124123. https://doi.org/10.1016/j.matchemphys.2020.124123.
[764] Seidi F, Arabi Shamsabadi A, Dadashi Firouzjaei M, Elliott M, Saeb MR, Huang Y, et al. MXenes Antibacterial Properties and Applications: A Review and Perspective. Small 2023;19:2206716. https://doi.org/10.1002/smll.202206716.
[765] Liu Y, Chen X, Sun J, Xu N, Tang Q, Ren J, et al. Large-scale production of MXenes as nanoknives for antibacterial application. Nanoscale Adv 2023;5:6572–81. https://doi.org/10.1039/d3na00744h.
[766] Rasool K, Helal M, Ali A, Ren CE, Gogotsi Y, Mahmoud KA. Antibacterial Activity of Ti3C2Tx MXene. ACS Nano 2016;10:3674–84. https://doi.org/10.1021/acsnano.6b00181.
[767] Rozmysłowska-Wojciechowska A, Karwowska E, Poźniak S, Wojciechowski T, Chlubny L, Olszyna A, et al. Influence of modification of Ti 3 C 2 MXene with ceramic oxide and noble metal nanoparticles on its antimicrobial properties and ecotoxicity towards selected algae and higher plants. RSC Adv 2019;9:4092–105. https://doi.org/10.1039/c8ra07633b.
[768] Jakubczak M, Bury D, Wojciechowska A, Mitrzak J, Budnik K, Moszczyńska D, et al. The 2D Ti3C2Tx MXene-enabled self-cleaning and self-sterilizing lacquer coatings for offset printing. J Alloys Compd 2024;976:173318. https://doi.org/10.1016/j.jallcom.2023.173318.
[769] Li H, Mu M, Chen B, Zhou L, Han B, Guo G. MXene-based nanomaterials for antibacterial and wound healing. Mater Res Lett 2024;12:67–87. https://doi.org/10.1080/21663831.2023.2294882.
[770] Kagalkar A, Dharaskar S, Chaudhari N. Development of MXene for removal of lead (Pb+) ions from wastewater. Water Pract Technol 2024;19:911–36. https://doi.org/10.2166/wpt.2024.039.
[771] Othman Z, Mackey HR, Mahmoud KA. A critical overview of MXenes adsorption behavior toward heavy metals. Chemosphere 2022;295:133849. https://doi.org/10.1016/j.chemosphere.2022.133849.
[772] Liao M, Zheng Z, Jiang H, Ma M, Wang L, Wang Y, et al. MXenes as emerging adsorbents for removal of environmental pollutants. Science of the Total Environment 2024;912:169014. https://doi.org/10.1016/j.scitotenv.2023.169014.
[773] Nezami S, Ghaemi A, Yousefi T. Application of titanium carbide/nitride (MXene)-based NPs in adsorption of radionuclides and heavy metal ions for wastewater remediation: A review. Case Studies in Chemical and Environmental Engineering 2023;7:100326. https://doi.org/10.1016/j.cscee.2023.100326.

[774] Zhu J, Chroneos A, Eppinger J, Schwingenschlögl U. S-functionalized MXenes as electrode materials for Li-ion batteries. Appl Mater Today 2016;5:19–24. https://doi.org/10.1016/j.apmt.2016.07.005.
[775] Ilyas M, Younas M, Shah MUH, Rehman WU, Rehman AU, Yuan ZH, et al. MXene-based 2D Ti3C2Tx nanosheets for highly efficient cadmium (Cd2+) adsorption. Journal of Water Process Engineering 2023;55:104131. https://doi.org/10.1016/j.jwpe.2023.104131.
[776] Yan X, Ma J, Yu K, Li J, Yang L, Liu J, et al. Highly green fluorescent Nb2C MXene quantum dots for Cu2+ ion sensing and cell imaging. Chinese Chemical Letters 2020;31:3173–7. https://doi.org/10.1016/j.cclet.2020.05.020.
[777] Bu F, Sun Z, Zhou W, Zhang Y, Chen Y, Ma B, et al. Reviving Zn0 Dendrites to Electroactive Zn2+ by Mesoporous MXene with Active Edge Sites. J Am Chem Soc 2023;145:24284–93. https://doi.org/10.1021/jacs.3c08986.
[778] Fu K, Liu X, Yu D, Luo J, Wang Z, Crittenden JC. Highly Efficient and Selective Hg(II) Removal from Water Using Multilayered Ti3C2O xMXene via Adsorption Coupled with Catalytic Reduction Mechanism. Environ Sci Technol 2020;54:16212–20. https://doi.org/10.1021/acs.est.0c05532.
[779] Ren CE, Hatzell KB, Alhabeb M, Ling Z, Mahmoud KA, Gogotsi Y. Charge- and Size-Selective Ion Sieving Through Ti3C2Tx MXene Membranes. Journal of Physical Chemistry Letters 2015;6:4026–31. https://doi.org/10.1021/acs.jpclett.5b01895.
[780] Ding L, Wei Y, Wang Y, Chen H, Caro J, Wang H. A Two-Dimensional Lamellar Membrane: MXene Nanosheet Stacks. Angewandte Chemie - International Edition 2017;56:1825–9. https://doi.org/10.1002/anie.201609306.
[781] Khazaei M, Arai M, Sasaki T, Estili M, Sakka Y. The effect of the interlayer element on the exfoliation of layered Mo 2AC (A = Al, Si, P, Ga, Ge, As or In) MAX phases into two-dimensional Mo2C nanosheets. Sci Technol Adv Mater 2014;15:14208. https://doi.org/10.1088/1468-6996/15/1/014208.
[782] Fan X, Liu L, Jin X, Wang W, Zhang S, Tang B. MXene Ti 3 C 2 T x for phase change composite with superior photothermal storage capability. J Mater Chem A Mater 2019;7:14319–27.
[783] Lin P, Xie J, He Y, Lu X, Li W, Fang J, et al. MXene aerogel-based phase change materials toward solar energy conversion. Solar Energy Materials and Solar Cells 2020;206:110229.
[784] Solangi NH, Mubarak NM, Karri RR, Mazari SA, Jatoi AS, Koduru JR, et al. MXene-based phase change materials for solar thermal energy storage. Energy Convers Manag 2022;273:116432. https://doi.org/10.1016/j.enconman.2022.116432.
[785] Jamil F, Ali HM, Janjua MM. MXene based advanced materials for thermal energy storage: A recent review. J Energy Storage 2021;35:102322. https://doi.org/10.1016/j.est.2021.102322.
[786] Demirelli K, Barim E, Çelik A, Yegin M, Aksoy Y, Hanay Ö, et al. Photoresponse, thermal and electrical behaviors of MXene-based polysulfone nanocomposite. Polymer Bulletin 2024. https://doi.org/10.1007/s00289-023-05121-9.
[787] Wang Q, Wang S, Guo X, Ruan L, Wei N, Ma Y, et al. MXene-Reduced Graphene Oxide Aerogel for Aqueous Zinc-Ion Hybrid Supercapacitor with Ultralong Cycle Life. Adv Electron Mater 2019;5:1900537. https://doi.org/10.1002/aelm.201900537.
[788] Qiao H, Qin W, Chen J, Feng L, Gu C, Yang M, et al. AuCu decorated MXene/RGO aerogels towards wearable thermal management and pressure sensing applications. Mater Des 2023;228:111814. https://doi.org/10.1016/j.matdes.2023.111814.
[789] Liu H, Fu R, Su X, Wu B, Wang H, Xu Y, et al. MXene confined in shape-stabilized phase change material combining enhanced electromagnetic interference shielding and thermal management capability. Compos Sci Technol 2021;210:108835. https://doi.org/10.1016/j.compscitech.2021.108835.
[790] Du Y, Huang H, Hu X, Liu S, Sheng X, Li X, et al. Melamine foam/polyethylene glycol composite phase change material synergistically modified by polydopamine/MXene with enhanced solar-to-thermal conversion. Renew Energy 2021;171:1–10. https://doi.org/10.1016/j.renene.2021.02.077.
[791] Wang F, Guo J, Li S, Wang Y, Hu X, Li Z, et al. Facile self-assembly approach to construct a novel MXene-decorated nano-sized phase change material emulsion for thermal energy storage. Ceram Int 2022;48:4722–31. https://doi.org/10.1016/j.ceramint.2021.11.008.
[792] Sheng X, Dong D, Lu X, Zhang L, Chen Y. MXene-wrapped bio-based pomelo peel foam/polyethylene glycol composite phase change material with enhanced light-to-thermal conversion efficiency, thermal energy storage capability and thermal conductivity. Compos Part A Appl Sci Manuf 2020;138:106067. https://doi.org/10.1016/j.compositesa.2020.106067.
[793] Khan AA, Yahya SM, Ali MA. Synthesis and Characterization of Titania–MXene-Based Phase Change Material for Sustainable Thermal Energy Storage. Sustainability (Switzerland) 2023;15. doi: 10.3390/su15010516.
[794] Luo Y, Xie Y, Jiang H, Chen Y, Zhang L, Sheng X, et al. Flame-retardant and form-stable phase change composites based on MXene with high thermostability and thermal conductivity for thermal energy storage. Chemical Engineering Journal 2021;420:130466. https://doi.org/10.1016/j.cej.2021.130466.
[795] Cheng H, Xing L, Zuo Y, Pan Y, Huang M, Alhadhrami A, et al. Constructing nickel chain/MXene networks in melamine foam towards phase change materials for thermal energy management and absorption-dominated electromagnetic interference shielding. Adv Compos Hybrid Mater 2022;5. doi: 10.1007/s42114-022-00487-2.
[796] Shao Y, Hu W, Gao M, Xiao Y, Huang T, Zhang N, et al. Flexible MXene-coated melamine foam based phase change material composites for integrated solar-thermal energy conversion/storage, shape memory and thermal therapy functions. Compos Part A Appl Sci Manuf 2021;143:106291. https://doi.org/10.1016/j.compositesa.2021.106291.
[797] Gao XY, Lu P, Xu ZM, Tang GG. Synthesis and tribological properties of MXene/TiO2/MoS2 nanocomposite. Chalcogenide Letters 2022;19:513–27. https://doi.org/10.15251/CL.2022.198.513.
[798] Rajan AC, Mishra A, Satsangi S, Vaish R, Mizuseki H, Lee KR, et al. Machine-learning-assisted accurate band gap predictions of functionalized mxene. Chemistry of Materials 2018;30:4031–8. https://doi.org/10.1021/acs.chemmater.8b00686.
[799] Lampropoulos AS, Tsihrintzis GA. Machine Learning Paradigms: Applications in Recommender Systems, vol. 92. Cham: Springer International Publishing; 2015.
[800] Zhang X, Tian Y, Chen L, Hu X, Zhou Z. Machine Learning: A New Paradigm in Computational Electrocatalysis. Journal of Physical Chemistry Letters 2022;13:7920–30. https://doi.org/10.1021/acs.jpclett.2c01710.
[801] Sun S, Liao C, Hafez AM, Zhu H, Wu S. Two-dimensional MXenes for energy storage. Chemical Engineering Journal 2018;338:27–45. https://doi.org/10.1016/j.cej.2017.12.155.
[802] Liu Y, Li Y, Kang H, Jin T, Jiao L. Design, synthesis, and energy-related applications of metal sulfides. Mater Horiz 2016;3:402–21. https://doi.org/10.1039/c6mh00075d.
[803] Guo Z, Zhu L, Zhou J, Sun Z. Microscopic origin of MXenes derived from layered MAX phases. RSC Adv 2015;5:25403–8. https://doi.org/10.1039/c4ra17304j.
[804] Khazaei M, Ranjbar A, Esfarjani K, Bogdanovski D, Dronskowski R, Yunoki S. Insights into exfoliation possibility of MAX phases to MXenes. Physical Chemistry Chemical Physics 2018;20:8579–92. https://doi.org/10.1039/c7cp08645h.
[805] Yorulmaz U, Özden A, Perkgöz NK, Ay F, Sevik C. Vibrational and mechanical properties of single layer MXene structures: A first-principles investigation. Nanotechnology 2016;27:335702. https://doi.org/10.1088/0957-4484/27/33/335702.
[806] Mouhat F, Coudert FX. Necessary and sufficient elastic stability conditions in various crystal systems. Phys Rev B Condens Matter Mater Phys 2014;90:224104. https://doi.org/10.1103/PhysRevB.90.224104.
[807] Nye JF. Physical Properties oc Crystals: Their Represantation by Tensor and Mechanics 2012.
[808] Fecht HJ, Wunderlich R, Battezzati L, Etay J, Ricci E, Seetharaman S, et al. Thermophysical properties of materials. Elsevier 2008;39. https://doi.org/10.1051/epn:2008501.
[809] Chen X, Gudda F, Hu X, Waigi M, Gao Y. Degradation of bisphenol A in an oxidation system constructed from Mo2C MXene and peroxymonosulfate. NPJ Clean Water 2022;5:66. https://doi.org/10.1038/s41545-022-00214-w.
[810] Cui W, Hu Z-Y, Unocic RR, Van Tendeloo G, Sang X. Atomic defects, functional groups and properties in MXenes. Chinese Chemical Letters 2021;32:339–44. https://doi.org/10.1016/j.cclet.2020.04.024.
[811] Shein IR, Ivanovskii AL. Graphene-like titanium carbides and nitrides Tin+1Cn, Tin+1Nn (n=1, 2, and 3) from de-intercalated MAX phases: First-principles probing of their structural, electronic properties and relative stability. Comput Mater Sci 2012;65:104–14. https://doi.org/10.1016/j.commatsci.2012.07.011.
[812] Berdiyorov GR, Mahmoud KA. Effect of surface termination on ion intercalation selectivity of bilayer Ti3C2T2 (T= F, O and OH) MXene. Appl Surf Sci 2017;416:725–30.

[813] Schultz T, Frey NC, Hantanasirisakul K, Park S, May SJ, Shenoy VB, et al. Surface Termination Dependent Work Function and Electronic Properties of Ti 3 C 2 T x MXene. Chemistry of Materials 2019;31:6590–7. https://doi.org/10.1021/acs.chemmater.9b00414.
[814] Monkhorst HJ, Pack JD. Special points for Brillouin-zone integrations. PhysRevB 1976;13:5188–92. https://doi.org/10.1103/PhysRevB.13.5188.
[815] Grimme S. Semiempirical GGA-type density functional constructed with a long-range dispersion correction. J Comput Chem 2006;27:1787–99. https://doi.org/10.1002/jcc.20495.
[816] Stradi D, Martinez U, Blom A, Brandbyge M, Stokbro K. General atomistic approach for modeling metal-semiconductor interfaces using density functional theory and nonequilibrium Green's function. PhysRevB 2016;93:155302. https://doi.org/10.1103/PhysRevB.93.155302.
[817] Zhang P, Richard P, Qian T, Xu YM, Dai X, Ding H. A precise method for visualizing dispersive features in image plots. Review of Scientific Instruments 2011;82. https://doi.org/10.1063/1.3585113.
[818] Wang Z, Xiao B, Lin Z, Shen S, Xu A, Du Z, et al. In-situ surface decoration of RuO2 nanoparticles by laser ablation for improved oxygen evolution reaction activity in both acid and alkali solutions. Journal of Energy Chemistry 2021;54:510–8. https://doi.org/10.1016/j.jechem.2020.06.042.
[819] Chen S, Liu T, Olanrele SO, Lian Z, Si C, Chen Z, et al. Boosting electrocatalytic activity for CO2 reduction on nitrogen-doped carbon catalysts by co-doping with phosphorus. Journal of Energy Chemistry 2021;54:143–50. https://doi.org/10.1016/j.jechem.2020.05.006.
[820] Zhou L, Zhou P, Zhang Y, Liu B, Gao P, Guo S. 3D star-like atypical hybrid MOF derived single-atom catalyst boosts oxygen reduction catalysis. Journal of Energy Chemistry 2021;55:355–60. https://doi.org/10.1016/j.jechem.2020.06.059.
[821] Gouveia JD, Morales-García Á, Viñes F, Illas F, Gomes JRB. MXenes as promising catalysts for water dissociation. Appl Catal B 2020;260:118191. https://doi.org/10.1016/j.apcatb.2019.118191.
[822] Ding B, Ong WJ, Jiang J, Chen X, Li N. Uncovering the electrochemical mechanisms for hydrogen evolution reaction of heteroatom doped M2C MXene (M = Ti, Mo). Appl Surf Sci 2020;500:143987. https://doi.org/10.1016/j.apsusc.2019.143987.
[823] Du CF, Sun X, Yu H, Liang Q, Dinh KN, Zheng Y, et al. Synergy of Nb Doping and Surface Alloy Enhanced on Water–Alkali Electrocatalytic Hydrogen Generation Performance in Ti-Based MXene. Advanced Science 2019;6:1900116. https://doi.org/10.1002/advs.201900116.
[824] Kuznetsov DA, Chen Z, Kumar PV, Tsoukalou A, Kierzkowska A, Abdala PM, et al. Single Site Cobalt Substitution in 2D Molybdenum Carbide (MXene) Enhances Catalytic Activity in the Hydrogen Evolution Reaction. J Am Chem Soc 2019;141:17809–16. https://doi.org/10.1021/jacs.9b08897.
[825] Li H, Wei S, Wang H, Cai Q, Zhao J. Enhanced catalytic activity of MXene for nitrogen electoreduction reaction by carbon doping. J Colloid Interface Sci 2021;588:1–8. https://doi.org/10.1016/j.jcis.2020.12.034.
[826] Gao Y, Zhuo H, Cao Y, Sun X, Zhuang G, Deng S, et al. A theoretical study of electrocatalytic ammonia synthesis on single metal atom/MXene. Cuihua Xuebao/Chinese Journal of Catalysis 2019;40:152–9. https://doi.org/10.1016/S1872-2067(18)63197-3.
[827] Liu A, Liang X, Ren X, Guan W, Gao M, Yang Y, et al. Recent Progress in MXene-Based Materials: Potential High-Performance Electrocatalysts. Adv Funct Mater 2020;30:2003437. https://doi.org/10.1002/adfm.202003437.
[828] Qi S, Fan Y, Zhao L, Li W, Zhao M. Two-dimensional transition metal borides as highly efficient N2 fixation catalysts. Appl Surf Sci 2021;536:147742. https://doi.org/10.1016/j.apsusc.2020.147742.
[829] Sun Y, Chen D, Liang Z. Two-dimensional MXenes for energy storage and conversion applications. Mater Today Energy 2017;5:22–36. https://doi.org/10.1016/j.mtener.2017.04.008.
[830] Shariq M, Marimuthu S, Dixit AR, Chattopadhyaya S, Pandiaraj S, Muthuramamoorthy M, et al. Machine learning models for prediction of electrochemical properties in supercapacitor electrodes using MXene and graphene nanoplatelets. Chemical Engineering Journal 2024;484:149502. https://doi.org/10.1016/j.cej.2024.149502.
[831] Ren A, Zou J, Lai H, Huang Y, Yuan L, Xu H, et al. Direct laser-patterned MXene–perovskite image sensor arrays for visible-near infrared photodetection. Mater Horiz 2020;7:1901–11. https://doi.org/10.1039/D0MH00537A.
[832] Fatima S, Hakim MW, Akinwande D, Rizwan S. Self-generated double transition-metal carbide MXene/Graphene oxide trilayered memristors for flexible electronics. Materials Today. Physics 2022;26. https://doi.org/10.1016/J.MTPHYS.2022.100730.
[833] Chauhan NK, Singh K. A review on conventional machine learning vs deep learning. 2018 International Conference on Computing, Power and Communication Technologies, GUCON 2018, 2019, p. 347–52. doi: 10.1109/GUCON.2018.8675097.
[834] Hachmann J, Olivares-Amaya R, Atahan-Evrenk S, Amador-Bedolla C, Sánchez-Carrera RS, Gold-Parker A, et al. The harvard clean energy project: Large-scale computational screening and design of organic photovoltaics on the world community grid. Journal of Physical Chemistry Letters 2011;2:2241–51. https://doi.org/10.1021/jz200866s.
[835] Hachmann J, Olivares-Amaya R, Jinich A, Appleton AL, Blood-Forsythe MA, Seress LR, et al. Lead candidates for high-performance organic photovoltaics from high-throughput quantum chemistry-the Harvard Clean Energy Project. Energy Environ Sci 2014;7:698–704. https://doi.org/10.1039/c3ee42756k.
[836] Jain A, Ong SP, Hautier G, Chen W, Richards WD, Dacek S, et al. Commentary: The materials project: A materials genome approach to accelerating materials innovation. APL Mater 2013;1. https://doi.org/10.1063/1.4812323.
[837] Raccuglia P, Elbert KC, Adler PDF, Falk C, Wenny MB, Mollo A, et al. Machine-learning-assisted materials discovery using failed experiments. Nature 2016;533:73–6. https://doi.org/10.1038/nature17439.
[838] Sanchez-Lengeling B, Aspuru-Guzik A. Inverse molecular design using machine learning:Generative models for matter engineering. Science 1979;2018(361):360–5. https://doi.org/10.1126/science.aat2663.
[839] Bartók AP, Kondor R, Csányi G. On representing chemical environments. Phys Rev B Condens Matter Mater Phys 2013;87:184115. https://doi.org/10.1103/PhysRevB.87.184115.
[840] Duvenaud D, Maclaurin D, Aguilera-Iparraguirre J, Gómez-Bombarelli R, Hirzel T, Aspuru-Guzik A, et al. Convolutional networks on graphs for learning molecular fingerprints. Adv Neural Inf Process Syst 2015; 2015-Janua:2224–32..
[841] Hansen K, Biegler F, Ramakrishnan R, Pronobis W, Von Lilienfeld OA, Müller KR, et al. Machine learning predictions of molecular properties: Accurate many-body potentials and nonlocality in chemical space. Journal of Physical Chemistry Letters 2015;6:2326–31. https://doi.org/10.1021/acs.jpclett.5b00831.
[842] Hirn M, Mallat S, Poilvert N. Wavelet scattering regression of quantum chemical energies. Multiscale Modeling and Simulation 2017;15:827–63. https://doi.org/10.1137/16M1075454.
[843] Yaseen ZM, Deo RC, Hilal A, Abd AM, Bueno LC, Salcedo-Sanz S, et al. Predicting compressive strength of lightweight foamed concrete using extreme learning machine model. Advances in Engineering Software 2018;115:112–25. https://doi.org/10.1016/j.advengsoft.2017.09.004.
[844] Han Q, Gui C, Xu J, Lacidogna G. A generalized method to predict the compressive strength of high-performance concrete by improved random forest algorithm. Constr Build Mater 2019;226:734–42. https://doi.org/10.1016/j.conbuildmat.2019.07.315.
[845] Ma X, Lan C, Lin H, Peng Y, Li T, Wang J, et al. Designing desalination MXene membranes by machine learning and global optimization algorithm. J Memb Sci 2024;702:122803. https://doi.org/10.1016/j.memsci.2024.122803.
[846] Tesh SJ, Scott TB. Nano-composites for water remediation: A review. Advanced Materials 2014;26:6056–68. https://doi.org/10.1002/adma.201401376.
[847] Allam O, Cho BW, Kim KC, Jang SS. Application of DFT-based machine learning for developing molecular electrode materials in Li-ion batteries. RSC Adv 2018;8:39414–20. https://doi.org/10.1039/c8ra07112h.
[848] Tawfik SA, Isayev O, Stampfl C, Shapter J, Winkler DA, Ford MJ. Efficient Prediction of Structural and Electronic Properties of Hybrid 2D Materials Using Complementary DFT and Machine Learning Approaches. Adv Theory Simul 2019;2:1800128. https://doi.org/10.1002/adts.201800128.
[849] Boonpalit K, Kinchagawat J, Prommin C, Nutanong S, Namuangruk S. Efficient exploration of transition-metal decorated MXene for carbon monoxide sensing using integrated active learning and density functional theory. Physical Chemistry Chemical Physics 2023;25:28657–68. https://doi.org/10.1039/d3cp03667g.
[850] Diaz C, Vanzulli M, Galione P. Exploring the capability of PINNs for solving material identification problems. 2023.
[851] Cuomo S, Di Cola VS, Giampaolo F, Rozza G, Raissi M, Piccialli F. Scientific Machine Learning Through Physics–Informed Neural Networks: Where we are and What's Next. J Sci Comput 2022;92:88. https://doi.org/10.1007/s10915-022-01939-z.

[852] Tan T, Jin H, Sullivan M, Anasori B, Gogotsi Y. A High-Throughput Survey of Ordering Configurations in MXene Alloys Across Compositions and Temperatures. ACS Nano 2017;11. https://doi.org/10.1021/acsnano.6b08227.
[853] Zheng J, Sun X, Qiu C, Yan Y, Yao Z, Deng S, et al. High-Throughput Screening of Hydrogen Evolution Reaction Catalysts in MXene Materials. Journal of Physical Chemistry C 2020;124:13695–705. https://doi.org/10.1021/acs.jpcc.0c02265.
[854] Syuy A, Shtarev D, Lembikov A, Gurin M, Kevorkyants R, Tselikov G, et al. Effective Method for the Determination of the Unit Cell Parameters of New MXenes. Materials (Basel) 2022;15. https://doi.org/10.3390/ma15248798.
[855] Kang S, Jeong W, Hong C, Hwang S, Yoon Y, Han S. Accelerated identification of equilibrium structures of multicomponent inorganic crystals using machine learning potentials. NPJ Comput Mater 2022;8:108. https://doi.org/10.1038/s41524-022-00792-w.
[856] Ye W, Chen C, Dwaraknath S, Jain A, Ong SP, Persson KA. Harnessing the Materials Project for machine-learning and accelerated discovery. MRS Bull 2018;43:664–9. https://doi.org/10.1557/mrs.2018.202.
[857] Song Z, Niu X, Chen H. Leveraging all-fixed transfer framework to predict interpretable formation energy of MXene with hybrid terminals. Physical Chemistry Chemical Physics 2024. https://doi.org/10.1039/D4CP00386A.
[858] Wang Y, Sorkun MC, Brocks G, Er S. ML-Aided Computational Screening of 2D Materials for Photocatalytic Water Splitting. J Phys Chem Lett 2024;15:4983–91. https://doi.org/10.1021/acs.jpclett.4c00425.
[859] Liu F, Li Y, Hao S, Cheng Y, Zhan Y, Zhang C, et al. Well-aligned MXene/chitosan films with humidity response for high-performance electromagnetic interference shielding. Carbohydr Polym 2020;243:116467. https://doi.org/10.1016/j.carbpol.2020.116467.
[860] Chen Z, Huang S, Huang B, Wan M, Zhou N. Transition metal atoms implanted into MXenes (M2CO2) for enhanced electrocatalytic hydrogen evolution reaction. Appl Surf Sci 2020;509:145319. https://doi.org/10.1016/j.apsusc.2020.145319.
[861] Parashar N, Aslfattahi N, Yahya SM, Saidur R. ANN Modeling of Thermal Conductivity and Viscosity of MXene-Based Aqueous IoNanofluid. Int J Thermophys 2021;42:24. https://doi.org/10.1007/s10765-020-02779-5.
[862] Gao Y, Zhang S, Sun X, Zhao W, Zhuo H, Zhuang G, et al. Computational screening of O-functional MXenes for electrocatalytic ammonia synthesis. Chinese Journal of Catalysis 2022;43:1860–9. https://doi.org/10.1016/S1872-2067(21)64011-1.
[863] Goldsmith B, Boley M, Vreeken J, Scheffler M, Ghiringhelli L. Uncovering structure-property relationships of materials by subgroup discovery. New J Phys 2017;19. https://doi.org/10.1088/1367-2630/aa57c2.
[864] Heracleous E, Lemonidou A. Ni–Me–O mixed metal oxides for the effective oxidative dehydrogenation of ethane to ethylene – Effect of promoting metal Me. J Catal 2010;270:67–75. https://doi.org/10.1016/j.jcat.2009.12.004.
[865] Tan AYS, Awan HTA, Cheng F, Zhang M, Tan MTT, Manickam S, et al. Recent advances in the use of MXenes for photoelectrochemical sensors. Chemical Engineering Journal 2024;482:148774. https://doi.org/10.1016/j.cej.2024.148774.
[866] Sanchez-Lengeling B, Aspuru-Guzik A. Inverse molecular design using machine learning: Generative models for matter engineering. Science 1979;2018(361):360–5. https://doi.org/10.1126/SCIENCE.AAT2663.
[867] Wang Z, Zhang H, Li J. Accelerated discovery of stable spinels in energy systems via machine learning. Nano Energy 2021;81:105665.
[868] Cai J, Chu X, Xu K, Li H, Wei J. Machine learning-driven new material discovery. Nanoscale Adv 2020;2:3115–30.
[869] Li Y, Kong Y, Peng J, Yu C, Li Z, Li P, et al. Rapid identification of two-dimensional materials via machine learning assisted optic microscopy. Journal of Materiomics 2019;5:413–21.
[870] Podryabinkin EV, Tikhonov EV, Shapeev AV, Oganov AR. Accelerating crystal structure prediction by machine-learning interatomic potentials with active learning. Phys Rev B 2019;99:64114.
[871] Pugar JA, Gang C, Huang C, Haider KW, Washburn NR. Predicting Young's modulus of linear polyurethane and polyurethane–polyurea elastomers: Bridging length scales with physicochemical modeling and machine learning. ACS Appl Mater Interfaces 2022;14:16568–81.
[872] Tao Q, Xu P, Li M, Lu W. Machine learning for perovskite materials design and discovery. NPJ Comput Mater 2021;7:23.
[873] Mai H, Le TC, Chen D, Winkler DA, Caruso RA. Machine learning for electrocatalyst and photocatalyst design and discovery. Chem Rev 2022;122:13478–515.
[874] Ryu B, Wang L, Pu H, Chan MKY, Chen J. Understanding, discovery, and synthesis of 2D materials enabled by machine learning. Chem Soc Rev 2022;51:1899–925. https://doi.org/10.1039/d1cs00503k.
[875] Ramprasad R, Batra R, Pilania G, Mannodi-Kanakkithodi A, Kim C. Machine learning in materials informatics: recent applications and prospects. NPJ Comput Mater 2017;3:54.
[876] Kirklin S, Saal JE, Meredig B, Thompson A, Doak JW, Aykol M, et al. The Open Quantum Materials Database (OQMD): assessing the accuracy of DFT formation energies. NPJ Comput Mater 2015;1:15010. https://doi.org/10.1038/npjcompumats.2015.10.
[877] Chanussot L, Das A, Goyal S, Lavril T, Shuaibi M, Riviere M, et al. Open Catalyst 2020 (OC20) Dataset and Community Challenges. ACS Catal 2021;11:6059–72. https://doi.org/10.1021/acscatal.0c04525.
[878] Winther KT, Hoffmann MJ, Boes JR, Mamun O, Bajdich M, Bligaard T. Catalysis-Hub.org, an open electronic structure database for surface reactions. Sci Data 2019;6:75. https://doi.org/10.1038/s41597-019-0081-y.
[879] Gjerding MN, Taghizadeh A, Rasmussen A, Ali S, Bertoldo F, Deilmann T, et al. Recent progress of the Computational 2D Materials Database (C2DB). 2d Mater 2021;8:44002. https://doi.org/10.1088/2053-1583/ac1059.
[880] Zhou J, Shen L, Costa MD, Persson KA, Ong SP, Huck P, et al. 2DMatPedia, an open computational database of two-dimensional materials from top-down and bottom-up approaches. Sci Data 2019;6:86. https://doi.org/10.1038/s41597-019-0097-3.
[881] Hashimoto K, Yoshimura Y, Ushio T. Learning Self-Triggered Controllers With Gaussian Processes. IEEE Trans Cybern 2021;51:6294–304. https://doi.org/10.1109/TCYB.2020.2980048.
[882] Li N, Zong T, Zhang Z. Prediction of the Electronic Work Function by Regression Algorithm in Machine Learning. In: 2021 IEEE 6th International Conference on Big Data Analytics (ICBDA); 2021. p. 87–91.
[883] Kumar R, Singh AK. Chemical hardness-driven interpretable machine learning approach for rapid search of photocatalysts. NPJ Comput Mater 2021;7:197. https://doi.org/10.1038/s41524-021-00669-4.
[884] Wexler RB, Martirez JMP, Rappe AM. Chemical Pressure-Driven Enhancement of the Hydrogen Evolving Activity of Ni2P from Nonmetal Surface Doping Interpreted via Machine Learning. J Am Chem Soc 2018;140:4678–83. https://doi.org/10.1021/jacs.8b00947.
[885] Atamuradov V, Camci F. Segmentation Based Feature Evaluation and Fusion for Prognostics, 2020.
[886] Tao H, Wu T, Aldeghi M, Wu TC, Aspuru-Guzik A, Kumacheva E. Nanoparticle synthesis assisted by machine learning. Nat Rev Mater 2021;6:701–16. https://doi.org/10.1038/s41578-021-00337-5.
[887] Ahmadi M, Ayyoubzadeh SM, Ghorbani-Bidkorpeh F. Toxicity prediction of nanoparticles using machine learning approaches. Toxicology 2024;501:153697. https://doi.org/10.1016/j.tox.2023.153697.
[888] Pereira LM, Salazar A, Vergara L. A Comparative Study on Recent Automatic Data Fusion Methods. Computers 2024;13. https://doi.org/10.3390/computers13010013.
[889] Wu X, Liao H, Ma D, Chao M, Wang Y, Jia X, et al. A wearable, self-adhesive, long-lastingly moist and healable epidermal sensor assembled from conductive MXene nanocomposites. J Mater Chem C Mater 2020;8:1788–95. https://doi.org/10.1039/c9tc05575d.
[890] Zheng S, Wang H, Das P, Zhang Y, Cao Y, Ma J, et al. Multitasking MXene Inks Enable High-Performance Printable Microelectrochemical Energy Storage Devices for All-Flexible Self-Powered Integrated Systems. Advanced Materials 2021;33. https://doi.org/10.1002/adma.202005449.
[891] Jing L, Li K, Yang H, Chen PY. Recent advances in integration of 2D materials with soft matter for multifunctional robotic materials. Mater Horiz 2020;7:54–70. https://doi.org/10.1039/c9mh01139k.
[892] Chen Y, Zhang Y, Li H, Shen J, Zhang F, He J, et al. Bioinspired hydrogel actuator for soft robotics: Opportunity and challenges. Nano Today 2023;49:101764. https://doi.org/10.1016/j.nantod.2023.101764.
[893] Luo XJ, Li L, Bin ZH, Zhao S, Zhang Y, Chen W, et al. Multifunctional Ti3C2TxMXene/Low-Density Polyethylene Soft Robots with Programmable Configuration for Amphibious Motions. ACS Appl Mater Interfaces 2021;13:45833–42. https://doi.org/10.1021/acsami.1c11056.

[894] Li Y, Yang H, Zhang T, Li S, Li S, He S, et al. Stretchable Zn-Ion Hybrid Battery with Reconfigurable V 2 CT x and Ti 3 C 2 T x MXene Electrodes as a Magnetically Actuated Soft Robot. Adv Energy Mater 2021;11:2101862. https://doi.org/10.1002/aenm.202101862.
[895] Cao J, Zhou Z, Song Q, Chen K, Su G, Zhou T, et al. Ultrarobust Ti 3 C 2 T x MXene-Based Soft Actuators via Bamboo-Inspired Mesoscale Assembly of Hybrid Nanostructures. ACS Nano 2020;14:7055–65. https://doi.org/10.1021/acsnano.0c01779.
[896] Tu S, Xu L, El-Demellawi JK, Liang H, Xu X, Lopatin S, et al. Autonomous MXene-PVDF actuator for flexible solar trackers. Nano Energy 2020;77:105277. https://doi.org/10.1016/j.nanoen.2020.105277.
[897] Jia G, Zheng A, Wang X, Zhang L, Li L, Li C, et al. Flexible, biocompatible and highly conductive MXene-graphene oxide film for smart actuator and humidity sensor. Sens Actuators B Chem 2021;346:130507. https://doi.org/10.1016/j.snb.2021.130507.
[898] Garai M, Mahato M, Nam S, Kim E, Seo D, Lee Y, et al. Metal Organic Framework-MXene Nanoarchitecture for Fast Responsive and Ultra-Stable Electro-Ionic Artificial Muscles. Adv Funct Mater 2023;33:2212252. https://doi.org/10.1002/adfm.202212252.
[899] Tang ZH, Bin ZuW, Mao YQ, Zhu ZC, Li YQ, Huang P, et al. Multiresponsive Ti3C2Tx MXene-Based Actuators Enabled by Dual-Mechanism Synergism for Soft Robotics. ACS Appl Mater Interfaces 2022;14:21474–85. https://doi.org/10.1021/acsami.2c03157.
[900] Zarepour A, Ahmadi S, Rabiee N, Zarrabi A, Iravani S. Self-Healing MXene- and Graphene-Based Composites: Properties and Applications. Nanomicro Lett 2023;15:100. https://doi.org/10.1007/s40820-023-01074-w.
[901] Shen Z, Chen F, Zhu X, Yong KT, Gu G. Stimuli-responsive functional materials for soft robotics. J Mater Chem B 2020;8:8972–91. https://doi.org/10.1039/d0tb01585g.
[902] Guzelturk B, Kamysbayev V, Wang D, Hu H, Li R, King SB, et al. Understanding and Controlling Photothermal Responses in MXenes. Nano Lett 2023;23:2677–86. https://doi.org/10.1021/acs.nanolett.2c05001.
[903] Sun Z, Song C, Zhou J, Hao C, Liu W, Liu H, et al. Rapid Photothermal Responsive Conductive MXene Nanocomposite Hydrogels for Soft Manipulators and Sensitive Strain Sensors. Macromol Rapid Commun 2021;42:2100499. https://doi.org/10.1002/marc.202100499.
[904] Hu Y, Yang L, Yan Q, Ji Q, Chang L, Zhang C, et al. Self-Locomotive Soft Actuator Based on Asymmetric Microstructural Ti3C2TxMXene Film Driven by Natural Sunlight Fluctuation. ACS Nano 2021;15:5294–306. https://doi.org/10.1021/acsnano.0c10797.
[905] Liu M, Wang Q, Li AW, Sun HB. Laser defined and driven bio-inspired soft robots toward complex motion control. Physical Chemistry Chemical Physics 2023;25:9753–60. https://doi.org/10.1039/d2cp05487f.
[906] Pang D, Alhabeb M, Mu X, Dall'Agnese Y, Gogotsi Y, Gao Y. Electrochemical Actuators Based on Two-Dimensional Ti 3 C 2 T x (MXene). Nano Lett 2019;19:7443–8. https://doi.org/10.1021/acs.nanolett.9b03147.
[907] Yang H, Xiao X, Li Z, Li K, Cheng N, Li S, et al. Wireless Ti3C2TxMXene Strain Sensor with Ultrahigh Sensitivity and Designated Working Windows for Soft Exoskeletons. ACS Nano 2020;14:11860–75. https://doi.org/10.1021/acsnano.0c04730.
[908] Xue P, Valenzuela C, Ma S, Zhang X, Ma J, Chen Y, et al. Highly Conductive MXene/PEDOT:PSS-Integrated Poly(N-Isopropylacrylamide) Hydrogels for Bioinspired Somatosensory Soft Actuators. Adv Funct Mater 2023;33:2214867. https://doi.org/10.1002/adfm.202214867.
[909] Ruth DJS, Sohn JW, Dhanalakshmi K, Choi SB. Control Aspects of Shape Memory Alloys in Robotics Applications: A Review over the Last Decade. Sensors 2022;22:4860. https://doi.org/10.3390/s22134860.
[910] Lalegani Dezaki M, Bodaghi M. A Review of Recent Manufacturing Technologies for Sustainable Soft Actuators. International Journal of Precision Engineering and Manufacturing - Green Technology 2023;10:1661–710. https://doi.org/10.1007/s40684-023-00533-4.
[911] Jiang W, Niu D, Liu H, Wang C, Zhao T, Yin L, et al. Photoresponsive soft-robotic platform: Biomimetic fabrication and remote actuation. Adv Funct Mater 2014;24:7598–604. https://doi.org/10.1002/adfm.201402070.
[912] Yang Y, Liu Y, Shen Y. Plasmonic-Assisted Graphene Oxide Films with Enhanced Photothermal Actuation for Soft Robots. Adv Funct Mater 2020;30:1910172. https://doi.org/10.1002/adfm.201910172.
[913] Xu M, Li L, Zhang W, Ren Z, Liu J, Qiu C, et al. MXene-Based Soft Actuators with Multiresponse and Diverse Applications by a Simple Method. Macromol Mater Eng 2023;308:2300200. https://doi.org/10.1002/mame.202300200.
[914] Yu M, Feng X. Scalable Manufacturing of MXene Films: Moving toward Industrialization. Matter 2020;3:335–6. https://doi.org/10.1016/j.matt.2020.07.011.
[915] Liu W, Cheng Y, Liu N, Yue Y, Lei D, Su T, et al. Bionic MXene actuator with multiresponsive modes. Chemical Engineering Journal 2021;417:129288. https://doi.org/10.1016/j.cej.2021.129288.
[916] Overbury SH, Kolesnikov AI, Brown GM, Zhang Z, Nair GS, Sacci RL, et al. Complexity of Intercalation in MXenes: Destabilization of Urea by Two-Dimensional Titanium Carbide. J Am Chem Soc 2018;140:10305–14. https://doi.org/10.1021/jacs.8b05913.
[917] Xu X, Yang L, Zheng W, Zhang H, Wu F, Tian Z, et al. MXenes with applications in supercapacitors and secondary batteries: A comprehensive review. Materials Reports: Energy 2022;2:100080. https://doi.org/10.1016/j.matre.2022.100080.
[918] Ihsanullah I, Ali H. Technological challenges in the environmental applications of MXenes and future outlook. Case Studies in Chemical and Environmental Engineering 2020;2:100034. https://doi.org/10.1016/j.cscee.2020.100034.
[919] Wang L, Liu ZQ, Li SF, Yang YF, Misra RDK, Li J, et al. Few-layered Ti3C2 MXene-coated Ti–6Al–4V composite powder for high-performance Ti matrix composite. Composites Communications 2022;33:101238. https://doi.org/10.1016/j.coco.2022.101238.
[920] Uzun S, Seyedin S, Stoltzfus A, Levitt A, Alhabeb M, Anayee M, et al. Knittable and Washable Multifunctional MXene-Coated Cellulose Yarns. Adv Funct Mater 2019;29:1905015. https://doi.org/10.1002/adfm.201905015.
[921] Lim KRG, Shekhirev M, Wyatt B, Anasori B, Gogotsi Y, Seh Z. Fundamentals of MXene synthesis. Nature. Synthesis 2022;1. https://doi.org/10.1038/s44160-022-00104-6.
[922] Marinho ALA, Comminges C, Habrioux A, Célérier S, Bion N, Morais C. Reactivity of nitrogen atoms from Zif-8 structure deposited over Ti3C2 MXene in the electrochemical nitrogen reduction reaction. Chem Commun 2023;59:10133–6. https://doi.org/10.1039/D3CC02693K.
[923] Liu N, Li Q, Wan H, Chang L, Wang H, Fang J, et al. High-temperature stability in air of Ti3C2Tx MXene-based composite with extracted bentonite. Nat Commun 2022;13:5551. https://doi.org/10.1038/s41467-022-33280-2.
[924] Li X, Qiu J, Cui H, Chen X, Yu J, Zheng K. Machine Learning Accelerated Discovery of Functional MXenes with Giant Piezoelectric Coefficients. ACS Appl Mater Interfaces 2024;16:12731–43. https://doi.org/10.1021/acsami.3c14610.
[925] Shuck CE, Sarycheva A, Anayee M, Levitt A, Zhu Y, Uzun S, et al. Scalable Synthesis of Ti3C2Tx MXene. Adv Eng Mater 2020;22:1901241. https://doi.org/10.1002/adem.201901241.
[926] Sangu S, Mohammad Illias N, Ong CC, Gopinath S, Shuaib M. MXene-Based Aptasensor: Characterization and High-Performance Voltammetry Detection of Deoxynivalenol. Bionanoscience 2021;11:1–10. https://doi.org/10.1007/s12668-021-00847-0.
[927] Rasheed T, Rasheed A, Munir S, Ajmal S, Muhammad Shahzad Z, Alsafari IA, et al. A cost-effective approach to synthesize NiFe2O4/MXene heterostructures for enhanced photodegradation performance and anti-bacterial activity. Advanced Powder Technology 2021;32:2248–57. https://doi.org/10.1016/j.apt.2021.05.006.
[928] Kang MS, Yu Y, Park R, Heo HJ, Lee SH, Hong SW, et al. Highly Aligned Ternary Nanofiber Matrices Loaded with MXene Expedite Regeneration of Volumetric Muscle Loss. Nanomicro Lett 2024;16:73. https://doi.org/10.1007/s40820-023-01293-1.
[929] Zhou X, Hao Y, Li Y, Jiahe P, Wang G, Ong W-J, et al. MXenes: An Emergent Materials for Packaging Platforms and Looking Beyond. Nano Select 2022;3. https://doi.org/10.1002/nano.202200023.
[930] Safarkhani M, Aldhaher A, Lima EC, Zargar M, Jung EE, Huh Y, et al. Engineering MXene@MOF Composites for a Wide Range of Applications: A Perspective. ACS Applied Engineering Materials 2023;1:3080–98. https://doi.org/10.1021/acsaenm.3c00529.
[931] Nahirniak S, Ray A, Saruhan B. Challenges and Future Prospects of the MXene-Based Materials for Energy Storage Applications. Batteries 2023;9. https://doi.org/10.3390/batteries9020126.
[932] Kumarov A, Chisom Nwaogu E, Zhumadil A, Bakenov Z, Nurpeissova A. Current collector-free printed three-dimensional MXene-based anodes for lithium-ion batteries. Electrochem Commun 2023;157:107621. https://doi.org/10.1016/j.elecom.2023.107621.

[933] Zhang Y-Z, Wang Y, Jiang Q, El-Demellawi JK, Kim H, Alshareef HN. MXene Printing and Patterned Coating for Device Applications. Advanced Materials 2020; 32:1908486. https://doi.org/10.1002/adma.201908486.
[934] Zaed M, Tan K, Rahman S, Panday A, Saleque A. Cost analysis of MXene for low-cost production, and pinpointing of its economic footprint. 2023. doi: 10.21203/rs.3.rs-2817391/v1.
[935] Li J, Xi S, Lei T, Yao R, Zeng F, Wu J, et al. Machine learning assisted prediction in the discharge capacities of novel MXene cathodes for aluminum ion batteries. J Energy Storage 2024;82:110196. https://doi.org/10.1016/j.est.2023.110196.
[936] Aghayar Z, Malaki M, Zhang Y. MXene-Based Ink Design for Printed Applications. Nanomaterials 2022;12. https://doi.org/10.3390/nano12234346.
[937] Yan Q, Zhou Y, Cheng Y, Shi L, Wang R, Gao L, et al. Lithographic printing inspired in-situ transfer of MXene-based films with localized topo-electro tunability for high-performance flexible pressure sensors. Nano Res 2023;16:12670–9. https://doi.org/10.1007/s12274-023-5974-6.
[938] Ravikumar T, Thirumalaisamy L, Thomas A, Nallakumar S, Pandiaraj S, Mr M, Alodhayb AN, Pitchaimuthu S, Dananjaya V, Abeykoon C, Sivaperuman K. Impact of annealing temperature on the response and sensitivity of spinel $ZnFe_2O_4$ thin film to ammonia gas sensing at room temperature. Materials Today Chemistry 2025;43:102515. https://doi.org/10.1016/j.mtchem.2025.102515.
[939] Dananjaya SV, Fortichiari C, Perera YS, Dasanayaka CH, Abeykoon C. Investigation of the effect of reprocessing on thermal and mechanical properties of polymers and polymer nanocomposites. Advanced Engineering Materials 2025;27(2):2401260. https://doi.org/10.1002/adem.202401260.
[940] Li M, Wang S, Wang Q, Ren F, Wang Y. Preparation, microstructure and tensile properties of two dimensional MXene reinforced copper matrix composites. Materials Science and Engineering: A 2021;803:140699. https://doi.org/10.1016/j.msea.2020.140699.